Aspects of Quantum Transport in DNA origami nanostructures and in topological Kondo insulator SmB_6

Matthew Steggles

Wolfson College

University of Oxford

A thesis submitted for the degree of

Doctor of Philosophy

Michaelmas term 2023

'I urge you to please notice when you are happy, and exclaim or murmur or think at some point, "If this isn't nice, I don't know what is."'

- Kurt Vonnegut

Acknowledgements

There are a great many people without whom this thesis would not exist and I would like to extend the full depth of my gratitude to all of them.

I would first like to thank the many people in the Oxford Condensed Matter department who have helped make this thesis a reality. First and foremost among these are my supervisors Arzhang Ardavan and Marina Filip and my groupmate Junjie Liu. Your unfailing patience and guidance when I was struggling helped me through tough times. To Junjie in particular; you taught me nearly everything I know about nanofabrication and experimentalism. My warm thanks also goes out to the members of the Quantum Materials subdepartment and room 105, who made me feel extremely welcome.

Next I would like to thank my friends: work kept me busy, but you kept me sane. Thank you all the friendly faces from OUMC: Eddy, Joe, Mats, Leonie, Henry, Emma and many more. Thank you also Oscar, Lewis, Ben and Cleo for your friendship in and out of Oxford. Miska especially, you will forever be my physics sparring partner. I love each and every one of you greatly.

My gratitude is also extended to my family. Mum, Dad and Jamie, you have always supported me through everything and you are always in my heart. To my partner, Jess: your endless love and comfort means nothing less than the world to me. This simply would not have been possible without you.

I finally would like to graciously acknowledge the extensive financial support of EPSRC and the Oxford Physics department, who funded me throughout my doctoral studies. Thank you sincerely, particularly for your help during and after the Covid pandemic.

Abstract

For the past seventy years, condensed matter physics has produced ever smaller and more energy efficient information processing devices based on quantum transport processes. In order to continue this trend into the future and also to develop platforms for the emerging industry of quantum computing it is necessary to explore new methods. This thesis details two studies performed with the aim of deepening our understanding of the quantum transport in meso- and nanoscale systems such that they might be used in future information processing.

In the first section, I discuss the fabrication, measurement and characterisation of nanogap devices and single molecule electronics. These devices are of strong interest for the role they could play in energy efficient classical computing and as novel qubit platforms. By exploiting DNA origami techniques developed by collaborators, devices can be fabricated with significantly higher yields than current methodologies. The major result of this is the fabrication of high yield nanogaps and a possible Copper porphyrin molecular device. This moves us significantly closer to achieving the deterministic fabrication of devices with multiple functional molecular components.

In the second section, I present a theoretical study of the surface states of SmB_6, a topological insulator. These materials are of strong interest in spintronics due to their spin polarised surface states. I demonstrate DFT studies that accurately reproduce some of the important experimentally observed features, providing insight into the role of interactions in the material.

Contents

List of Figures

Part I

Novel approaches to fabrication in single molecule electronics using DNA origami

1

Introduction

1.1 Introduction to single molecule electronics

Over the past decades, the world has been dominated by miniaturised Silicon based devices. Silicon information processing devices have shrunk by orders of magnitude since the 1980s with feature size down to the single nanometre scale, but the past decade has begun to see the faltering of Moore's law. Fundamental limitations on the scaling down of devices due to complications in fabrication and lack of understanding of transport mechanisms inhibit further progress. Further miniaturisation requires a greater level of control over degrees of freedom at the nanoscale, and therefore requires a mature knowledge of *nanotechnology*. This term was coined in the 1970s and became more widely known in the public eye following the popularisation of Feynman's lecture 'There's Plenty Room at the Bottom [1].' Throughout this thesis nanotechnology will be defined as the study and development of technological and

scientific methods for the control of matter at the single nanometre and atomic scales. Note that this is distinct from the way some authors have used the word to mean something similar but at anything under micron scale.

One such avenue of research for improving the understanding of transport at the nanoscale and developing control at this scale is single molecule electronics [1]. In 1974, Aviram and Ratner presented a model [2] for a rectifier based around a single molecule (figure 1.1), featuring electron donor and acceptor sites as analogues of the p/n junction in a conventional rectifier, separated by an insulating central region. This demonstrated for the first time the plausibility of using organic and molecular devices to achieve the same function as semiconductor based systems. There are several clear advantages to the use of molecules here; molecules are extremely small, on the order of 1 nm. These factors provide us with an excellent opportunity to improve on the current state of nanoelectronics, firstly in their own right if molecular electronic devices may be fabricated reliable and scalably and secondly for the role they may play in elucidating the quantum mechanical mechanisms in transport in interacting systems. The small Hilbert spaces of molecules provide an excellent potential experimental playground for exploring quantum transport in detail and may be thought of as qualitatively similar to quantum dots, exhibiting many analagous behaviours [3] [4].

Another major motivator for developing molecular electronics is their use in quantum information processing [5] [6]. The tunability of molecular devices offers a compelling route towards designing platforms for quantum information that give distinct advantages in the short to medium term. In a manner similar to spin qubit transistors in defect based semiconductor quantum computers [7], molecular devices can be used to implement the manipulation of single nuclear spins [8] [9]. The nuclear spins in transition metal complexes have higher spins than single electrons,

[1] I shall henceforth use the phrases single molecule electronics and molecular electronics interchangeably, although strictly speaking this is loose terminology as mesoscale and ensemble molecular electronic devices have been investigated.

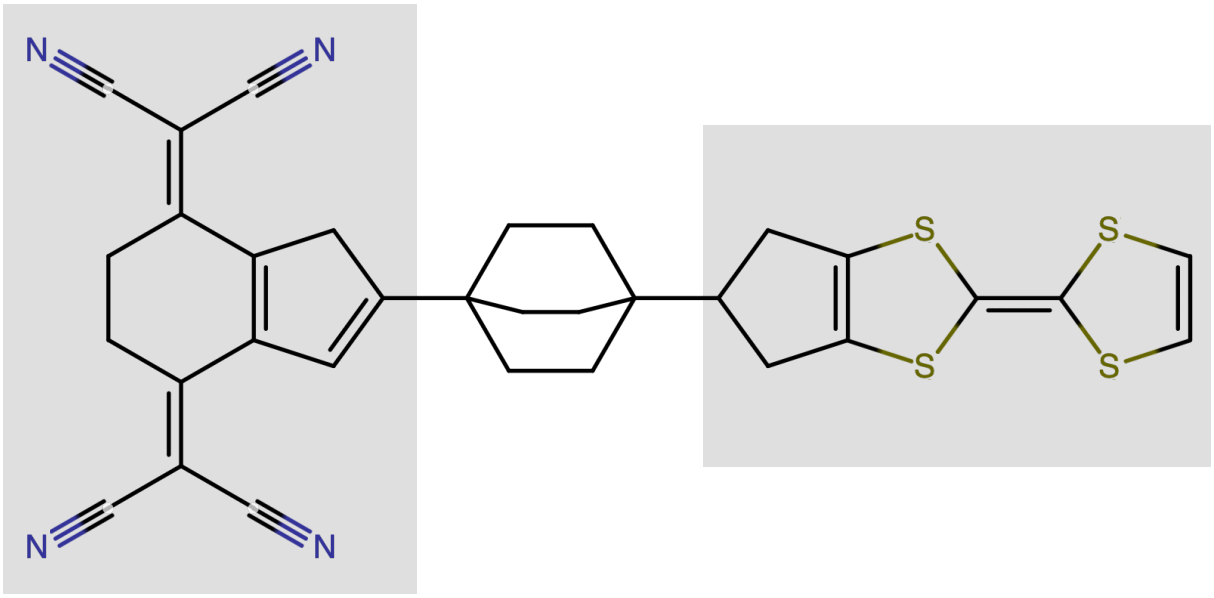

Figure 1.1: Aviram and Ratner's example of a rectifying molecule. The group on the left can accept electrons as the nitrogen nuceli are partially exposed and the group on the right can donate electrons from the sulfur lone pairs. The central organic section is insulating. [2]

so can be used as qudits; the size of the Hilbert space accessible for quantum information processing from N coupled spin s qudits is $(2s+1)^N$. If, as technology currently permits, only a relatively small number of qubits (qudits) may be coupled together, then a large advantage could be gained through coupling higher spin systems together. A second benefit is that the coherence times of nuclear spins can be many times longer than for electron spins as they are only weakly coupled to the environmental degrees of freedom.[2]

Possibly the largest current issue in single molecule electronics is the reliability and scalability of fabrication. In order to use molecular systems in classical information processing contexts, the natural next step after fabricating single molecule transistors is scaling up to a logic gate. Unfortunately, this has proved

[2]This observation is of course not unique to the molecular context and enormous progress on silicon-photonic qudit computers has been made in recent years [10]

extremely difficult; some progress has been achieved in engineering molecules with native logic gate capabilities [11], but connecting together multiple molecular devices reliably to achieve a molecular integrated circuit remains out of reach. The extremely small scale of devices presents a significant problem for fabrication and several ingenious methods have been already devised, summarised in 1.2. Each of these have their own benefits and drawbacks, relying either on stochastic processes or being nonscalable for other reasons. In this thesis I will present experimental work developing a novel method that is reliable, reproducible and plausibly scalable. The hope is that these techniques may eventually be used to achieve molecular devices with multiple functional molecular components.

1.2 Existing approaches to molecular electronics

Here I shall summarise the main classes of device fabrication methodologies conventionally used in the field. The first class is the use of break junctions and encompasses several closely related techniques, although the underlying principle is similar enough to group them. The second is the use of Scanning Tunnelling Microscopy (STM) on molecules deposited on surfaces. Both methods have seen significant success, replicating some of the rich quantum phenomena familiar from quantum dots, such as single electron transport [12], quantum interference [13] and Kondo resonances [14].

1.2.1 Break Junction techniques

There are several very closely related techniques used frequently in molecular electronics, which I will refer to collectively as Break Junction techniques. They all involve fabricating a conducting device with a constriction where the molecule will eventually be contacted, before using various methods to break a nanometre scale gap. I mention three common ones here for specificity, although variations are also seen:

- **Electromigration:** By preparing a constriction in a gold sample, high voltage and feedback may be applied to migrate gold across to form a gap [15].

- **Electroburned junctions:** In a manner very similar to the above, a piece of graphene can be used in place of gold. Via Joule heating and a feedback mechanism, a gap can be burned out [16].

- **Mechanically controlled break junctions (MCBJ):** By creating a 'bowtie' shaped constriction in metallic contacts with a pivot underneath, applying a bending force can break the constriction. Monitoring the current during this breaking process allows some control over the size of the gap. The molecule can either be deposited into the gap after breaking, or onto the side of the constriction so that it can slide into the gap [17].

Schematic cartoons of these three methods are shown in figure 1.2. These methods have the advantage that the gap precursors are in principle scalable en masse, but there are two drawbacks. The first is that the conformational arrangement of the molecule in the gap is not necessarily guaranteed to be consistent across devices, which can affect transport [18]. Significant progress has been made on remedying this by altering the way the molecule makes contact with the electrodes, by using thiol groups or π-electron systems as anchoring groups (with gold or graphene leads, respectively). The second drawback is more severe: the functional elements are typically applied in solution and allowed to diffuse into the gap. Therefore, the number of molecules positioned in the gap is governed by a Poisson process. This places a fundamental limitation on the maximum yield achievable if a device with exactly one molecule is desired in the gap: Even if every other step of fabrication can be controlled perfectly, the maximum yield from such a process is $1/e = 37\%$. This not only limits the scalability of the methodology but prevents the taking of good statistics on a variety of devices.

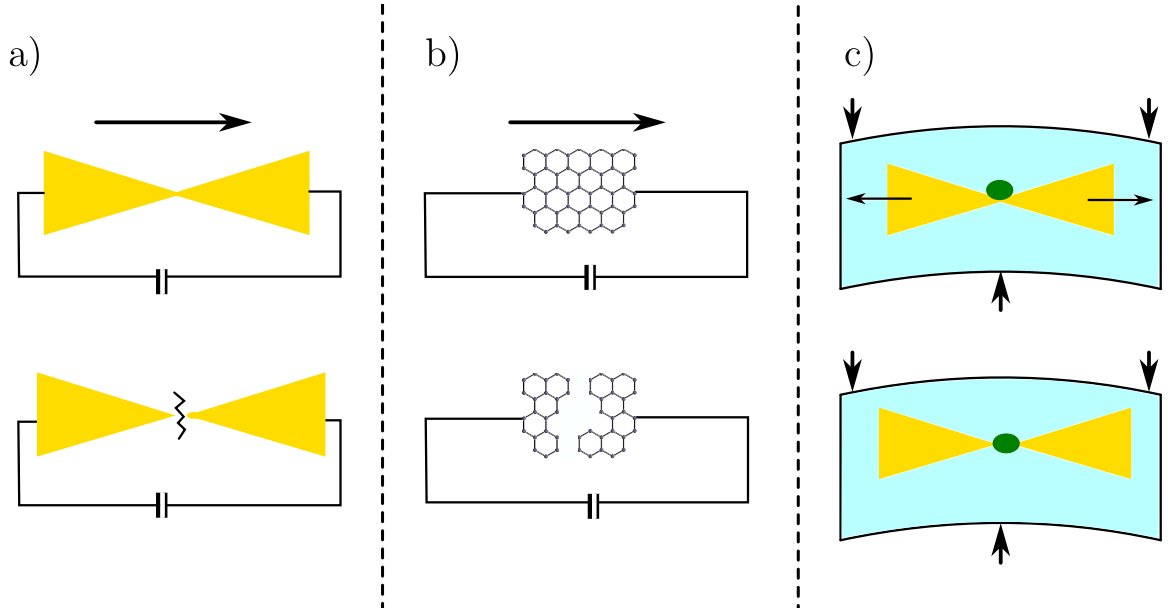

Figure 1.2: Three common approaches to break junction based molecular electronics. a) depicts electromigration, where a current is used to migrate gold atoms across a gap. b) shows electroburning where a similar technique is used to burn a gap in graphene. c) depicts the MCBJ method, where a piezo driven lever is used to distort and then mechanically break the gap.

1.2.2 Scanning Tunnelling Microscopy

Scanning Tunnelling Microscopy (STM) is a form of Scanning Probe Microscopy [19] [20], using an atomically sharp tip to measure a rasterised tunnelling current between the tip and a surface. The method thereby probes the local real space electronic structure of the substrate, and the standard Tersoff-Hamann model [21] finds the differential conductance proportional to the surface density of states $\frac{dI}{dV} \sim g(\varepsilon_{F,\,\mathrm{surface}})$. The atomic precision with which the tip meets the surface makes STM an appealing platform for achieving electrical contact to single molecules. This was first achieved in reference [22], and is a commonly practiced method in the field. A variant of this technique involves repeatedly lifting the STM tip off the surface at kHz frequencies; by identifying the last plateau of resistance before the contact is broken the resistance of the molecule is obtained [23]. The high frequency of measurement allows statistics to be taken. A success of the STM method of contacting devices is that this method leaves relatively little doubt that

a single molecule has been contacted. However, an obvious downside is that STM is not scalable; contacting two or more molecules into a logic gate or comparable information processing device is not reasonable.

1.3 DNA Origami nanoelectronics

A potential solution to the above problems may be found by approaching the problem from a different angle. One should note that the break junction techniques fall broadly under the umbrella of reductive manufacturing, that is, the practice of removing material from a substance in order to achieve a desired geometry. There are no tools which act directly and precisely on the length scales involved, which motivates the use of aforementioned techniques as electroburning and mechanical breakage. However, these have profound implications on the replicability and scalability achievable via these methods, as they crucially lack deterministic control over the atomic scale degrees of freedom. What means, therefore, exist to assemble devices at this scale? In this thesis I will present an alternative method of producing molecular devices via *additive* manufacturing worked on by myself and collaborators, using DNA origami for reliable self-assembly of nanoscale structures which may be contacted into devices. The use of self-assembly provides an elegant solution to the lack of nanoscale control and the unique properties of DNA make it ideally suited to this task.

DNA is an organic polymer that occurs in nature in all cellular life, as a storage repository of genetic information. It comprises two interlocked helices of *nucleotides*, a particular class of organic compounds that have one of 4 functionalisations, denoted A, T, C, G. The two helices are bonded together via hydrogen bonding between these functionalisations, where A may only bond with T and C may only bond with G. It is this specificity and the relative strength of the overall structure that allows DNA to act as a stable store of genetic information [24]. This specificity

however, is precisely a quantity that may be manipulated and consequently used to facilitate the fabrication of nanoscale structures. A schematic image of the structure of DNA is shown in figure 1.3.

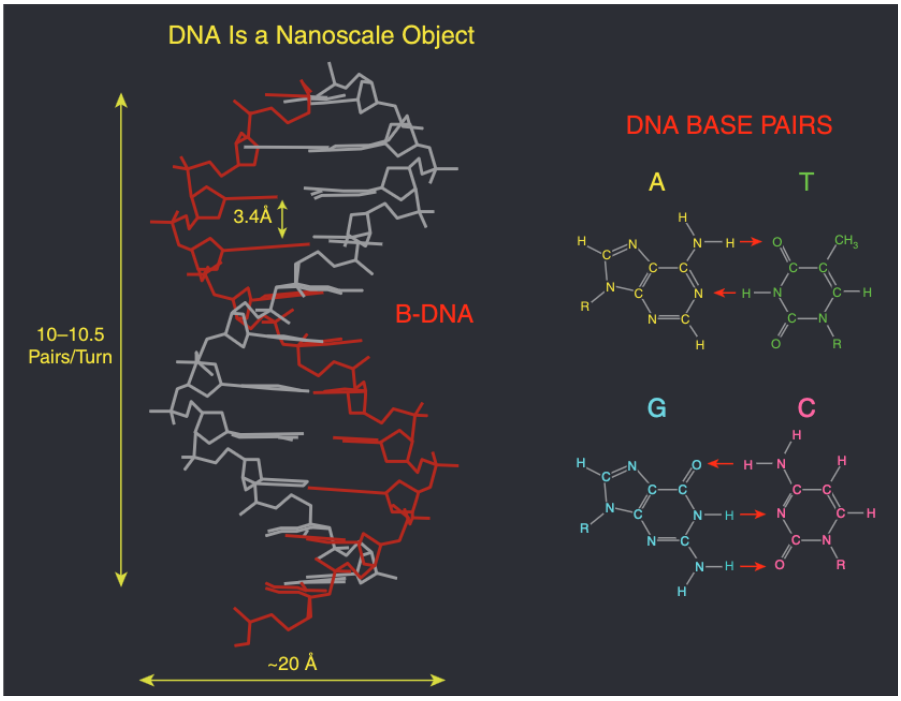

Figure 1.3: The molecular structure of DNA. Two intertwined helices form the backbones, joined by base pairs. Each base may only bond with a specific other base, ensuring the stability of the information storage capabilities of the molecule. Reproduced with permission from [24].

The idea of using DNA in nanotechnological and nanoelectronic contexts has been around for roughly 20 years [25] [24], with various groups exploring the possibility of exploiting DNA's self assembling properties. A major breakthrough came in 2006, when Rothemund devised a particularly powerful method of exploiting the known base sequence of a single strand of DNA for precisely this purpose [26], known as DNA origami. By taking a long strand of DNA and several shorter 'staples', the DNA may be folded into arbitrary 2 and 3 dimensional shapes with high precision. The specific bonding of A to T and C to G guarantees that the staples bond the desired pieces of DNA together.

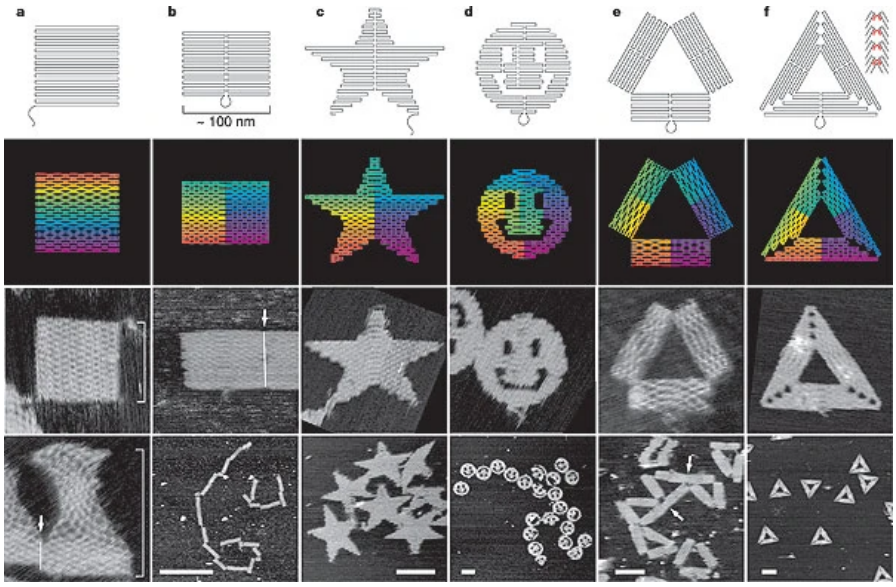

Figure 1.4: Examples of the use of DNA origami to create arbitrary 2D patterns. Patterns shown are for a) square, b) rectangle, c) star, d) smiley face, e) rectangles arranged into a triangle, f) trapezoids arranged into a triangle. The first row is the arrangement of the main DNA strand, the second row shows the twisting orientation of the DNA and is not relevant for my discussion. The bottom two rows are AFM images of the resulting origamis. White arrows show assembly faults. Reproduced with permission from [26].

1.3.1 Application to the fabrication of single molecule devices

This technology may also be applied to the field of molecular electronics. The largest technical problems towards reliable, scalable fabrication of molecular devices are the difficulty with which nanogaps may be reliably produced and the uncertainty in the placing of a molecule in the gap. Significant progress can be achieved by exploiting self-assembling DNA nanostructures. The principle is to construct a 3-dimensional scaffold of DNA origami that can trap single molecules. These molecules are functionalised to DNA oligomers via click chemistry [27] which bond them covalently into the origami. Thiol groups on the molecule then facilitate covalent bonding to gold nanoparticles. These gold nanoparticles are of a suitable lengthscale to use traditional lithographic techniques to construct single molecule devices. The DNA origami structures discussed in this thesis were designed and

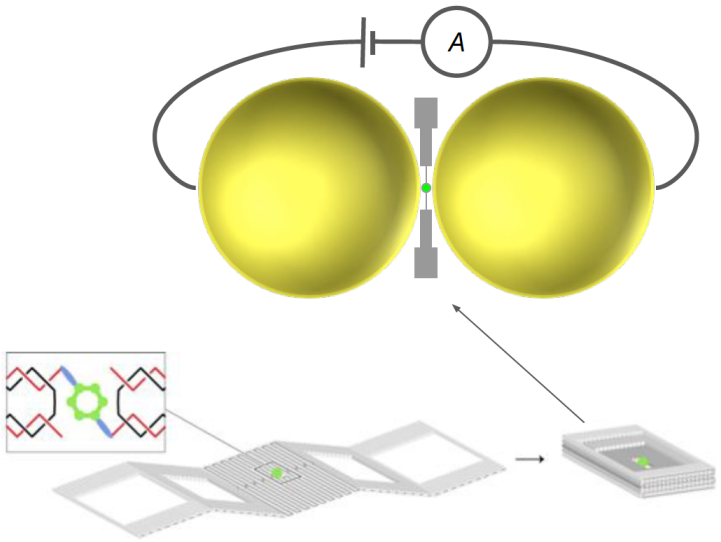

Figure 1.5: A cartoon of the origami layout depicting the central molecule and its formation into the dimer structure. The molecule is placed within a single layer of DNA and covalently bonded to the structure. The DNA may then fold to attach the dimers. Reproduced with permission from [28].

made by Dr Seham Helmi, in the group of Andrew Turberfield of Oxford Biophysics. The design of the DNA scaffolding is depicted in figure 1.5 and consists of a central 'hole' for the molecule surrounded by a solid ring of DNA and two regions of negative space to make room for two gold nanobeads, which will be attached to leads to create a device. The nanoparticles themselves are 60 nm across and oligofunctionalised, that is, they are covered in a monolayer of short strands of DNA. This allows them to dissolve into the DNA origami, stabilising the structure further. The method produces stable, consistent nanobead dimers, as seen under atomic force microscopy (AFM) in figure 1.6. Beads 60 nm across are chosen as they strike a balance between availability and being as small as possible while still allowing a reasonable contacting area with electron beam lithography.

The most crucial aspect of this procedure, which addresses the shortcomings of other methods, is that the device assembly process arising from this is deterministic, not stochastic. The origami design allows only one molecule to enter in a specific

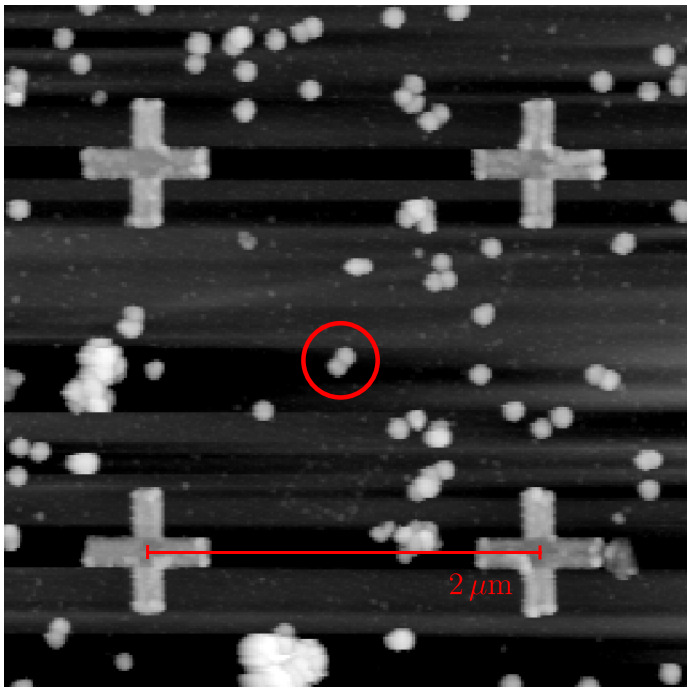

Figure 1.6: An AFM image of a device site, with many nanobeads. Several dimers are visible, with one ringed in red for clarity.

orientation. This allows a highly specific method of contacting the devices, where one set of leads corresponds to at most one molecule that is highly likely to be in a known conformational arrangement with the leads. This contrasts with the previously described methods relying on applying molecules in solution to the device and guiding them into the gap, which are fundamentally stochastic. The potential benefits of this are clear: in order to develop scalable molecular nanoelectronics it is crucial to have sufficient control over the nanoscale fabrication of devices to allow the contacting of *multiple* molecules or of *multiterminal* molecular devices. Achieving this is brought significantly closer to being within reach with deterministic control over fabrication.

References

[1] Richard P. Feynman. “There’s Plenty of Room at the Bottom”. In: *Feynman and computation*. CRC Press, 2018.

[2] Arieh Aviram and Mark A. Ratner. “Molecular rectifiers”. In: *Chemical Physics Letters* 29.2 (1974), pp. 277–283. URL: https://www.sciencedirect.com/science/article/pii/0009261474850311.

[3] Mickael L. Perrin, Enrique Burzurí, and Herre S. J. van der Zant. “Single-molecule transistors”. en. In: *Chemical Society Reviews* 44.4 (2015), pp. 902–919. URL: http://xlink.rsc.org/?DOI=C4CS00231H (visited on 04/06/2020).

[4] Dong Xiang et al. “Molecular-Scale Electronics: From Concept to Function”. In: *Chemical Reviews* 116.7 (Apr. 2016). Publisher: American Chemical Society, pp. 4318–4440. URL: https://doi.org/10.1021/acs.chemrev.5b00680 (visited on 03/06/2023).

[5] Michael N. Leuenberger and Daniel Loss. “Quantum computing in molecular magnets”. en. In: *Nature* 410.6830 (Apr. 2001). Number: 6830 Publisher: Nature Publishing Group, pp. 789–793. URL: https://www.nature.com/articles/35071024 (visited on 03/29/2023).

[6] Eufemio Moreno-Pineda et al. “Molecular spin qudits for quantum algorithms”. en. In: *Chemical Society Reviews* 47.2 (Jan. 2018). Publisher: The Royal Society of Chemistry, pp. 501–513. URL: https://pubs.rsc.org/en/content/articlelanding/2018/cs/c5cs00933b (visited on 03/29/2023).

[7] Andrea Morello et al. “Single-shot readout of an electron spin in silicon”. In: *Nature* 467.7316 (2010), pp. 687–691.

[8] Romain Vincent et al. “Electronic read-out of a single nuclear spin using a molecular spin transistor”. en. In: *Nature* 488.7411 (Aug. 2012). Number: 7411 Publisher: Nature Publishing Group, pp. 357–360. URL: https://www.nature.com/articles/nature11341 (visited on 03/29/2023).

[9] C. Godfrin et al. “Operating Quantum States in Single Magnetic Molecules: Implementation of Grover’s Quantum Algorithm”. In: *Phys. Rev. Lett.* 119.18 (Nov. 2017). Publisher: American Physical Society, p. 187702. URL: https://link.aps.org/doi/10.1103/PhysRevLett.119.187702 (visited on 03/29/2023).

[10] Yulin Chi et al. “A programmable qudit-based quantum processor”. en. In: *Nature Communications* 13.1 (Mar. 2022). Number: 1 Publisher: Nature Publishing Group, p. 1166. URL: https://www.nature.com/articles/s41467-022-28767-x (visited on 04/05/2023).

[11] Fanben Meng et al. “Orthogonally modulated molecular transport junctions for resettable electronic logic gates”. en. In: *Nature Communications* 5.1 (Jan. 2014). Number: 1 Publisher: Nature Publishing Group, p. 3023. URL: https://www.nature.com/articles/ncomms4023 (visited on 04/05/2023).

[12] Sergey Kubatkin et al. “Single-electron transistor of a single organic molecule with access to several redox states”. In: *Nature* 425.6959 (2003), pp. 698–701.

[13] Marco Carlotti et al. “Systematic experimental study of quantum interference effects in anthraquinoid molecular wires”. In: *Nanoscale Adv.* 1 (5 2019), pp. 2018–2028. URL: http://dx.doi.org/10.1039/C8NA00223A.

[14] Gavin David Scott and Douglas Natelson. “Kondo Resonances in Molecular Devices”. In: *ACS Nano* 4.7 (2010). PMID: 20568709, pp. 3560–3579. eprint: https://doi.org/10.1021/nn100793s. URL: https://doi.org/10.1021/nn100793s.

[15] Hongkun Park et al. “Nanomechanical oscillations in a single-C60 transistor”. In: *Nature* 407.6800 (2000), pp. 57–60.

[16] Ferry Prins et al. “Room-Temperature Gating of Molecular Junctions Using Few-Layer Graphene Nanogap Electrodes”. In: *Nano Letters* 11.11 (2011). PMID: 22011188, pp. 4607–4611. eprint: https://doi.org/10.1021/nl202065x.

[17] Mark A Reed et al. “Conductance of a molecular junction”. In: *Science* 278.5336 (1997), pp. 252–254.

[18] Latha Venkataraman et al. “Dependence of single-molecule junction conductance on molecular conformation”. In: *Nature* 442.7105 (2006), pp. 904–907.

[19] Ke Bian et al. “Scanning probe microscopy”. en. In: *Nature Reviews Methods Primers* 1.1 (May 2021). Number: 1 Publisher: Nature Publishing Group, pp. 1–29. URL: https://www.nature.com/articles/s43586-021-00033-2 (visited on 03/06/2023).

[20] G. Binnig, H. Rohrer, Ch. Gerber, and E. Weibel. “Surface Studies by Scanning Tunneling Microscopy”. In: *Phys. Rev. Lett.* 49.1 (July 1982). Publisher: American Physical Society, pp. 57–61. URL: https://link.aps.org/doi/10.1103/PhysRevLett.49.57 (visited on 04/24/2023).

[21] J. Tersoff and D. R. Hamann. “Theory of the scanning tunneling microscope”. In: *Phys. Rev. B* 31.2 (Jan. 1985). Publisher: American Physical Society, pp. 805–813. URL: https://link.aps.org/doi/10.1103/PhysRevB.31.805 (visited on 03/29/2023).

[22] L. A. Bumm et al. “Are Single Molecular Wires Conducting?” In: *Science* 271.5256 (1996), pp. 1705–1707. eprint: https://www.science.org/doi/pdf/10.1126/science.271.5256.1705. URL: https://www.science.org/doi/abs/10.1126/science.271.5256.1705.

[23] Suman Gunasekaran et al. “Near Length-Independent Conductance in Polymethine Molecular Wires”. In: *Nano Letters* 18.10 (2018). PMID: 30187756, pp. 6387–6391. eprint: https://doi.org/10.1021/acs.nanolett.8b02743. URL: https://doi.org/10.1021/acs.nanolett.8b02743.

[24] Nadrian C. Seeman. “DNA Nicks and Nodes and Nanotechnology”. In: *Nano Letters* 1.1 (2001), pp. 22–26. eprint: https://doi.org/10.1021/nl000182v. URL: https://doi.org/10.1021/nl000182v.

[25] Erez Braun, Yoav Eichen, Uri Sivan, and Gdalyahu Ben-Yoseph. "DNA-templated assembly and electrode attachment of a conducting silver wire". In: *Nature* 391.6669 (1998), pp. 775–778.

[26] Paul W. K. Rothemund. "Folding DNA to create nanoscale shapes and patterns". en. In: *Nature* 440.7082 (Mar. 2006). Number: 7082 Publisher: Nature Publishing Group, pp. 297–302. URL: https://www.nature.com/articles/nature04586/ (visited on 01/16/2023).

[27] Hartmuth C Kolb, MG Finn, and K Barry Sharpless. "Click chemistry: diverse chemical function from a few good reactions". In: *Angewandte Chemie International Edition* 40.11 (2001), pp. 2004–2021.

[28] S Helmi and A Ardavan. Private communication. Jan. 2020.

2

Methodology: Device design and theoretical methods

In the previous chapter I introduced the design of the DNA origami/nanogold dimers that constitute the functional component of the devices, and in this chapter I will discuss the methods used to transform these into a working device, from device architecture to fabrication. I shall emphasise the specifics of the lithographic processes and some of the challenges we faced as well as the computational methods required to locate prospective molecular devices.

I would like to acknowledge the collaboration of several people who have developed various parts of this process. Dr Junjie Liu developed the original nanofabrication protocols for SEM imaged devices, which we then both modified extensively. The DNA origami dimer structures were produced by Dr Seham Helmi of Prof Andrew Turberfield's group in Oxford Biophysics and the molecules were syn-

thesised by Dr Keith Andrews of Prof Harry Anderson's group in Oxford Chemistry.

2.1 Device Design

There are several main steps between receiving the nanostructures and being able to measure them as completed devices:

- Deposition
- Location of nanostructures
- Device lithography.

The overall chip architecture consists of a four by four grid of device locations, minus the bottom right position, giving up to 15 devices per chip. Each device location has lithographically etched chip markers to provide good alignment through later stages of fabrication, surrounding a grid of local coordinates (used interchangeably with 'fiducial markers' or 'fiducials' throughout this text) into which the dimers are deposited. These local coordinates are used to accurately locate the deposited dimers using microscopy and computational image processing techniques, then a lead pattern designed that can contact the dimer structure. These contacts connect to the chip pinout in such a way as to connect to braided pairs in the transport probe (for details of the measurement methodology, refer to 3.1). Figure 2.1 shows the large scale architecture of the chip under optical microscopy.

Given that accurately locating and contacting the devices comprises a significant source of the difficulty of the project it is worth briefly discussing a plausible alternative to this that was not used and the reasons why. Given the size of the devices, it could be suggested to use dielectrophoresis/electromigration and a feedback mechanism to electrically guide the molecule into the gap, such as explored in references [29] and [30]. There are two downsides to this: firstly and most importantly it shares the same drawback as break junction techniques in

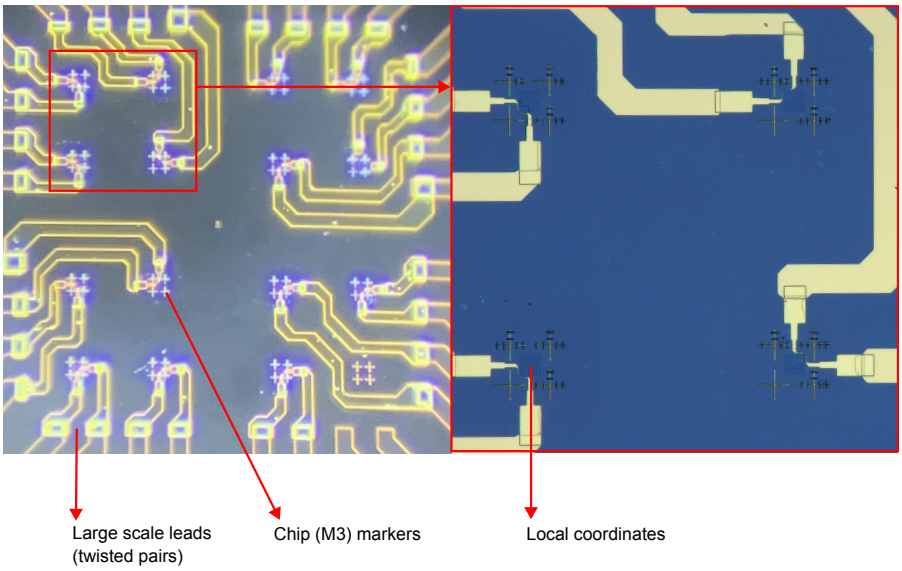

Figure 2.1: The large scale architecture of the chip. Labelled are the large scale leads, which connect to twisted pairs in the measurement setup. The M3 markers provide greater alignment for fine scale exposures at the device locations and the local coordinates are used to locate the deposited dimers.

that the contacting is stochastic and therefore by the arguments of chapter 1 it is unsuitable for scalable molecular electronics. Secondly, the high impedance of the devices (on the order of many Gigaohms for nanogap tunnelling devices) makes current based feedback unfeasible.

2.2 Device fabrication

Having established the principle of using DNA origami structures to stabilise functionalised molecules into a device, I will now describe the fabrication process. The question to be answered is whether standard lithographic recipes can be used to interface with the DNA nanotechnology components to produce working devices. The ability to use standard lithographic techniques is strongly desirable, given that we set out to develop scalable and replicable methods for molecular electronic fabrication. I will describe the standard methods in section 2.2.1 before detailing the modifications made to the methods for our fabrication process in

section 2.2.2. An overview of standard methods in nano- and microfabrication can be found in, for example, reference [31].

2.2.1 Principles of lithography

In order to distinguish the specific fabrication requirements of our devices, I must first describe the standard procedure used to produce lithographically defined structures. Each step is shown schematically in diagram 2.2.

I The substrate must be cleaned extremely thoroughly to guarantee nanoscale cleanliness. Rinsing the wafer in acetone and then isopropyl alcohol, then drying with purified Nitrogen leaves the wafer very clean.

II A layer of photoresist is applied with a spin coater and then typically baked. Some fabrication processes use multiple layers baked onto the wafer.

III The photoresist is exposed using an electron beam. The exposure breaks chemical bonds in the photoresist and the resulting products are soluble in developer solutions. Careful control of the dose allows production of a good undercut; scattering of the secondary electrons produces the hemispherical overhanging pattern in figure III. The undercut is extremely important as it allows the evaporation steps to not interfere with the resist, leading to a clean lift off. The exposure process often leaves a thin layer of organic residue, so to guarantee nanoscale cleanliness before evaporation the sample should then be 'descummed,' typically by exposing the device to oxygen plasma.

IV The first evaporated layer can then be applied. The final traces in our case are made of 99.99% gold, but the adhesion properties of gold on the Silicon dioxide substrate are poor. Standard practice is to use a thin layer with better adhesion, such as a 5 nm layer of chromium.

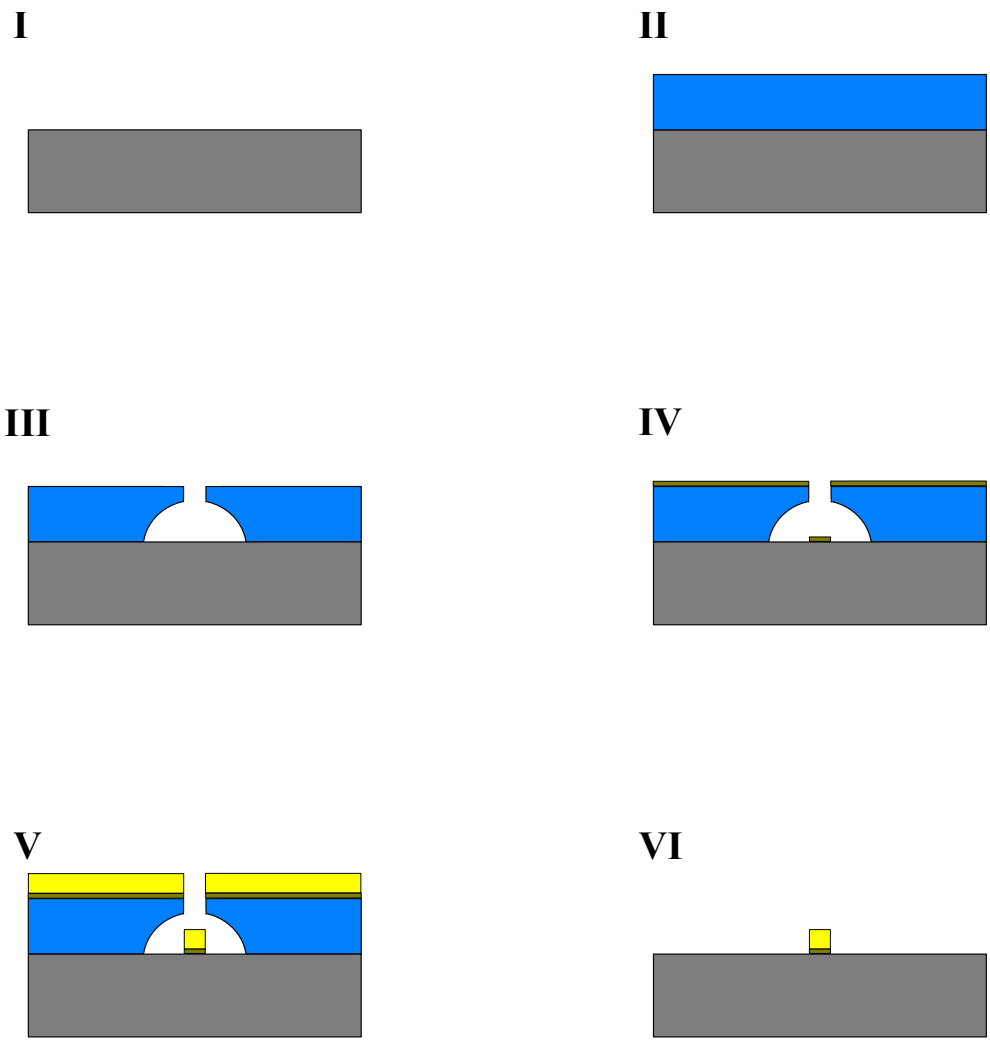

Figure 2.2: The lithography procedure, outlining visually the 6 steps detailed in the main text. The scales have been exaggerated for visual clarity.

V The main trace can now be applied. The main layer is gold, which adheres well to the chromium layer. In order for the trace to not interfere with the resist, the thickness should be no more than around a third of the thickness of the resist. This highlights the importance of a good undercut in getting a good trace.

VI The photoresist can be dissolved off using an appropriate solvent, typically heated to around 60 degrees. There is a large surface area of contact between the resist and the substrate so using ultrasonic vibration (sonication) is often useful to remove the excess gold. This leaves behind the evaporated structure.

2.2.2 Specific challenges for the fabrication of DNA origami molecular devices

The above demonstrates the general principle of lithography as it is commonly practiced in materials science. Nonetheless, the specific requirements of any fabrication process inform the exact recipe that should be used. I shall therefore elaborate on the processes and any relevant modifications used to fabricate our devices. All techniques used are viable in a conventional clean room, using standard machines and processes, albeit sometimes in nonstandard ways[1]. The major challenge of the device fabrication procedure is to have high confidence on the exact location of the deposited molecular devices with respect to the local coordinates while not damaging the relatively fragile DNA. These specific requirements of extremely high resolution and noninvasiveness inform the choice of resist and variations on the processing. The nanobeads are 60 nm in diameter, and a sufficient gap must be left between the leads to make space for the device and also to prevent shorting during fabrication. This constrains the placement of the leads to be aligned to a roughly 20 nm by 20 nm area on each bead. Analysis of the

[1]Such as using single resist layers and RIE descumming, detailed in this section.

feasibility of this is presented in section 2.3.3.

Masking off the grid

Each chip is prepared with 15 sets of lithographically defined local coordinates, aligned with respect to individual chip (M3) markers. These will form the basis of the location detection algorithms explained in 2.3. However, before deposition of the samples these coordinates must be masked off. Resist is applied and exposed to leave a mask over the gold local coordinates. This is required because when the nanobeads are deposited in solution, they perform a random walk while the solution dries, until they reach their final locations. If the nanobeads randomly contact the local cooodinates during this process they will stick. This can lead to aggregation of large numbers of nanostructures on the coordinates. Not only does this prevent the dimers from being usable for contacting but the conglomerated beads interfere with the local marker detection used in the image processing stages.

Choice of resist

The resist used for this and all other parts of the fabrication is PMMA, as it conforms to the requirements of high resolution and noninvasiveness. PMMA is very well understood and can yield a very high resolution when well exposed and developed. Furthermore, the developer (MIBK) and solvent (acetone) used are compatible with the DNA origami structure without destroying it. There is however a departure from standard procedure used here: typically a double layer of resist is applied, with the first layer being of a lower molecular weight. These layers are baked onto the chip, where they undergo a glassy transition to form a strong layer of resist. The double layer aids in the production of a good undercut and therefore an easy liftoff. However, baking the chip is not possible, as the DNA is only stable at temperatures up to around 50 degrees. Single layers can also be used for high resolution purposes, but care is required to have a good undercut to facilitate liftoff.

EBL dosage and development

The exposure and development procedure should also be examined. The requirement to only use a single layer means that our devices will in general be much more sensitive to the quality of undercut. Using a high electron beam dosage can be helpful here, as the greater number of secondary electron scattering events contribute to a larger undercut. This must however be balanced with constraints due to the dimer geometry: to attach leads to a dimer the design must have a gap at the position of the dimer, of at least 50-60 nm so that they do not short during descumming. The secondary electrons which allow for a good undercut can also damage the gap, leading to shorted devices. We find EBL dosages of 1400-1600 μC/cm^{-2} sufficient to fully expose the resist. The development is further influenced by these requirements; high resolutions can be achieved by performing the development at low temperature, which we do at 0 degrees in an ice bath.

Descumming with Reactive Ion Etching

The device geometry has strong implications on the descumming (de-ashing). In order to obtain good ohmic contacts from the lead onto the devices the exposed areas must be extremely clean. The standard practice is to expose the sample to oxygen plasma for a short time to oxidise the (typically nanometre thickness) residues. The aspect ratio and size of the features makes this challenging; the oxygen plasma cleaning can be modelled as a gas of oxygen radicals incident on the surface. The small scale of the leads and contacting area as compare to the resist thickness posed severe challenges. It was frequently (although not always) observed that test devices de-ashed with oxygen plasma, even at high dosages, would not display good ohmic conduction but would show tunnelling behaviour with a characteristic resistance of 20 GΩ. This implies that the plasma is not reaching the deepest part of the exposed area. To attempt to achieve a more reliable etching,

we instead used Reactive Ion Etching (RIE) on subsequent devices, which has a more anisotropic etch pattern and higher etching rate. This helps the plasma to penetrate down to the devices to clean them. Using RIE, ohmic contact yields increased from 10% to near 100% on test devices.

The RIE de-ashing procedure is, however, extremely aggressive, and somewhat inconsistent as a result. I observed that while it was ordinarily possible to preserve a 50 nm gap, suitable for contacting a dimer, occasionally the contacting would be more aggressive unpredictably. When contacting molecular devices (as in chapter 3), this lead to many shorted devices, where the entire gap would be etched away. This is likely caused by fluctuations in the power and gas pressure when the process starts. RIE is typically used for much more aggressive etching processes, removing many tens of nanometres from semiconductors, so it is unsurprising that our approach of using it to descum results in a very delicate recipe, sensitive to timing. There also may be contributions stemming from the difference in electrostatic environment resulting from having a dimer in the gap as compared to an empty tester gap. These issues could potentially be solved by developing a very weak RIE etching process[2] or perhaps using a different plasma etcher[3].

Device cleaning and liftoff

A further difficulty is presented by the nature of the sample's bonding to the surface. As with many fabrication processes involving the deposition of particulate material on a surface, the adhesion is purely from Van der Waals interactions. This makes using sonication impossible, as exposing the deposited samples to ultrasonic risks moving or detaching them from the surface. Even in the event that the dimers merely move and are not removed, this is unacceptable as exact knowledge of the

[2]We tried this, although there are issues with the plasma not striking at lower powers.

[3]We observed also that using a different plasma etcher gave higher yields even at the same nominal dosages, suggesting that the homogeneity of the field distribution inside the chamber is important.

position of each candidate device is required. This has implications in particular for lifting off the evaporated layer: It is common to sonicate at this stage to dislodge the evaporated material, which has a very large surface area in contact with the sample, but this is forbidden. This imposes yet greater constraints on the quality of undercut that must be achieved on the devices when using the electron beam, to make sure the fabricated nanostructure is well separated from the layer of refuse.

2.3 Locating the nanostructures

Once the DNA dimer structures have been deposited onto the substrate, they must be located with respect to the local coordinate system. I have used two microscopy techniques to accomplish this; SEM and AFM. SEM is an efficient and natural choice and was used for the original tests and some of the gap characterisation, but on the molecular samples I used AFM instead. The reasoning is straightforward; the molecules involved are sensitive and we did not know a priori whether they would be damaged by the electron beam or not. I will later be comparing the IV curves from DNA nanogaps produced with AFM imaging and SEM imaging, to assess the invasiveness.

Nevertheless, imaging with AFM holds significant drawbacks as well: it is extremely slow and requires considerable skill to image non invasively with sufficient resolution (What is meant by a 'sufficiently' high resolution will be made precise later in section 2.3.3 when I calculate an estimate for the accuracy of the dimer detection protocol). If the AFM feedback voltage is too aggressive the dimer structures, which are held to the surface purely by Van der Waals' interactions, may be scrubbed off the device. The image quality is also highly sensitive to the surface quality in a manner that SEM is not: organic residues are frequently left behind by the lithography process. As these are nonconductive, they are transparent to the SEM electrons and so do not interfere with the image registration procedure.

However, they contribute to the topography of the chip and therefore are picked up by AFM in a way that can contribute to mislocating the samples.

Having imaged the structures there is a significant problem of image recognition and registration[4] that must be addressed in order to confidently locate the samples. My strategy was to refine the image obtained to binarise it into *features* and *background*, then to use image recognition techniques to register the local coordinates. These can be used to provide accurate coordinates for the dimers.

2.3.1 Image processing I: background detection algorithm

The AFM images as obtained often contain 'trenches' where the bottom values of the amplitude trace are not correctly aligned with subsequent rows. If the local coordinates may be removed from the image, then by aligning the mean values of the lines this error can be corrected. The separation of image into foreground and background proceeds via a process of k-means classification. K-means classification is an unsupervised learning technique capable of generating labels on 'clusters' of data, separating it into k classes [32]. This is commonly used to categorise high dimensional data, but also provides a convenient way of segmenting the image into 2 classes: 'foreground' and 'background.' Given that the pixel brightness is the only parameter, k-means classification is exactly equivalent to Otsu's method for segmentation [33].

The segmentation method applied to the images is fairly effective due to the large separation in length scales between foreground and background; the features are of height 60 nm and the background is of approximately constant height. Once partitioned, the background layer may be aligned by offsetting the mean height of each line such that they are all equal. It is to be noted that doing this once is often insufficient, but that iterating applications of this method converges with near certainty very quickly to a sufficiently accurately binarised image. This is a

[4]The process of matching the position of known objects to an image is known in computer vision as registration.

nontrivial assertion and does not hold in complete generality but follows in this case from the fact that the misregistration that typically occurs is assigning a piece of cross to the 'background' layer, when it is near a deep trench. The alignment step will then increase its amplitude, bringing it in line with the characteristic height of the foreground layer. The stages of this process and the result are shown in figure 2.3.

2.3.2 Image processing II: detecting local coordinates

Now that the areas containing deposited gold have been correctly identified, the local coordinates may be detected. The method I have employed to do this is by first using frequency domain cross-correlation techniques to obtain a rough position using a template, then by edge detection techniques to better estimate the centre of each cross.

Given that the size of the coordinates is known to reasonable accuracy, and the size of the image known too, a template of approximately the size of the cross may be easily generated. The principle of the preprocessing step is to identify regions with a high degree of similarity to the template. Finding approximate locations of this template on the image can be performed by taking the cross correlation with the whole image. In the continuous 1-dimensional case this operation is described by:

$$[f * g](\tau) = \int_{-\infty}^{\infty} \mathrm{d}t f(t)^* g(t+\tau) \tag{2.1}$$

with $f(t)^*$ denoting the complex conjugate. In the case of an image, f and g are real, discrete 2-dimensional functions and the cross-correlation reduces to the matrix convolution with elements

$$[f * g]_{m,n} = \sum_i \sum_j f_{i,j} g_{m-i,n-j} \tag{2.2}$$

where areas of the target image that match the target have a greater cross-correlation.

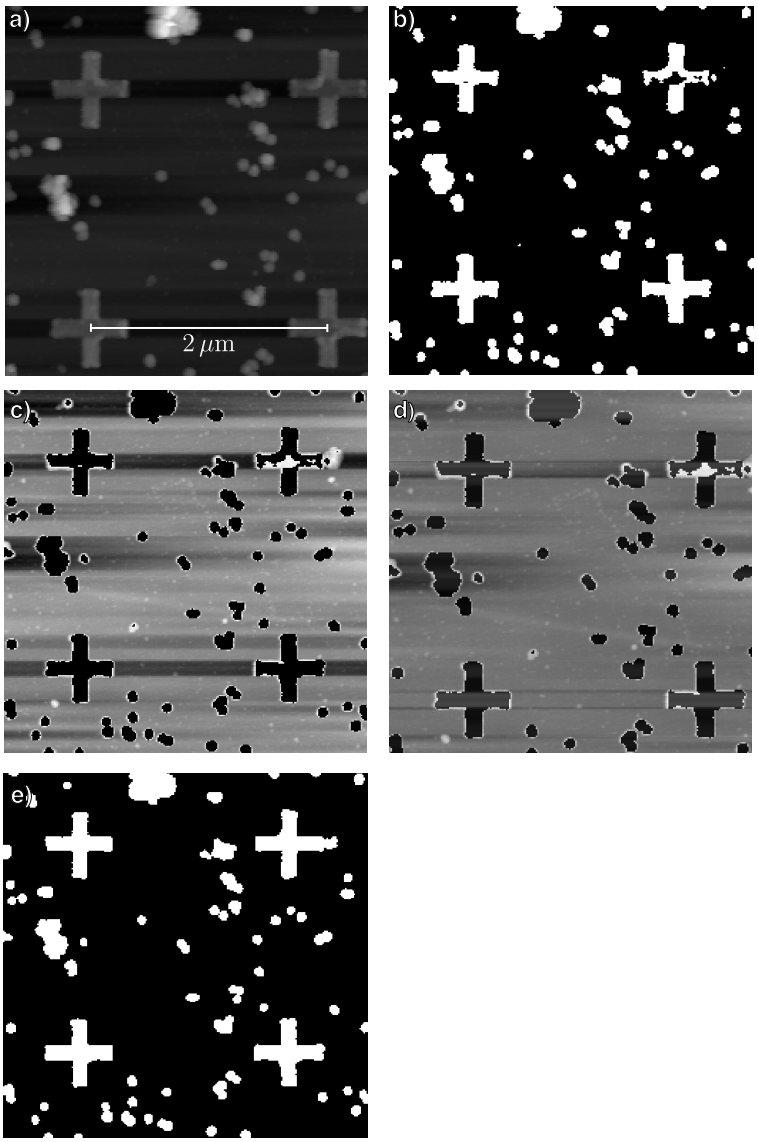

Figure 2.3: Illlustration of the k-means binarisation procedure. Figure a) shows the unprocessed AFM image, including the trench shaped visual artefacts between the fiducials. Figure b) shows this image once binarised using k-means. Notice the top right cross is not correctly identified. Figures c) and d) show the background layer identified by k-means before and after one iteration of the levelling procedure. Figure e) shows the binarised image after several iterations of this method. The top right cross has been healed and is correctly binarised.

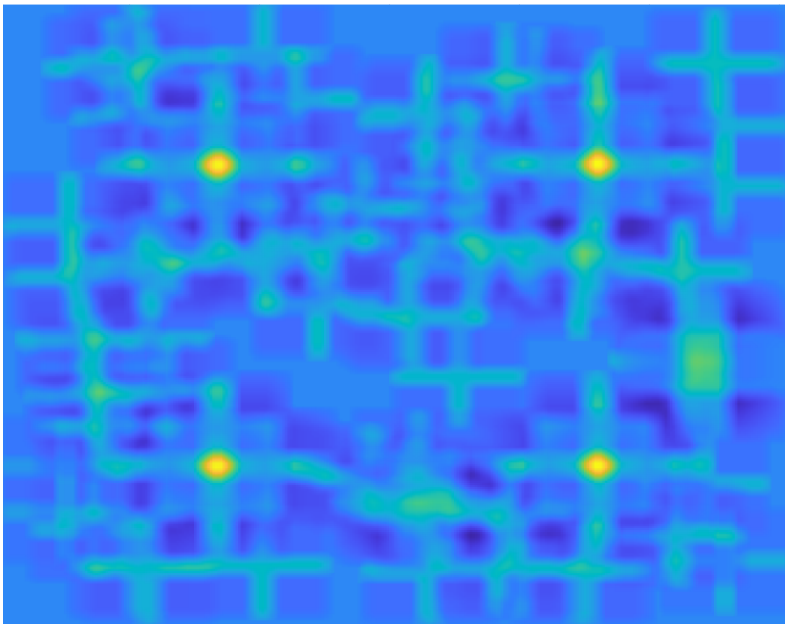

Figure 2.4: The cross correlation resulting from convolving figure 2.3 with a cross shaped template. The bright yellow local maxima are the 4 candidate positions for the local coordinates.

This operation can be performed fairly efficiently in the frequency domain where the convolution becomes a simple multiplication. The peaks of the resulting matrix after transforming back correspond to approximate positions of the local coordinates. The cross correlation of figure 2.3e with the template is shown in figure 2.4.

These candidate positions can then be refined using edge detection. At the location of each candidate cross, a smaller subsection of the image is taken, containing the desired feature. The sides of the crosses constitute a set of 4 lines; two vertical, two horizontal (allowing the lines to 'skip' over the middle of the cross). By finding a method to identify these lines the implied centre of the cross can be calculated and therefore the local coordinate system can be linked to the larger features of the chip. To accomplish this I have used a method based around the Hough transform [34] [35]. This is a transform devised originally for the analysis of bubble chamber traces, although it has been used widely in computer vision since the 1970s for edge

detection. The transform maps the space (x, y) to the space (r, θ) such that

$$\begin{pmatrix} \cos\theta \\ \sin\theta \end{pmatrix} \cdot \begin{pmatrix} x \\ y \end{pmatrix} = r \tag{2.3}$$

where the equation of a line $\hat{n} \cdot \vec{x} = r$ is easily recognised. So, a straight line in (x, y) space is mapped to a single point in (r, θ) space. This can be exploited for detection of lines: peaks in the values of a Hough transformed image correspond well to lines in an image. By detecting maxima in Hough space it is simple to extract lines in the original image. Efficient implementations of this transform are widely available in computer vision packages; I have used Python's `OpenCV` and MATLAB's computer vision library. I have additionally segmented the Hough space into the regions corresponding to $\theta \approx 0$, $\pi/2$, π, $3\pi/2$. This biases the program towards picking only those lines which have a high likelihood of belonging to the local coordinates. The result of identifying lines using this transform is shown in 2.5. The lines identified fall into 4 classes, 1 for each edge of the arms of the crosses as discussed in the previous paragraph. By taking a weighted average within each class I produce a 'representative line' for each side of the cross. Averaging these into one horizontal and one vertical line allows the implied centre of their corresponding cross to be calculated at the intersection. Provided the fiducial markers are clean and isolated, this line detection technique is more robust than the Fourier domain technique, which is sensitive to clusters of beads near the crosses and relies on finding the maximum of a broad, pixellated distribution in Fourier space.

2.3.3 Assessing the accuracy of the predicted positions

The above paragraphs describe the methods I have devised, but it is critical to quantitatively assess the method to be sure that the positions obtained are robust to misregistration of the fiducial markers. There are two plausible causes for this

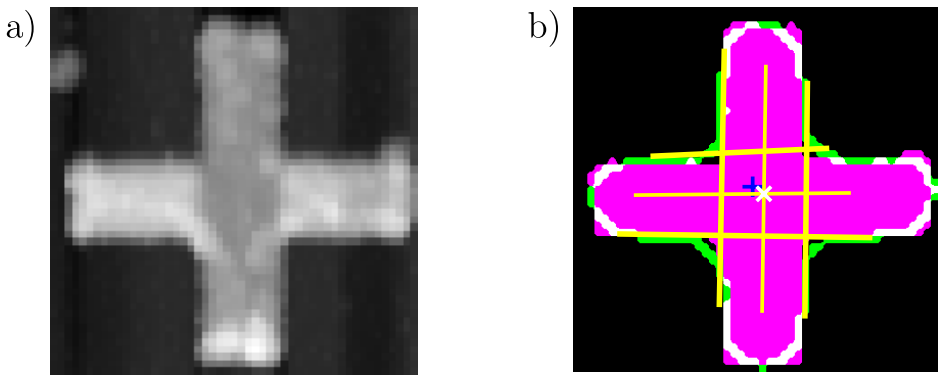

Figure 2.5: The result of using the Hough line detection technique to register the cross' location. The initial trial location is given by the blue 'plus'. The detected lines are in gold, with the implied centre given by the white cross.

kind of error to occur: firstly, in order for the imaging to be practical, the resolution of the scan is limited, potentially impacting the accuracy of the predicted positions. The second is that if the quality of the fiducial markers is compromised, or if the sample has some nanoscale contamination, the centres of the crosses may be misattributed. It is important therefore to numerically test the effects of these errors on the predicted position.

Allow the positions of the crosses $\vec{x}_i$ to be offset by a random small amount $\delta\vec{x}_i$. Allow also the true position of one of the nanobeads to be $\vec{x}_b$, near the middle of the device. Under the random perturbation, the bead is calculated to be at $\vec{a}(\vec{X}_i)$ where $\vec{X}_i = \vec{x}_i + \delta\vec{x}_i$. It is then desired to find the average deviation $\delta = |\vec{x}_b - \vec{a}|$ in the derived position of the bead obtained from the incorrect position of the crosses. This is amenable to a simple Monte Carlo simulation; randomising the position of each cross by gaussian noise $\mu = 0$, $\sigma = 1$ pixel and recalculating the position of the bead allows a estimate for the distribution of errors in bead registration to be obtained. These values were chosen as deviations more than 1 pixel are obvious to the human eye; any candidate devices that return cross positions wrong to a greater degree than this can be analysed by hand. As discussed in 2.2.2, the required precision in the bead's position is <20 nm . The distribution of deviations arising

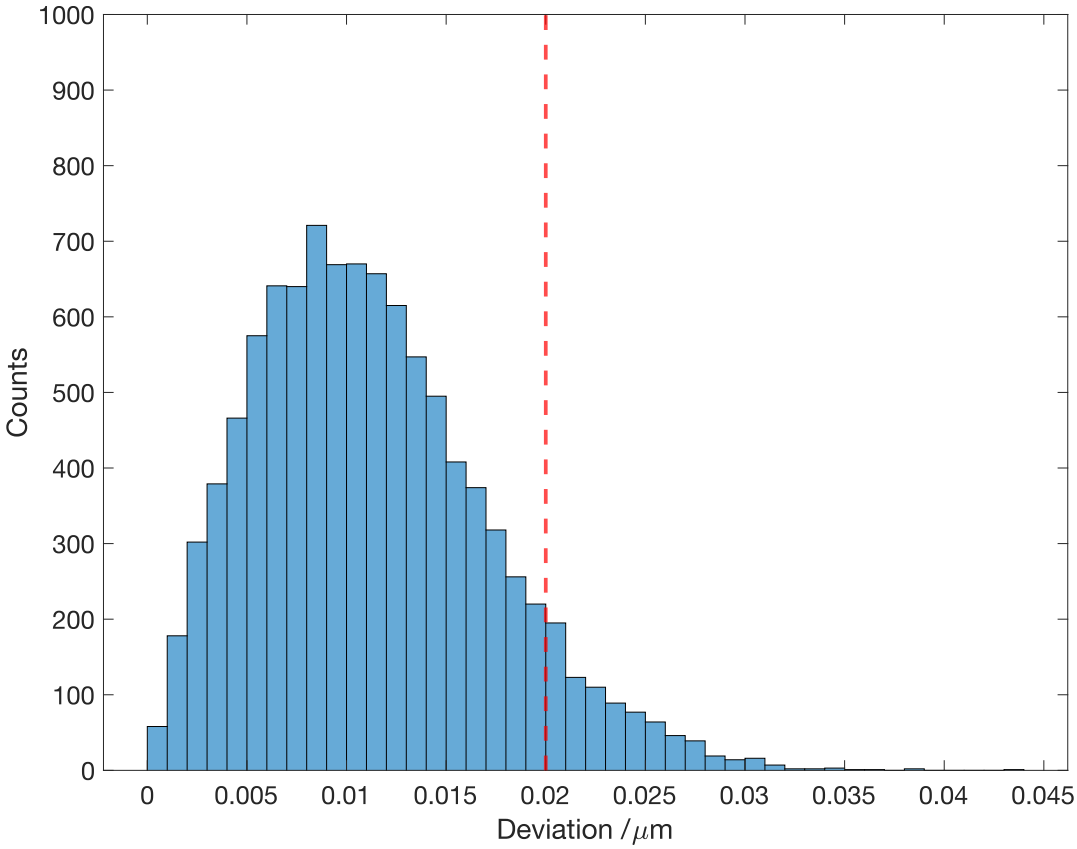

Figure 2.6: The distribution of errors in position for a bead located near the middle of a chip, under random variation of the fiducial marker positions. The red line denotes the required tolerance.

from the Monte Carlo simulation is shown in figure 2.6: the method clearly passes, with mean deviation 11 nm. 8% of the distribution lies outside the acceptable tolerances, but these correspond to multiple crosses being notably misregistered or single crosses being dramatically misplaced. These errors are, as mentioned, visible and devices with particularly bad registration may be processed by hand. This vindicates the effectiveness of the algorithm as well as confirming that the 256×256 pixel AFM image used is sufficient for identifying the bead locations.

2.3.4 Offset correction

An unfortunate reality of working with fabrication at the nanoscale is that equipment can not always be relied upon to produce impeccable focus and alignment; using the given positions for the leads results frequently in misaligned devices, with the offset fairly consistent across a single chip (hosting up to 15 devices). The two most frequent causes of this error are imprecision in the focus used for different stages of the fabrication process and, occasionally, damaged chip markers. To remedy this, a manual focusing procedure was implemented by burning a contamination spot at fixed dose at a fixed location and focusing on this, iterating until good focus is achieved. Repeated exposures using this focusing procedure result in very good alignment. Nonetheless, an extra step was still required to detect any offsets that exist on the chips from exposures prior to using the manual focusing method. A small extra feature of known position and size was added to the edges of some devices. The positions of these markers are easily detectable using similar methods to the above. These offsets were imaged with both AFM and SEM: the offset corrections are sufficiently far away from any of the molecular devices that the risk of secondary electrons ionising the devices is extremely low, and SEM provides a more reliable measurement on long, thin objects like the offset markers. Imaging in AFM as well allows a check on the performance of the AFM location detection compared to SEM. Sample images of the offset markers in AFM and SEM are shown in 2.7. Note the relatively far higher quality achieved in the SEM image.

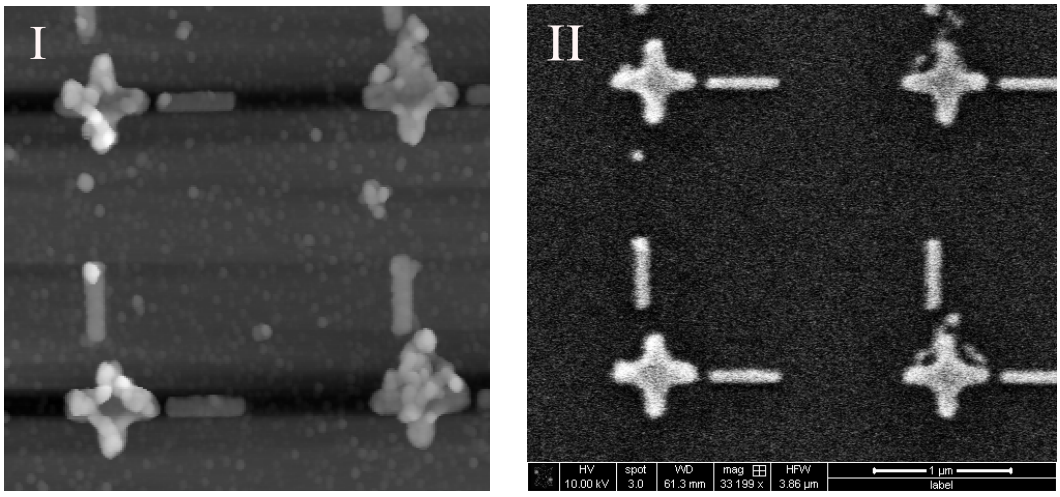

Figure 2.7: AFM (I) and SEM (II) images of the same location, illustrating a set of coordinates with a large offset. The offset markers (vertical/horizontal bars) are meant to be located along the axes defined by the crosses, with the deviation being the result of imprecise focus. There is some organic debris visible to AFM but transparent to SEM at the site of the image.

2.4 Electrostatic screening: Finite element analysis of the device architecture

It is highly desirable on a molecular device given the end goal of post-CMOS information processing to have control over the local electrostatic potential at the molecule, via a gate. The chip architecture was originally designed with this in mind, with a conductive back gate. The devices are separated from this conductive back gate by an oxide layer of thickness 200 nm. This in principle allows for probing the molecular energy levels by sweeping gate voltages, allowing the device to function as a molecular transistor. Nonetheless, when our devices are measured, sweeping the back gate has no measurable effect. In order to diagnose this I modelled the experimental geometry in COMSOL, a commercial finite element solver, as depicted in figure 2.8. The finite element model allows the potential profile as a function of applied voltage to be calculated, so including the effects of screening on the gating. The results of this analysis are shown in figure 2.9. The explanation for

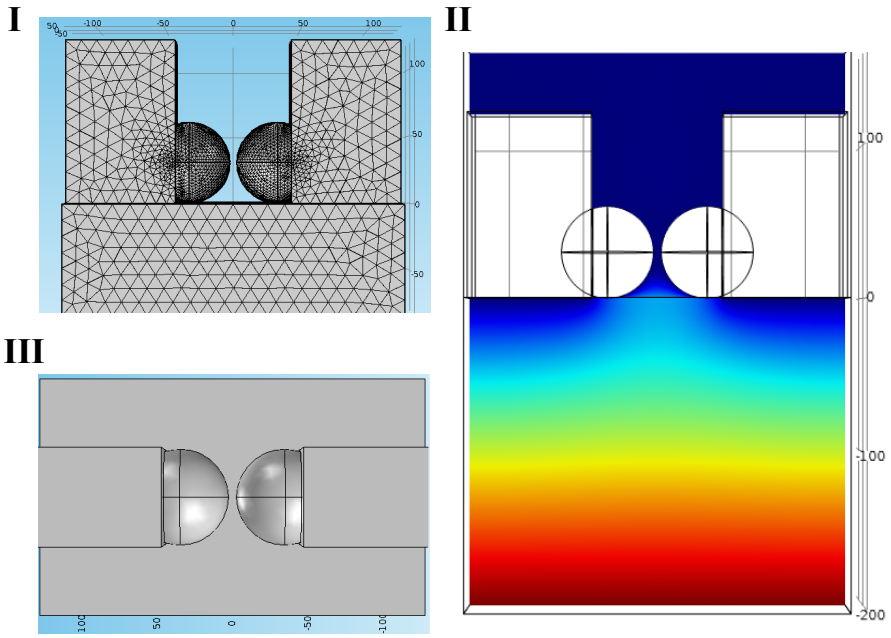

Figure 2.8: The 3D model of the experiment. Subfigure I shows the geometry in the (x, z) plane with the adaptively constructed mesh. Subfigure II shows the voltage profile through the plane $(x, 0, z)$ when a voltage is applied from the bottom with the gold leads clamped at 0V.

the lack of gating in the experiment is readily visible: the gold spheres provide an incredibly effective screening environment and the voltage is unable to penetrate. The gate coupling from the computational model is approximately 10^{-3}, far below the threshold that is usable to gate - molecular transitions are on the order of electron volts, so many thousands of volts would need to be applied to effectively gate the device[5]. With this in mind, can the geometry be modified in a sensible way so as to allow a nontrivial gate coupling? The constraints imposed by the geometry make this challenging; one reasonable modification is to use a third bead integrated into the scaffolding, to allow a closer approach of the applied voltage. This geometry, shown in figure 2.10 allows for gate couplings up to around 0.01 (1%). This is still very small and not usable. Going beyond a two terminal device to a three terminal device therefore would require a complete redesign, using

[5]A similar model constructed on a typical MCBJ geometry yields a gate coupling $V/V_{\text{applied}} \approx 0.2$

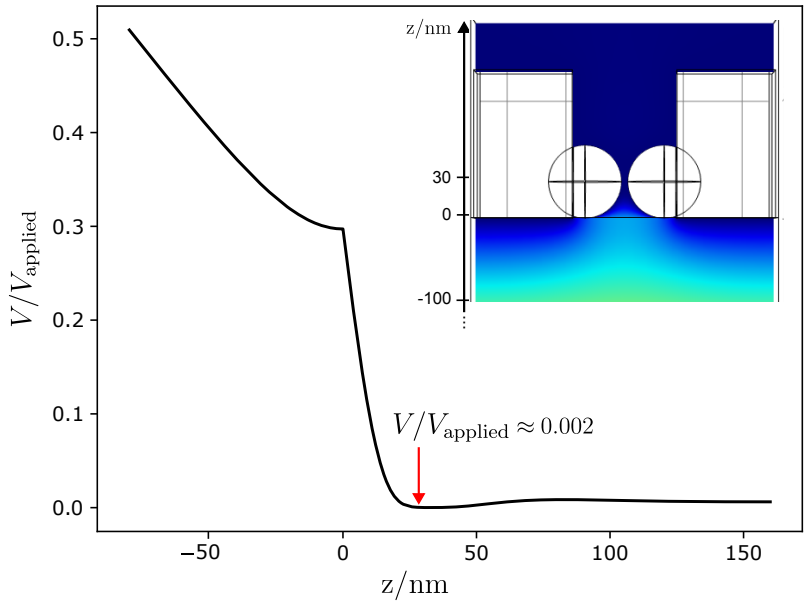

Figure 2.9: The voltage profile along a vertical line through the centre of the device on application of a gate voltage, depicted in the inset. The molecule is positioned at $z = 30$ nm. The cusp at $z = 0$ is at the transition between the dielectric substrate and air.

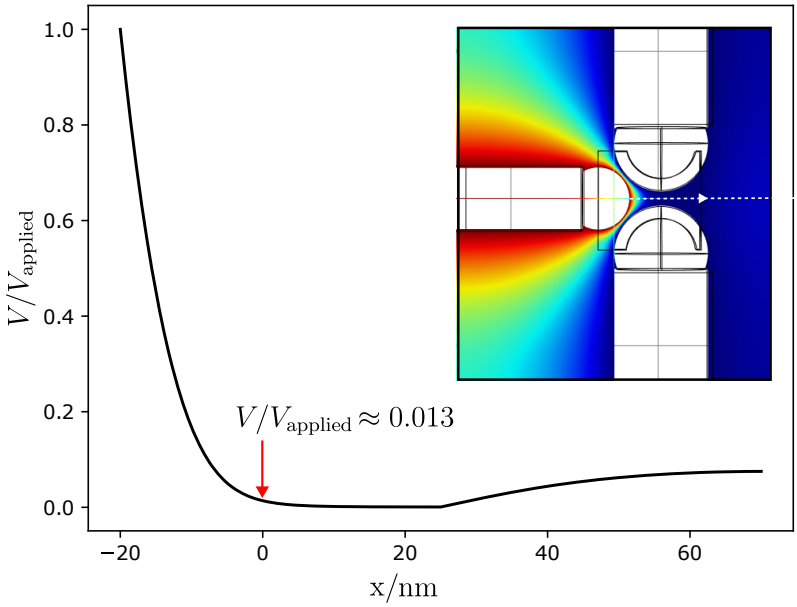

Figure 2.10: The voltage profile along a line parallel to x, through the centre of the device, from a third gating terminal. The line is depicted in the inset. The molecule is positioned at $x = 0$ nm.

multiple functional components such as molecular wires to deliver a local gate voltage. For a theoretical analysis of a molecular wire system and its potential use in future generations of devices for capacitive gate coupling refer to appendix A. True three-terminal local electrical gating has been implemented in MCBJ devices [36], although outside of this architecture it has been difficult to achieve. Lo et al [37] have demonstrated electrochemical gating across a family of single molecule devices in the STM architecture by altering anchoring groups on the conducting molecule. Non-local back gating is relatively routine, implemented in MCBJ devices in, for example [9] and [38].

2.5 Models for tunnelling at the nanoscale

I shall later be presenting data from devices both with and without molecules in the gap and with varying thicknesses of DNA origami. What are the theoretical expectations for the behaviours of such devices? The empty junctions feature no delocalised electrons that might facilitate conduction, so the only electron transport that can occur is via tunnelling or hopping, and the most commonly used model is due to Simmons [39]. I will also describe a simple model for the current through a molecule, based on the Landauer-Büttiker formula [40], where hybridisation between the leads and molecular energy levels facilitate transport. There is a great deal more that could be said on nanoscale transport through junctions, see for example reference [41], but more detail is beyond the scope of this thesis. The derivation and a more detailed discussion of each of these models are presented in Appendix B.

2.5.1 Vacuum tunnelling in Simmons' model

For tunnelling between two electrodes through a resistive barrier, the most appropriate model for transport is a form of vacuum tunnelling. Tunnelling is presumed to be along x, through an insulating region of thickness s with a barrier of potential

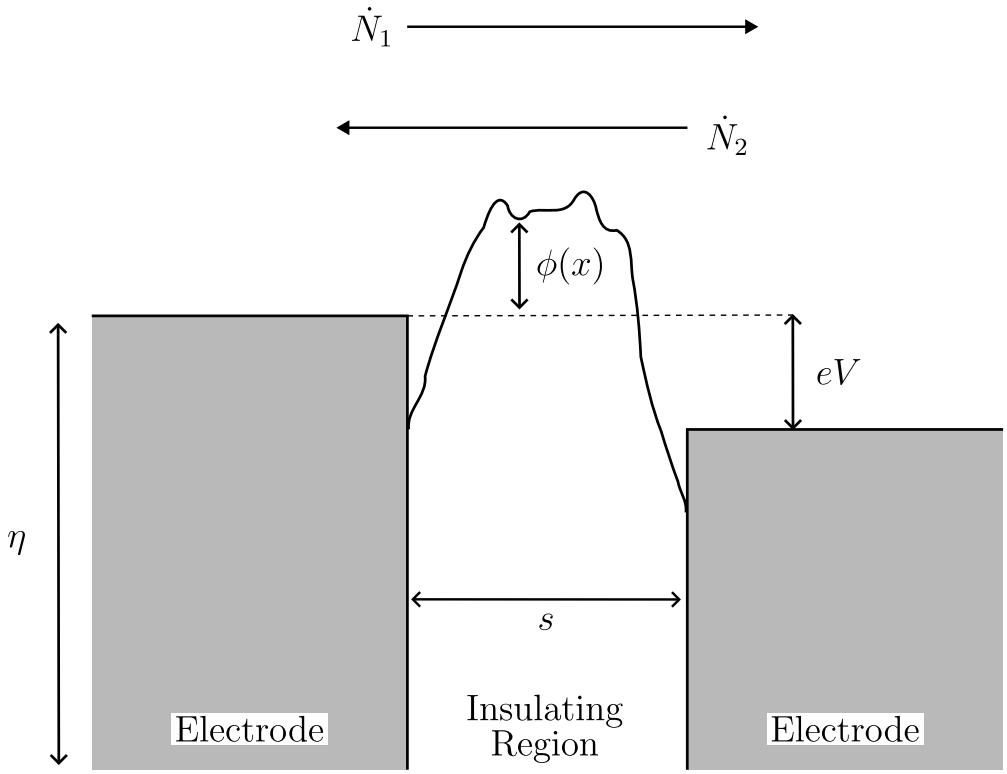

Figure 2.11: The geometry for the tunnelling problem. Electrons tunnel between two electrodes, offset from each other by a voltage eV. The tunnelling is through a region of potential $\phi(x)$, thickness s.

$\phi(x)$. Simmons makes the following assumptions:

- The probability for an electron to tunnel through the barrier is governed by the WKB approximation
- The band structure of the leads can be neglected and the density of states orthogonal to the transport is approximately constant
- The voltage is not significantly larger than the barrier height

and thereby reaches a profile for the current density of

$$J = \frac{e}{4\pi^2\hbar(\beta s)^2}\left[\bar{\phi}\exp\left(-\frac{2\beta s(2m)^{\frac{1}{2}}}{\hbar}\bar{\phi}^{\frac{1}{2}}\right) - (\bar{\phi}+eV)\exp\left(-\frac{2\beta s(2m)^{\frac{1}{2}}}{\hbar}(\bar{\phi}+eV)^{\frac{1}{2}}\right)\right], \tag{2.4}$$

where $\bar{\phi}$ is the average barrier height [42].

It is worth noting that temperature has been excluded, but does not play a significant role as the only effect of adding temperature is to smear out the Fermi functions featuring in the electron distribution functions. It is also relevant to note the exponential sensitivity of 2.4 on both $\bar{\phi}$ and s. This can make fitting the data to this model numerically challenging.

Another technicality is that the above formula relies on the effective area for tunnelling to be well defined and the assumption of a constant density of states in y, z to hold. This is equivalent the statement that $\sqrt{A} \gg \lambda_F$; in the opposite limit mode quantisation should be expected to be significant and therefore a Landauer-Büttiker formula [40] would be likely to be successful. In gold, the Fermi wavelength is on order 1 nm: considering the geometry of the molecular devices, this is right on the edge of the regions of applicability of either approach; the geometry likely satisfies $\sqrt{A} \approx 1$ nm. Furthermore, it is not possible to fit the area independently of the gap size and barrier height using tunnelling curves. The work of [43] presents fits to data with both of these methods on geometries of comparable scale to those investigated in this work and found similar parameters between the different methods, vindicating taking this simple approach, although they had to insert a phenomenological area over which transport occurs. A candidate method to explore the transport in a more systematic theoretical way would be the use of nonequilibrium Green functions [41], but there are further complications with the use of these techniques to achieve quantitative agreements to experiment.

2.5.2 Resonant tunnelling through a molecular energy level

When there is a molecule coupled to the leads, the situation is somewhat different. The molecule can be thought of as having states occupied up to the 'highest occupied molecular orbital' (HOMO) coupled to leads filled up to the Fermi level. After

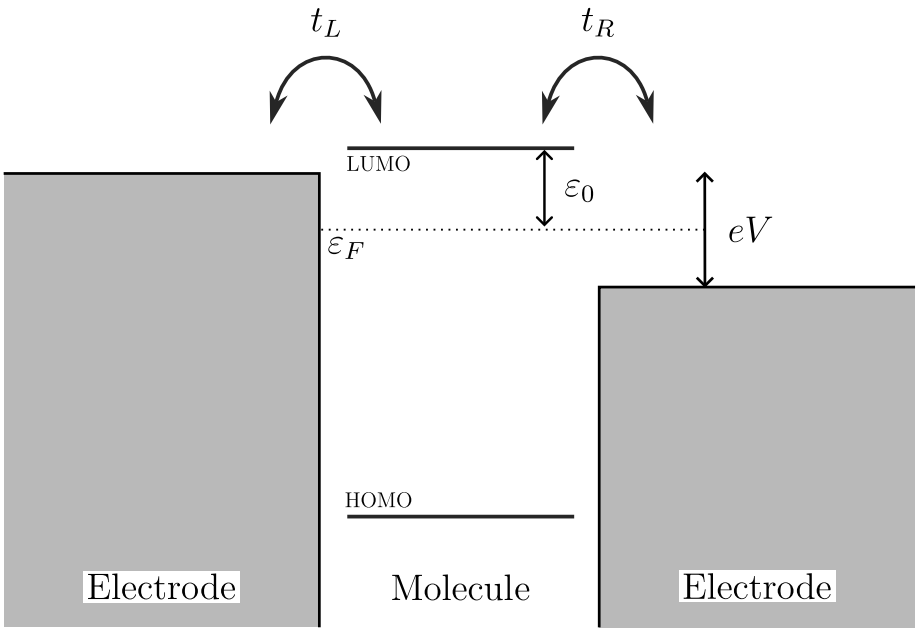

Figure 2.12: The resonant tunnelling through a single molecular level at energy ε_0. The leads are offset from each other by eV, and the HOMO and LUMO are both shown. Only the LUMO will be considered when discussing the transport here.

interaction there may be some changing of the levels due to hybridisation and the final situation will look somewhat like figure 2.12, where the Fermi level of the leads lies somewhere in the gap between the HOMO and the lowest unoccupied molecular orbital (LUMO). I will assume that the transport is dominated by transport through only a single level ε_0, such that the Hamiltonian is given by

$$\mathcal{H} = \mathcal{H}_L + \mathcal{H}_R + \sum_\sigma \varepsilon_0 a_\sigma^\dagger a_\sigma + \sum_{j=L/R} \left(t_j \sum_\sigma (a_\sigma^\dagger c_{j\sigma} + h.c.) \right) \tag{2.5}$$

where the lead Hamiltonians are given by $\mathcal{H}_{L/R}$. The $a_\sigma^\dagger$ operator creates an electron on the molecule with spin σ. The $c_{j\sigma}^\dagger$ operators create an electron on lead j with spin σ. Scenarios such as the above are best considered within the Landauer-Büttiker approach [40], where the problem is treated in terms of scattering. The probability

for an electron incident to be transmitted is given by the transmission function $T(E)$. For a single level, this is approximately Lorentzian:

$$T(E,V) = \frac{4\Gamma_L\Gamma_R}{(E-\varepsilon(V))^2 + (\Gamma_L+\Gamma_R)^2} \tag{2.6}$$

where the molecular level incorporating voltage dependence is $\varepsilon = \varepsilon_0 + \frac{V}{2}\frac{\Gamma_L-\Gamma_R}{\Gamma_L+\Gamma_R}$ and $\Gamma_{L/R}$ are the couplings to the leads in the Wide Band Limit Approximation [42]. The current is then given by

$$I(V) = \frac{G_0}{e}\int \mathrm{d}E\; T(E,V)\left[n_F(E-eV/2) - n_F(E+eV/2)\right]. \tag{2.7}$$

Again, detailed derivations and explanations of assumptions are given in appendix B.

2.5.3 Variable Range Hopping

The above theories make very little use of temperature and including the temperature has little influence on the shapes of the curves. Nonetheless, deviations at higher temperatures are observed in the data, which will be seen later. Therefore, I mention here a plausible temperature dependent transport mechanism that is easily testable, due to Mott [44] [45]. Some authors have argued that treating DNA as an insulating layer is not totally justified: when measured along a single strand conduction has been observed, likely due to π electron stacking [46], although others see no conduction in similar experimental geometries [47]. In the case that this hybridisation occurs, the DNA origami structure could plausibly be modelled as a random network of sites between which electron hopping may occur, behaving like a disordered material with a thermally activated hopping. This leads to a temperature dependent resistivity of

$$\rho = \rho_0 \exp[(T_0/T)^{1/(d+1)}]. \tag{2.8}$$

2.5.4 Distinguishing vacuum tunnelling from resonant tunnelling

The two tunnelling models discussed above, vacuum tunnelling (2.5.1) and resonant tunnelling (2.5.2), are both examples of coherent transport, where the phase of the electrons participating is preserved and inelastic processes occur only deep within the leads. On universal grounds, these processes both admit a current of the form $I = AV + BV^3$, which may appear superficially similar to each other. It is therefore important to be able to distinguish between these two scenarios. In the absence of any inelastic processes between molecular levels, there are no extra features to diagnose. Here the fact that the DNA origami structure provides fairly tight bounds on the size of the gap is useful, as the characteristic conductances of the two models are found to be significantly different. A simple analysis for the conductance of a Simmons like tunnel junction with sensible values ($s = 2.5$ nm, $\phi = 0.3$ eV, tunnelling area 10 nm^2) yields a characteristic conductance of $10^{-9}\,G_0$ in the linear region. The same exercise on the resonant tunnelling model with realistic values ($\Gamma = 1$ meV, $\varepsilon_0 = 0.5$ eV) yields a characteristic conductance of $10^{-4}\,G_0$ in the linear region when on resonance. The exact values obviously depend on the energetics of the system being studied, but the point remains that these are significant differences, easily detected in the data.

References

[9] C. Godfrin et al. “Operating Quantum States in Single Magnetic Molecules: Implementation of Grover’s Quantum Algorithm”. In: *Phys. Rev. Lett.* 119.18 (Nov. 2017). Publisher: American Physical Society, p. 187702. URL: https://link.aps.org/doi/10.1103/PhysRevLett.119.187702 (visited on 03/29/2023).

[29] Veikko Linko and J. Jussi Toppari. "Self-Assembled DNA-Based Structures for Nanoelectronics". en. In: *Journal of Self Assembly and Molecular Electronics* (2012), pp. 101–124. URL: https://www.journals.riverpublishers.com/index.php/JSAME/ (visited on 04/24/2023).

[30] Tali Dadosh et al. "Measurement of the conductance of single conjugated molecules". In: *Nature* 436.7051 (2005), pp. 677–680.

[31] Sami Franssila. *Introduction to microfabrication*. John Wiley & Sons, 2010.

[32] James MacQueen et al. "Some methods for classification and analysis of multivariate observations". In: *Proceedings of the fifth Berkeley symposium on mathematical statistics and probability*. Vol. 1. 14. Oakland, CA, USA. University of California Press, Berkeley, 1967, pp. 281–297.

[33] Nobuyuki Otsu. "A Threshold Selection Method from Gray-Level Histograms". In: *IEEE Transactions on Systems, Man, and Cybernetics* 9.1 (1979), pp. 62–66.

[34] P. V. C. Hough. "Machine Analysis of Bubble Chamber Pictures". In: *Conf. Proc. C* 590914 (1959). Ed. by L. Kowarski, pp. 554–558.

[35] Dana H Ballard. "Generalizing the Hough transform to detect arbitrary shapes". In: *Pattern recognition* 13.2 (1981), pp. 111–122.

[36] Dong Xiang et al. "Three-terminal single-molecule junctions formed by mechanically controllable break junctions with side gating". In: *Nano Letters* 13.6 (2013), pp. 2809–2813.

[37] Wai-Yip Lo et al. "Edge-on Gating Effect in Molecular Wires". In: *Nano Letters* 15.2 (2015). PMID: 25603411, pp. 958–962. URL: https://doi.org/10.1021/nl503745b.

[38] Mickael L Perrin et al. "Large tunable image-charge effects in single-molecule junctions". In: *Nature Nanotechnology* 8.4 (2013), pp. 282–287.

[39] John G. Simmons. "Generalized Formula for the Electric Tunnel Effect between Similar Electrodes Separated by a Thin Insulating Film". In: *Journal of Applied Physics* 34.6 (June 1963). Publisher: American Institute of Physics, pp. 1793–1803. URL: https://aip.scitation.org/doi/10.1063/1.1702682 (visited on 04/05/2023).

[40] M. Büttiker, Y. Imry, R. Landauer, and S. Pinhas. "Generalized many-channel conductance formula with application to small rings". In: *Phys. Rev. B* 31 (10 1985), pp. 6207–6215. URL: https://link.aps.org/doi/10.1103/PhysRevB.31.6207.

[41] Gianluca Stefanucci and Robert van Leeuwen. *Nonequilibrium Many-Body Theory of Quantum Systems: A Modern Introduction*. eng. New York: Cambridge University Press, 2013.

[42] Juan Carlos Cuevas and Elke Scheer. *Molecular electronics: an introduction to theory and experiment (World scientific series in nanoscience and nanotechnology, vol. 1)*. eng. Singapore: World Scientific Publishing Co. Pte. Ltd, 2010.

[43] A. Mangin et al. "Reduced work functions in gold electromigrated nanogaps". In: *Phys. Rev. B* 80 (23 Dec. 2009), p. 235432. URL: https://link.aps.org/doi/10.1103/PhysRevB.80.235432.

[44] N.F. Mott. "Conduction in glasses containing transition metal ions". In: *Journal of Non-Crystalline Solids* 1 (1 1968), pp. 1–17.

[45] Boris I. Shklovskii and Alex L. Efros. "Variable-Range Hopping Conduction". In: *Electronic Properties of Doped Semiconductors*. Berlin, Heidelberg: Springer Berlin Heidelberg, 1984, pp. 202–227. URL: https://doi.org/10.1007/978-3-662-02403-4_9.

[46] Danny Porath, Alexey Bezryadin, Simon De Vries, and Cees Dekker. "Direct measurement of electrical transport through DNA molecules". In: *Nature* 403.6770 (2000), pp. 635–638.

[47] P. J. de Pablo et al. “Absence of dc-Conductivity in λ-DNA”. In: *Phys. Rev. Lett.* 85 (23 Dec. 2000), pp. 4992–4995. URL: https://link.aps.org/doi/10.1103/PhysRevLett.85.4992.

3

Measurements on nanoscale devices

In this chapter I shall describe the results of transport experiments on devices produced using the fabrication techniques described in the previous chapter. The main aims are firstly to characterise the transport through empty DNA origami nanostructures and then to present a proof of concept fabrication of a device that appears to be a Copper porphyrin single molecule device. I shall emphasise the way that the three layer origami nanostructures used in the molecular devices are essentially inactive in transport, and also the high device yield. As all of these are fabricated using the deterministic techniques developed in the previous chapter, the device yield is well in excess of what is seen for comparable break junction studies.

I would like to acknowledge the collaboration of Dr Junjie Liu in this matter, who has developed analogous methods for the contacting of molecular devices using SEM imaging instead of AFM imaging, and to thank him for the data shown in the right panel of 3.3. I also acknowledge the collaboration of Dr Seham Helmi

again for producing the dimer structures and Dr Keith Andrews for synthesising the porphyrin molecule measured in 3.4.1.

3.1 Measurement techniques

The devices presented in this chapter are by their nature extremely high impedance and so it is important to take care with experimental methodologies. The resistance of an empty DNA nanogap device is 50-100 GΩ; what techniques should be used to measure this accurately? The simplest method, and the one employed in these measurements, is using a DC voltage and a high sensitivity current preamplifier for a two wire measurement, depicted in figure 3.1. The differences between a two and four wire measurement are here irrelevant as the resistance of the sample is so large compared to a typical contact resistance. There are a few points worth labouring: firstly, the probe wiring isolation is extremely important. Each terminal must be isolated by over 100 GΩ to avoid cross-talk between channels. Secondly, using DC for the transport is a choice also stemming from the high impedance. One could contend that using an AC lock-in technique would be desirable for greater signal to noise and for some further measurement techniques: to investigate inelastic effects it is common to measure the resistivity as a function of voltage using an AC differentiating amplifier. However this becomes extremely bandwidth limited in the high impedance case: if the stray capacitance in the wiring is taken to be $O(10\,\mathrm{pF})$, the highest frequency that can be measured is 1 Hz. Any measurement made using this technique is limited to be impractically slow as a consequence.

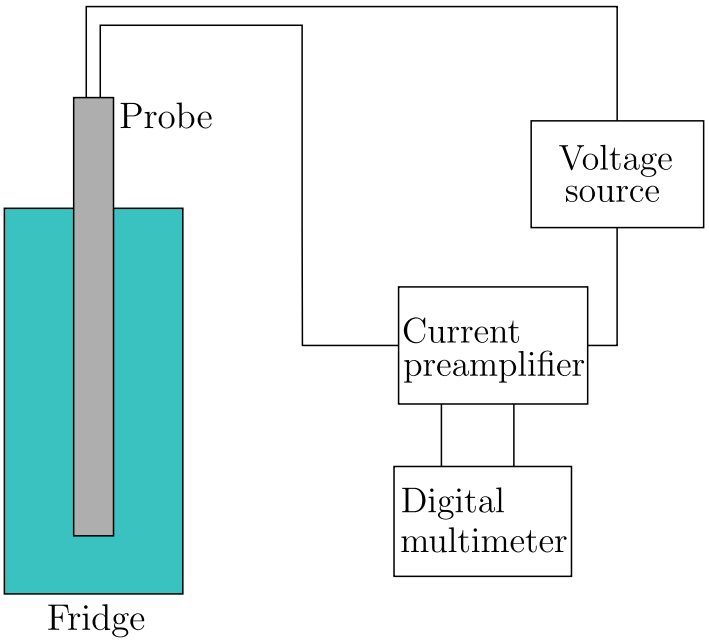

Figure 3.1: Schematic of the two wire DC measurement setup. Samples are measured at 4.2 K in an Oxford Instruments refrigerator in the nanogap devices, and at 4.2 K immersed in Helium in the molecular device measurement. The voltage source is a Stahl BS Precision DC voltage source, the current amplifier is a Stanford Research SR570 and the multimeter is a Keithley 2001.

3.2 Defining yields for nanogap devices

One of the stated goals of this experimental project is to develop fabrication methods that are reliable and replicable. In order to discuss this in a concrete way it is necessary to discuss what exactly is meant by the yields. This is relevant for the discussion on empty DNA nanogap devices, which I successfully fabricated with high yield. There are two notions of the yield that I will make reference to, which I will call R_1, R_2. I define R_1 to be the percentage of successful devices obtained after a dimer has been imaged and I have attempted to attach leads. This yield therefore includes losses due to misalignment and misfocusing as well as due to the structure failing to couple to the leads, which are systematic errors linked to equipment and user error. The second yield R_2 is defined to be the percentage of devices that appear

connected under SEM which produce a successful device. This yield does not include the misalignment losses and so is only sensitive to the quality of contact achieved on the device and is defined this way due to the difficulties we had with achieving good contacts, detailed in 2.2.2. Future work will focus on achieving high yield fabrication on molecular devices, where R_2 also evaluates how successful forming placing the molecule inside the origami structure is. Under those circumstances, from the perspective of evaluating the possibility of using DNA nanotechnology as a scalable information processing platform R_2 is the most relevant figure, but as an evaluation of the fabrication process as a whole R_1 is clearly also useful.

3.3 Characterisation of nanogap devices

Using the above methodology, it is possible to test the method and characterise devices comprising two nanobeads separated by a small number of layers of DNA. This is a desirable check, as it allows an assessment of the extent to which the DNA origami is participating in the transport. In order to fulfil the role of a 'scaffolding' to achieve high yield molecular devices, it is desirable for the DNA to be essentially absent from the transport considerations, so that features of the molecules under investigation can be reliably ascertained. In order to characterise the processes happening when electrons undergo transport through these devices, relevant questions to answer are:

1. What is the characteristic resistance of the nanogap?

2. How does this resistance change with distance?

3. What does this say about the transport processes taking place?

4. To what extent does the imaging methodology influence the data obtained?

3.3.1 Assessing the imaging methods on nanogap devices

One of the aims of the characterisation should be to compare the resistivities of devices contacted using SEM imaging with AFM imaging in order to be confident that secondary electron scattering is not damaging the relatively fragile molecular devices. The reasoning for this may be seen as part of the greater stated goal of developing a method that allows confidence that an assembled device contains one molecule in a known configuration in a gap of known width. For details of the fabrication process and image processing methods refer to 2.3. In that section I said that a disadvantage to using AFM to contact is that the image quality obtainable is on average significantly worse than with SEM, and it should be a priori expected that mislocating the devices happens slightly more frequently than when using SEM. This appears to be borne out in the data although not to a significant degree. The devices in this section are empty nanogap devices with one layer of DNA separating the nanobeads, of nominal thickness 1.7 nm.

I prepared a total of 28 candidate devices across 4 chips. A typical successful trace is shown in figure 3.2, measured using the techniques detailed in 2.2 at 4 K. Out of the 28 candidate devices prepared, 10 yielded successful tunnelling devices, giving a yield $R_1 = 35.7\%$. There were also no devices that looked connected that did not produce a tunnelling curve, so $R_2 = 100\%$ in this case: all of the failed devices came from misalignment of the leads to the dimer. The absence of a molecule at the centre of the device renders R_2 less meaningful than in devices with molecules, but indicates that the contacting process works well. It is worth noting also that obtaining an average of 2.5 successful devices per chip is extremely high by the standards of the field.

The resistance of the devices in the ohmic $V \to 0$ limit can be found from the data, shown in figure 3.3. The median resistance of these devices is $R = 42$ GΩ; equivalently the conductance is $G = 3.1 \times 10^{-7}\, G_0$. This compares favourably to

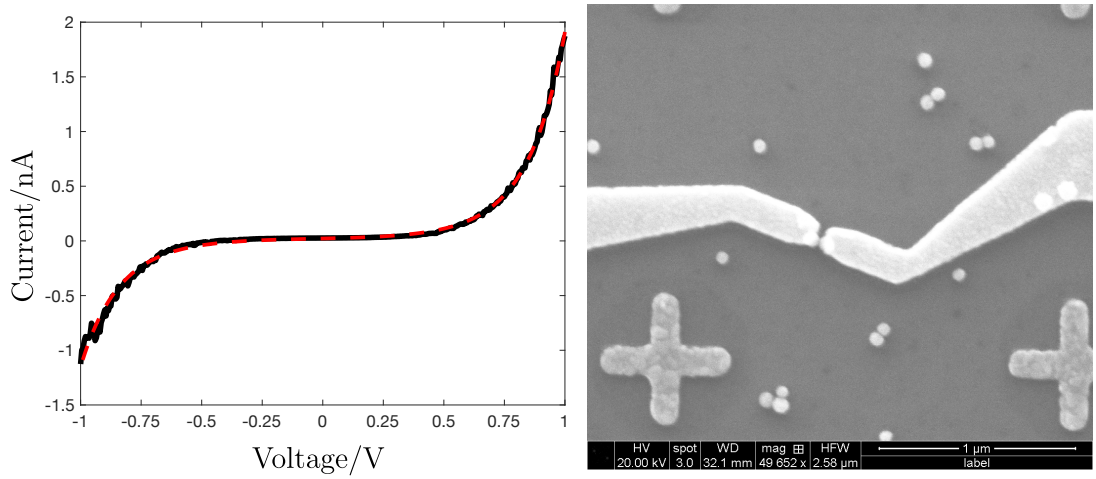

Figure 3.2: The forward current trace from an AFM imaged device and a post-measurement SEM image confirming very good alignment. The tunnelling behaviour is clearly seen and the data are fit to Simmons' model with barrier width $d = 1.7$ nm and barrier height $\varphi = 0.77$ eV. The area is left as a free parameter, with fit area 10 nm^2.

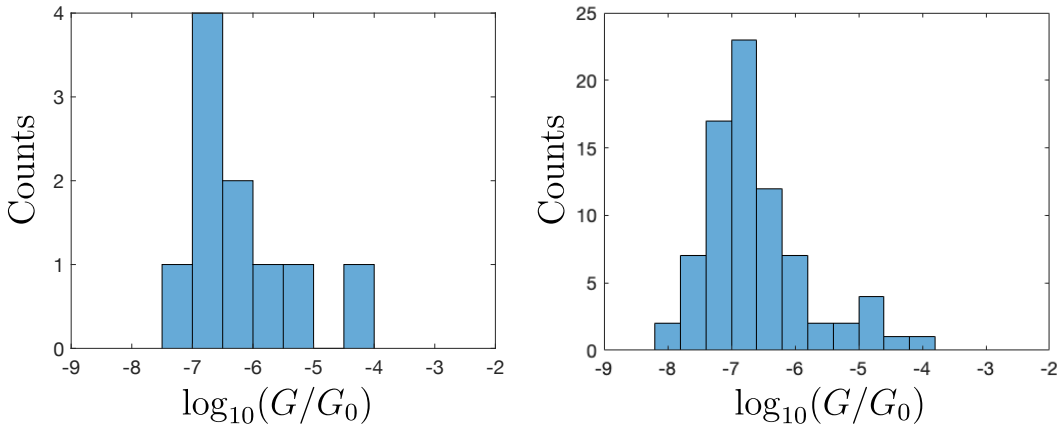

Figure 3.3: Left: Zero bias conductance of 10 AFM imaged single layer nanogap devices. Right: Zero bias conductance of a larger number of SEM imaged single layer nanogap devices, produced by my groupmate Dr Junjie Liu. The two histograms of the measured conductance are extremely similar.

the median conductance obtained by my collaborator Dr Junjie Liu using SEM imaging. This is heartening, as it implies that the DNA is not being directly damaged by the imaging step.

3.3.2 Comparing one and three layer devices

If DNA origami nanostructures are to be used in order to provide a scaffolding for conductive molecules, it is important that the origami does not interfere with the electron transport: that is, that the resistivity of the gap is significantly higher than the resistivity of the molecule. I have already demonstrated above that vacuum tunnelling is a plausible mechanism for transport through the devices and that the resistivity is large. Nonetheless, in order to characterise the transport through the nanogaps further it is also instructive to see how the transport varies as the size of gap is altered. To this end, a set of devices were prepared with three layers of DNA, nominal thickness 5.1 nm, to compare to the 1 layer devices. Under the significant increase in gap size, it is reasonable to expect that the current should be significantly reduced. It is important to note that these devices were imaged using SEM, but the discussion of section 3.3.1 implies that in the case of empty DNA nanogaps the SEM imaging does not interfere with fabrication[1]. These were measured identically to the one layer devices above, taking the $V \to 0$ resistance. 45 devices were prepared, with 15 devices producing tunnelling curves up to 2.5 V. A portion of the nonconductive devices however did appear connected under post-imaging. Contacting tests at the time returned no indication of poor device contacting so it is consistent to conclude that these devices have the tunnelling switched off as the gap is too large, but this is not necessarily the case. To explore this, in the following, I will explore the properties of the devices which did produce tunnelling behaviour. R_1 is for these devices is 33% although the R_2 yield analysis is less applicable here; firstly there is no reliable way to distinguish between a device that has a gap too resistive to tunnel across at the voltages used and one that is not contacted and secondly the switching off of current at larger gap sizes is a desired feature.

As figure 3.4 demonstrates, the three layer devices are significantly more resistive.

[1]These devices were in fact fabricated *first*, before deciding to attempt to fabricate devices with AFM for comparison. This does not however change the analysis.

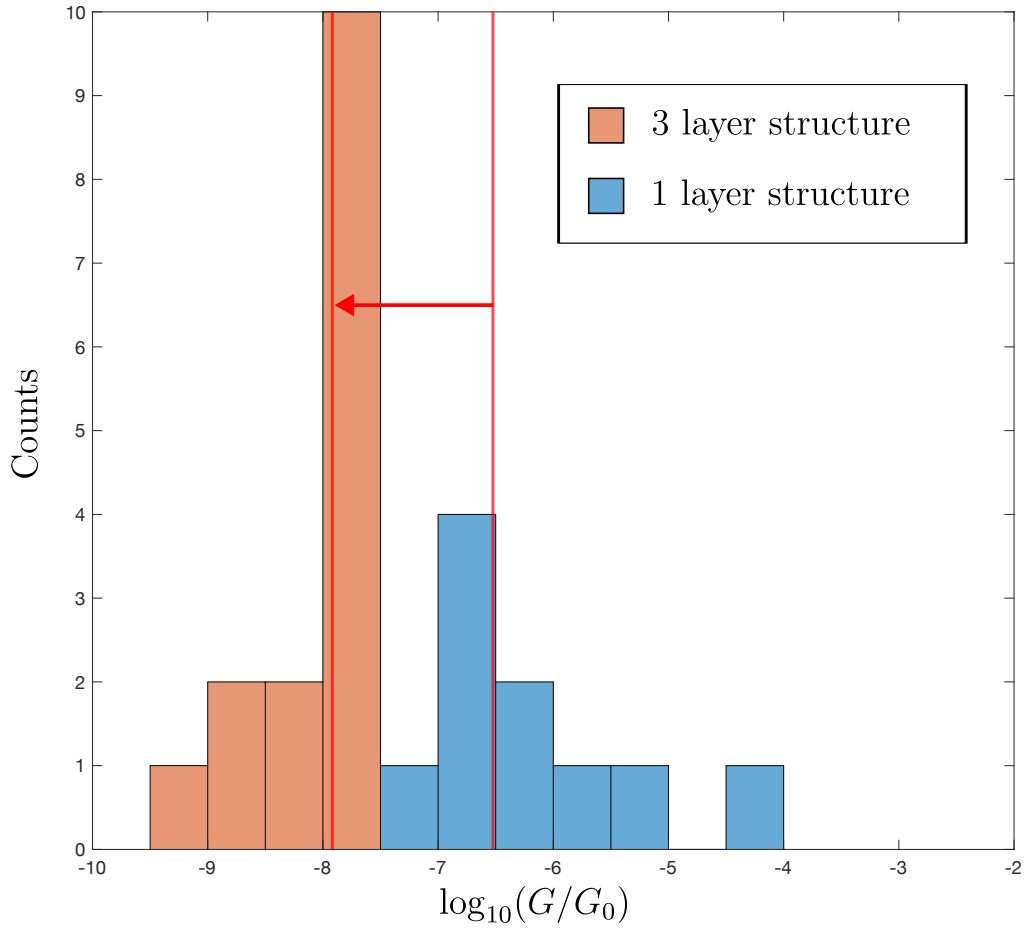

Figure 3.4: Histograms of the conductance of one and three layer DNA nanogap devices, with the median conductances in red. The shift towards high resistances with increasing gap size is clearly observed; the zero bias resistance measured is consistent with being purely leakage.

The median resistance of the three layer devices increases with respect to the one layer devices by a factor 25, to $R = 1.1$ TΩ ($G = 1.2 \times 10^{-7}\, G_0$), implying that tunnelling processes which are strongly dependent on distance are contributing. It should be noted that the extremely high zero bias resistance of the three layer devices results in a current the same order of magnitude as the leakage current measured if two open wires are measured on the chip, implying that the transport is mostly switched off.

We can however go further with this analysis, by fitting Simmons' model to each dataset and attempting to partition the devices into classes by the implied barrier height and gap size. This is a nontrivial task: following the discussion of

section 2.5.1, the model is underconstrained and therefore the parameters can *not* be relied upon to be physically meaningful. The graphs are relatively featureless and exponentially sensitive to the two physical parameters d, φ. Furthermore, the model predicts a current density, so the effective area over which transport occurs must be fit. This can not be done independently of the other parameters. Some authors have had success fitting using a phenomenological fixed estimate for the area [43], but consideration of the geometry for this problem implies that the effective area should be gap size dependent: the exponential switch on implies that the effective area for the one layer devices should be larger than for the three layer devices, with no reliable way of estimating this area in either case. Therefore, it must be left as a free parameter. Third, the model becomes inaccurate at voltages larger than the barrier height. Finally, the applicability of the model altogether is questionable, as the integration over k_y, k_z (for transport along x) assumes that the area satisfies $\sqrt{A} \gg \lambda_F$. The result of this is that the parameters obtained from this method can not be relied upon to be physical.

Despite these complications, by fitting and categorising the data into groups with a k-means algorithm [32] we can nonetheless test whether the two datasets are distinguishable. This algorithm partitions unstructured data into a given number of classes c_i , $i = 1 \ldots k$ such that the sum of the distances between a datapoint and the centre of its class r_{c_i} is minimised. The algorithm varies the position of r_{c_i} until this condition is fulfilled:

$$\min_{r_{c_i}} R = \min_{r_{c_i}} \sum_{i=1}^{k} \sum_{r \in c_i} \sqrt{(r - r_{c_i})^2}. \tag{3.1}$$

Clearly, if the number of classes is equal to the number of datapoints, the residual $R = 0$. To choose the number of categories, a standard test is the 'elbow' test; by varying the number of classes k the number may be chosen such that the residual

decreases much more slowly with k any larger[2].

Figure 3.5 shows the result of applying this analysis the tunnelling curves: a range of φ and d are obtained for each dataset lying roughly on a line[3], but the two datasets can be partitioned exactly into 2 classes, corresponding to the 3 layer and 1 layer devices. This demonstrates that regardless of the physical interpretation of the transport in the three layer case, they can be reliably distinguished from the one layer devices and correspond to distinct classes of device. The quality of fit for the one layer devices was generally good, returning gap sizes of around 1.5-2 nm and barrier heights of 0.5-1 eV, consistent with expectations for tunnelling through a single layer of DNA. The quality of fit for the three layer devices was poor, producing fits with wildly unphysical parameters due to the numerical instabilities and model limitations discussed above. An example of this is depicted in figure 3.6. Indeed, the order of magnitude of the current in the flat region before the switch on in the three layer devices is the same as the leakage current measured through open terminals.

One could reasonably propose a resonant tunnelling model for the transport here, with a molecular level on the DNA origami entering the transport window at the switch on around 1.5 V. This is not a viable model either: from the discussion of section B.2, the zero bias conductance scales like $(\Gamma_L\Gamma_R/\Gamma)G_0$. Here, the zero bias conductance is on order $10^{-8}\,G_0$, which would imply couplings Γ_L, Γ_R of 10 neV, which are unphysically small.

Taking the above arguments altogether, these data demonstrate that the vacuum tunnelling picture describes the behaviour of the single layer devices well and that as the gap size is increased up to a nominal 5.1 nm the transport switches off entirely for voltages under one volt. After this point, a fraction of the three layer devices exhibit transport where the mechanism is difficult to diagnose but roughly consistent with some type of vacuum tunnelling. These results together vindicate the

[2]This assignment is not totally unambiguous

[3]As could be expected for an underconstrained model

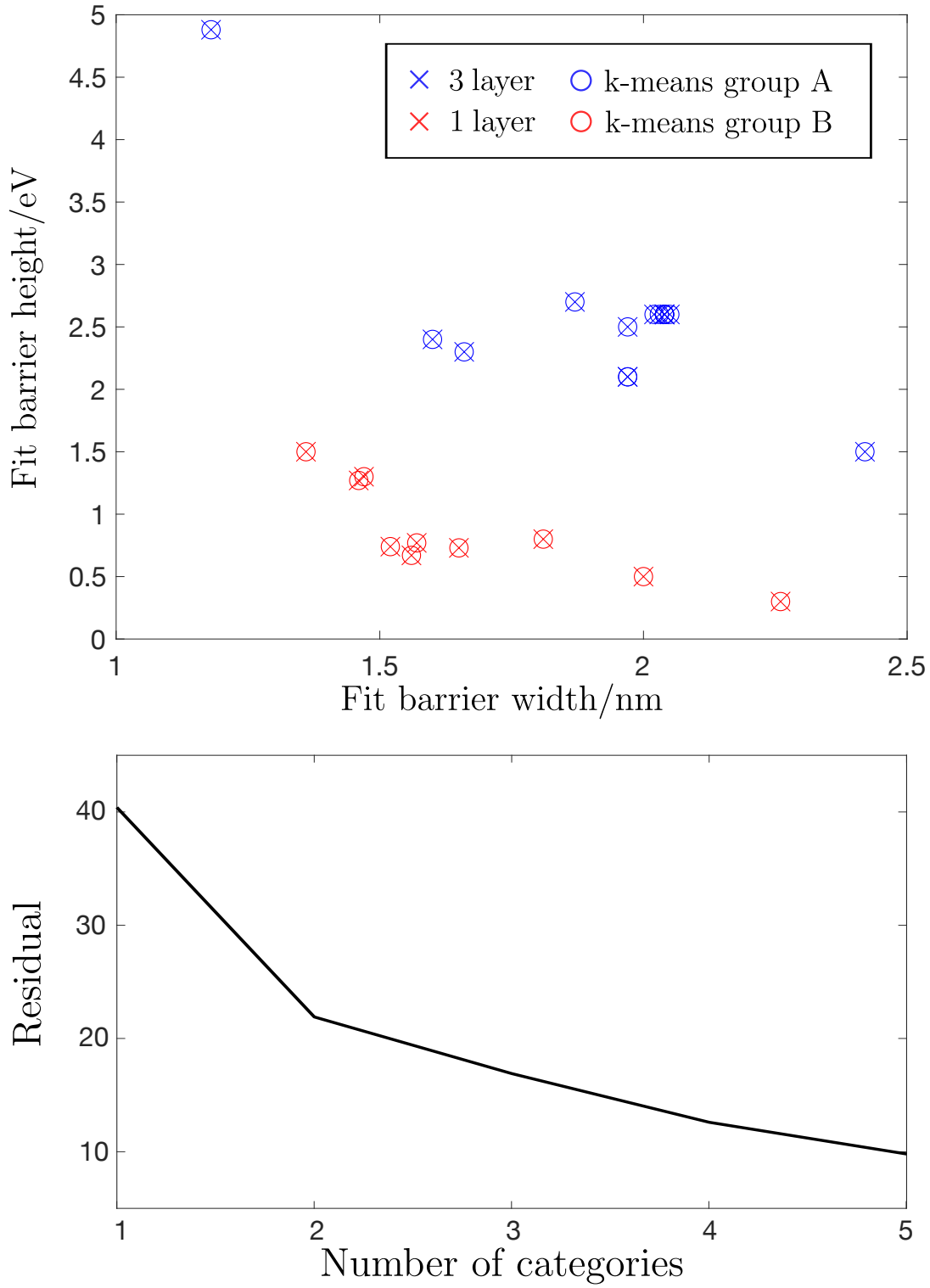

Figure 3.5: Partitioning the data, the two classes of device can be distinguished using unsupervised learning. The red crosses are the fit barrier heights φ and widths d for the 1 layer devices and the blue crosses are the fit barrier heights and widths for the 3 layer devices. Each cross corresponds to one device. The circles then correspond to the classes assigned to each data point from the k-means algorithm, k=2. There is perfect agreement between the assigned classes and real classes. The second graph shows the residual as a function of the number of classes: a simple elbow test confirms that k=2 is a valid assignment for the data.

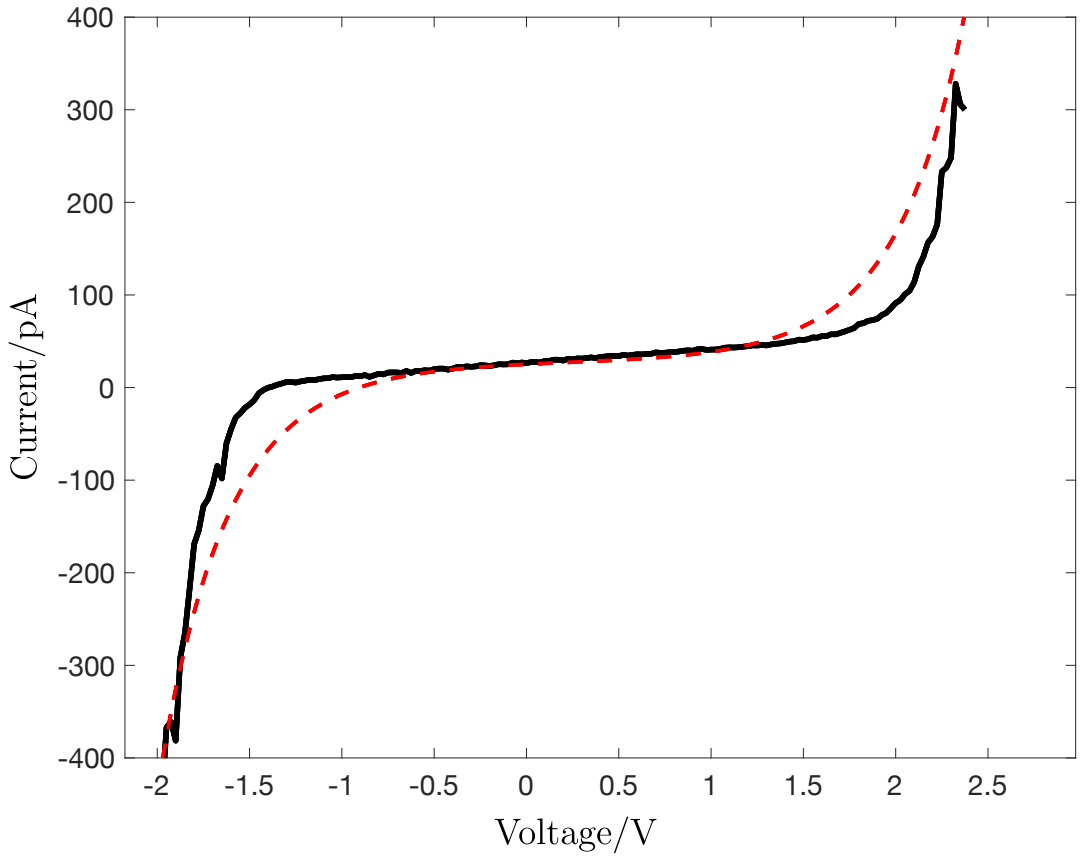

Figure 3.6: A tunnelling curve from a three layer device, producing unphysical fit parameters. The fit width and barrier height are 1.6 nm, 3.0 eV and the fit tunnelling area is of order $10^{-7}\,\mathrm{nm}^{-2}$, which is many times smaller than a single atom and so unphysical. The fitting is unstable due to large exponentials, rendering physically believable parameters impossible to obtain, although by the treatment shown in 3.5 these devices can be reliably distinguished.

suitability of the DNA origami structure as a scaffolding for molecular components.

3.3.3 Temperature dependence of the transport

I have demonstrated in the previous sections that some form of tunnelling process is a likely candidate for the transport in the one layer devices; as a check on this it is instructive to look at the temperature variation of transport. Figure 3.7 shows the variation in the transport through four one layer devices, at 1.8 K and at 140 K. The conductance of the devices increases by factors order unity - it is interesting to note that a naive vacuum tunnelling model cannot account for this variation.

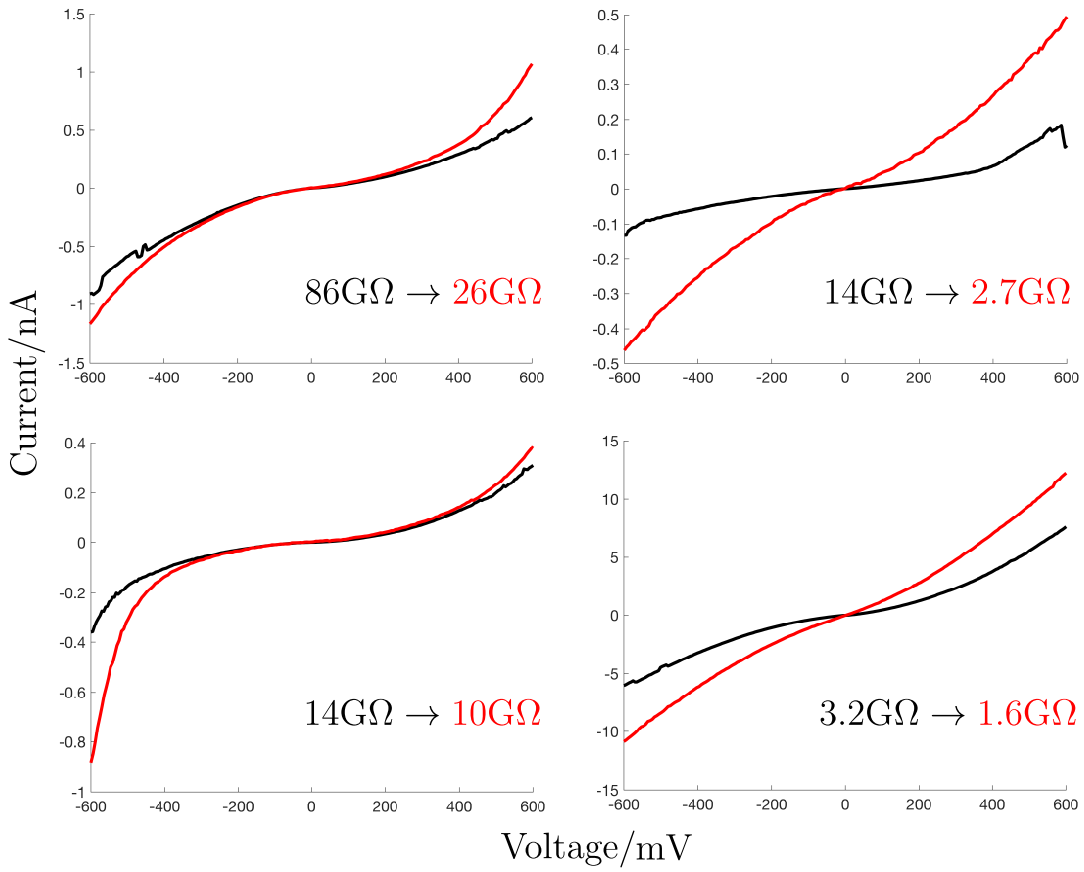

Figure 3.7: The variation of resistivity of four devices with temperature: the zero bias resistivity varies by constants of order 1, consistent with expansion effects rather than a change in transport mechanism.

The only change to a vacuum tunnelling model is through broadening of the Fermi surface, which should induce corrections on the order T/T_F, which is around 1% at room temperature. However, the experimental situation is far from this.

A candidate mechanism to explain this is nanoscale thermal expansion causing a decrease in the gap size. Examining this claim more closely, consider the data shown in figure 3.8. Here I show one of the above graphs with tunnelling models fit. The low temperature data is fit to an unconstrained Simmons' model, producing physically reasonable fit parameters of $d = 1.3$ nm and $\varphi = 0.87$ eV. Assuming the thermal expansion effects do not significantly change the average barrier height through which tunnelling occurs, we can constrain the barrier height to be the same

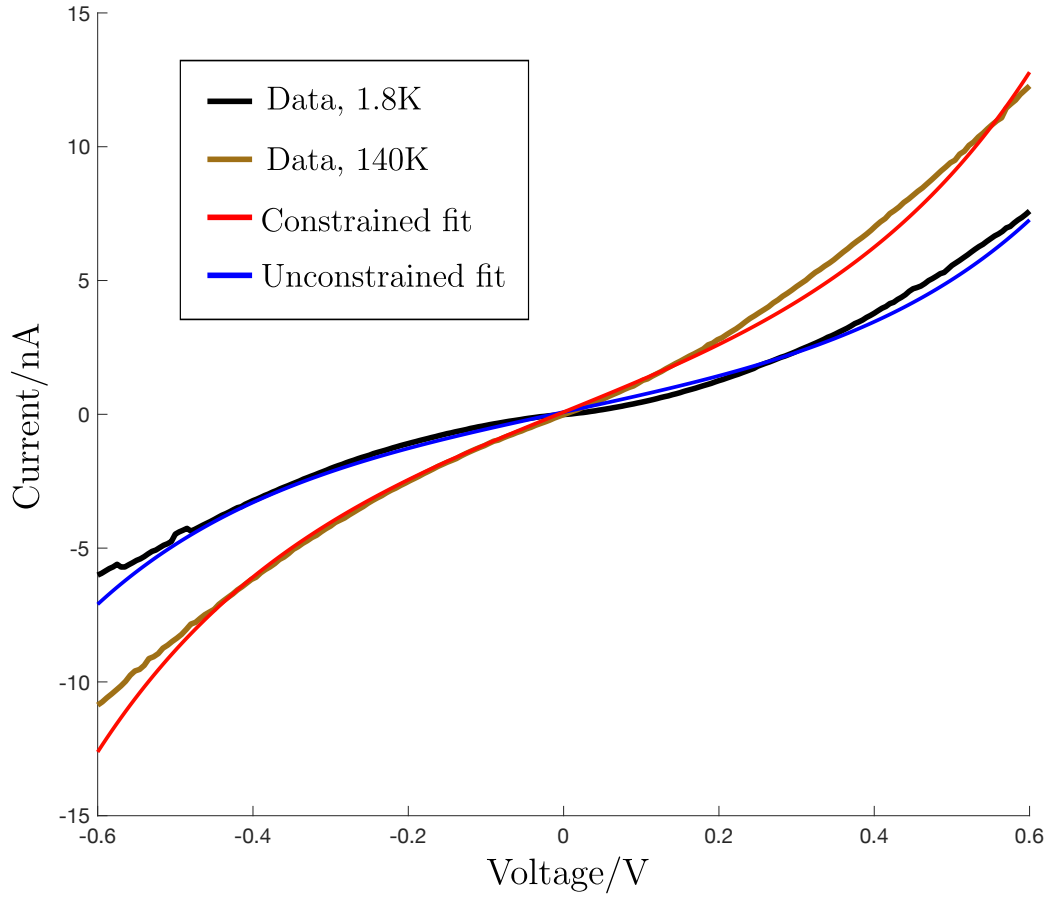

Figure 3.8: The tunnelling at different temperatures through a nanogap, with fits to Simmons model. The red fit is to the low temperature data, with $d = 1.3$ nm and $\varphi = 0.87$ eV. The red fit has φ constrained to 0.87 eV and is fit to the higher temperature data, with $d = 1.2$ nm. This is a small change in distance, consistent with the interpretation that the temperature variation in transport is caused by thermal expansion. There are some signs of asymmetry in the data, not accounted for in the model implementation.

as in the low temperature case. This is not true in general but should be a reasonable first order approximation: in reality the potential landscape across the gap from the DNA origami will experience distortions from electrostatic interactions. Fitting the data taken at high temperature with the same model but with the barrier height constrained produces the constrained fit, which is reasonably good, with $d = 1.2$ nm. This small change in barrier width is consistent with the interpretation of thermal expansion causing the variation, and is not an unphysically large variation in gap size.

Another plausible mechanism for transport is a type of variable range hopping, in which the origami structure behaves like a disordered network of states around the

Fermi level, leading to thermally assisted hopping. The data are insufficient to test this hypothesis however, as we do not have temperature sweeps for these devices.

3.4 Measurements on metalloporphyrin devices

The main focus of my fabrication methodologies has been to develop reliable methods for contacting molecular devices. The above establishes that the procedure functions well for producing nanogaps, but it still remains to demonstrate the methods on devices containing a molecule. In this section I shall present experimental transport data for the current through a proof of concept copper (II) metalloporphyrin molecular device. This establishes that the methods are applicable to molecular devices, and therefore it is possible to achieve high yield fabrication on devices of this type, although this has not been achieved in this work.

3.4.1 A candidate porphyrin molecular device

The molecules I have attempted to contact are porphyrin metal complexes, consisting of an organic ring surrounding a single metal ion core. Two opposite corners are functionalised such that they can covalently bond with the DNA origami structure via click chemistry [27] and the other two corners feature Sulfur groups to covalently bond to the gold leads [48]. This molecule is embedded into a one layer DNA nanogap structure (nominal thickness 1.7 nm) and contacted. The device I present here has copper (II) as the metal component; the copper has a ground state spin of $\frac{1}{2}$, which will be considered further in section 3.4.3. A diagram of the molecular structure is shown in figure 3.9. I also attempted to contact zinc (II) porphyrin origami structures, although issues with the fabrication process (leading to some of the discussion of 2.2.2) meant that the fabrication of these devices was unsuccessful.

A chip of copper porphyrin dimers was contacted and measured at room temperature and at 4.2 K. In the data, the devices appeared to be mostly shorted

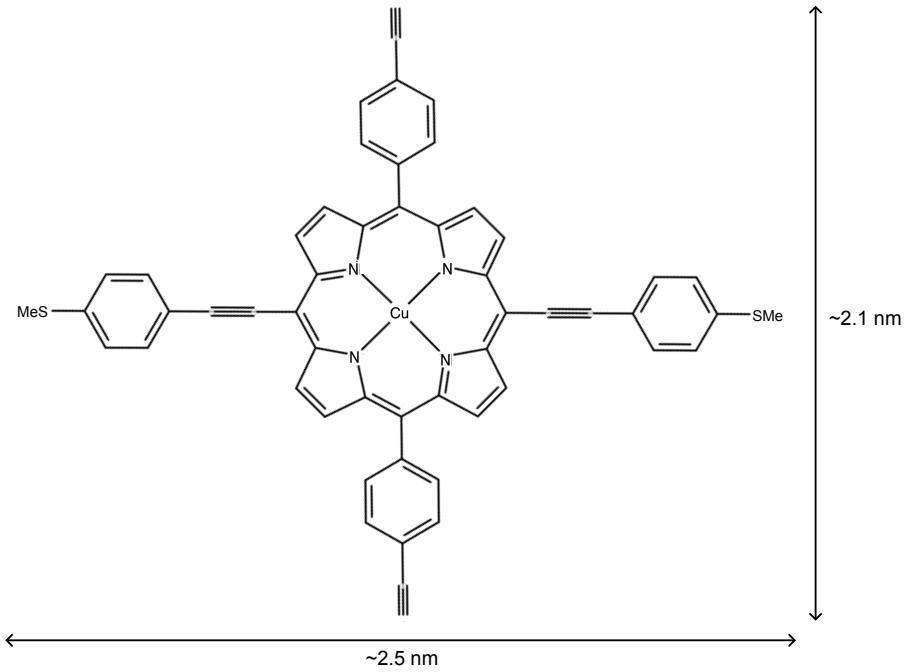

Figure 3.9: The copper porphyrin molecular structure. A central copper (II) ion is coordinated by a porphyrin ring. The corners provide the structure to fix the molecule into the origami structure: The thiol groups aid in covalently bonding the molecule to the gold leads and the acetylene groups are clickable into the DNA origami. In the image, 'Me' denotes a methyl group, and the 2.5 nm length includes these methyl groups. Reproduced with permission from [48].

[4] but with one device exhibiting a tunnelling curve, depicted below in figure 3.10. The curves are fit with a resonant tunnelling model, as described in 2.5.2 and B.2, yielding fit parameters for the molecular energy level ε_0 and the left and right tunnelling rates Γ_L, Γ_R. The 4.2 K and room temperature fit parameters are summarised in table 3.1. Numerically extracting the zero-bias conductance yields $3 \times 10^{-2}\, G_0$ at room temperature, decreasing to $2 \times 10^{-3}\, G_0$ at 4.2 K.

The fit parameters are consistent with tunnelling through the HOMO; this should be compared to the findings of Zotti et al [49], who experimentally and theoretically probed the effects of the terminating groups on single molecule electrical transport. They find that as the Sulfur component of the thiol-Gold anchor groups is electron

[4] This is likely due to aggressive RIE etching; indeed the shorted devices are visibly so under SEM

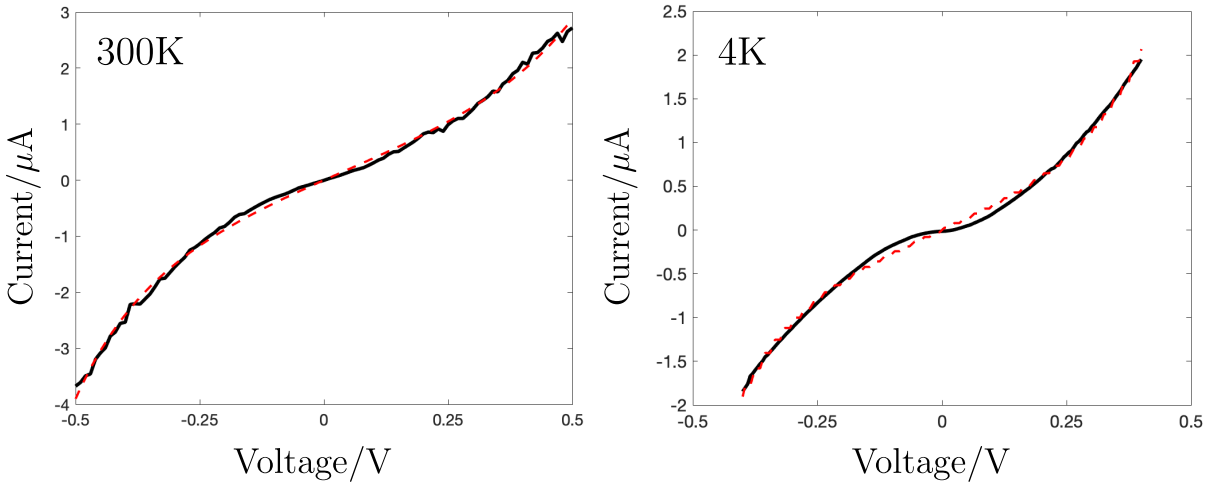

Figure 3.10: Room temperature and low temperature transport data for the candidate copper porphyrin molecular device, in black, with numerical fit to a single level resonant tunnelling model, in red. At low temperatures the resistivity of the device increases, particularly in the low bias region, where the model describes the transport less well.

Temperature	ε_0 / eV	Γ_L / meV	Γ_R / meV
300 K	-0.34	34	38
4.2 K	-0.28	26	25

Table 3.1: Fit parameters for a single level resonant tunnelling model applied to the candidate copper porphyrin device. The symmetry of the fit couplings in the 4 K data mean an almost identical fit can be achieved with $\varepsilon_0 = +0.28$ eV, although the room temperature fit values motivate taking the negative sign

donating, the HOMO is renormalised closer to the Fermi level, leading to HOMO dominated transport. It is highly plausible that a similar mechanism is at work here. There are some discrepancies in the simple model with the data in the low bias region $V < 15$ meV; there are several possible explanations for this. The model itself, of tunnelling only through one Lorentzian level may be unjustifiable: even if one level dominates the transport, there may be complex contributions from many other states, and the levels may change significantly as a function of applied voltage. Secondly, the model is only strictly valid for perturbative couplings Γ, which may not be valid in this instance, especially considering the fairly large conductance.

After measuring, the device was post imaged under SEM, depicted in figure 3.11.

The temperature dependence of the transport was also measured by taking a

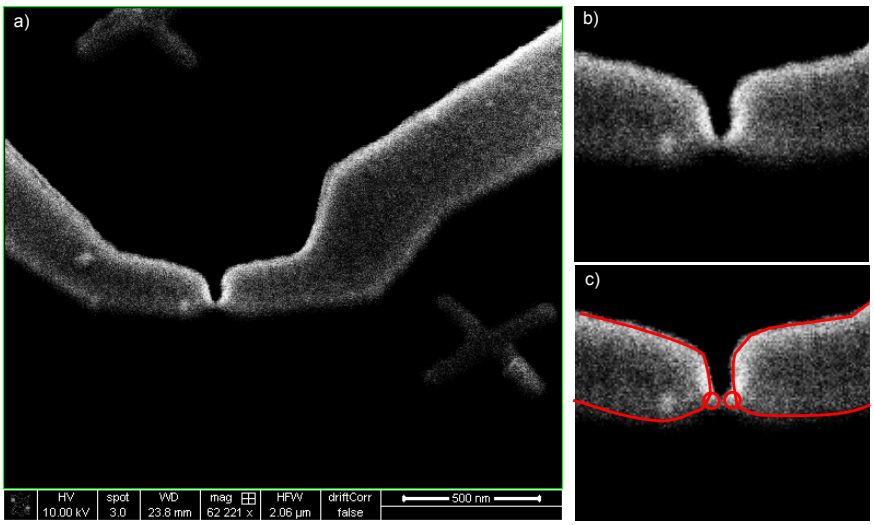

Figure 3.11: The candidate copper porphyrin device under SEM, imaged under tilt. The nanobead dimer is clearly seen. Subfigures b) and c) show the dimer zoomed in and with the relevant features outlined for clarity, respectively.

fixed bias cooling curve, explored in some detail later in figure 3.13.

3.4.2 Analysis of the transport

The difference between the room temperature and low temperature transport is far higher than would be expected purely from Fermi surface broadening. However, given the discussions of section 3.3.3, we have already seen that the data are consistent with the presence of mechanical fluctuations.

As mentioned above, the zero bias conductivity of the device is $2 \times 10^{-3}\, G_0$, which is significantly higher than that observed in STM experiments on comparable porphyrins (reviewed in [50]); these molecules typically have a zero bias conductance of around $10^{-5}\, G_0$. In the following I will attempt to provide some potential reasons for this discrepancy and also some criticisms, to explore the extent to which my result can be trusted. Of course, the most reliable check that could confirm or refute this result would be greater statistics.

Conformational arrangement of the molecule

One factor that could lead to an increased conductivity is the conformational arrangement of the molecule inside the origami structure. Leary et al [51] have reported high conductances of $10^{-3}\,G_0$ on zinc porphyrin MCBJ devices, which they attribute to a tilted configuration of the molecule inside the gap. The Sulfur to Sulfur distance of the copper porphyrin molecule is under 2 nm [48], but there could be some discrepancy in the size of the origami structure leading to a tilted configuration, explaining the higher than normal conductance.

Electrostatic effects

It is worth also considering that the electrostatic environment of the DNA origami is significantly different to the environment typical in single molecule experiments. I have demonstrated in the first half of this chapter that the origami appears to behave like a vacuum gap but a molecule embedded in this matrix will nonetheless experience some electrostatic perturbation. If this perturbation contributes to a strong coupling of the molecule with the leads or aligns the molecular energy levels well with those in the leads this could well increase the measured conductance. However, the observed increase in conductance with respect to MCBJ experiments of two orders of magnitude does not seem likely although should not be ruled out.

Possible bridging by a gold nanowire

Another possible explanation for the high conductivity could be the presence of a gold nanowire 'bridge' shorting the two contacts, depicted in figure 3.12. Over etching from the RIE process could destroy the photoresist around the dimer structure as to allow gold to bridge across, especially if the evaporation pressure is high and the deposition is diffusive rather than ballistic. However, there are some criticisms of this interpretation. Notably, if there were a perfect bridge of gold

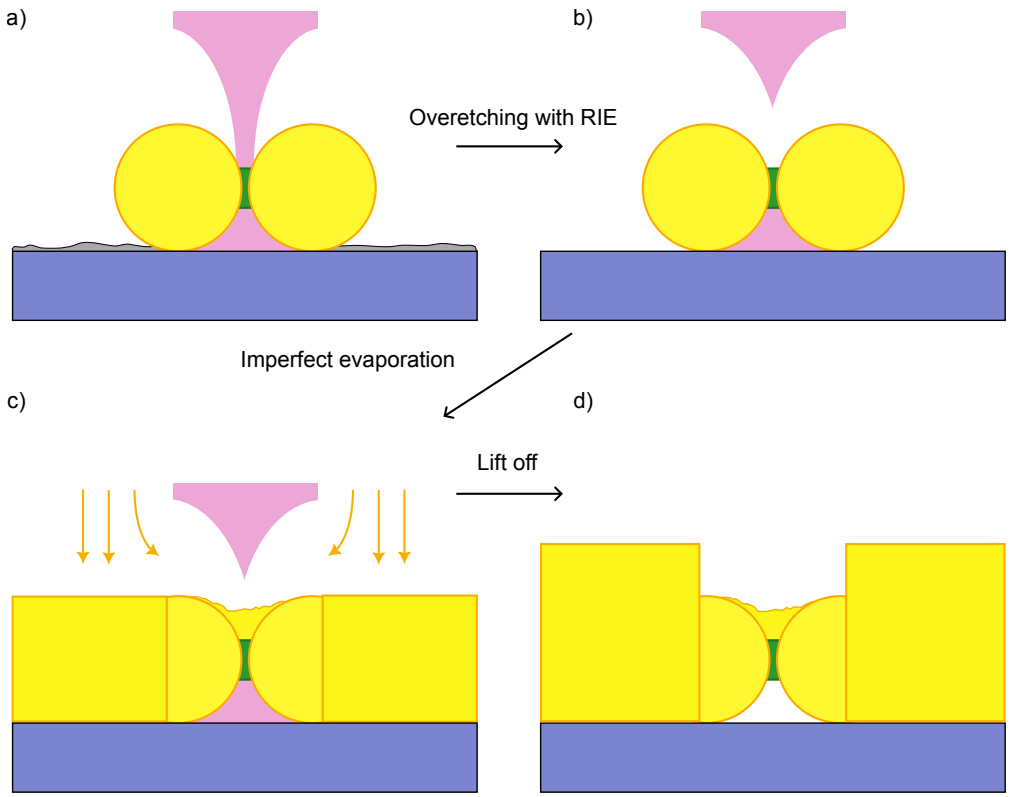

Figure 3.12: A speculative mechanism for the formation of a gold bridge. Subfigure a) depicts the unetched dimer after electron beam exposure. If the etching from the RIE is too aggressive and insufficiently anisotropic, the undercut could be sufficiently degraded to make a hole through the resist, shown in subfigure b). If the evaporation proceeds at too high a pressure the gold is not applied perfectly vertically as in subfigure c), which could scatter gold across the dimer, forming a bridge. After liftoff, this could cause a shorted device with a gold nanowire bridging the gap, pictured in subfigure d).

across the gap, this would likely produce a region with perfect coherent transmission, with $T(E) = 1$ (in the Landauer-Büttiker sense) per channel. This would lead to a minimum conductance of G_0, far higher than that observed [52].

In light of this, if this hypothesis holds there can not be a continuous piece of gold and there should instead be gold puddles where coherent transport may occur, coupled by scattering regions of imperfect transmission. These puddles would form a disordered network in position and energy, similar again to Variable Range Hopping (VRH), and it is reasonable to expect a strong temperature dependence in the transport. If one dimensional VRH is responsible for the transport, we should

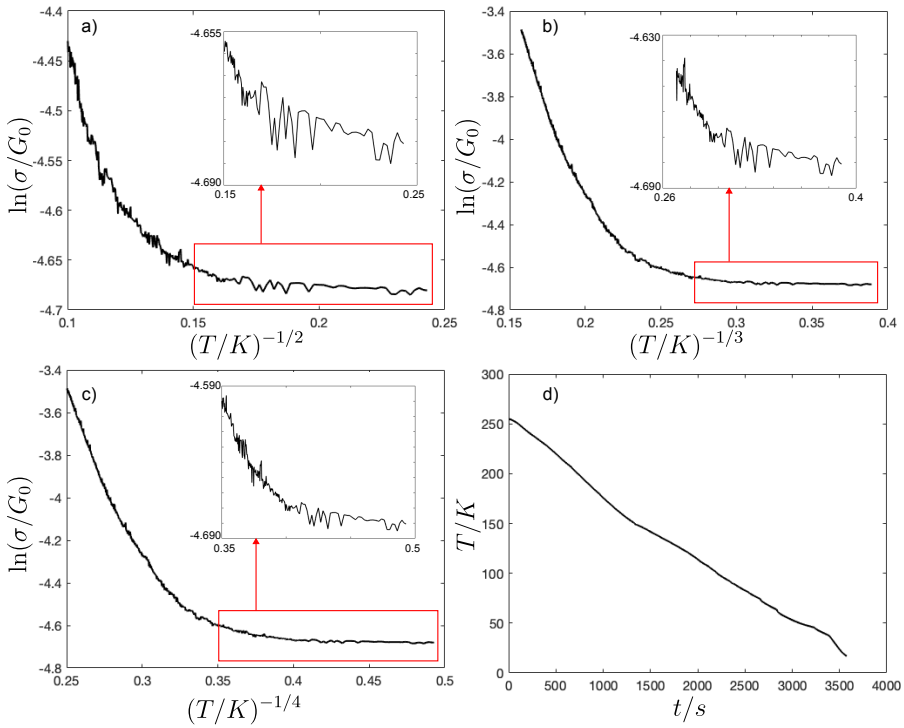

Figure 3.13: The first three plots (a, b, c) show tests of Variable Range Hopping for the candidate device in $d = 1$, 2, 3 respectively. This mechanism predicts a $\log(\sigma) \sim T^{-1/(d+1)}$ relationship. Inset in each is the same curve zoomed in on the highlighted region, to demonstrate that there is no significant temperature range over which the data can be considered linear. The noise increases somewhat under 50 K; this is due to an increase in cooling rate, visible in the cooling curve (d).

see $\log(\sigma) \sim T^{-1/(d+1)}$ at low temperatures over a reasonably large temperature range. I have tested this for $d = 1$, 2, 3 in figure 3.13. The data do not appear to be consistent with this interpretation, although the potential coexistence of temperature dependent mechanical effects could reasonably modify the VRH signal.

The above discussion demonstrates that resonant tunnelling through a molecular energy level is a plausible model for the transport, and there are no obvious failure modes that would mimic this signal. However, this assertion is not ironclad and the *only* true test of experimental success would be the fabrication of a statistically large number of similar devices demonstrating qualitatively similar transport characteristics.

3.4.3 On the possibility of observing the Kondo effect

As there is a free spin on the copper atom at the heart of the molecule, it is reasonable to question whether the Kondo effect could be observed, particularly given the fairly strong coupling of the molecule to the leads. The Kondo effect is a strong coupling effect between localised impurity spins and delocalised states, leading to a resonance at the Fermi level below a characteristic Kondo temperature [53]. This effect was traditionally thought of in the context of magnetic impurities in metals [54], but applies equally well in quantum dot systems [55]. The cooling data of figure 3.13 provide some experimental insight; there is a monotonic (up to noise) decrease in the conductivity at low temperatures, with no evidence of the logarithmic rise that would be expected for a Kondo resonance. From this we should infer that the Kondo temperature of the molecular system is below 4 K. The Kondo temperature is exponentially sensitive to the local electrostatic properties [56]; so while some estimates in the case of molecular systems place the Kondo temperature as high as tens of Kelvin [42], this should be expected to vary wildly on a per system basis.

3.5 Future outlooks

Through this chapter I have demonstrated that DNA origami provides a viable platform for deterministic fabrication of nanogap devices and a proof of concept fabrication of a single molecule device. This demonstration of the success of the DNA origami architecture opens the path to a great many more experiments, even with the two terminal devices demonstrated here and the myriad fabrication challenges. There is significant opportunity to apply these methods to the many already existing successful demonstrations of molecular electronics, to replicate them at scale and gain greater statistical certainty over any results. Achieving true mass fabrication of high yield molecular devices is therefore the most immediate priority for this architecture.

There are two longer term goals related to validation of the architecture as a

viable information processing platform. One of the ultimate goals of this architecture should be to couple together multiple molecular devices and to demonstrate the constituent molecules' functionality as coupled classical or quantum bits. A major modification of the design for future iterations is the addition of a third terminal in order to locally gate the molecular degrees of freedom. As explained in section 2.4, this does indeed require a significant modification, although I explore a possible avenue towards overcoming this problem in appendix A. Manipulating the voltage at the molecule allows operation of the molecular device as a single electron transistor. If this and the previous goal of coupling multiple devices together can be achieved, this could be used to fabricate modular molecular logical processing devices. A half-adder requires only 4 transistors: making this with stochastically contacted devices would be near impossible, but deterministic fabrication makes this goal much more achievable provided local electrical control can be added to the devices.

3.6 Conclusion

Throughout this section, I have presented experimental and computational results detailing the development of our DNA origami single molecule electronics platform. I have detailed the fabrication process and simulations of the experimental architecture, before presenting measurements on devices fabricated with these processes. The major results are the successful high yield fabrication of nanoscale tunnelling junctions and a likely fabrication of a copper (II) porphyrin molecular device with our DNA origami methods. These results herald a major step towards fully scalable deterministic fabrication of single molecule electronic devices.

References

[27] Hartmuth C Kolb, MG Finn, and K Barry Sharpless. “Click chemistry: diverse chemical function from a few good reactions”. In: *Angewandte Chemie International Edition* 40.11 (2001), pp. 2004–2021.

[32] James MacQueen et al. “Some methods for classification and analysis of multivariate observations”. In: *Proceedings of the fifth Berkeley symposium on mathematical statistics and probability*. Vol. 1. 14. Oakland, CA, USA. University of California Press, Berkeley, 1967, pp. 281–297.

[42] Juan Carlos Cuevas and Elke Scheer. *Molecular electronics: an introduction to theory and experiment (World scientific series in nanoscience and nanotechnology, vol. 1)*. eng. Singapore: World Scientific Publishing Co. Pte. Ltd, 2010.

[43] A. Mangin et al. “Reduced work functions in gold electromigrated nanogaps”. In: *Phys. Rev. B* 80 (23 Dec. 2009), p. 235432. URL: https://link.aps.org/doi/10.1103/PhysRevB.80.235432.

[48] K Andrews. Private communication. Feb. 2023.

[49] Linda A Zotti et al. “Revealing the role of anchoring groups in the electrical conduction through single-molecule junctions”. In: *Small* 6.14 (2010), pp. 1529–1535.

[50] Patrick Zwick, Diana Dulić, Herre S. J. van der Zant, and Marcel Mayor. “Porphyrins as building blocks for single-molecule devices”. In: *Nanoscale* 13 (37 2021), pp. 15500–15525. URL: http://dx.doi.org/10.1039/D1NR04523G.

[51] Edmund Leary et al. “Detecting mechanochemical atropisomerization within an STM break junction”. In: *Journal of the American Chemical Society* 140.2 (2018), pp. 710–718.

[52] Francesca Tavazza et al. “Electron transport in gold nanowires: Stable 1-, 2-and 3-dimensional atomic structures and noninteger conduction states”. In: *Phys. Rev. Lett.* 107.12 (2011), p. 126802.

[53] Jun Kondo. "Resistance minimum in dilute magnetic alloys". In: *Progress of Theoretical Physics* 32.1 (1964), pp. 37–49.

[54] P. W. Anderson. "Localized Magnetic States and Fermi-Surface Anomalies in Tunneling". In: *Phys. Rev. Lett.* 17 (2 July 1966), pp. 95–97. URL: https://link.aps.org/doi/10.1103/PhysRevLett.17.95.

[55] Michael Pustilnik and Leonid Glazman. "Kondo effect in quantum dots". In: *Journal of Physics: Condensed Matter* 16.16 (2004), R513.

[56] F. D. M. Haldane. "Scaling Theory of the Asymmetric Anderson Model". In: *Phys. Rev. Lett.* 40 (6 Feb. 1978), pp. 416–419. URL: https://link.aps.org/doi/10.1103/PhysRevLett.40.416.

Part II

DFT investigations into the surface states of topological Kondo insulator SmB_6

4

Topological insulators in DFT

4.1 Introduction

In the first chapters of this thesis I presented novel approaches to the fabrication of truly nanoscale devices. In the following I will present a computational study on a different topic relevant to device physics, investigating the surface states of a topological insulator with potential applications in spintronics. When working with materials that are not fully understood, computational work can be extremely useful in bridging the gap between theory and experiment. Computations may provide an independent check on the way that microscopic causes are attributed to observed effects. The main title of the thesis alludes to transport specifically; this is because the topological surface states which I shall be studying here are the states directly involved in transport and responsible for the device physics applications.

The past 15 years has seen a huge interest in so called *topological materials*,

following the prediction and observation of symmetry protected topological phases of matter in HgTe/CdTe quantum wells and in certain bismuth compounds. The origins of this field lie in a now landmark paper published in 1982 [57], where it was discovered that the Quantum Hall conductance of certain 2D materials can be derived purely in terms of global (that is, topological) properties of the electron wavefunction, as opposed to local operators. The hallmarks of these states are the presence of gapless edge modes between topologically trivial and nontrivial regions. These materials and their surface states are of great interest, partly due to the richness of the underlying physical mechanisms but also due to their potential applications. A particular class of topological insulators, the so called $\mathbb{Z}_2$ insulators [58] [59], features surface states with emergent Dirac cone excitations with strong spin momentum locking, where electrons with a given momentum have definite spin.

These spin momentum locked states feature strong suppression of back scattering, making them attractive materials from a device physics perspective where they could provide transport without dissipation from scattering or feature in spintronic applications [60]. However, the most studied topological insulators (the bismuth based compounds) have a fairly high contribution to conductivity from the bulk. Topological insulators also have a role to play in achieving topological superconductivity, which has attracted much attention for its uses in topological quantum computing [61] and for displaying emergent Majorana physics [62]. It is therefore highly desirable to study materials with more robustly insulating bulks.

Samarium hexaboride (SmB_6) is a material believed by many to be a topological insulator, but with several outstanding mysteries. SmB_6 was the first Kondo insulator discovered, where localised f electrons hybridise with mobile d electrons below the Kondo temperature to open a small gap. Experimentally a plateau in conductance is observed at low temperatures: this was originally deemed to be a result of mid-gap impurity states but later reinterpreted as being a product of conducting surface states. Interestingly from the perspective of device physics, the

bulk resistivity of SmB_6 appears to be much higher than in the bismuth compounds. This makes it a plausible candidate for use in devices where it is desirable for all of the conduction to be through the (spin-momentum locked) surface, instead of through the dissipative bulk. Certain questions remain however unanswered. From a theoretical point of view, the Kondo effect is a strongly coupled problem and the topological band theory in which these systems are commonly understood is phrased in terms of semiclassical Bloch band theory, which is noninteracting. ARPES experiments observe spin polarised Dirac-like states, consistent with the topological explanation, but this likely does not capture the full picture. Quantum oscillation studies have also returned complex results when attempting to explore the origins of the conduction [63]. A transport study [64] finds strong sensitivity of the conduction to local electrostatic perturbation, motivating questions into the nature of the surface band filling and the role of the local electrostatics. A summary and brief discussion of prior experimental data is given in section 4.4.

In the following chapters I will motivate and demonstrate Density Functional Theory (DFT) studies performed with the aim of understanding the local electrostatics and band fillings of the SmB_6 [100] surface states. A greater understanding of both of these is essential not only to accurately diagnose the many body physics of the bulk ground state, but also to enable future spintronic devices to be designed. In particular, I will be looking at the way in which local electrostatic effects dope the surface bands and move the Dirac cone to expand upon the experimental results of reference [64] and the qualitative explanations in reference [65]. Given that the interactions between the local moments and conduction electrons is fundamentally in strong coupling, it is striking the degree to which qualitative agreements can be reached between experiment and DFT, which does not incorporate strong correlation effects.

4.2 Band theory, symmetry and topological band theory

The previous section motivates studying the properties of solids and the way that a crystal's structure influences the quantum mechanical properties of the material. Since the 1950s the central paradigm of condensed matter has been to use the periodicity of crystalline quantum matter to work in terms of reciprocal space, where the eigenfunctions of the Hamiltonian have a convenient form as Bloch functions [66]. This may further be built upon by discussing the constraints placed upon these eigenfunctions by the crystal symmetries. In this section I will briefly review the basic concepts of band theory and then I will introduce the topological band theory, to demonstrate the ways in which the theory can be expanded by considering under what conditions the symmetries and structure do not necessarily give a complete picture of a material's phenomenology.

4.2.1 Bloch's theorem and symmetry

For any periodic crystal, one may define a periodic Hamiltonian invariant under translation by a lattice vector $\mathbf{R}$. This translational invariance necessarily implies Bloch's theorem, which is the statement that for a Hamiltonian periodic in some lattice with lattice vectors $\mathbf{R}$,

$$\mathcal{H}(\mathbf{r}) = \mathcal{H}(\mathbf{r} + \mathbf{R}), \tag{4.1}$$

then the wavefunctions transform under the one-dimensional fundamental irreducible representation given by

$$\psi(\mathbf{r} + \mathbf{R}) = e^{i\mathbf{k}\cdot\mathbf{R}}\psi(\mathbf{r}). \tag{4.2}$$

Each eigenfunction can then be written as

$$\psi_{n\mathbf{k}}(\mathbf{r}) = e^{i\mathbf{k}\cdot\mathbf{r}} u_{n\mathbf{k}}(\mathbf{r}) \tag{4.3}$$

where $u_{n\mathbf{k}}(\mathbf{r})$ has the same periodicity as the lattice. The proof of this is straightforward and can be found in, for example, references [67], [68]. The quantum numbers n and $\mathbf{k}$ label the infinite set of states $\{n\}$ that exist at each $\mathbf{k}$. These functions are known as Bloch functions, and the eigenfunction labelled by a singular n as a function of $\mathbf{k}$ is known as a band. The periodicity in real space imposes a periodicity in $\mathbf{k}$-space as well, which is generated by translations by the reciprocal lattice vectors $\mathbf{G}$, defined by $\mathbf{R}_i \cdot \mathbf{G}_j = 2\pi\delta_{ij}$. The space spanned by the set of $\mathbf{k}$'s is known as the Brillouin zone.

These bands, collectively known as the band structure of the material, form the major object of interest in much of condensed matter. Just as the translational symmetry imposes representation theoretical constraints upon the mathematical form of the bands, the crystallographic symmetries impose their own constraints on the systems' energies. The wavefunctions of the electrons in a solid must transform under an irreducible representation of the symmetry imposed by the crystal field, splitting the energies found from an isolated ion; when phrased in terms the effects in the Brillouin zone, this gives the irreducible representations of the wavefunction at the point $\mathbf{k} = 0$, known as Γ [68]. Similar arguments may be devised for high symmetry paths in $\mathbf{k}$-space: the wavefunction as a function of $\mathbf{k}$ must transform under a representation of the symmetry group of $\mathbf{k}$, that is the set of operations in the symmetry group of the crystal which map $\mathbf{k}$ onto itself[1].

As points in $\mathbf{k}$-space that are equivalent under some symmetry transformation must have the same energy, high symmetry lines (where $\mathbf{k}$ may map onto itself under several symmetries) will frequently contain several degeneracies. In this way

[1] Or an equivalent $\mathbf{k}' = \mathbf{k} + \mathbf{G}$ for some reciprocal lattice vector $\mathbf{G}$.

the degeneracies of the states represented in the band structure are completely determined and the energetic ordering of these states must then be determined with physical data. However, this does not completely describe the material, for reasons that will be explained in the next section.

4.2.2 Introduction to topological band theory

In this section I will give a short overview of the main relevant results of topological band theory in order to clarify my later theoretical investigations. A treatment in significantly greater detail is presented in appendix C.

In introductory condensed matter texts, the notion of bands is often introduced in terms of tight binding models with respect to the atomic limit. Bands are considered as developing continuously as a result of orbital overlap between neighbouring hopping sites [67]. This does not, however, completely describe the situation in general: there are materials where it is *impossible* to write a tight binding model where the hopping orbitals are atomic[2] and exponentially localised [69]. This describes a class of materials that can not be obtained by smooth transformations from 'trivial' insulators, distinguished by global properties of their wavefunctions, which are named topological. These materials have several properties making them appealing to device physicists.

This fact is less mysterious when phrased in terms of the mathematics of the Brillouin zone wavefunction. From the above, we see that the wavefunction $\psi(\mathbf{k})$ maps a point $\mathbf{k}$ onto a Hilbert space $\mathfrak{H}_{\mathbf{k}} \cong \mathbb{C}^n$ [70–72]. The total Hilbert space of filled bands forms a manifold, so the wavefunction can be considered in its fullest generality to encode arbitrary maps between two manifolds. The mathematical treatment of these types of problems is known as the theory of characteristic classes [70]. The first major use of this fact was the discovery that the Quantum Hall conductance is directly related to the Chern number, a topological property of the

[2]Meaning here adiabatically connected to atomic limit orbitals of the constituent atoms.

wavefunction, in the now famous 'TKNN' paper [57].

Different maps can be considered as the different wavefunctions resulting from the Hamiltonians of distinct materials. Just as mapping one circle onto another circle admits a winding number, the wavefunction may also be similarly 'twisted,' with higher dimensional analogs of winding numbers characterising the map between momenta and the Hilbert space. These 'twisted' wavefunctions can not be smoothly deformed into wavefunctions without encountering discontinuities in the definition of the filled bands, and are hereby denoted as 'topological'. In physics, this is often seen by computing windings of the celebrated Berry connection

$$\mathcal{A} = \frac{1}{i} \langle u | \mathrm{d}u \rangle \tag{4.4}$$

where the $|u\rangle$ are Bloch functions. In two dimensions, scenarios where the wavefunction exhibits a twist are distinguished by the presence of a non-zero *Chern number*

$$Ch = \frac{1}{2\pi} \int \mathrm{d}k_x \mathrm{d}k_y (\nabla \times \mathcal{A}) \cdot \hat{k}_z \in \mathbb{Z} \tag{4.5}$$

which measures the degree to which Stokes' theorem fails [73] and is sensitive to nonanalytic behaviour in the Berry connection. How can we see this? Consider the following: if Stokes' theorem held fully, equation 4.5 would give zero. However, if there are nonanalyticities in the Berry connection then $\mathcal{A}$ may not be defined over the entire Brillouin zone and a nonzero Chern number results. These vortices may not be removed via gauge transformations: they are fundamental properties of the wavefunctions. 'Undoing' one of these twists results in a fundamental change in the Hilbert space of filled bands, forcing the wavefunction to have a different number of twists. Physically, this presents as the bandgap closing as the wavefunctions are tuned between each other and is the origin of the metallic states seen when moving between states of differing topological invariant. As mentioned above, a

more complete discussion of the mathematics involved is presented in appendix C.

4.2.3 Time reversal symmetric insulators in two dimensions

In the above I have motivated the possibility of quantum matter to admit nonzero Chern numbers, corresponding to generalised winding numbers in the wavefunction over the Brillouin zone. However, the admissible topological invariants are strongly dependent on the symmetries present in the material. A symmetry with a particularly strong influence on the topological structure is time reversal symmetry (TRS).

Time reversal symmetry is an antiunitary symmetry Θ obeyed by non-magnetic fermionic matter, satisfying

$$\Theta\mathcal{H}(\mathbf{k}) = -\mathcal{H}(-\mathbf{k})\Theta^{-1} \tag{4.6}$$

on the Hamiltonian, and

$$\Theta\left|u_n(\mathbf{k})\right\rangle = \left|u_{n'}(-\mathbf{k})\right\rangle \tag{4.7}$$

on the eigenstates. For our purposes I will discuss two consequences of this. The first of these is Kramers' theorem: the time reversed partner of a state $|u(\mathbf{k})\rangle$ is also an eigenstate, with the same energy. This partitions the Hilbert space into a $U(2)$ symmetric set of Kramers pairs [73]. The second useful consequence is the vanishing of the total Chern number. To see this, partition the Hilbert space under the time reversal symmetry into $\{\{|u^I(\mathbf{k})\rangle\},\{|u^{II}(\mathbf{k})\rangle\}\}$, where the $\{|u^{II}(\mathbf{k})\rangle\}$ are the time reversed partners of the $\{|u^I(\mathbf{k})\rangle\}$. This partitioning is in some sense fictitious; it is not meaningful to isolate single members of Kramers pairs, but the result will not depend on this partitioning. Then, under time reversal the Berry

connection evaluated on one 'half' of each Kramers doublet is

$$\Theta\mathcal{A}^I = \frac{1}{i}\sum_n \Theta\left[\langle u^I(\mathbf{k})|\,\partial_{\mathbf{k}}\,|u^I(\mathbf{k})\rangle\right] \tag{4.8}$$

$$= \frac{1}{i}\sum_n \langle u^{II}(\mathbf{k})|\,(-\partial_{\mathbf{k}})\,|u^{II}(\mathbf{k})\rangle \tag{4.9}$$

$$= -\mathcal{A}^{II} \tag{4.10}$$

so the overall Berry connection $\mathcal{A} = \mathcal{A}^I + \mathcal{A}^{II}$ vanishes, leading to zero total Berry curvature and zero Chern number [74]. Nonetheless, this system does in fact admit a topological invariant. Imagine again that it were possible to isolate a single member of each Kramers doublet. Then, in $d = 2$ the $\mathbb{Z}_2$ invariant is given by

$$\nu = (-1)^{Ch^I} = (-1)^{Ch^{II}} \in \mathbb{Z}_2 \tag{4.11}$$

This partitioning into single members of Kramers pairs is of course fictitious, but the result is independent of the choice so this is a viable topological invariant, counting the parity of the number of vortices in the Berry connection over the Brillouin zone [75].

4.2.4 Three dimensions: Strong and weak topological insulators

The above considerations are specific to the case of $d = 2$, but there are generalisations of this into $d = 3$. I shall only briefly touch on these points as the fine details are slightly technical, but can be found in, for example, Fu et al [76]. The structure of the Brillouin zone in $d = 3$ is different, where the number of time-reversal invariant momenta (TRIM) changes from 4 to 8. This defines a series of 6 time reversal invariant planes, each analogous to a 2 dimensional Brillouin zone, although only 4 of these are independent. Topological indices $v_{0,1,2,3}$ may be defined

for these, with slightly differing properties. Three of these are analogues of the two dimensional invariant, corresponding to layers of two dimensional topological insulators stacked along z: this phase is known as a *weak* topological insulator. The fourth phase is unique to 3 dimensions and is the full higher dimensional version of the $\mathbb{Z}_2$ insulator, known as a *strong* topological insulator. The topological index is sometimes written in the form $\nu = (\nu_0; \nu_1, \nu_2, \nu_3)$, where ν_0 is the strong invariant and the latter three are weak invariants. For example, the bismuth 3DTIs are in topological class $(1; 0, 0, 0)$ [73]. The case I shall be devoting attention to from here on is the three dimensional $\mathbb{Z}_2$ insulator.

These discussions have demonstrated the possibility of realising a 3 dimensional insulator with nontrivial bulk topology, but offer little to explain what microscopic physics might lead to this phenomenon or how to calculate the invariants without recourse to detailed analysis of the degree of components of the Hamiltonian. There are fortunately many equivalent ways of phrasing and calculating the topological index ν, and I shall in the remainder of this thesis be using a particularly elegant one derived by Fu and Kane [58] [59], for the case that the system has inversion symmetry as well as time reversal symmetry. In this case, the vectors of the bundle of filled bands (i.e. the wavefunctions) have definite parity ξ at the high symmetry points, and the topological index is given by the product of this overall parity at the time reversal invariant high symmetry points. The parity is given by

$$\xi(k) = \prod_m \xi_{2m}(k) \tag{4.12}$$

where ξ_{2m} is the parity eigenvalue of the m^{th} 2-dimensional Kramers subspace[3]. Note that this parity is calculated from all of the filled bands: it is the entire filled band

[3]The right hand side of this equation can be thought of as a parity operator $P^{\otimes m}$ acting on a single Slater determinant of the filled bands.

bundle that is nontrivial. Once this has been found the $\mathbb{Z}_2$ index is then given by

$$\nu = \prod_{\lambda \in \{\text{TRIM}\}} \xi(\lambda), \tag{4.13}$$

with a negative value of ν corresponding to the topological phase.

4.2.5 Band inversion and surface states

Given the above formula in terms of band parities, it is reasonable to search for places in nature where this occurs. A natural place to look for this physics is in insulators with strong spin orbit coupling, where the coupling between bands can lead to band inversion. If the bands which invert are of opposite parity, this can lead to precisely the above scenario, where inverting at some high symmetry points can lead to an overall negative ν. This behaviour is captured by the Bernevig-Hughes-Zhang model [77] [78] [79], consisting of two time reversed sets of bands of opposite parity that undergo a Chern insulator transition at the band inversion. Tuning away from this point towards vacuum, at the critical point the topological surface states are visible. The coupling between bands must be parity odd as the bands are opposite parity, so to first order it is taken to be linear in components of $\mathbf{k}$. Let the parity even and odd states be written A, B. Then at the surface, the Hamiltonian is given in the basis $\{|A\uparrow\rangle, |B\uparrow\rangle, |A\downarrow\rangle, |B\downarrow\rangle\}$ by

$$\mathcal{H} = \begin{pmatrix} M(\mathbf{k}) & v_F(k_y - ik_x) & 0 & 0 \\ v_F(k_y + ik_x) & -M(\mathbf{k}) & 0 & 0 \\ 0 & 0 & M(\mathbf{k}) & -v_F(k_y + ik_x) \\ 0 & 0 & -v_F(k_y - ik_x) & -M(\mathbf{k}) \end{pmatrix} \tag{4.14}$$

where $M(\mathbf{k}) = \mu - Bk^2$. This is of the form

$$\begin{pmatrix} h(\mathbf{k}) & 0 \\ 0 & h(-\mathbf{k})^* \end{pmatrix} \tag{4.15}$$

so that the time reversal symmetry is obviously satisfied. The labelling of the coupling as v_F will become clear in the following.

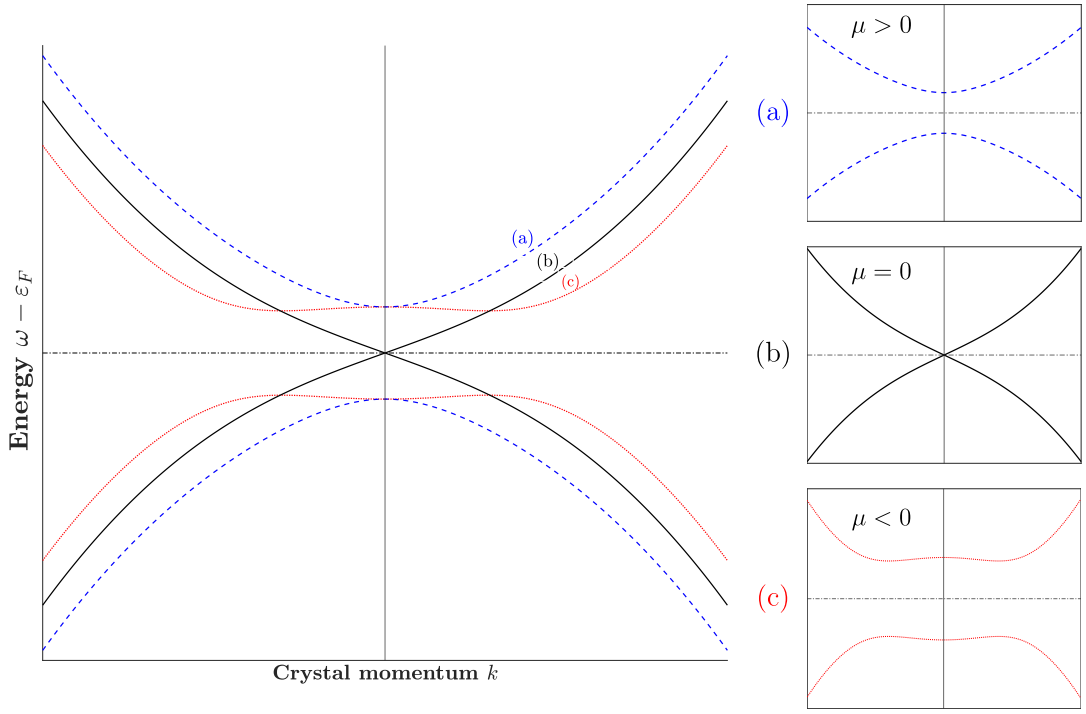

Figure 4.1: The band structure when tuning through the surface of a topological insulator. By tuning the band inversion parameter μ between positive and negative values, a Dirac point emerges. Subfigure a) shows the uninverted bands in the trivial region, c) shows the inverted bands in the topological region and b) shows the critical point at the surface with the Dirac cone.

The band structure of this model at various values of μ is shown in figure 4.1. The most notable feature is the $\mu = 0$ band structure, corresponding to the crossover between a trivial and topological phase, which features a band inversion at the high symmetry point where the local Hamiltonian exhibits an emergent Dirac cone with

velocity v_F, with local Hamiltonian $\mathcal{H} = v_F \boldsymbol{\sigma} \times \mathbf{k}$[4]. This band structure is analogous to that of the Dirac cone in graphene, but with the pseudospin sublattice index replaced by the physical spin. The spin dependence induces spin-momentum locking in the surface states and is the driving feature behind the lack of backscattering observed in transport [64]. By considering the way the topological surface states emerge at the region between $\mu < 0$ and $\mu > 0$ they can be considered a consequence of necessary fine tuning, forcing the Hamiltonian to be degenerate at the TRIM. Band crossings are in general rare except as the result of some symmetry protecting them and so the $\mathbb{Z}_2$ insulator can be thought of as one way of symmetries forcing this fine tuning band crossing to occur as we tune μ. The fact that the surface state must be there follows from the fact that the vacuum outside the material is by definition in the trivial phase, so there must be a point in physical space where the bands cross critically, yielding a Dirac cone.

4.3 Density Functional Theory for band structure calculations

The above discussions describe the ways that band structures can be categorised based on symmetry principles, but do not fix the order of bands or give quantitative predictions. More explicit methods for dealing with the electron-electron interactions must be used for this, which I shall elaborate on here. The most natural starting point is the many body Schrödinger equation for the electrons, which can be seen as the 'true' determining equation for the system. In the Born-Oppenheimer

[4]This Hamiltonian is sometimes derived in a way such that the 2D Dirac cone Hamiltonian is $\mathcal{H} = v_F \boldsymbol{\sigma} \cdot \mathbf{k}$. This is equivalent to the above under a unitary rotation in spin space.

approximation and without spin-orbit effects for the time being [80], this is

$$\left[\underbrace{-\hbar^2 \sum_i \frac{\nabla_i^2}{2m_e}}_{\text{Electron kinetic energy}} + \underbrace{\frac{1}{2}\frac{e^2}{4\pi\epsilon_0}\sum_{i\neq j}\frac{1}{|\mathbf{r}_i-\mathbf{r}_j|}}_{\text{e-e repulsion}} + \underbrace{\frac{e^2}{4\pi\epsilon_0}\sum_{iJ}\frac{Z_J}{|\mathbf{r}_i-\mathbf{R}_J|}}_{\text{e-n attraction}} \right]\Psi = E\Psi. \quad (4.16)$$

Using the simplifications granted by Bloch's theorem to express this in terms of plane waves, it might be hoped that this yields a useful solution. Unfortunately, there is a significant exponential scaling problem rendering this implausible for all but the simplest systems. The most common approach to overcome this problem in computational materials science is Density Functional Theory. In a series of papers from 1964 to 1965, Hohenberg and Kohn [81] proved a theorem that enable a dramatic computational simplification of the above equation. By recasting the Schrödinger equation for the electrons in a solid in terms of the electron density, an exact reformulation is possible, that can then be recast into forms particularly amenable to computational evaluation [82].

4.3.1 Hohenberg-Kohn-Sham DFT

Following the discussion of 4.3, I shall state Hohenberg-Kohn theorem and explore the ways in which it can be used fruitfully with the Kohn-Sham equations. Hohenberg and Kohn proved that an exact reformulation of the Schrödinger equation may be made in terms of the overall electron density $n(\mathbf{r}) = \int |\Psi(\mathbf{r}, \mathbf{r}_2, ..., \mathbf{r_N})|^2 \mathrm{d}\mathbf{r}_2 ... \mathrm{d}\mathbf{r}_N$, Ψ being the many body wavefunction[5]. This only depends on 3 variables (in 3 dimensions) and is therefore much more computationally tractable than the exponentially hard many body Schrödinger equation above.

The theorem consists of two statements:

- The electron density $n(\mathbf{r})$ uniquely determines the external potential V and

[5] If Ψ is expressed in terms of a finite set of orthonormal orbitals ψ_i, then the density is given by $n(\mathbf{r}) = \sum_i |\psi_i(\mathbf{r})|^2$.

so the energy is a functional of the density $E = E[n]$

- The total energy is variational in this density $\frac{\delta E[n]}{\delta n} = 0$

and is exact, but still rather difficult to work with for performing calculations. A significant advancement was introduced by Kohn and Sham [82]. By expressing the wavefunction as a Slater determinant of the single particle eigenstates ψ_i, the Schrödinger equation can be written as a set of independent particle equations. The electron-electron interaction is replaced by two functionals: the Hartree energy and the so-called exchange-correlation energy. The Hartree potential V_H is a classical electrostatic potential arising from a charge distribution $n(\mathbf{r})$, with the exchange-correlation potential V_{xc} incorporating the rest of the effective potential experienced by electron density. This may seem like mere sleight of hand, but the exchange-correlation potential may be approximated in a systematic fashion. The results of this approach are the Kohn-Sham equations [83]

$$\left[\frac{-1}{2m}\nabla^2 + V_H + V_{xc} + V_{nuc}\right]\psi_i(\mathbf{r}) = \varepsilon_i\psi_i(\mathbf{r}) \tag{4.17}$$

where the Kohn-Sham orbitals ψ_i satisfy $n(\mathbf{r}) = \sum_i |\psi_i(\mathbf{r})|^2$ and V_{nuc} is the external potential of the nuclei. Further corrections to the Hamiltonian can be made, such as including relativistic effects like spin-orbit coupling. In order to do this, the Schrödinger equation above is replaced with a Dirac equation and the wavefunction replaced by a two component spinor. The charge density in this case becomes a spin-density matrix [80]

$$\mathcal{N}_{\alpha\beta}(\mathbf{r}) = \sum_i \psi_i^*(\mathbf{r},\alpha)\psi_i(\mathbf{r},\beta) \tag{4.18}$$

and the total charge density is given by the trace of this matrix $n(\mathbf{r}) = \mathrm{Tr}[\mathcal{N}]$.

The Kohn-Sham equations can then be solved self-consistently, as depicted in figure 4.2. All DFT calculations in this thesis have been produced with the

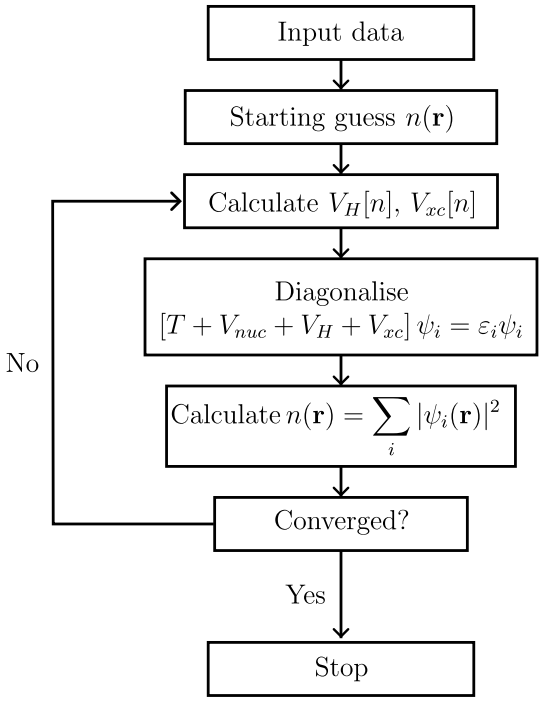

Figure 4.2: The self-consistency loop used in Kohn-Sham DFT. The DFT calculations in this thesis are performed using `QuantumESPRESSO`, which implements DFT based on plane waves: the diagonalisation is done up to a maximum plane wave energy `ecut` and the electron density is found by summing over discretised points in $\mathbf{k}$ space. T is shorthand for the kinetic energy term.

open-source package `QuantumESPRESSO` [84] [85], which implements plane wave DFT for materials modelling.

4.3.2 Pseudopotentials and exchange-correlation functionals

The above statement of DFT is in principle applicable to materials but in practice several more approximations must be made. A particularly common one is the use of a pseudopotential [86] for the atomic potential to incorporate certain aspects of the screening of the nuclear charge by core electron states, so that only some of the valence electrons need to be considered. The simplest type of pseudopotential uses a *norm-conserving* approach [80, 87, 88], with the following steps:

- Perform an all electron Kohn-Sham calculation with a specific choice of exchange-correlation functional to obtain the electron potential
- Decide on a radial cutoff below which the core states will be smoothed out. Above this the pseudopotential and the all electron potential are identical
- Replace the potential within this cutoff with a smooth, nodeless function with which it is easier to perform calculations, with the constraint that the charge density integrated up to the cutoff is the same between the pseudopotential and the all electron potential (hence norm-conserving). A commonly used method is the Troullier-Martins scheme [89] (or its relativistic generalisation [90]).

I have not performed pseudopotential generation myself; generating accurate pseudopotentials, particularly for rare earth elements such as Samarium which I will be using later, is a technical and involved process. Quality pseudopotentials may be found in open-source databases; all pseudopotentials used in this thesis are from `pslibrary` [91].

The choice of approximation used for the exchange-correlation functional is not insignificant and many variations exist. An early form of functional is Local (Spin) Density Approximation [92], where the exchange correlation energy is taken to be

$$E_{xc}^{LSDA}[n_\uparrow, n_\downarrow] = \int \mathrm{d}^3 r \, \epsilon_{xc}(n_\uparrow, n_\downarrow) \tag{4.19}$$

and various aspects of this function are then fit numerically to reproduce desirable features. A different frequently used choice is the Generalised Gradient Approximation (GGA) [93], where the exchange-correlation energy includes one further term in the Taylor expansion with respect to density,

$$E_{xc}^{GGA}[n_\uparrow, n_\downarrow] = \int \mathrm{d}^3 r \, f(n_\uparrow, n_\downarrow, \nabla n_\uparrow, \nabla n_\downarrow). \tag{4.20}$$

The choice of pseudopotential can have significant implications for calculations: While it should be hoped that the qualitative features of a calculation do not depend on the choice of pseudopotential, some varieties are more or less optimal in certain scenarios. I have used relativistic Perdew-Becke-Ernzerhof (PBE) pseudopotentials [94] throughout this thesis; these are generated with a form of GGA which retains the desirable LDA feature of linear response to small variations in spin density:

$$E[n(r) + \delta n(r)] = E[n(r)] + \int \mathrm{d}^3 r' \, \chi(r - r')\delta n(r'). \tag{4.21}$$

A related type of pseudopotential is PBEsol [95], which are formulated to give more accurate structural parameters for solid state purposes than PBE pseudopotentials, which are prone to underestimating bond lengths. However, PBEsol does not retain linear response to small variations in spin density. All pseudopotentials used in this thesis are relativistic PBE - the pseudopotentials used are not norm-conserving; they fall into a different class of pseudopotential known as Plane Augmented Wave (PAW)[6] [96].

4.3.3 Qualitative methods for highly correlated materials

The above formulation of DFT has been used to great success in many materials, but it does not reproduce certain aspects of strongly interacting systems, particularly those with d and f electrons. The strong Coulomb repulsion of these atoms is not correctly modelled in such materials, leading to incorrect predictions in Mott insulators such as NiO, where the bandgap is significantly underestimated. Early approaches corrected this by deriving new exchange-correlation functionals [97],

[6]Technically, the PAW method does not produce a pseudopotential as it retains the full all-electron wavefunction, but in practice it is used in exactly the same way as a pseudopotential [88].

but more recent approaches add a further term to the energy [98]

$$E_U[n^{i\sigma}] = \frac{U}{2}\sum_{i\sigma}\mathrm{Tr}\left[n^{i\sigma}(1-n^{i\sigma})\right] \tag{4.22}$$

where $n^{i\sigma}$ is the occupation of atom i. This penalises multiple occupations of orbital states while removing any double counting occurring due to some interaction already featuring in E_{xc}. Qualitatively, this partially corrects the propensity of DFT to favour fractional occupations of states and is observed to offer an improvement in predicting the ground states of strongly correlated systems. This treatment is often referred to as DFT+U. Its uses with a specific choice of exchange-correlation functional, such as LDA or GGA, are referred to as LDA+U and GGA+U respectively.

4.3.4 Wannierisation

Having obtained a plane wave description of a material from plane wave DFT it is often desirable to be able to switch to an equivalent tight binding model. This may be to perform calculations more efficiently, or to gain insight through the construction of a minimal low energy Hamiltonian. For example; calculating a band's velocity is inefficient with a plane wave model due to the large k-point mesh required, but is trivial in tight binding where an analytical form can be written down. In order to accomplish this, the standard method is to apply a unitary transformation to obtain *Wannier functions* [99]

$$w(\mathbf{x}) = \frac{1}{Vol}\int d\mathbf{k}\, e^{i\mathbf{k}\cdot\mathbf{x}}\psi(\mathbf{k}) \tag{4.23}$$

which provide a real space representation of the Bloch functions. The process of taking a set of bands and converting them into tight binding orbitals that produce the same band structure is known as *wannierisation.*

Now, there is plainly a large ambiguity in the definition of $|\psi\rangle$ related to the phase. The normalisation condition $\langle\psi(\mathbf{k})|\psi(\mathbf{k}')\rangle = \delta(\mathbf{k}-\mathbf{k}')$ allows the transformation

$$\psi(\mathbf{k}) \to e^{i\phi(\mathbf{k})}\psi(\mathbf{k}) \tag{4.24}$$

for any function ϕ. In the event that a cluster of N mutually entangled bands are wannierised, the above condition is generalised to a unitary matrix $\mathcal{U}(\mathbf{k})$, so that the Wannier functions are

$$w_n = \frac{1}{Vol}\int d\mathbf{k}\, e^{ikx}\,[\,\sum_m^N \mathcal{U}_{nm}(\mathbf{k})\psi_m(\mathbf{k})\,] \tag{4.25}$$

The choice of unitary function $\mathcal{U}(\mathbf{k})$ is called a *gauge*. There are several choices of gauge frequently made, to be discussed shortly (although for reasons relating to the band symmetries I have used solely unit gauge $\mathcal{U}(\mathbf{k}) = 1$ after projection onto atomic orbitals).

Much attention since the introduction of Wannier functions has been devoted to their localisation. This is a natural question; if a tight binding model is sought, it is in some sense obvious to desire that the Wannier functions drop off quickly in real space. A 'localised' Wannier function is here defined as

$$w_i(\mathbf{r}-\mathbf{r}_i) \sim \exp(-\alpha|\mathbf{r}-\mathbf{r}_i|)\,,\ |\mathbf{r}-\mathbf{r}_i| \to \infty \tag{4.26}$$

where $\mathbf{r}_i = \int d\mathbf{r}\,\mathbf{r}w(\mathbf{r}-\mathbf{r}_i)$ defines the *Wannier centre*. It has been shown in up to 3 dimensions that the existence of an exponentially localised basis of Wannier functions is equivalent to the existence of a smooth choice of gauge for the $\mathcal{U}$. This has an interesting relationship with the content in sections 4.2.2 to 4.2.5. The presence of a non-zero Chern number provides a direct topological obstruction to the definition of a smooth Bloch gauge, and a consequence of this is the definition of a set $\{w_n\}$ of ideally localised Wannier functions is not possible. The breakdown in the Chern

insulator case is illustrated clearly in an argument in [100], sketched here. When defining a smooth periodic gauge $|\psi(\mathbf{k}+\mathbf{G})\rangle = |\psi(\mathbf{k})\rangle$ is not possible, there are by definition regions of nonanalytic behaviour in certain small patches. This leads to an argument analogous to 4.2.2 where integrating the Berry curvature around the discontinuous region must lead to a vortex like singularity in integrals over the whole Brillouin zone. This provides barriers to the theorems granting localised Wannier functions to systems with smooth gauges. In general it is seen that non-analyticities in $|\psi(\mathbf{k})\rangle$ are associated with changes to the long distance behaviour of $w(\mathbf{x})$.

A non-trivial extension of the above statement shows that a similar topological obstruction exists in the definition of localised Wannier functions when the $\mathbb{Z}_2$ invariant is nonzero, even though the total Chern number is zero. The proof of this is technical, but the statement is roughly equivalent to the statement once again that the wavefunction is not everywhere defined, even though the Kramers doublets lead to a cancelling of the Chern number [101].

Therefore, if one were to define a tight binding model from Wannier functions for a topologically non-trivial system, one should reasonably expect to find that the $w_n(\mathbf{r}-\mathbf{r}_n)$ do not drop off exponentially for all n at long distances. Nonetheless, the tight binding Hamiltonian will still have by construction the same eigenvalues as the plane wave model and should still be interpreted as valid; it may just be necessary to keep track of couplings to further away neighbours to maintain sufficient accuracy. I close this discussion of the topological obstructions by noting that whatever the specific theoretical limits to defining localised tight binding models are, it is be observed that non-optimally localised Wannier functions are indeed sufficient to obtain a Hamiltonian for the system that has the same band structure and also exhibits topological surface states. This can be seen in other works which study topological insulators through ab initio tight binding methods, such as references [102] and [103].

Atomic orbital projection

In order to go from some DFT Bloch bands to a tight binding prescription, it is common to make certain further simplifications. Typically it is desirable to obtain a Wannier Hamiltonian that functions as a minimal model, retaining only the relevant orbitals to describe the vicinity of the Fermi level. The most straightforward method is to simply project the wavefunctions onto a chosen set of orbitals, typically Gaussians or spherical harmonics, with unit gauge. Denote this set of orbitals $|g_n\rangle$. Defining the matrices $A(k)_{mn} = \langle\psi_m(\mathbf{k})|g_n\rangle$ the wavefunctions are projected as

$$|\phi_n(\mathbf{k})\rangle = \sum_m |\psi_m(\mathbf{k})\rangle\, A(\mathbf{k})_{mn} \tag{4.27}$$

These projected wavefunctions are used in the wannierisation procedure of equation 4.23. In unit gauge the projected Wannier functions are then [104]

$$w_n = \frac{1}{Vol}\int d\mathbf{k}\, e^{i\mathbf{k}\cdot\mathbf{x}}\, \phi_n(\mathbf{k}) \tag{4.28}$$

Maximally Localised Wannier Functions (MLWF)

A frequently used choice of gauge for Wannier functions is the MaximalIy Localised gauge, introduced by Marzari and Vanderbilt in [105]. This is a commonly used method to achieve Wannier functions with relevant hoppings to only a few close neighbours, as I have described is sometimes desirable. Marzari and Vanderbilt define the spread of n Wannier functions

$$\Omega = \sum_n \left[\, \langle r^2\rangle_n - \langle r\rangle^2 \,\right] \tag{4.29}$$

They then derive a procedure to update the $\mathcal{U}_n(\mathbf{k})$ to minimise Ω. From an initial choice of wavefunctions this then obtains optimally localised Wannier functions. If the system is topological, by the arguments above the localisation will not be

exponential. This minimisation also mixes components of different atomic orbitals and spins, which can have further drawbacks. I will later be symmetrising a wannierised model [106] which is much easier when the Wannier orbitals correspond to specific atomic orbitals. I will also be obtaining topological spin textures, so it is important that the wannier orbitals have definite spin. In order to preserve this information, in this thesis I have used exclusively atomic projections with no further localisation. All wannierisation tasks were performed with the open-source package `Wannier90` [104].

4.3.5 Surface spectral function through Green function methods

In this section I will briefly describe a method used to obtain spectral functions of the surface state, that I have used to obtain results on the pristine SmB_6 [100] surface in chapter 5. The method was first devised by Lopez-Sancho et al in [107], before the current wave of interest in topological insulators, but it has found use recently for these purposes. The method has been implemented in the open-source package `WannierTools`[108], which can be used as a post processing tool on top of Wannier functions obtained from `Wannier90`.

For any Hamiltonian $\mathcal{H}(\mathbf{k})$, one may write its retarded Green function $G(\mathbf{k}, \omega)$ as

$$G(\mathbf{k}, \omega) = \lim_{\eta \to 0} (\omega - \mathcal{H}(\mathbf{k}) + i\eta)^{-1} \tag{4.30}$$

The small imaginary part is required to preserve certain analytic properties, see for example [109], but I shall omit it for clarity in the following. When expressed in terms of a basis of Bloch (or Wannier) functions for $\mathcal{H}$, this is exactly equivalent to the Schrödinger equation. If we use a Wannierised tight binding Hamiltonian to express the Green function, all manipulations are on small matrices and so can

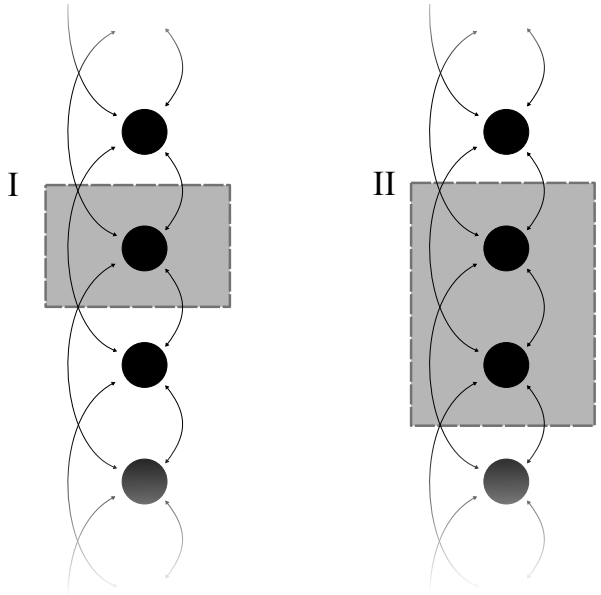

Figure 4.3: A demonstration of converting a tight binding model with next-nearest layer couplings into one with only nearest neighbour couplings.

be performed extremely efficiently. Lopez-Sancho's derivation proceeds as follows: Consider that the surface of a perfect crystal can be described as a semi-infinite stack of layers of the material. Let there be a tight binding Hamiltonian $\mathcal{H}$ for a bulk unit cell of this system. The desired result is a spectral function for the surface layer of the material incorporating any effects of the bulk caused by the coupling to it. Within each of the layers of the semi-infinite system (that is, along x and y) the periodicity is uninterrupted, so $\mathbf{k}_{||}$ is a good quantum number and Bloch functions $\psi_n(\mathbf{k}_{||})$ may be defined along these directions. By redefining unit cells into supercells it is possible to make these effective layers coupled only to nearest neighbours *principle layers*, shown in figure 4.3. In this way the semi-infinite slab can be recast as an effective one dimensional model where the onsite degrees of freedom and couplings become functions of $\mathbf{k}_{||}$. The effective one dimensional model is then solvable by way of a type of real space renormalisation group calculation [110].

By substituting the Green functions into each other, an equation for the surface

Green function incorporating an arbitrarily high number of couplings can be obtained

$$(\omega - \varepsilon^s)G_{00} \approx \mathbf{1}\,. \tag{4.31}$$

The renormalised energy ε^s contains frequency and momentum dependence and is in general complex. Standard properties of Green functions yield a result for the spectral function from this Green function[7]. This treatment is equivalent to a Dyson equation.

$$A(\mathbf{k}_{||}, \omega) = \frac{2}{\pi}\Im(G(\mathbf{k}_{||}, \omega)). \tag{4.32}$$

Therefore, by calculating this along a given high symmetry path, a band structure can be obtained from the surface Green function incorporating the spectral effects of the bulk topology.

4.4 Samarium hexaboride: a strongly coupled topological insulator?

Samarium hexaboride is a material that has attracted strong attention in the past fifteen or so years, on the back of a great many experimental and theoretical results predicting it to be a topological Kondo insulator. It crystallises in the $Pm\bar{3}m$ symmetry group, with lattice constant 4.13 Å, with boron atoms that are positioned in a cage at the centre of each cubic unit cell and a B-B bond length of $\sim$ 1.75 Å [111]. The structural data are shown in figure 4.4. It was first discovered in 1969, when Menth and Buehler [112] described it as a paramagnetic metal down to 2 K, when it undergoes an insulating transition. This insulating transition was described later in [113] as an example of a Kondo insulator. The Kondo

[7]Notice that substituting the uninteracting Green function in 4.30 the corresponding spectral function has a Lorentzian linewidth η.

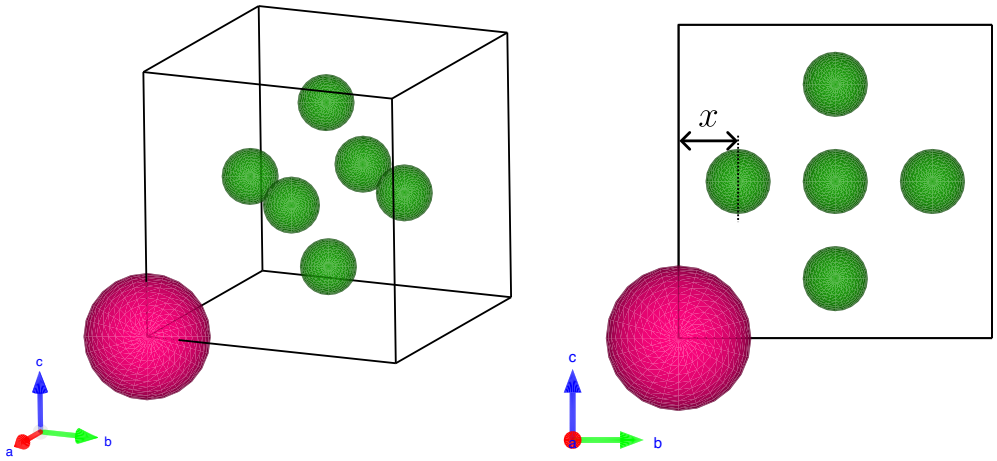

Figure 4.4: The atomic structure of samarium hexaboride. The symmetry group is $Pm\bar{3}m$, comprising Sm ions at the cubic lattice corners and a central boron cage. The boron position parameter x is approximately 0.2. The [100] face is also shown.

effect is a famous strong coupling effect between conduction electrons and localised moments, where the coupling between the degrees of freedom becomes screened above the Kondo temperature [53]. If instead of single impurities, there is a lattice of localised moments with delocalised conduction electrons, such as in the case of a d/f electron material, below this temperature hybridisation between the d and f electrons will open a gap, depicted in figure 4.5. In a Kondo insulator, the chemical potential is positioned mid-gap, so that under the Kondo temperature the material transitions from metal to insulator.

Notably however, the resistance of SmB_6 saturates at low temperatures unlike what would be expected in a regular insulator. This was originally ascribed to in gap impurity states, but this explanation was questioned after the discovery of topological insulators and expanded upon by Dzero et al in [114] and Takimoto in [115], suggesting that SmB_6 is the first known topological Kondo insulator. A consensus has emerged in the theoretical community that this is indeed the case, and that the X point band inversion between the d and f bands leads to the emergent surface metallic states. The crystal field splittings for the d and f electrons are

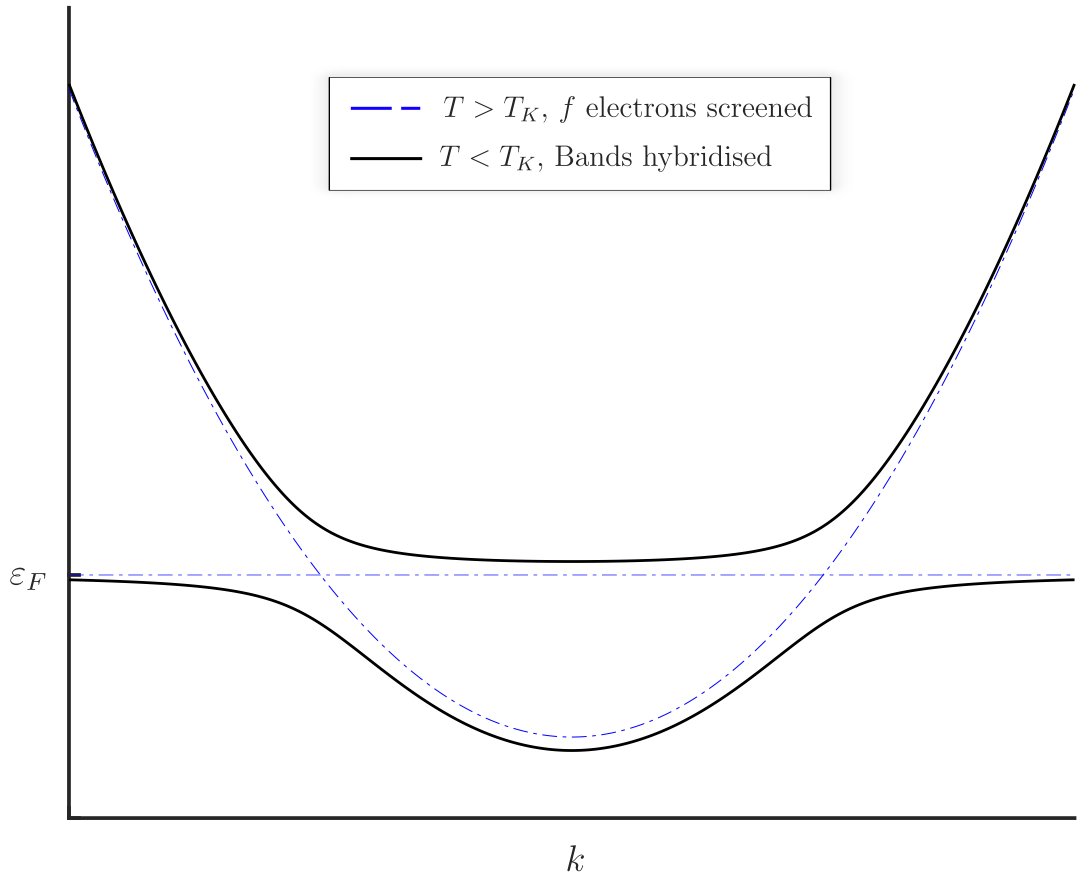

Figure 4.5: The band structure of a prototypical Kondo insulator. At high temperatures a Kondo bound state forms between the mobile conduction electrons and the local moments, but at lower temperatures the interaction allows the bands to hybridise and a gap opens.

shown in figures 4.6 and 4.7; for further discussion of the band symmetries refer to [116]. Notice that are the splittings for a single electron: the Sm ions are mixed valance in SmB_6, with a ground state electron configuration of $4f^6 \rightleftharpoons 4f^5 + e$. This extra electron is doped into the $5d$ conduction band, yielding the splittings shown [117]. The splittings given are only strictly true for the Sm^{3+} valence configuration; this is the ground state that DFT finds. As the mixed valence is a consequence of the strong Kondo correlations, bare DFT is not capable of producing mixed valence configurations. However, the work of Lu et al in reference [118] shows us that employing a methodology that can incorporate some aspects of the correlations

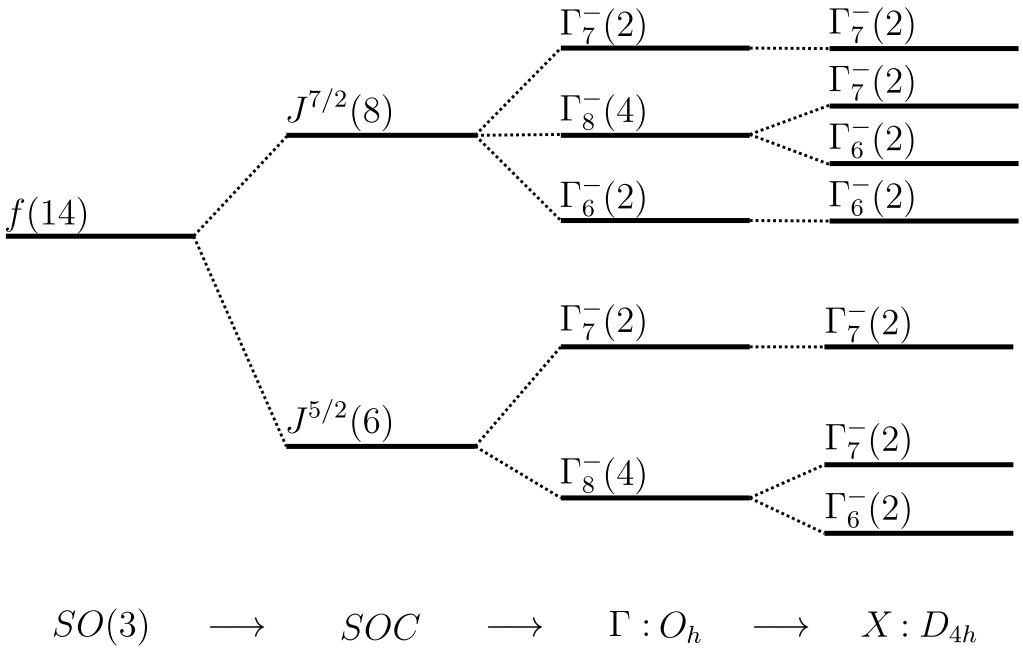

Figure 4.6: The f electron irreducible representation content of SmB_6. The f electrons experience spin orbit coupling as the strongest perturbation, which is then split by the cubic crystal field. At the X point, the symmetry reduces to D_{4h} and the bands split further. The $J = \frac{5}{2}$ states are the states which will be important in the band structure. The energies are not necessarily shown accurately here, the intention is to demonstrate the irreducible representation content.

and predicts the correct valence leads to a ground state with the same irreducible representation content as shown here.

A notable feature of this model for the low temperature ground state of SmB_6 is the interplay between strongly correlated physics and topological band theory. The topological band theory strictly speaking only applies in the non-interacting limit, where Bloch theory is applicable. Once there are strong correlations in the material, these arguments may fail. Early results imply that the noninteracting classification should be valid in the interacting case [119] but more detailed recent results cast a degree of doubt on the universality of this approach [120]. Indeed even if the exact same topological classifications do apply to strongly correlated condensed systems, the exact impact of strong interactions on the band structure and phase diagram of symmetry protected topological phases is not fully understood.

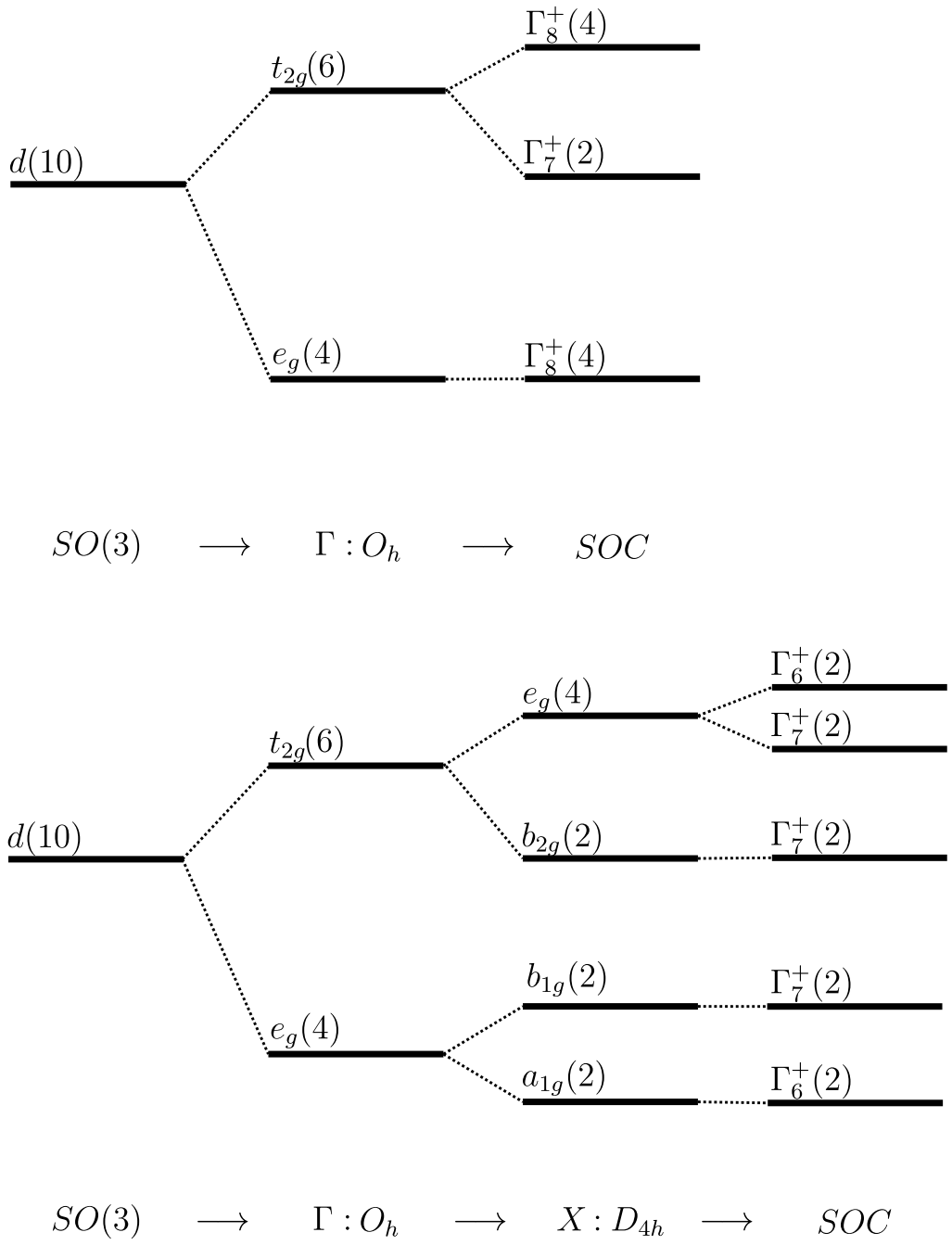

Figure 4.7: The d electron irreducible representation content of SmB_6. The d electrons are more delocalised and experience crystal field as a stronger perturbation than spin orbit coupling. I have shown the splittings as the symmetry is reduced at the X point as well. The energies are not necessarily shown accurately here, the intention is to demonstrate the irreducible representation content. The crystal field analysis suggests that the e_g orbitals are lower in energy than the t_{2g} orbitals, but under further symmetry breaking the energies may cross.

4.4.1 Experimental evidence for the TI state

There has been ample evidence from multiple sources for the existence of the conducting surface state and several confirming the spin texture expected from the bulk topology. In addition to the conductivity plateau seen in transport, multiple ARPES studies have been performed, imaging fast Dirac states [121] [122] and even the topological spin texture [123] on the [100] surface. The results of Jiang et al are shown in figure 4.8. These results should be compared to reference [124], which studies topological insulating surface states as well as topological crystalline insulator states on the [110] and [111] surfaces.

A further valuable technique for investigating the surface is STM [20] [19], as through quasiparticle interference the Fermi surface can be inferred, providing a way to corroborate the findings of ARPES. Several high quality STM studies on the material exist [125] [126] [127], which all confirm the same basic picture although in some regards conflict with the ARPES data; that there is significant density of states from the hybridised bands but lingering spectral density mid gap, providing a conductive surface state. Quasiparticle interference allows the linear states to be seen, though frequently the Dirac masses observed are rather different to those found in ARPES.

Some work that attempts to clarify this and emphasises the importance of electrostatic effects at the surface comes from Matt et al [65]. Noting the discrepancies between the Fermi velocities measured in quasiparticle interference compared to ARPES, the authors suggest that a surface electrostatic renormalisation caused by surface polarity explains the data. STM is an extremely local measurement, over length scales of tens to hundreds of nanometres, whereas an ARPES spot size is on order tens of microns. This has the effect of averaging over many unit cells and many surface terminations. STM studies have commonly observed a non-polar 2x1 surface reconstruction with a spectral density peak at only -5 meV, around

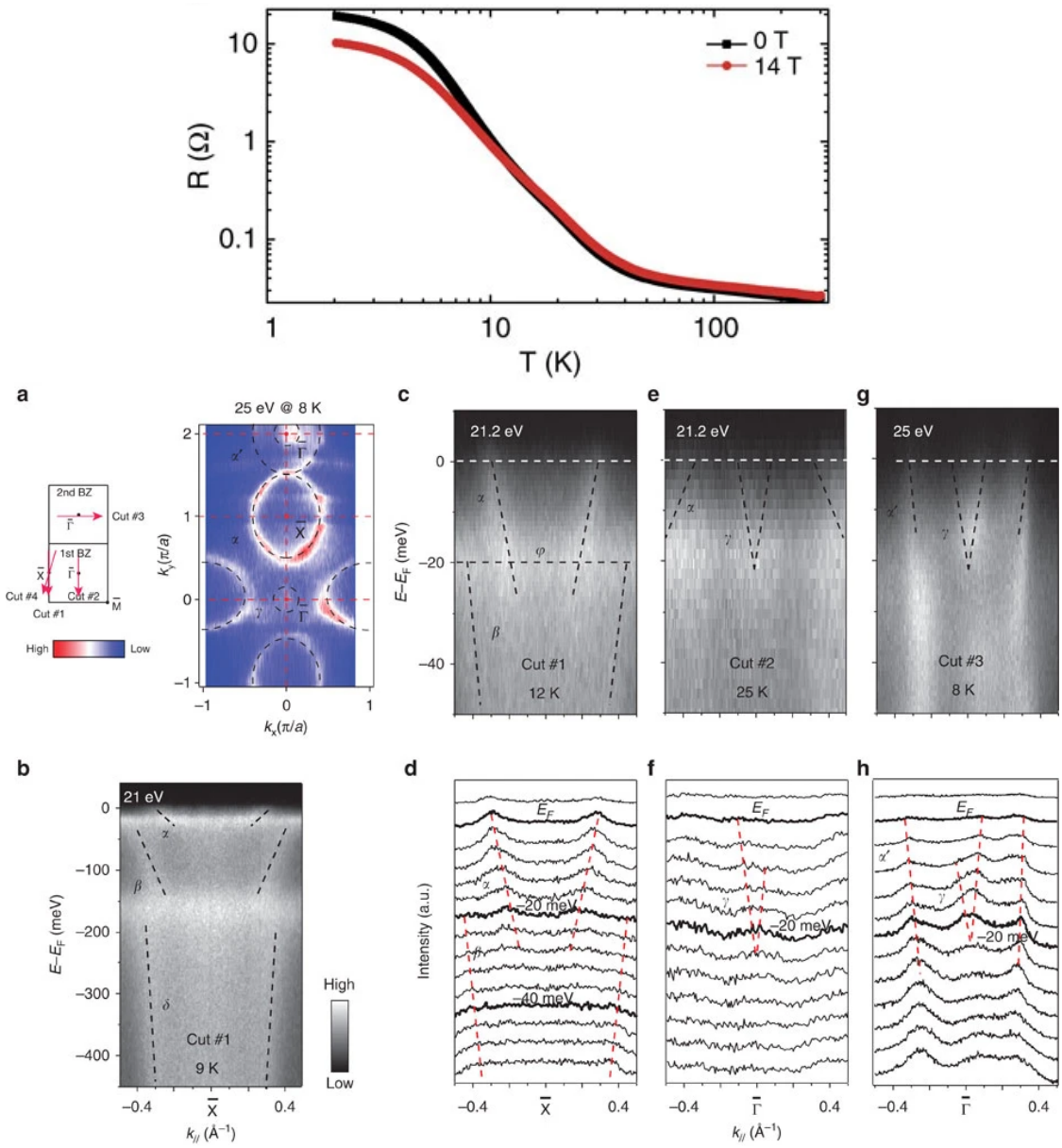

Figure 4.8: A collection of experimental data indicating the presence of a topological surface state. The top figure demonstrates the resistive plateau at low temperatures, indicating the metallic surface. The bottom images collate ARPES data: a) Photoemission intensity map integrated over $\varepsilon \pm 5$ meV, showing oval $\bar{X}$ point Fermi arcs. b) Large energy scale photoemission intensity around $\bar{X}$. c,d) Photoemission intensity and momentum distribution curves (MDC) along cut 1, indicated in a). e,f) Photoemission intensity and MDC along cut 2. g,h) Photoemission intensity and MDC along cut 3, in the second Brillouin zone. The α bands are attributed to the $\bar{X}$ point Dirac cone, and have a velocity 240 meVÅ. The γ bands are attributed to the $\bar{\Gamma}$ point surface states but are rather indistinct and identified differently in, for example, [123]. Reproduced with permission from [121].

20 meV higher than observed in ARPES. By interpreting the effects of non-polar terminations as a kind of band bending [128] and crudely approximating the effects of this difference in terminations as a rigid band shift, they are capable of explaining the discrepancies in observed Fermi velocities from the two methods. I will expand further on this with first principles theoretical data in 5.6.

There are nonetheless some curious experiments that hint at complexities beyond the picture of SmB_6 as equivalent to a weakly coupled topological insulator which may have their origins in the strong d/f correlations. Quantum oscillation studies confirm the presence of the two dimensional, putatively topological, surface states [129] although further studies reveal the presence of oscillations from a further, three dimensional Fermi surface [63] [130]. There are several exotic explanations for this, notably that the bulk ground state may form a fluid of emergent neutral fermions [131] [132] in addition to the surface topological states. I shall not consider the oscillation data or these exotic explanations further in this thesis, as I am primarily concerned with the electrostatics of the surface, although I shall briefly speculate on the role DFT calculations can play in elucidating the nature of the true ground state and what instabilities may be present.

4.4.2 The importance of local electrostatics on band fillings

Another picture of the [100] surface demonstrating a sensitivity to electrostatic perturbations is found in Nam et al [64], who studied the modulation of the surface conductivity through the application of molecular systems to the surface. Two different molecular systems were used, one carrying an overall magnetic moment and one not. These two are chosen as they are very similar electrostatically and differ solely by their magnetic moment. This allows the relative contribution of the magnetic degree of freedom to scattering to be probed. The effect is that *both* sets of conductivities are modified.

The change in conductivity resulting from the magnetic perturbation is unsurprising from the topological Kondo insulator picture; recalling the form of the Hamiltonian for the surface states of a topological insulator (equation 4.2.5) $\mathcal{H} = v_F \boldsymbol{\sigma} \times \mathbf{k}$, the eigenspinors for the upper and lower branches of the Dirac cone are

$$v_1 = \frac{1}{\sqrt{2}} \begin{pmatrix} i \\ e^{i\theta} \end{pmatrix}, \; v_2 = \frac{1}{\sqrt{2}} \begin{pmatrix} 1 \\ ie^{i\theta} \end{pmatrix}, \; \theta = \arg(k_x + ik_y). \tag{4.33}$$

This imposes a 'no backscattering' condition on states under elastic scattering. Assuming some weak time-reversal preserving (electrostatic) scattering potential V, the contribution from scattering to the resistivity will be proportional to

$$|\langle \mathbf{k}'|V|\mathbf{k}\rangle|^2 = V^2 \cos^2\left(\frac{\theta' - \theta}{2}\right), \tag{4.34}$$

which goes to zero for perfect backscattering. Therefore, in the absence of time-reversal breaking scatterers such that a spin flip can be induced, there is no backscattering to first order in the scattering potential.

What then should we make of the modulation in the conductivity from the purely electrostatic perturbation? This has a different explanation; while there is no activation of different scattering channels, the electrostatic perturbation can change the local band fillings, in direct analogy to gating effects. This modulates the local density of states, having direct impact on the conductivity. Scenarios similar to this have been explored in the study of metal-solvent interface effects [133]. The results of this experiment imply that the local electrostatics on the surfaces of topological insulators have consequences on transport parameters, and motivates searching for other sources of local electrostatic perturbation in order to understand the surface band structure and effects on the band fillings. The overarching principle of this is that the *existence* of the surface states is guaranteed via the nontrivial topology, but the exact features of the surface band structure

are subject to electrostatic effects just like any other set of bands.

4.5 Outstanding questions

The previous sections have summarised some of the experimental and theoretical results leading to our current understanding of samarium hexaboride, but leave a few questions unanswered. I have emphasised the role of electronic perturbation at the surface states and in the following chapter will provide insight into three main questions about the surface states

- To what extent are electrostatic surface effects important in determining the surface band structure?
- Can the simple arguments explaining differences in STM vs ARPES band structures be critiqued with evidence from ab initio methods?
- To what extent can the experimental data be considered consequences of the strongly correlated electronic ground state?

I will be investigating these problems through a combination of DFT and tight binding calculations, which provide well established methodologies for dealing with *weakly* interacting systems, although surprisingly strong agreement can be obtained with the experimental data of this likely *strongly* interacting material.

References

[19] Ke Bian et al. “Scanning probe microscopy”. en. In: *Nature Reviews Methods Primers* 1.1 (May 2021). Number: 1 Publisher: Nature Publishing Group, pp. 1–29. URL: https://www.nature.com/articles/s43586-021-00033-2 (visited on 03/06/2023).

[20] G. Binnig, H. Rohrer, Ch. Gerber, and E. Weibel. "Surface Studies by Scanning Tunneling Microscopy". In: *Phys. Rev. Lett.* 49.1 (July 1982). Publisher: American Physical Society, pp. 57–61. URL: https://link.aps.org/doi/10.1103/PhysRevLett.49.57 (visited on 04/24/2023).

[53] Jun Kondo. "Resistance minimum in dilute magnetic alloys". In: *Progress of Theoretical Physics* 32.1 (1964), pp. 37–49.

[57] D. J. Thouless, M. Kohmoto, M. P. Nightingale, and M. den Nijs. "Quantized Hall Conductance in a Two-Dimensional Periodic Potential". In: *Phys. Rev. Lett.* 49 (6 Aug. 1982), pp. 405–408. URL: https://link.aps.org/doi/10.1103/PhysRevLett.49.405.

[58] Liang Fu and C. L. Kane. "Topological insulators with inversion symmetry". In: *Phys. Rev. B* 76 (4 July 2007), p. 045302. URL: https://link.aps.org/doi/10.1103/PhysRevB.76.045302.

[59] C.L. Kane. "Topological Band Theory and the Z2 Invariant". en. In: *Contemporary Concepts of Condensed Matter Science*. Vol. 6. Elsevier, 2013, pp. 3–34. URL: https://linkinghub.elsevier.com/retrieve/pii/B9780444633149000019 (visited on 01/16/2023).

[60] Qing Lin He et al. "Topological spintronics and magnetoelectronics". In: *Nature materials* 21.1 (2022), pp. 15–23.

[61] Sankar Das Sarma, Michael Freedman, and Chetan Nayak. "Majorana zero modes and topological quantum computation". In: *npj Quantum Information* 1.1 (2015), pp. 1–13.

[62] A Yu Kitaev. "Unpaired Majorana fermions in quantum wires". In: *Physics-uspekhi* 44.10S (2001), p. 131.

[63] BS Tan et al. "Unconventional Fermi surface in an insulating state". In: *Science* 349.6245 (2015), pp. 287–290.

[64] Moon-Sun Nam et al. “How to probe the spin contribution to momentum relaxation in topological insulators”. In: *Nature Communications* 9.1 (2018), p. 56.

[65] Christian E. Matt et al. “Consistency between ARPES and STM measurements on SmB_6”. In: *Phys. Rev. B* 101 (8 Feb. 2020), p. 085142. URL: https://link.aps.org/doi/10.1103/PhysRevB.101.085142.

[66] Felix Bloch. “Quantum mechanics of electrons in crystal lattices”. In: *Zeitschrift fur Phys* 52 (1928), pp. 555–600.

[67] Neil W Ashcroft and N David Mermin. *Solid state physics*. Cengage Learning, 1976.

[68] Mildred S Dresselhaus, Gene Dresselhaus, and Ado Jorio. *Group theory: application to the physics of condensed matter*. Springer Science & Business Media, 2007.

[69] Barry Bradlyn et al. “Topological quantum chemistry”. In: *Nature* 547.7663 (2017), pp. 298–305.

[70] Mikio Nakahara. *Geometry, topology and physics*. CRC press, 2003.

[71] Michel Fruchart and David Carpentier. “An introduction to topological insulators”. In: *Comptes Rendus Physique* 14.9-10 (2013), pp. 779–815. URL: https://doi.org/10.1016%2Fj.crhy.2013.09.013.

[72] David Bachman. *A geometric approach to differential forms*. Springer Science & Business Media, 2012.

[73] B.A. Bernevig and T.L. Hughes. *Topological Insulators and Topological Superconductors*. Princeton University Press, 2013. URL: https://books.google.co.uk/books?id=wOn7JHSSxrsC.

[74] Masatoshi Sato and Yoichi Ando. “Topological superconductors: a review”. In: *Reports on Progress in Physics* 80.7 (July 2017). arXiv:1608.03395 [cond-mat], p. 076501. URL: http://arxiv.org/abs/1608.03395 (visited on 01/15/2023).

[75] C. L. Kane and E. J. Mele. "Z_2 Topological Order and the Quantum Spin Hall Effect". In: *Phys. Rev. Lett.* 95 (14 Sept. 2005), p. 146802. URL: https://link.aps.org/doi/10.1103/PhysRevLett.95.146802.

[76] Liang Fu, C. L. Kane, and E. J. Mele. "Topological Insulators in Three Dimensions". In: *Phys. Rev. Lett.* 98 (10 Mar. 2007), p. 106803. URL: https://link.aps.org/doi/10.1103/PhysRevLett.98.106803.

[77] B. Andrei Bernevig, Taylor L. Hughes, and Shou-Cheng Zhang. "Quantum Spin Hall Effect and Topological Phase Transition in HgTe Quantum Wells". In: *Science* 314.5806 (2006), pp. 1757–1761. eprint: https://www.science.org/doi/pdf/10.1126/science.1133734. URL: https://www.science.org/doi/abs/10.1126/science.1133734.

[78] Chao-Xing Liu et al. "Model Hamiltonian for topological insulators". In: *Phys. Rev. B* 82 (4 July 2010), p. 045122. URL: https://link.aps.org/doi/10.1103/PhysRevB.82.045122.

[79] Haijun Zhang et al. "Topological insulators in Bi_2Se_3, Bi_2Te_3 and Sb_2Te_3 with a single Dirac cone on the surface". In: *Nature physics* 5.6 (2009), pp. 438–442.

[80] Feliciano Giustino. *Materials modelling using density functional theory: properties and predictions*. Oxford University Press, 2014.

[81] P. Hohenberg and W. Kohn. "Inhomogeneous Electron Gas". In: *Phys. Rev.* 136 (3B 1964), B864–B871. URL: https://link.aps.org/doi/10.1103/PhysRev.136.B864.

[82] W. Kohn and L. J. Sham. "Self-Consistent Equations Including Exchange and Correlation Effects". In: *Phys. Rev.* 140 (4A 1965), A1133–A1138. URL: https://link.aps.org/doi/10.1103/PhysRev.140.A1133.

[83] Robert G Parr. "Density functional theory of atoms and molecules". In: *Horizons of Quantum Chemistry: Proceedings of the Third International Congress of Quantum Chemistry Held at Kyoto, Japan, October 29-November 3, 1979*. Springer. 1980, pp. 5–15.

[84] Paolo Giannozzi et al. “QUANTUM ESPRESSO: a modular and open-source software project for quantum simulations of materials”. In: *Journal of Physics: Condensed matter* 21.39 (2009), p. 395502.

[85] Paolo Giannozzi et al. “Advanced capabilities for materials modelling with Quantum ESPRESSO”. In: *Journal of Physics: Condensed matter* 29.46 (2017), p. 465901.

[86] James C. Phillips and Leonard Kleinman. “New Method for Calculating Wave Functions in Crystals and Molecules”. In: *Phys. Rev.* 116 (2 1959), pp. 287–294. URL: https://link.aps.org/doi/10.1103/PhysRev.116.287.

[87] DR Hamann, M Schlüter, and C Chiang. “Norm-conserving pseudopotentials”. In: *Phys. Rev. Lett.* 43.20 (1979), p. 1494.

[88] Richard M Martin. *Electronic structure: basic theory and practical methods*. Cambridge university press, 2020.

[89] N. Troullier and Jose Luis Martins. “Efficient pseudopotentials for plane-wave calculations”. In: *Phys. Rev. B* 43 (3 Jan. 1991), pp. 1993–2006. URL: https://link.aps.org/doi/10.1103/PhysRevB.43.1993.

[90] E. Engel, A. Hock, and S. Varga. “Relativistic extension of the Troullier-Martins scheme: Accurate pseudopotentials for transition-metal elements”. In: *Phys. Rev. B* 63 (12 Mar. 2001), p. 125121. URL: https://link.aps.org/doi/10.1103/PhysRevB.63.125121.

[91] Andrea Dal Corso. “Pseudopotentials periodic table: From H to Pu”. In: *Computational Materials Science* 95 (2014), pp. 337–350.

[92] J. P. Perdew and Alex Zunger. “Self-interaction correction to density-functional approximations for many-electron systems”. In: *Phys. Rev. B* 23 (10 1981), pp. 5048–5079. URL: https://link.aps.org/doi/10.1103/PhysRevB.23.5048.

[93] John P. Perdew and Yue Wang. "Accurate and simple analytic representation of the electron-gas correlation energy". In: *Phys. Rev. B* 45 (23 1992), pp. 13244–13249. URL: https://link.aps.org/doi/10.1103/PhysRevB.45.13244.

[94] John P. Perdew, Kieron Burke, and Matthias Ernzerhof. "Generalized Gradient Approximation Made Simple". In: *Phys. Rev. Lett.* 77 (18 1996), pp. 3865–3868. URL: https://link.aps.org/doi/10.1103/PhysRevLett.77.3865.

[95] John P. Perdew et al. "Restoring the Density-Gradient Expansion for Exchange in Solids and Surfaces". In: *Phys. Rev. Lett.* 100 (13 Apr. 2008), p. 136406. URL: https://link.aps.org/doi/10.1103/PhysRevLett.100.136406.

[96] P. E. Blöchl. "Projector augmented-wave method". In: *Phys. Rev. B* 50 (24 Dec. 1994), pp. 17953–17979. URL: https://link.aps.org/doi/10.1103/PhysRevB.50.17953.

[97] Vladimir I. Anisimov, Jan Zaanen, and Ole K. Andersen. "Band theory and Mott insulators: Hubbard U instead of Stoner I". In: *Phys. Rev. B* 44 (3 July 1991), pp. 943–954. URL: https://link.aps.org/doi/10.1103/PhysRevB.44.943.

[98] Matteo Cococcioni and Stefano De Gironcoli. "Linear response approach to the calculation of the effective interaction parameters in the LDA+ U method". In: *Phys. Rev. B* 71.3 (2005), p. 035105.

[99] Gregory H. Wannier. "The Structure of Electronic Excitation Levels in Insulating Crystals". In: *Phys. Rev.* 52 (3 1937), pp. 191–197. URL: https://link.aps.org/doi/10.1103/PhysRev.52.191.

[100] Christian Brouder et al. "Exponential Localization of Wannier Functions in Insulators". In: *Phys. Rev. Lett.* 98.4 (Jan. 2007). Publisher: American Physical Society, p. 046402. URL: https://link.aps.org/doi/10.1103/PhysRevLett.98.046402 (visited on 01/16/2023).

[101] Horia D. Cornean, Domenico Monaco, and Stefan Teufel. "Wannier functions and Z_2 invariants in time-reversal symmetric topological insulators". en. In: *Reviews in Mathematical Physics* 29.02 (Mar. 2017). arXiv:1603.06752 [cond-mat, physics:math-ph], p. 1730001. URL: http://arxiv.org/abs/1603.06752 (visited on 01/16/2023).

[102] Irene Aguilera, Christoph Friedrich, Gustav Bihlmayer, and Stefan Blügel. "GW study of topological insulators Bi_2Se3, Bi_2Te_3, and Sb_2Te_3: Beyond the perturbative one-shot approach". In: *Phys. Rev. B* 88.4 (2013), p. 045206.

[103] Irene Aguilera, Christoph Friedrich, and Stefan Blügel. "Many-body corrected tight-binding Hamiltonians for an accurate quasiparticle description of topological insulators of the Bi_2Se_3 family". In: *Phys. Rev. B* 100.15 (2019), p. 155147.

[104] Giovanni Pizzi et al. "Wannier90 as a community code: new features and applications". In: *Journal of Physics: Condensed Matter* 32.16 (2020), p. 165902.

[105] Nicola Marzari et al. "Maximally localized Wannier functions: Theory and applications". In: *Rev. Mod. Phys.* 84 (4 Oct. 2012), pp. 1419–1475. URL: https://link.aps.org/doi/10.1103/RevModPhys.84.1419.

[106] Dominik Gresch et al. "Automated construction of symmetrized Wannier-like tight-binding models from ab initio calculations". In: *Physical Review Materials* 2.10 (2018), p. 103805.

[107] M P Lopez Sancho, J M Lopez Sancho, J M L Sancho, and J Rubio. "Highly convergent schemes for the calculation of bulk and surface Green functions". In: *Journal of Physics F: Metal Physics* 15.4 (Apr. 1985), p. 851. URL: https://dx.doi.org/10.1088/0305-4608/15/4/009.

[108] QuanSheng Wu et al. "WannierTools : An open-source software package for novel topological materials". In: *Computer Physics Communications* 224 (2018), pp. 405–416. URL: http://www.sciencedirect.com/science/article/pii/S0010465517303442.

[109] Alekseevich Abrikosov, Lev Petrovich Gorkov, and Igor Ekhielevich Dzyaloshinski. *Methods of quantum field theory in statistical physics*. Courier Corporation, 2012, pp. 51–54.

[110] M. Nauenberg. "Renormalization group solution of the one-dimensional Ising model". In: *Journal of Mathematical Physics* 16.3 (Sept. 1975), pp. 703–705. eprint: https://pubs.aip.org/aip/jmp/article-pdf/16/3/703/7453907/703_1_online.pdf. URL: https://doi.org/10.1063/1.522584.

[111] Shiro Funahashi, Kiyoaki Tanaka, and Fumitoshi Iga. "X-ray atomic orbital analysis of 4f and 5d electron configuration of SmB_6 at 100, 165, 230 and 298 K". In: *Acta Crystallographica Section B: Structural Science* 66.3 (2010), pp. 292–306.

[112] A. Menth, E. Buehler, and T. H. Geballe. "Magnetic and Semiconducting Properties of SmB_6". In: *Phys. Rev. Lett.* 22 (7 Feb. 1969), pp. 295–297. URL: https://link.aps.org/doi/10.1103/PhysRevLett.22.295.

[113] Z Fisk et al. "Kondo insulators". In: *Physica B: Condensed Matter* 223 (1996), pp. 409–412.

[114] Maxim Dzero, Kai Sun, Victor Galitski, and Piers Coleman. "Topological Kondo Insulators". In: *Phys. Rev. Lett.* 104 (10 Mar. 2010), p. 106408. URL: https://link.aps.org/doi/10.1103/PhysRevLett.104.106408.

[115] Tetsuya Takimoto. "SmB_6: A promising candidate for a topological insulator". In: *Journal of the Physical Society of Japan* 80.12 (2011), p. 123710.

[116] Chang-Jong Kang et al. "Band Symmetries of Mixed-Valence Topological Insulator: SmB_6". In: *Journal of the Physical Society of Japan* 84.2 (2015), p. 024722.

[117] Maxim Dzero, Jing Xia, Victor Galitski, and Piers Coleman. "Topological kondo insulators". In: *Annual Review of Condensed Matter Physics* 7 (2016), pp. 249–280.

[118] Feng Lu et al. “Correlated Topological Insulators with Mixed Valence”. en. In: *Phys. Rev. Lett.* 110.9 (Feb. 2013), p. 096401. URL: https://link.aps.org/doi/10.1103/PhysRevLett.110.096401 (visited on 05/18/2020).

[119] Zhong Wang, Xiao-Liang Qi, and Shou-Cheng Zhang. “Topological invariants for interacting topological insulators with inversion symmetry”. In: *Phys. Rev. B* 85 (16 Apr. 2012), p. 165126. URL: https://link.aps.org/doi/10.1103/PhysRevB.85.165126.

[120] Jinchao Zhao, Peizhi Mai, Barry Bradlyn, and Philip Phillips. *Failure of Topological Invariants in Strongly Correlated Matter*. 2023. arXiv: 2305.02341 [cond-mat.str-el].

[121] Juan Jiang et al. “Observation of possible topological in-gap surface states in the Kondo insulator SmB_6 by photoemission”. In: *Nature Communications* 4.1 (2013), p. 3010.

[122] Madhab Neupane et al. “Surface electronic structure of the topological Kondo-insulator candidate correlated electron system SmB_6”. In: *Nature Communications* 4.1 (2013), p. 2991.

[123] Nan Xu et al. “Direct observation of the spin texture in SmB_6 as evidence of the topological Kondo insulator”. In: *Nature Communications* 5.1 (2014), p. 4566.

[124] Dong-Choon Ryu et al. “Topological surface states on the nonpolar (110) and (111) surfaces of SmB_6”. In: *Phys. Rev. B* 103 (12 Mar. 2021), p. 125101. URL: https://link.aps.org/doi/10.1103/PhysRevB.103.125101.

[125] Harris Pirie et al. “Imaging emergent heavy Dirac fermions of a topological Kondo insulator”. In: *Nature Physics* 16.1 (2020), pp. 52–56.

[126] Michael M Yee et al. “Imaging the Kondo insulating gap on SmB_6”. In: *arXiv preprint arXiv:1308.1085* (2013).

[127] Lin Jiao et al. “Additional energy scale in SmB_6 at low-temperature”. In: *Nature Communications* 7.1 (2016), p. 13762.

[128] Zhen Zhang and John T. Yates Jr. "Band Bending in Semiconductors: Chemical and Physical Consequences at Surfaces and Interfaces". In: *Chemical Reviews* 112.10 (2012). PMID: 22783915, pp. 5520–5551. URL: https://doi.org/10.1021/cr3000626.

[129] Gang Li et al. "Two-dimensional Fermi surfaces in Kondo insulator SmB_6". In: *Science* 346.6214 (2014), pp. 1208–1212.

[130] Máté Hartstein et al. "Intrinsic bulk quantum oscillations in a bulk unconventional insulator SmB_6". In: *IScience* 23.11 (2020), p. 101632.

[131] Debanjan Chowdhury, Inti Sodemann, and T Senthil. "Mixed-valence insulators with neutral Fermi surfaces". In: *Nature Communications* 9.1 (2018), p. 1766.

[132] Inti Sodemann, Debanjan Chowdhury, and T. Senthil. "Quantum oscillations in insulators with neutral Fermi surfaces". In: *Phys. Rev. B* 97 (4 Jan. 2018), p. 045152. URL: https://link.aps.org/doi/10.1103/PhysRevB.97.045152.

[133] Wolfgang Schmickler. "The potential of zero charge of jellium". In: *Chemical Physics Letters* 99.2 (1983), pp. 135–139. URL: https://www.sciencedirect.com/science/article/pii/0009261483805454.

5

DFT investigations into the [100] surface states of SmB_6

5.1 Theoretical investigations on the surface state via plane wave DFT

This chapter details results of my computational investigations of the samarium hexaboride [100] electronic structure. The main aim is to evaluate the effects of various sources of electrostatic perturbation on the surface, in particular the surface states at the $\bar{X}$ point. Studying surfaces can be done in several different ways, all of which implicitly account for electrostatic effects in different ways: throughout the latter parts of this chapter I will emphasise the discrepancy between tight binding methods' and DFT slab based methods' treatments of charge reorganisation at the

surface. This leads to energy changes on the order of meV, which is comparable to the energies of the topological gap in SmB_6, in contrast to the Bismuth based TIs where the characteristic energy scales around the Fermi level are $O(0.1\,\mathrm{eV})$.

The original motivation of this work was to better understand the way that surface electrostatics influence the transport, following experiments performed by myself and Dr Moon-Sun Nam, not included here, continuing the work performed by her in reference [64]. This necessarily involves discussing the topological states, as these are the states active in transport.

5.1.1 Bulk band structure

The first step in developing a reliable model of the electronic structure is to obtain the bulk lattice parameter amd atomic positions. I have performed this by self consistently relaxing the unit cell size and position of the Boron cage until all forces are below 1 mRy/a_{Bohr}. For my pseudopotentials, this yields a lattice constant of 4.125 Å, with a B-B bond length 1.76 Å, in very close agreement with the experimental data in [111], which finds $a = 4.13$ Å, B-B bond length 1.75 Å. The parameter x from figure 4.4 is found to be 0.1988. This structure is then used to obtain the band structure 5.1. In calculating this I have accounted for some aspects of the correlation by using a Hubbard U parameter of 1 eV: this is a phenomenological choice which I explore in greater detail in 5.1.2.

The feature of the band structure most important from the perspective of the bulk topology is the spin orbit driven band inversion at the X point, visible twice in the given band structure. This hybridisation opens a small indirect band gap of 18 meV, which also drives the topological behaviour. This band structure can be compared with several existing results in the literature:

- Takimoto [115] performed LDA calculations without further accounting for strong correlation methods. His results have similar broad features to later

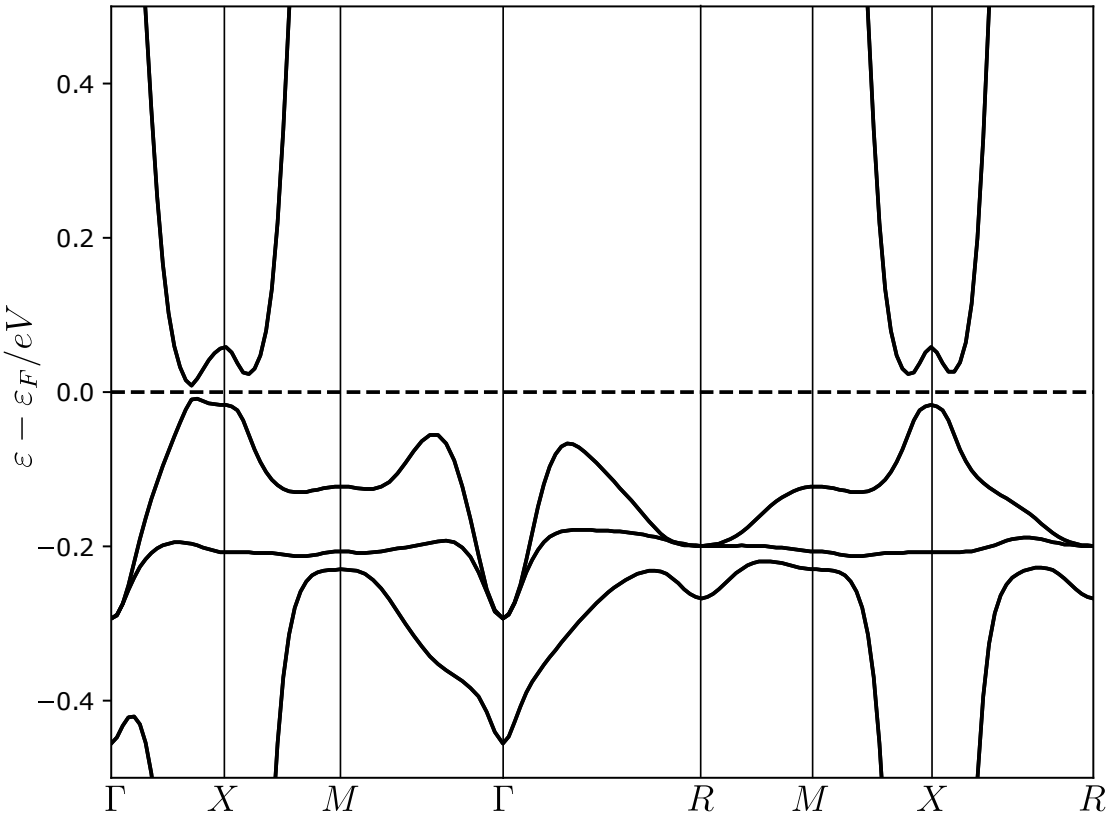

Figure 5.1: The bulk band structure of SmB_6 calculated using my obtained structural data. The notable feature is the band inversion at the X point, which leads to parity inversion. This band structure is in excellent agreement with other authors.

treatments, with a dispersive $5d$ band hybridising through a nondispersive f band, but the surface state spectrum he produces is somewhat different from experiment.

- Kang et al [116] performed calculations using GGA pseudopotentials with ten times the spin orbit coupling to attempt to model the splitting between the $j = 5/2$ and $j = 7/2$ multiplets, with an overall bulk result very similar to mine using Hubbard U.

- Lu et al [118] have employed a complex treatment, by projecting out multiply occupied states, a method known as Gutzwiller projection [134]. With these methods they obtain a band structure that better accounts for the bulk correlation than DFT does. The dispersion of the f bands is smaller than in

my GGA+U results but the features are otherwise very similar.

The similarity with comparable treatments lends credence to my GGA+U results. In order to split the f multiplets and raise the $j = 7/2$ multiplet outside the region of interest, I have instead used a Hubbard U parameter of 1 eV, to be discussed in section 5.1.2. This partially accounts for strong Coulomb interactions and is frequently useful when treating f electron systems. To first order, the main effect of the Hubbard U is to split the $j = 5/2$ and $j = 7/2$ by an energy U, comparable to a strong spin-orbit effect. This can be understood by considering the fact that the f states are not very dispersive and all the $j = 5/2$ states are occupied; this penalises putting an extra electron into the $j = 7/2$ bands by U.

The most important feature of the band structure is the band inversion and its corresponding effect on the parity eigenvalue. The Fu & Kane invariant [58] provides an indicator of the bulk topology in terms of the parity eigenvalue at the high symmetry points, which in turn by the bulk-boundary correspondence tells us about the surface state properties. By finding the product of the parity of the filled bands, counting each Kramers pair only once, a topological invariant can be found. I find the parities to be:

HSP	Γ	X	M	R
Parity	1	-1	1	1

There are 3 independent X and M points, giving an overall topological invariant of $\nu = -1$, in agreement with other authors [114–116]. This guarantees the existence of (topologically protected) helical surface states, although does not guarantee their fillings or their relative energy compared to the other bands at the surface.

5.1.2 Methods of treating the correlation

The mechanisms for opening a gap at the high symmetry points involve a highly correlated ground state of d and f orbitals interacting via the Kondo effect, so it is

natural to consider the validity of using DFT. Several methods to different levels of accuracy exist to modify DFT spectra to incorporate some aspects of electron correlation. I have included some of the qualitative effects of the correlation by including a Hubbard U term, as introduced in 4.3.3, which splits the $j = 5/2$ and $j = 7/2$ states by approximately U. This does in a certain respect fail to fully capture the strongly correlated physics of the f bands: the f bands are predicted by DFT to be more dispersive than observed in experiment; using a Gutzwiller projection onto singly occupied states as explored in reference [118] reproduces the observed XPS f band dispersion, but does not accurately capture the band velocities at the surface as I do in 5.2.1 onwards.

The choice of Hubbard U is partly informed by phenomenology, typically performed by tracking how some physical property evolves as a function of U and matching the desired case [1]. There are two clear choices: either the bandgap or the f electron $j = 5/2$ to $j = 7/2$ splitting. To match the experimental splitting, I find a value of around $U = 6$ eV but this badly overestimates the bandgap. Conversely, a smaller value of U reproduces the experimental bandgap well but underestimates the f electron splitting. I have chosen to use the smaller value of $U = 1$ eV for two reasons. Firstly, I am primarily interested in the electronic structure in the vicinity of the Fermi level, so accurately reproducing the bandgap is of significant importance. Secondly, even though the f electron splitting is not correctly produced, the higher energy $j = 7/2$ states are still moved well above the Fermi level and are unoccupied. The variation of the bandgap with Hubbard potential is demonstrated in figure 5.2. From the figure it is clear that to produce the experimentally observed bandgap of 15-20 meV choosing $U < 3$ eV is required.

Using a Hubbard parameter does not fully account for the correlation by any means: in section 5.7 I give two plausible extensions to my treatment capable

[1] There are perturbative schemes that aim to derive the Hubbard U from purely ab initio treatments, but these do not work with spin orbit coupling.

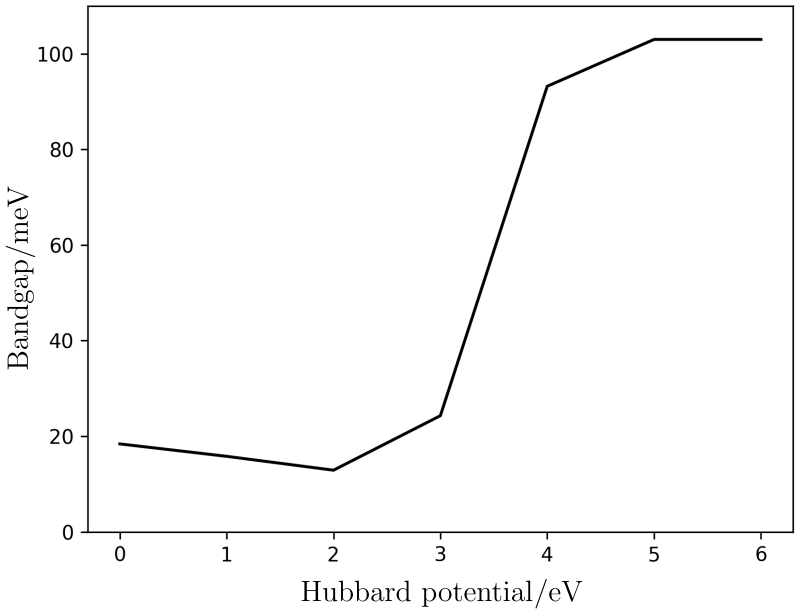

Figure 5.2: The variation of bandgap with Hubbard U. In order to match the experimental bandgap, choosing U around 1-2 eV is required. I have taken $U = 1$ eV; at this value the $j = 7/2$ states are not occupied so the fact the experimental f electron splitting is not observed is not critically important.

of systematically studying some of the correlation effects in SmB_6 and I briefly explore the sensitivity of some of my conclusions about the surface states to the Hubbard parameter in appendix D.

5.2 Wannierisation of the bulk model

Having obtained a plane wave band structure, it is desirable to convert this to a wannierised tight binding model in order to study the low energy effective Hamiltonian in a computationally efficient way and also to study the surface. By projecting onto a small subset of the bands close to the Fermi level, a tight binding model capturing the low energy physics is obtained. The first step towards this is to identify the relevant orbital content: the hybridisation gap is obtained due to hybridisation from a d character Γ_7^+ (originating from t_{2g}) band inverting below a group of f character Γ_6^- and Γ_7^- bands. Note the important fact that the d orbitals extend greatly above the Fermi level; the hybridisation has its origins in

the d orbital t_{2g} multiplet, which lies far above the Fermi level. These states must be included in the projections if a wannierised band structure with the correct symmetry properties is to be obtained.

The choice of projectors is very important for accurately modelling the band structure. Figure 5.3 shows the samarium $5d$ and $4f$ orbitals projected onto the bulk band structure; it is seen that these well describe the bands around the Fermi level. Therefore, the projections I use have azimuthal parts given by spherical harmonics Y_{lm}. Specifying the number of nodes in the radial part of the projection also allows selection of specific shells of electrons. The $5d$ orbitals have 2 radial nodes and $l = 2$ and the $4f$ orbitals have 0 radial nodes and $l = 3$. Using these projectors, I construct a wannierised model of the region around the bandgap using `Wannier90` [104].

In general the wannierisation procedure does not respect the symmetries of the lattice, but it is these symmetries, particularly the time reversal symmetry, that fix the topological data. Therefore, I also symmetrise the resulting tight binding Hamiltonian with respect to the crystal structure space group. Following the methods of Gresch et al [106], letting the representation matrix of some symmetry $g \in G$ be denoted $D^{\mathbf{k}}(g)$, the group averaged Hamiltonian is given by

$$\mathcal{H}_{\text{Symmetrised}}(\mathbf{k}) = \frac{1}{|G|} \sum_{g \in G} D^{\mathbf{k}}(g) \mathcal{H}(g^{-1}\mathbf{k}) D^{\mathbf{k}}(g^{-1}). \tag{5.1}$$

In this way, any small symmetry breaking terms introduced in the wannierisation process are averaged away and numerically exact degeneracy along high symmetry paths is preserved. To accomplish this, I have used the SYMMETRY-REPRESENTATION, TBMODELS and PYMATGEN python packages. The resulting tight binding model, shown in figure 5.4, is in near perfect agreement with the DFT bands in the vicinity of the bandgap. As outlined in section 4.3.4, it is common practice to choose the Bloch gauge $U_{n\mathbf{k}}$ such that the Wannier functions minimise their summed spread. This has not been performed here: in order to be able to generate the representation

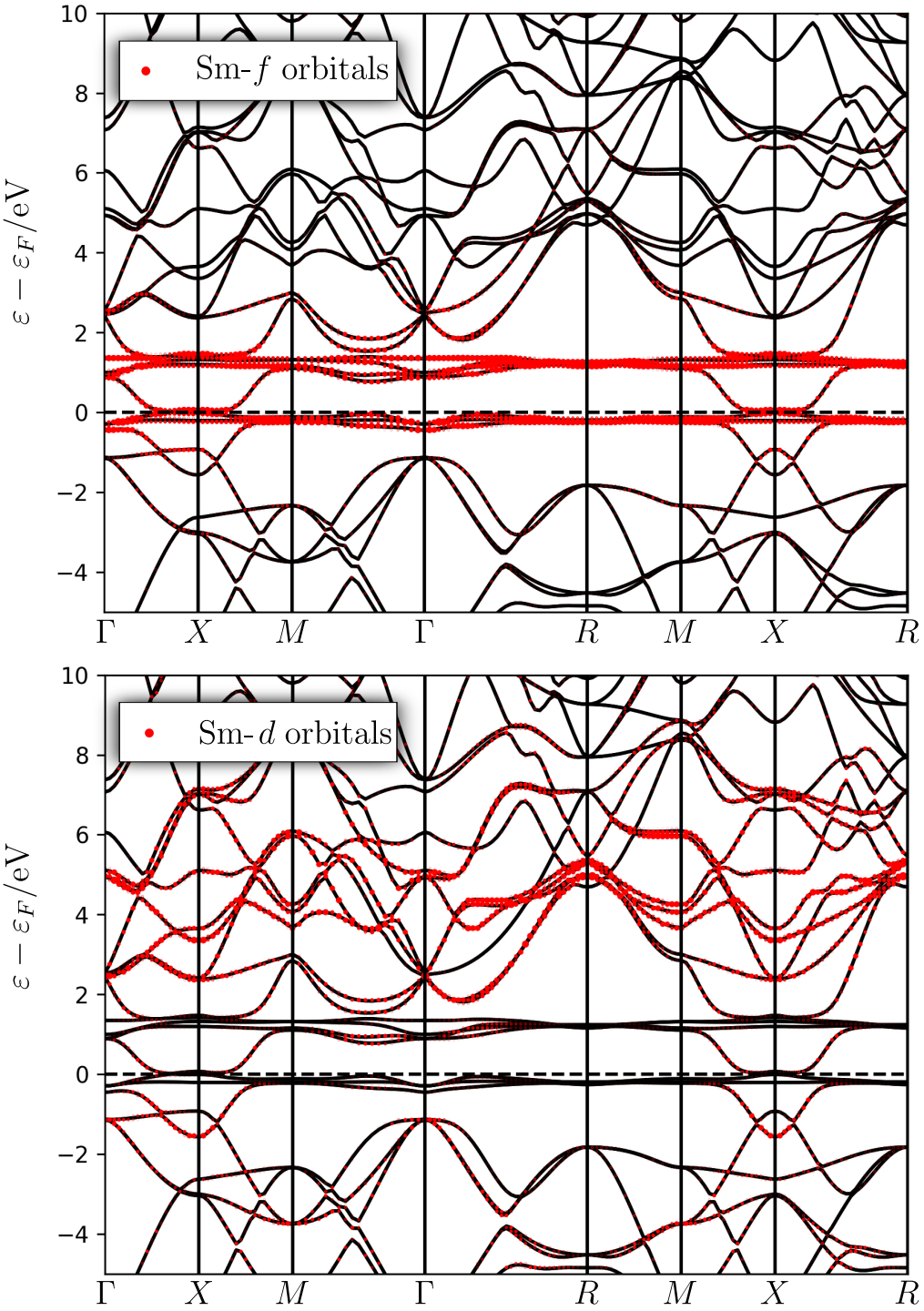

Figure 5.3: The fatbands of SmB_6 projected onto the $4f$ and $5d$ orbitals. Note the strongly localised states around the Fermi level, which are of f character, and the more mobile d states. The projections confirm the d/f orbitals to be the most relevant around the Fermi level. Larger sized dots indicate a larger overlap of that orbital on the Kohn-Sham state with that energy.

matrices under rotations it is required that each orbital corresponds closely to a known atomic orbital (eg d_{z^2}); if the orbitals are highly mixed under the localisation procedure then this process is much more difficult. As long as sufficiently long range couplings are retained, no information is lost by using a Wannier basis that is not maximally localised. Secondarily, as I have attempted to make clear throughout, the existence of an exponentially localised Wannier basis is contingent on the existence of a smooth Bloch gauge, which is violated in the topological case. We should therefore expect fairly long range interactions even if a localisation procedure is followed as a corollary of the nontrivial $\mathbb{Z}_2$ index.

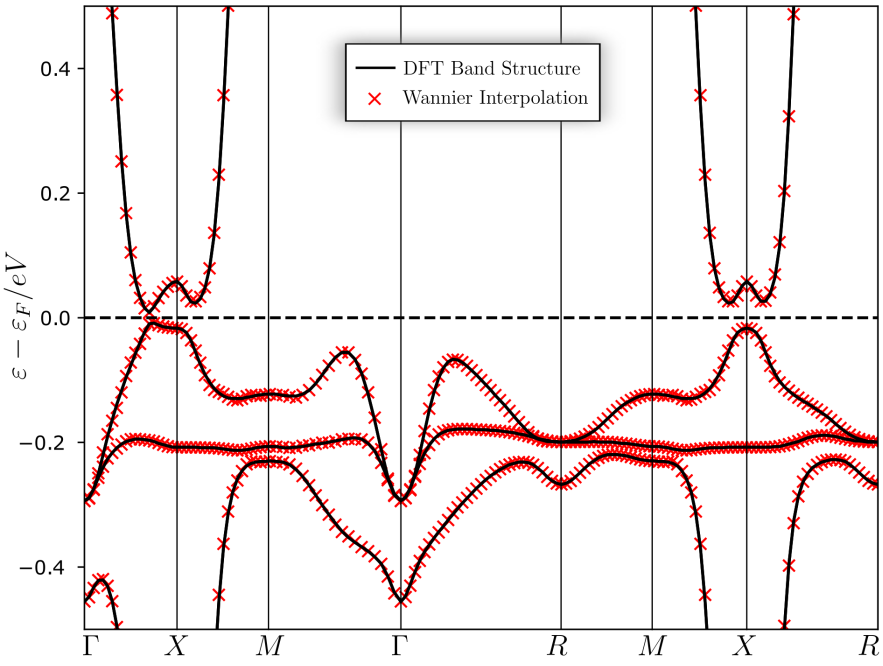

Figure 5.4: The wannierised band structure (red crosses), overlaid on the DFT bands (black lines). There is very good agreement at the Fermi level across the whole Brillouin zone. The Wannier model has 6 filled bands, consisting of 3 filled f electron Kramers doublets at Γ. This has consequences for the parities, detailed in the main text.

It is important to check that the wannierised model is in the same topological class as the bulk DFT model to ensure the Wannier model constitutes a reasonable low energy Hamiltonian: the band inversion at X leaves the overall parity eigenvalue *positive*, and in fact all the high symmetry point parities are flipped with respect to DFT. This is, however, exactly to be expected and not a problem. The orbitals

of the filled bands, which are not included, contribute an overall parity of (-1), which explains the change in parity. Because the $\mathbb{Z}_2$ index ν is the product of this over all 6 high symmetry points, it becomes

$$\nu_{DFT} \to \nu_{TB} = (-1)^6 \nu_{DFT} = \nu_{DFT} \tag{5.2}$$

and so the wannierised model is still topologically nontrivial by the Fu-Kane categorisation.

5.2.1 Surface state calculations

A simple method of studying the surface of materials is available in terms of a tight binding model. Having obtained the wannierised tight binding model, it is easy to construct slab geometries of varying thickness to study how the topological states emerge as the thickness grows. Because there are no Wannier functions centred on the Boron atoms, the slab model most accurately mimics the Sm 1x1 termination. The slab geometry is achieved by assembling a supercell geometry of many layers and at the surface, where couplings would connect to states that don't exist, the couplings are set to zero. This functionality is implemented within `WannierTools` [108]. The lower symmetry at the surface affords us different high symmetry points; the Brillouin zone projected onto the surface unit cell has high symmetry points at $\overline{\Gamma}$, $\overline{X}$, $\overline{M}$ as illustrated in figure 5.5. The reduction in symmetry from cubic to square at the surface also changes the irreducible representation content of the surface bands. For example[2], at the surface under the reduction of crystal symmetry from $O_h \to D_{4h}$ the Γ_8^- states split into $\Gamma_8^- \to \Gamma_7^- + \Gamma_6^-$.

The band structure of a slab of 40 layers is shown in figures 5.6 and 5.7.

What is most striking about these slab calculations is the fact that the $\bar{X}$

[2]Note this is the same splitting that occurs in the bulk between the Γ and X points, seen earlier in [116]

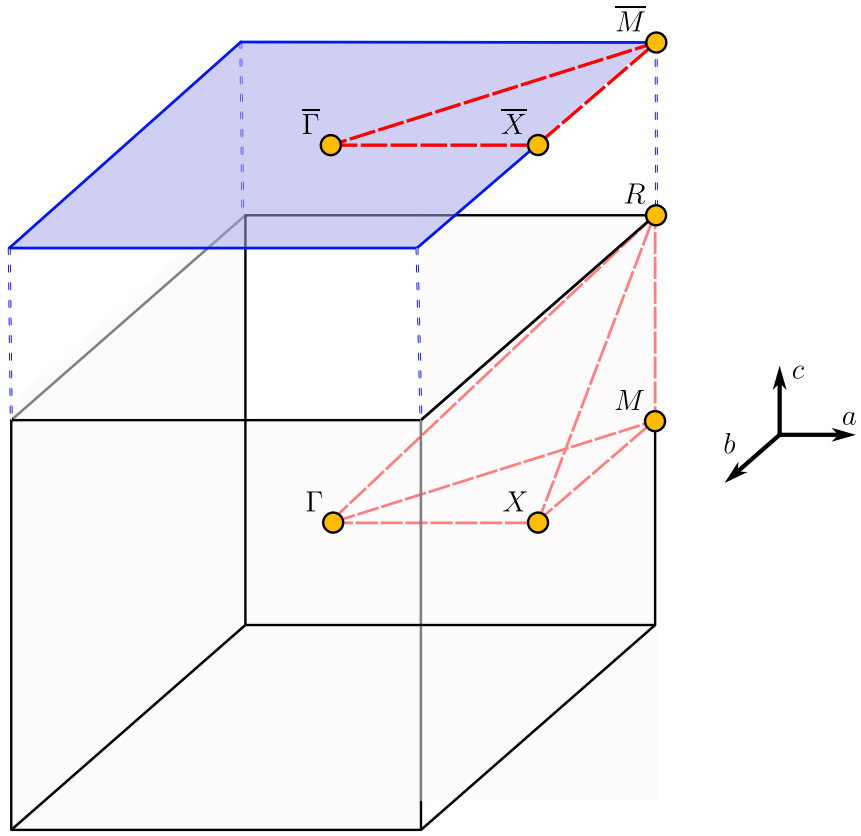

Figure 5.5: The cubic 3D Brillouin zone projected onto the square [100] surface. Under this projection the new high symmetry points are labelled $\overline{\Gamma}$, $\overline{X}$, $\overline{M}$

point Dirac cone is receded into the bulk by roughly 50 meV. These states show a Fermi velocity of 240 meVÅ along both the $\bar{X} - \bar{\Gamma}$ and $\bar{X} - \bar{M}$ high symmetry lines and agree qualitatively with the experimental data [121] [122] [123] which measure an $\bar{X}$ point Fermi velocity of 200-300 meVÅ. This agreement contrasts with some theoretical models of the surface states, which have velocities of 30-50 meVÅ: with their Gutzwiller projected band structure, Lu et al [118] construct a Wannier tight binding model and Alexandrov et al [135] construct a lattice model, using a slave boson approach to incorporate the correlations. Both of these methods

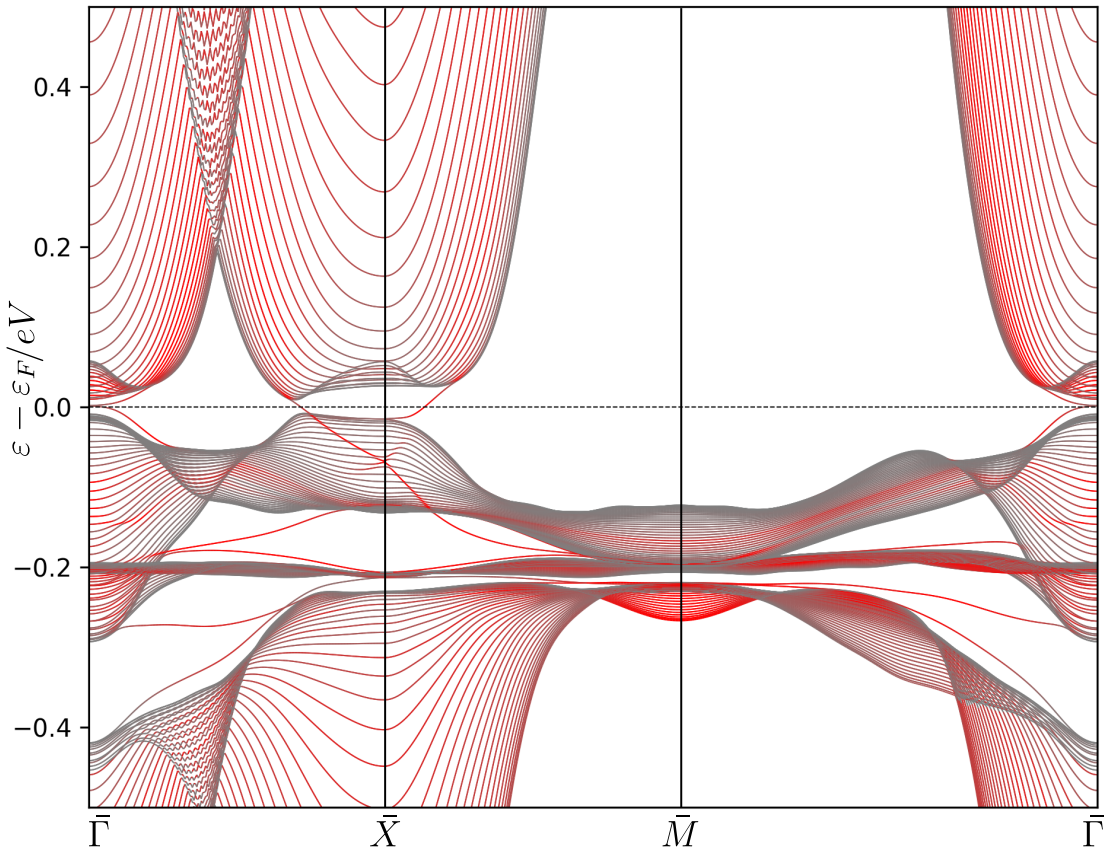

Figure 5.6: The slab band structure of a 40 layer slab, with projections onto the surface states in red. The topological surface bands are clearly visible, with the $\bar{X}$ point Dirac cone notable receded into the bulk. Features of the bulk bands are still visible at this scale.

produce heavy surface states. I demonstrate the relative insensitivity of my result on the Hubbard potential in appendix D.

This is of clear interest, as the band shape and Fermi velocity are similar to the proposal of Alexandrov et al [136] where the different coordination number of f electrons at the surface renormalises the Kondo temperature at the surface, resulting in the Dirac cone being doped. Given that result derives from vertex corrections to the d-f interaction which are not included in DFT, this mechanism can not be at work here, and the behaviour appears to be fairly well explained by my weak coupling treatment. As will be seen in 5.4, the doping effect at $\bar{X}$ is also seen at the pure DFT level. The high velocity states at $\bar{X}$ should be contrasted with the $\bar{\Gamma}$

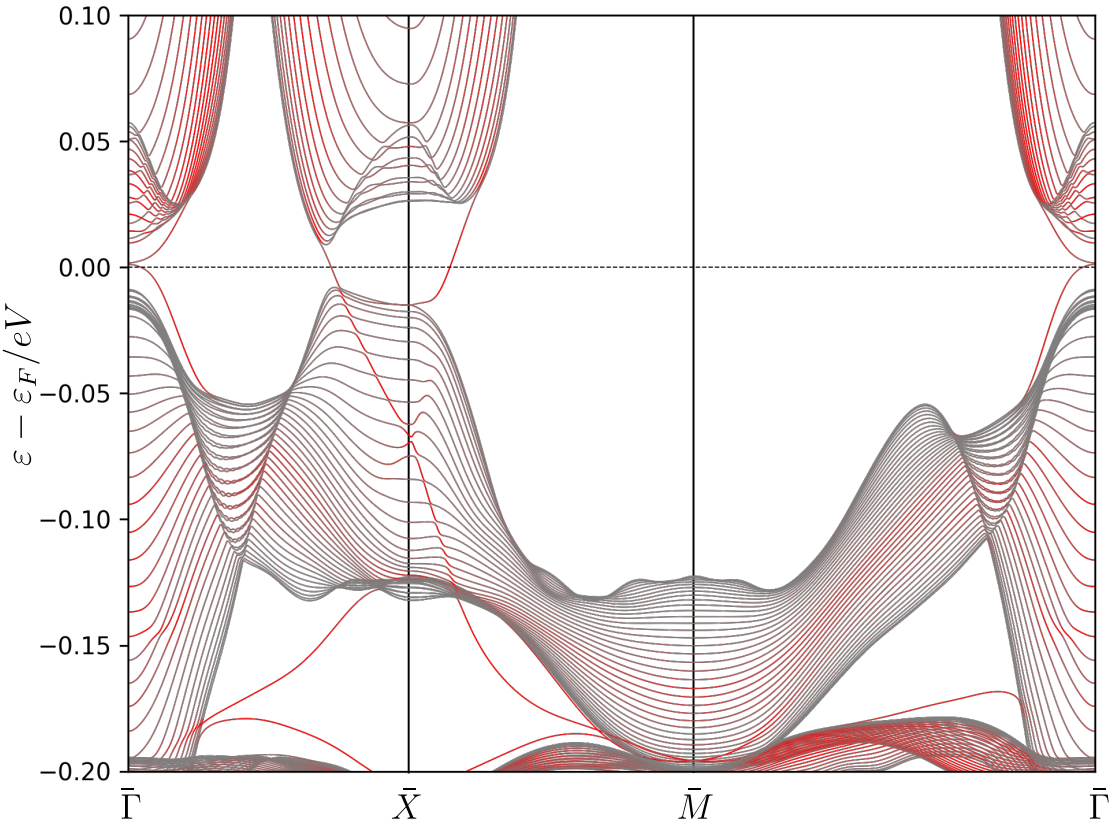

Figure 5.7: The same 40 thickness slab band structure as figure 5.6, but zoomed in to finer energy scales.

point surface states which are slower, with a small velocity of 25 meVÅ. The poor resolution at the $\bar{\Gamma}$ point of ARPES data makes comparison to experiment difficult. For further details on how I have obtained Fermi velocities refer to appendix D.

To facilitate easier comparison with experiment, consider also figure 5.8. Here, the surface Green function method 4.3.5 has been applied to the tight binding model along the same high symmetry path as the slab band structures. This produces a surface spectral density $A(\mathbf{k}, \omega)$ of an effectively infinite slab, in analogy to the result of an ARPES experiment.

Because I have not used any localisation of Wannier functions, every orbital maintains definite orbital character and, crucially, spin character. This allows the spin texture to be found, as spin operators can be easily constructed for the

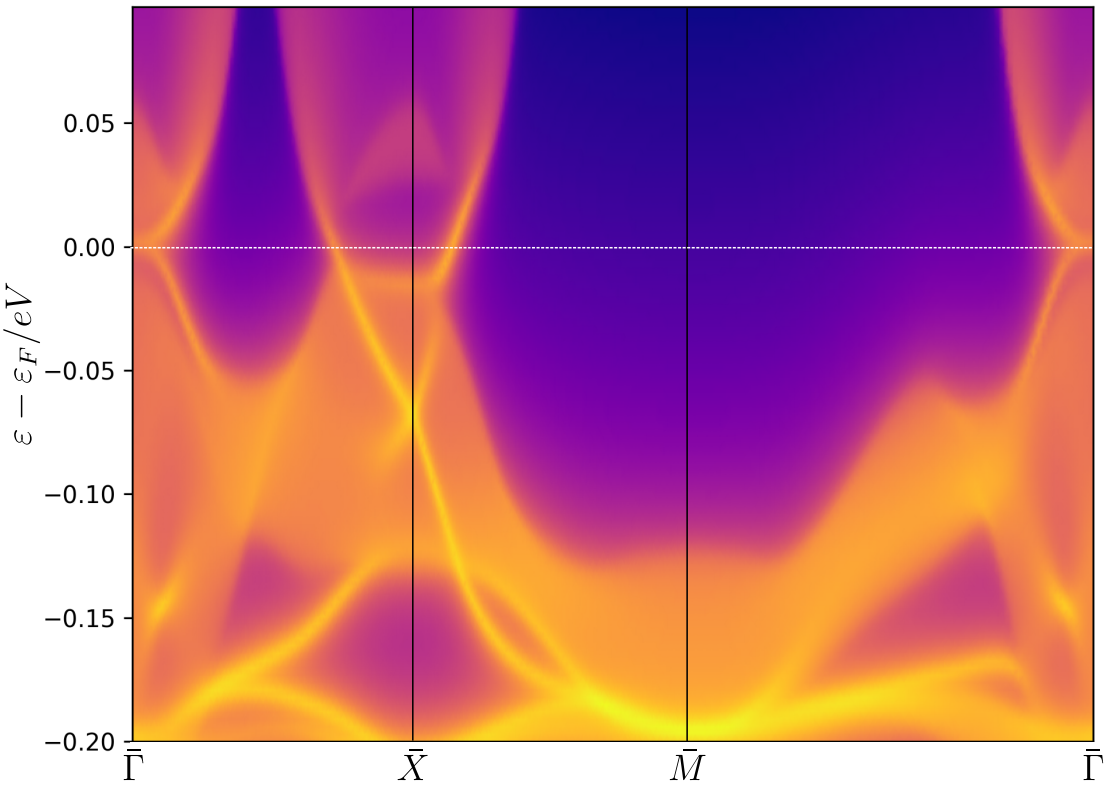

Figure 5.8: The surface Green function spectral function of the Wannier tight binding model as calculated in the surface Green function method. The same features are visible here as in the slab calculations. Brighter colours indicate higher spectral density.

surface spectral function. Plotting this, the spin texture and oval shape of the $\bar{X}$ point Dirac cone are clearly seen, depicted in figure 5.9. The same exercise is repeated in figure 5.10, where the same spin texture is also visible. This confirms the presence of three Dirac cones on the [100] surface.

The Fermi surface arcs also provides a further opportunity to compare these results quantitatively to the experimental data. By Luttinger's theorem [137], the area enclosed by the Fermi surface of any fermionic system is the carrier density, even in the presence of strong interactions. I find the total area enclosed by the closed Fermi arcs to be 0.15 Å^{-2}, or $1.5 \times 10^{15}\,\mathrm{cm}^{-2}$. This is the correct order of magnitude with respect to experiment, but slightly smaller: Nam et al [64] measure a carrier density in transport of $4 \times 10^{15}\,\mathrm{cm}^{-2}$ and Jiang et al [121] observe via ARPES that the enclosed areas occupy around a third of the surface Brillouin zone,

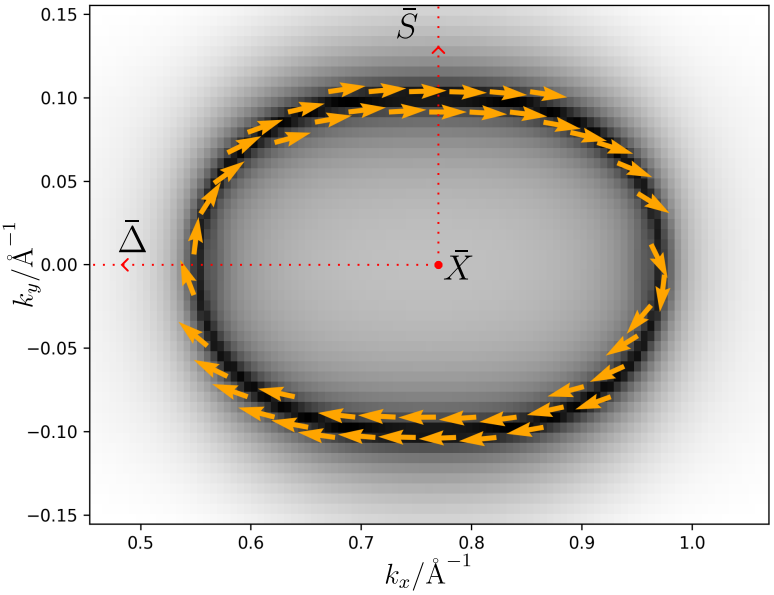

Figure 5.9: The Dirac cone spectral density at the $\bar{X}$ point imaged across a constant energy slice at the Fermi level, with spin projections. The helical spin texture is clearly seen. The area of the Brillouin zone depicted is around the $\bar{X}$ point - in reduced coordinates the extent of the oval is from $[0.35, 0.65]$ along k_x and from $[-0.15, 0.15]$ along k_y. The high symmetry lines are labelled: $\bar{\Delta}$ goes from $\bar{\Gamma}$ to $\bar{X}$ and $\bar{S}$ goes from $\bar{X}$ to $\bar{M}$.

corresponding to a surface carrier density of $7 \times 10^{15}\,\text{cm}^{-2}$.

There is a further, qualitative comparison with experiment that can be made here: Nam et al found that the surface carrier density increased by a factor 1.4 [64] upon modification with *nonconductive, nonmagnetic* impurities. This represents a purely electrostatic perturbation that should manifest in the band fillings. The $\bar{\Gamma}$ point Dirac cone is by my calculations highly tuned, looking fairly parabolic until a small region around the Fermi level where the linear Dirac states emerge. We should expect surface modification of this type to perturb the band fillings by order meV [133]; the rapid change of the Fermi surface at $\bar{\Gamma}$ can accommodate a fairly large change in surface conductivity under this perturbation[3].

[3]See also figure 5.29 for a related discussion of the effects of doping at the $\bar{\Gamma}$ point.

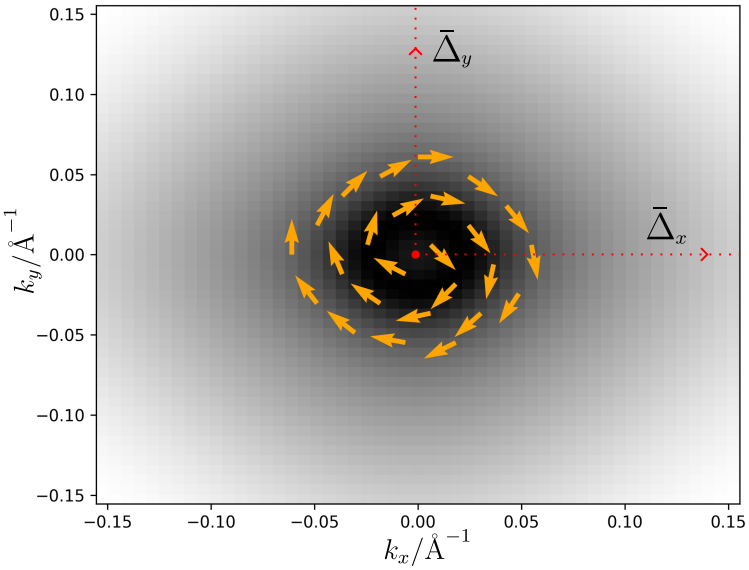

Figure 5.10: The $\bar{\Gamma}$ Dirac cone. The same helical texture is observed as around $\bar{X}$, although the cone is much smaller at ε_F as the Dirac point is close to the Fermi level. In reduced coordinates the extent of the Dirac cone is $[-0.05, 0.05]$ along k_x and k_y. Both high symmetry lines pictured are $\bar{\Delta}$ lines, labelled $\bar{\Delta}_x$, $\bar{\Delta}_y$ according to whether they go to $\bar{X} = (0.5, 0)$ or $\bar{Y} = (0, 0.5)$, respectively. The Gamma point label is offset for clarity. The spin texture is isotropic; visual deviations from isotropy are due to the aspect ratio and the algorithm used to only plot some of the spin arrows, used to avoid visual clutter.

5.3 Tight binding thin film models

It is desirable to explore also the limit of thin films in tight binding to facilitate comparison to the DFT slab models, which are limited in size by computational resources. By directly comparing the two, firstly we obtain a more accurate assessment of the extent of electrostatic effects and secondly we can form a tentative 'dictionary' between the thin slabs investigated in DFT and the thick slab DFT limit which is computationally inaccessible, by comparing to the thicker slab models. The band structures of 6 layer and 8 layer tight binding slabs are shown in figures 5.11 and 5.12 respectively.

The slab tight binding models bear much resemblance to the thicker slab models; the qualitative features are the same and the recessed $\bar{X}$ point Dirac cone is present in both models. In both of these models the 'bulk' is not yet fully defined; the $\bar{\Gamma}$ point Dirac cone is not yet well developed at 6 layers and at 8 layers a small gap

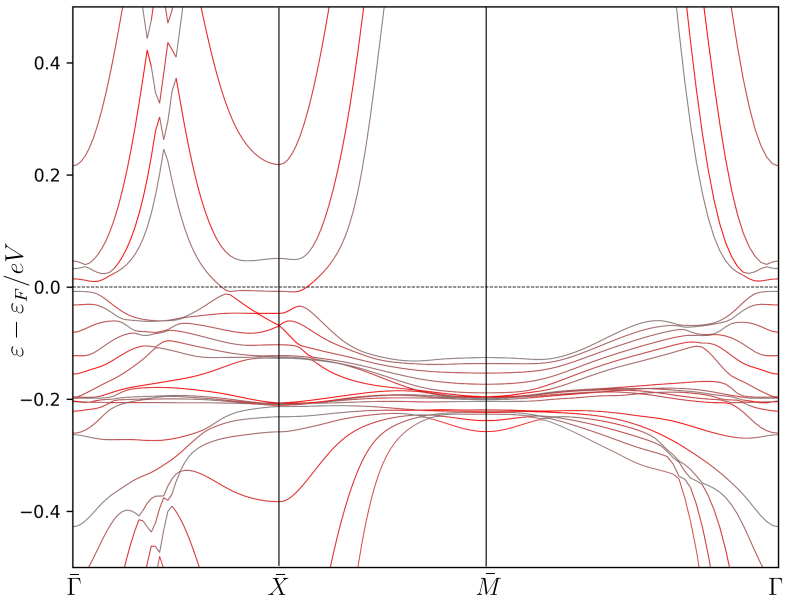

Figure 5.11: Band structure of a tight binding slab model 6 unit cells thick. Projections onto the surface orbitals are shown in red. The same qualitative features are seen as in the thicker slabs as well as the features of the bulk bands. The Dirac cone at $\bar{\Gamma}$ has not developed yet.

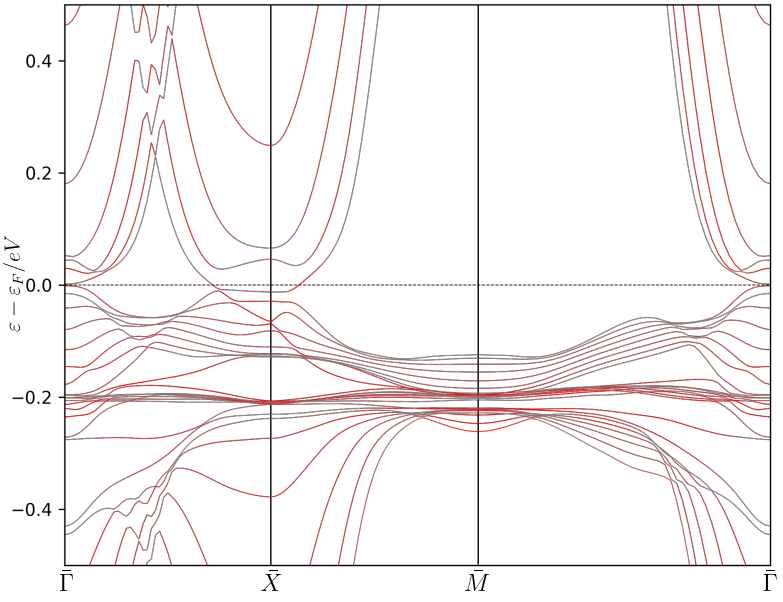

Figure 5.12: Band structure of a tight binding slab model 8 unit cells thick. Projections onto the surface orbitals are shown in red. The $\bar{\Gamma}$ point Dirac cone appears well developed here, although a small gap has appeared at the $\bar{X}$ point.

opens at the $\bar{X}$ point Dirac point caused by coupling between the surfaces. The coupling between the states is in general nonmonotonic, so this gap opening slightly at a greater thickness than the thickness 6 slab is not concerning.

5.4 DFT slab models: probing surface local electrostatics

As we have seen from the prior chapters and results, the band inversion guarantees the existence of topological surface states, seen in the tight binding models of section 5.2.1, as their existence is a function purely of global properties of the wavefunction. Any time reversal symmetry preserving perturbation will not destroy these states; they are robust to disorder and electrostatic perturbation. However, the surface bandstructure and band fillings may well change as a result of the local electrostatic properties. Where the previous calculations used a tight binding model, this is not guaranteed to accurately represent the surface potential: the effective potential in the tight binding model corresponds to the self-consistently determined single particle potential felt by an electron in a purely periodic system. At a surface, where this assumption is broken, the electron density may undergo a small relaxation due to the presence or absence of this change in potential, analogous to band bending in semiconductors [128]. This relaxation typically preserves the symmetry of the surface, but this is not true in general: materials with a shallow surface potential may break symmetries and form complex surface orders, as in the case of the 7×7 reconstruction in Silicon [138]. In order to describe the role and importance of this effect I shall therefore present models for the SmB_6 [100] surface in a DFT slab geometry. A slab geometry features several layers of the bulk unit cell layered along z with a vacuum gap in between. The full periodicity allows the x, y directions to form bands while the vacuum decouples the surfaces from each other.

After my discussion of the unrelaxed surface, I shall also consider surface relaxation of the nuclei. The reorganisation of surface charge at the unrelaxed surface is the driving force behind surface relaxation, the forces on the atoms being the gradient of this perturbing potential. These effects are necessarily not captured by the tight binding model, which sets the surface potential infinitely large outside the slab.

5.4.1 Unrelaxed slab geometry

Here I show the band structure of the [100] Sm terminated slab, at 6 and 8 layers. Following the discussion of section 5.2.1, it is clear that this is in a sense too few layers to reliably delineate between surface and bulk, but the calculations are severely limited by computational resources. The [100] also forms a natural cleavage plane for SmB_6, so performing calculations on this surface retains easy comparability with experimental results. Calculations of the [110] or [111] surface are of course possible but have several times the atoms per unit cell. The scaling with system size is $O(N^3)$, so this increase in the number of atoms would be extremely costly. By comparing the slab tight binding calculations at 6 and 8 layers a comparison between the treatments of the surface is possible, with the slab calculations forming a kind of 'dictionary' between the lower thickness slabs and the results of a many layer slab. These calculations are performed with the same parameters as the bulk. The termination I investigate here is the Sm 1x1 termination, in which a single samarium atom is positioned at the surface. The slabs are separated by several layers of vacuum in order to decouple the surfaces (the relevant convergence data are in appendix D). As this termination is symmetric about the middle of the slab, there is no need to consider dipole corrections [139].

The surface band structure on the same high symmetry path as in the tight binding models is depicted in figures 5.14 and 5.15. These preserve the qualitative

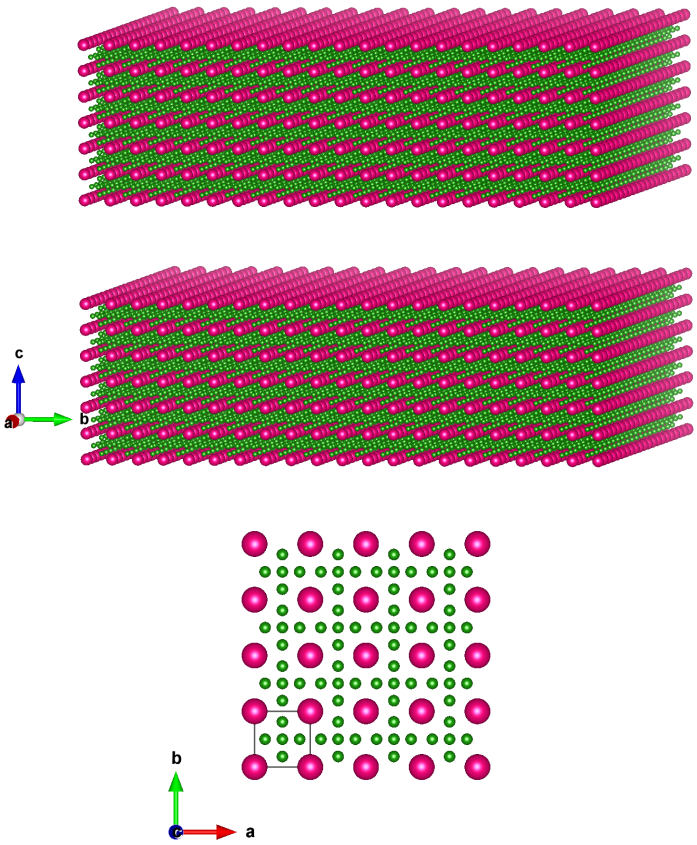

Figure 5.13: A large periodic section of the unrelaxed slab geometry, 6 layers. The calculation is performed with one primitive unit cell along x, y; many are shown here to illustrate the geometry. The lower part of the figure shows this geometry along the C axis, to show the Sm 1x1 termination.

features, with the exception of a region of significant renormalisation on the $\bar{X} \rightarrow \bar{M}$ high symmetry line. A set of bands rises up and leads to a small Fermi pocket, in contrast to the slab tight binding models which exhibit no such feature. These bands are not observed in ARPES experiments; I discuss these bands and their possible origin in detail in section 5.5.

Now I consider the band-structure projected onto the surface samarium atoms: this allows a better qualitative understanding of which bands contribute to the surface and which are bulk. This is necessary due to the added complexity of the surface, owing to the splittings due to the reduction in symmetry at the surface mentioned in 5.2.1. Figure 5.16 shows the 6 layer unrelaxed band structure with

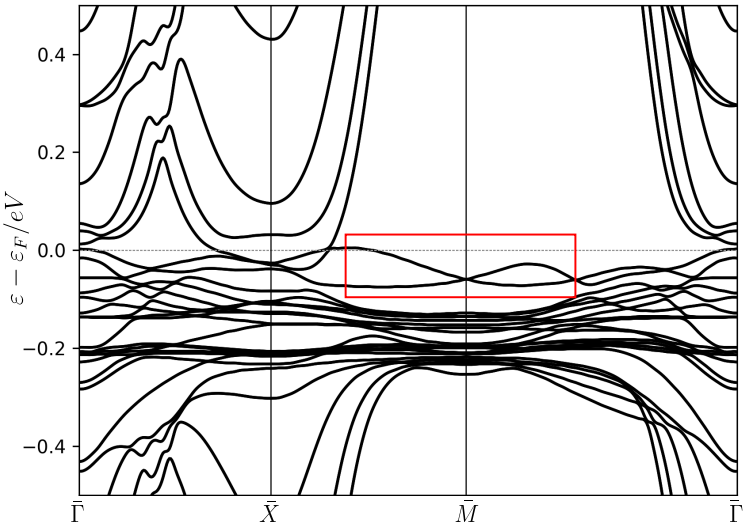

Figure 5.14: The DFT band structure for an unrelaxed slab 6 unit cells thick. The same qualitative features exist as in the the slab tight binding model, but surface electrostatic renormalisation has pushed a pocket of bands above the Fermi level along the $\bar{X} \to \bar{M}$ line, outlined in red.

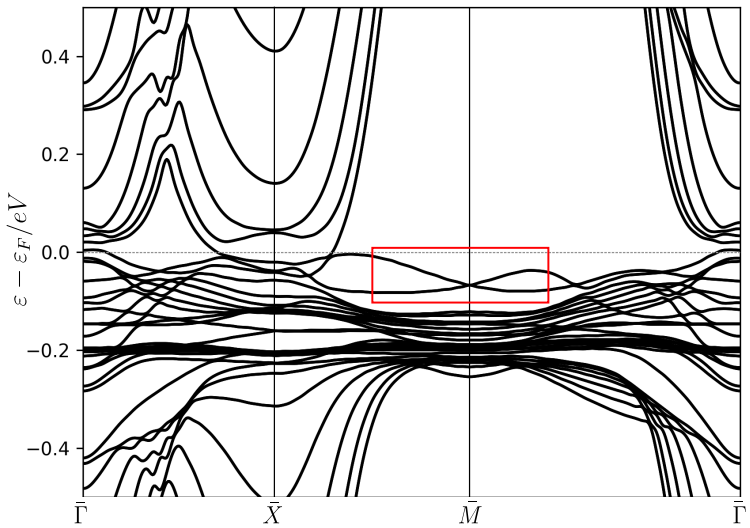

Figure 5.15: The DFT band structure for an unrelaxed slab 8 unit cells thick. As with the thickness 6 slab, the same qualitative features remain but with a set of bands pushed to the Fermi level along the $\bar{X} \to \bar{M}$ line, outlined in red.

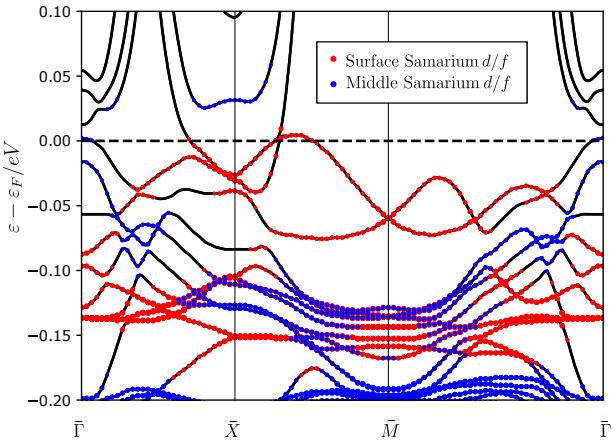

Figure 5.16: The 6 layer unrelaxed band structure, with projections onto the terminating samarium atom d and f orbitals in red and projections onto the middle samarium atom d and d orbitals in blue. The metallic states near $\bar{X}$ are shown to indeed be surface bands, as well as the unexpected pocket on the $\bar{X} \to \bar{M}$ line.

projections onto the surface and middle samarium d and f orbitals, compared to the tight binding model of the same size[4]. The same features are visible around $\bar{X}$, with a degree of renormalisation. The pocket seen along the $\bar{X} \to \bar{M}$ line is shown to indeed have surface character, implying it could be a contribution to surface conduction from a non-topological origin.

The qualitative same features are seen in the slab geometry and the tight binding model, but the band structure is notably slightly different. Figure 5.17 and 5.18 illustrate this effectively. The two methods provide qualitatively similar results but not identical; of particular note is the behaviour of the $\bar{X}$ point Dirac cone in the DFT calculation. Hybridisation between the surface and bottom as well as local perturbations renormalise the position of the Dirac cone and split it. The metallic states around $\bar{X}$ appear largely unaffected, and retain approximately the same velocity of 240 meVÅ.

[4]Recall that this tight binding model is composed of d and f orbitals only.

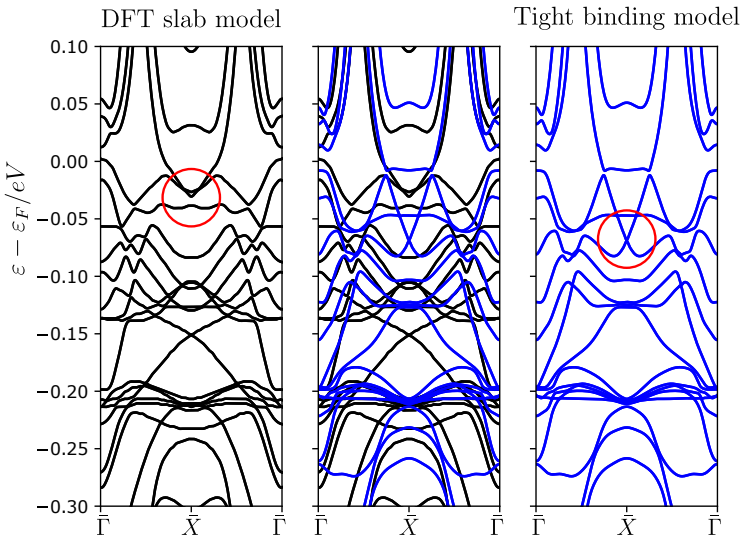

Figure 5.17: The 6 layer band structures for the unrelaxed slab and the tight binding model. The two band structures are qualitatively comparable, with the main features being reproduced well. There is a small renormalisation of the Fermi velocity from these effects, as well as a renormalisation of the location of the Dirac point. The Dirac point is shifted by 34 meV and a gap of 9 meV opened with respect to the slab model. There is a moderate dependence of the Dirac cone Fermi velocity on the chemical potential

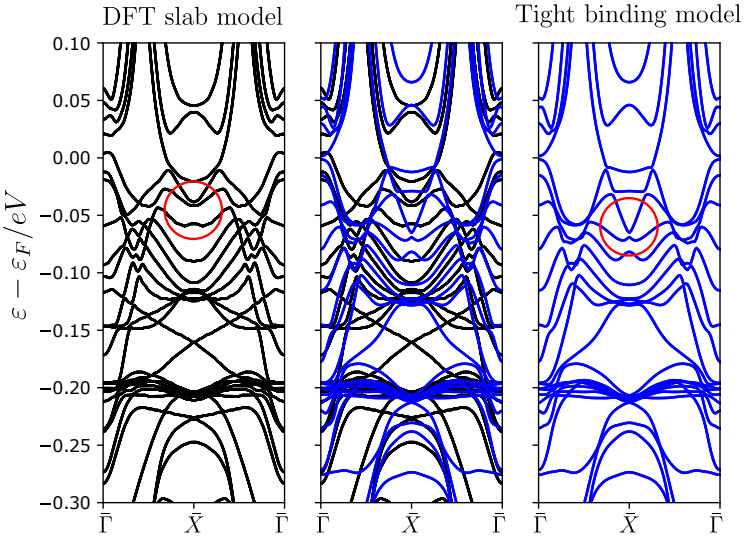

Figure 5.18: The 8 layer band structures for the unrelaxed slab and the tight binding model. As with the 6 layer structure, the qualitative features are the same but there is a degree of band bending which affects the Dirac point. The band velocities are again unchanged, but there is some renormalisation at the Dirac point.

5.4.2 Relaxed slab geometry

Next I wish to consider the effects of surface relaxation of the ions on the crystal structure and band structure. I have discussed already how the electron density at the surface experiences a perturbation due to the changed atomic potential, showing calculations in the Born-Oppenheimer approximation. The atoms experience an analogous change in potential as well as a force from the change in the electron potential via the Feynman-Hellman theorem [83]. By updating the positions and reiterating until all forces are below 1 mRy/a_{Bohr}, I obtain relaxed slab models for the six and eight layer slabs and find their band structures.

I allowed all atoms in the six layer slab to relax, and observe that only a very small change is seen in position for the atoms in the middle. For this reason, only the top and bottom two layers (four total) of the eight layer slab are allowed to relax. The very middle two layers are fixed at their bulk positions and the outer middle layers are set to the equilibrium relaxed positions from the six layer structure. This provides a much easier computational task. In both cases I find a significant relaxation of the surface, which recedes into the bulk by 9% of a unit cell in both cases. This value should not be taken as a precise quantitative prediction due to the choice of pseudopotential: I am using PBE rather than PBEsol pseudopotentials [95]. The exact reconstruction may depend on the exchange-correlation function chosen, but the choice of PBE is sufficient to understand the qualitative behaviour.

The band structure features the same pocket near the $\bar{M}$ point as in the unrelaxed 6 and 8 thickness slabs, but the relaxation has forced it higher. These bands peek above the Fermi level and can contribute to the surface conductivity, provided no electrostatic perturbations exist to shift the Fermi level. The $\bar{X}$ point Dirac cone is still recessed, although the Dirac point is rendered near unrecognisable by the band bending and resulting hybridisation. In contrast to the unrelaxed case which changes only somewhat, there is a significant renormalisation of the Fermi velocity

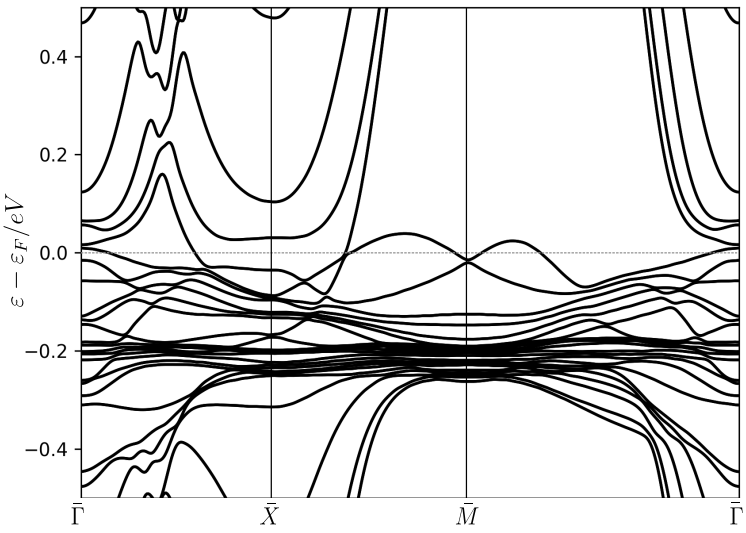

Figure 5.19: The DFT band structure of a 6 layer relaxed slab. As with the other slab calculations, the existence of the surface states is protected by the bulk topology but there is now significant renormalisation of the bands. The pocket of bands that crossed the Fermi level in the unrelaxed case have been pushed further up.

under the surface relaxation, increasing from 250 meVÅ to 850 meVÅ. This happens due to the crossover from the mobile d-electrons to immobile f electrons at the hybridisation gap, similar to the heavy fermion materials. This again highlights the sensitivity of these calculations to local electrostatic effects.

The relaxed 8 layer slab tells a similar story. Figures 5.21 and 5.22 show the band structure of the surface relaxed 8 layer slab; the unexplained pocket on the $\bar{X} \rightarrow \bar{M}$ path has been forced up above the Fermi level, as with the relaxed 6 layer slab. The Fermi velocity is again renormalised with respect to the unrelaxed and tight binding calculations, increasing to 800 meVÅ. The Dirac point in figure 5.22 is strongly renormalised, similar to the 6 layer case. In both the 6 and 8 layer cases, as expected from the topological protection there are still surface states but the surface electrostatics has caused renormalisations in the band positions and energies. The Fermi velocities in particular are renormalised, growing larger as a result of the band bending experienced under relaxation. However, the appearance of the pocket on $\bar{X} \rightarrow \bar{M}$ poses some questions on the reliability of these surface relaxed results;

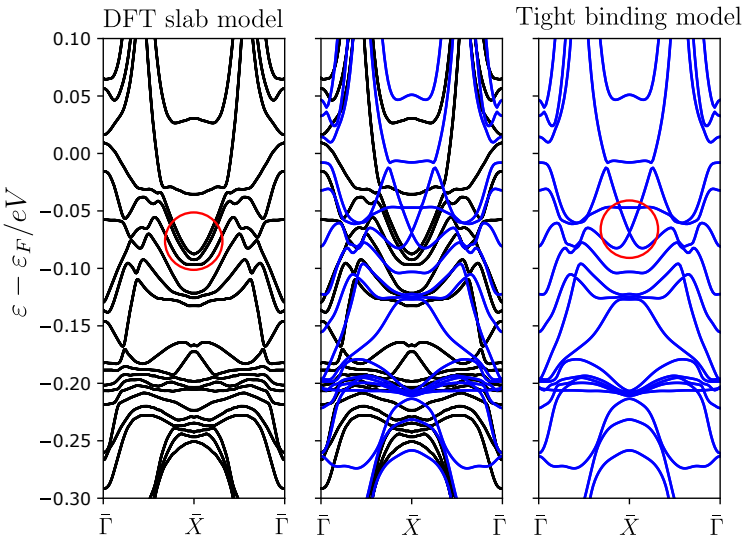

Figure 5.20: The X point band structure of the 6 layer relaxed DFT slab and the pristine 6 layer tight binding slab. The Dirac cone is heavily hybridised and the Fermi velocity is renormalised.

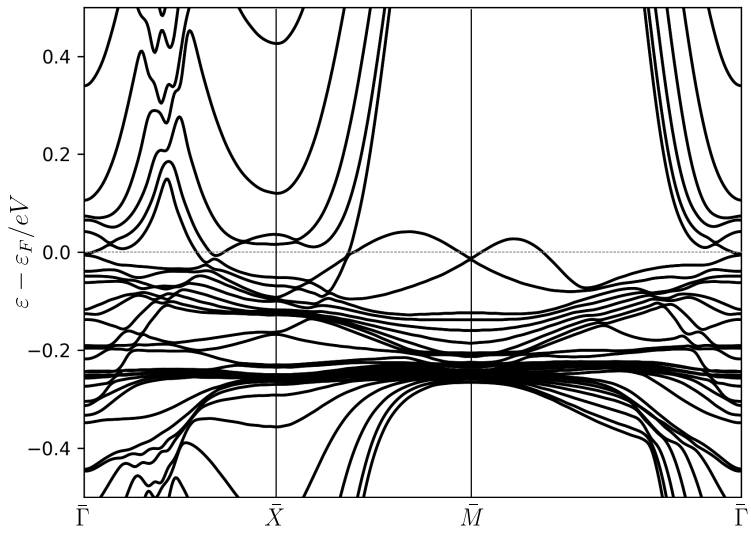

Figure 5.21: The DFT band structure of an 8 layer relaxed slab. Similarly to the relaxed 6 layer slab, the Fermi velocity is renormalised upwards. The band structure is fairly strongly renormalised under the perturbation.

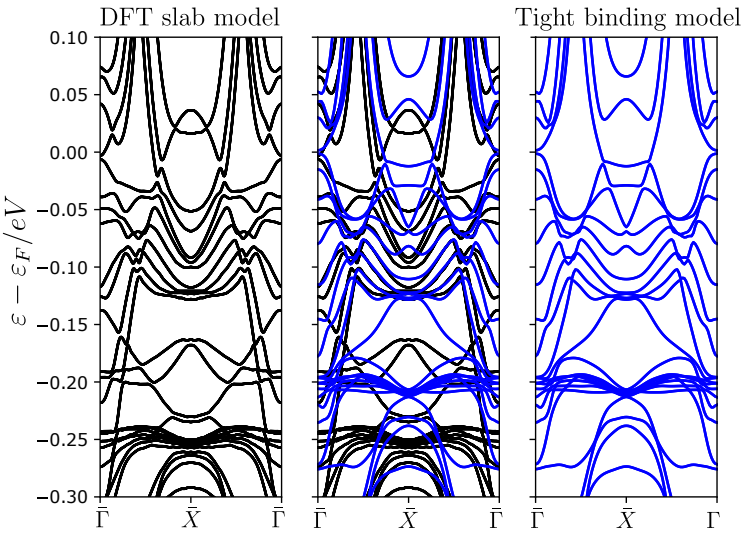

Figure 5.22: The X point band structure of the 8 layer relaxed DFT slab and the pristine 8 layer tight binding slab. The Dirac point is strongly renormalised in the DFT model.

this is not observed in experiment. The pocket on the eight layer slab protrudes above the Fermi level less than the six layer, so it is possible that if this feature is physical it recedes back below the Fermi level as layers are added but this is not clear. The projections in 5.16 show that this pocket has a large projection onto the surface, so if it is physical it should indeed be visible in photoemission.

The overall conclusions of these results are that as expected given the bulk topology the slab DFT calculations still behave like a topological insulator. Nonetheless, there are some inconsistencies between the TB models and DFT slab calculations stemming from the surface electrostatics, which I shall explore a little more in the following section. Given the relative sensitivity of the Fermi velocity to surface perturbations, I also discuss briefly in section 5.7 some possible methods that could give a more accurate first principles estimate of the Fermi velocity and carrier density.

5.5 Discussion of the $\bar{M}$ point bands

The DFT slab bands of the previous sections all feature a peculiar feature around the $\bar{M}$ point; a set of bands are pushed up to and above the Fermi surface originating from the surface samarium atoms (figures 5.19, 5.14, 5.16). I am not the first author to mention these bands: Kim et al [140] have also reported these same features in slab DFT models (using different DFT software), although they attribute them to being further topological surface states caused by including the Sm-f electrons as some early authors did not (Zhu et al [141] performed DFT calculations on this material but treated the $4f$ electrons as core states, attributing the surface conduction to dangling Boron bonds). They have also performed DMFT calculations and used this to justify rescaling the DFT bandstructures by a factor of ten; my GGA+U bandstructures are very similar to their unscaled DFT band structures. The bandgap they report is smaller than seen in experiment, by approximately the same factor of 10.

Given the f electron presence in my tight binding models, this explanation does not seem likely, although tight binding does not include the electrostatic renormalisation of the surface. The bands in my simulations vary significantly as a function of surface relaxation (compare figures 5.14 and 5.19), highlighting the electrostatic origin of these bands. It is worth also pointing out that the bands that cross the Fermi surface do so an *even* number of times on each high symmetry line, which means they do not influence the topology of the bands [76]. Kim et al further demonstrate a similar surface relaxation to me and show that the positions of the $\bar{M}$ point bands change with this relaxation, then postulate that the reason these bands are not observed experimentally is due to movement of the Sm atoms *opposite* to the direction of relaxation, or the surface termination differing from Sm 1x1, as they demonstrate DFT surface bands similar to the ones I computed with tight binding.

Furthermore, Kim and I both find that these bands recede back below the

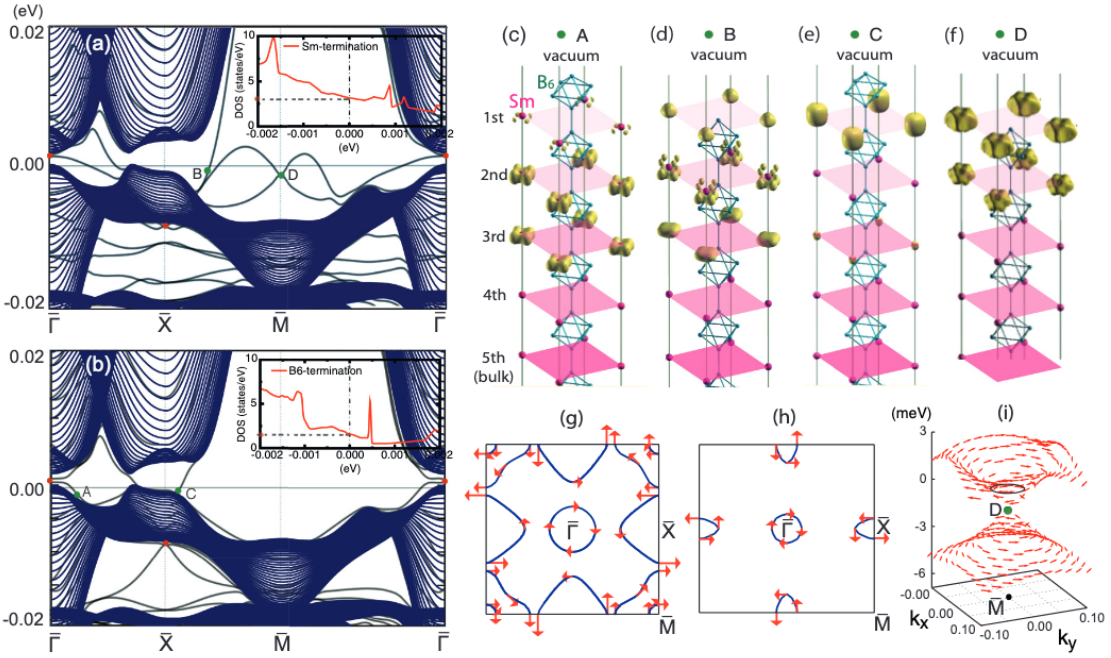

Figure 5.23: DFT results obtained by Kim et al. Subfigures a) and b) show the band structure of SmB_6 slabs with Sm and B_6 terminations respectively. Their Sm terminated slab bands closely resemble my DFT bands. The Boron terminated slab produces bands similar to my tight binding models. Figures c) through f) show the charge density at the labelled points A, B, C, D in the band structures. The spin texture is shown in g), h), i). The energy scales of the band structures have been rescaled by 1/10 in order to match the authors DMFT predictions; my band structures are in accordance with their unscaled calculations. Reproduced with permission from [140].

Fermi level under a change in termination from Sm to B_6, up to small discrepancies attributable to slab thickness, pseudopotential and implementation, shown in figure 5.24 [5]. This is an electrostatic perturbation that necessarily preserves the surface lattice symmetries, so it is therefore not possible for these states to be topological. The fact that I do not observe these bands in the non-interacting tight binding model lends further credence to my assertion that these bands exists purely as a result of the electrostatic perturbation existing in the electron density at the surface.

To further investigate the nature of these bands, figure 5.25 shows the spin polarised band structure of the unrelaxed 6 layer slab, demonstrating a spiral spin

[5] I also briefly demonstrate the relative insensitivity of this result on Hubbard potential in appendix D.

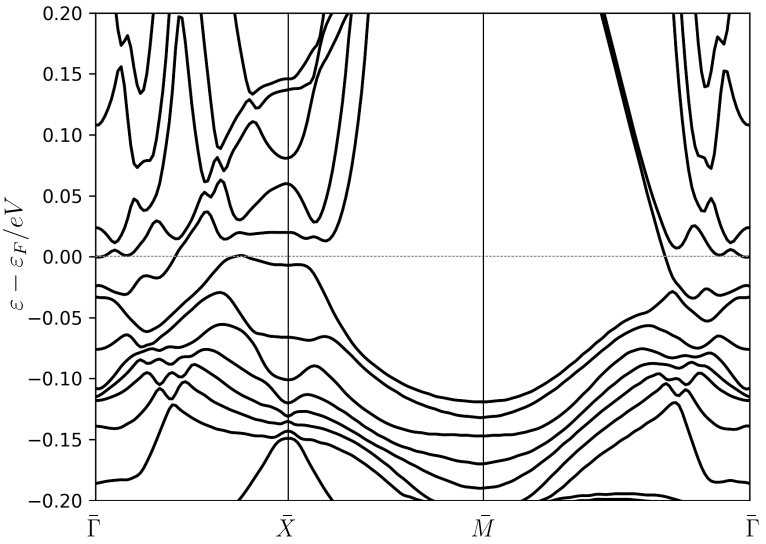

Figure 5.24: The 6 layer band structure with Boron termination. The $\bar{M}$ point states have disappeared, in agreement with Kim et al. The topological features are as before preserved, although the bands are somewhat indistinct along $\bar{\Gamma} \to \bar{X}$ due to the thin slab used. The energy scale matches that of Kim, disregarding their unphysical rescaling.

texture. This spin texture is indeed similar to the topological spin texture, but does not appear to stem from band inversion. Because of this, the pairs of bands appear more similar to a Rashba splitting [142] induced by the gradient in electrostatic potential at the surface. The coexistence of Rashba effect and topological spin textures is attested to theoretically in Bismuth compounds, see for example [143].

Ultimately, as these bands are *not* observed in any ARPES experiments they should serve either to suggest the failure of the DFT model to adequately represent the surface, or to indicate that Boron is in fact the terminating group. This viewpoint is consistent with some early XPS studies on the material [144], although contrary to the assertions of STM studies such as [126]. An alternative possibility is that these spurious bands vanish as the thickness of the slab grows very large. We have already seen how the slab surfaces may influence each other at small slab thicknesses; it could be that at very large DFT slab thicknesses these bands recede back into the bulk and more closely resemble the tight binding data.

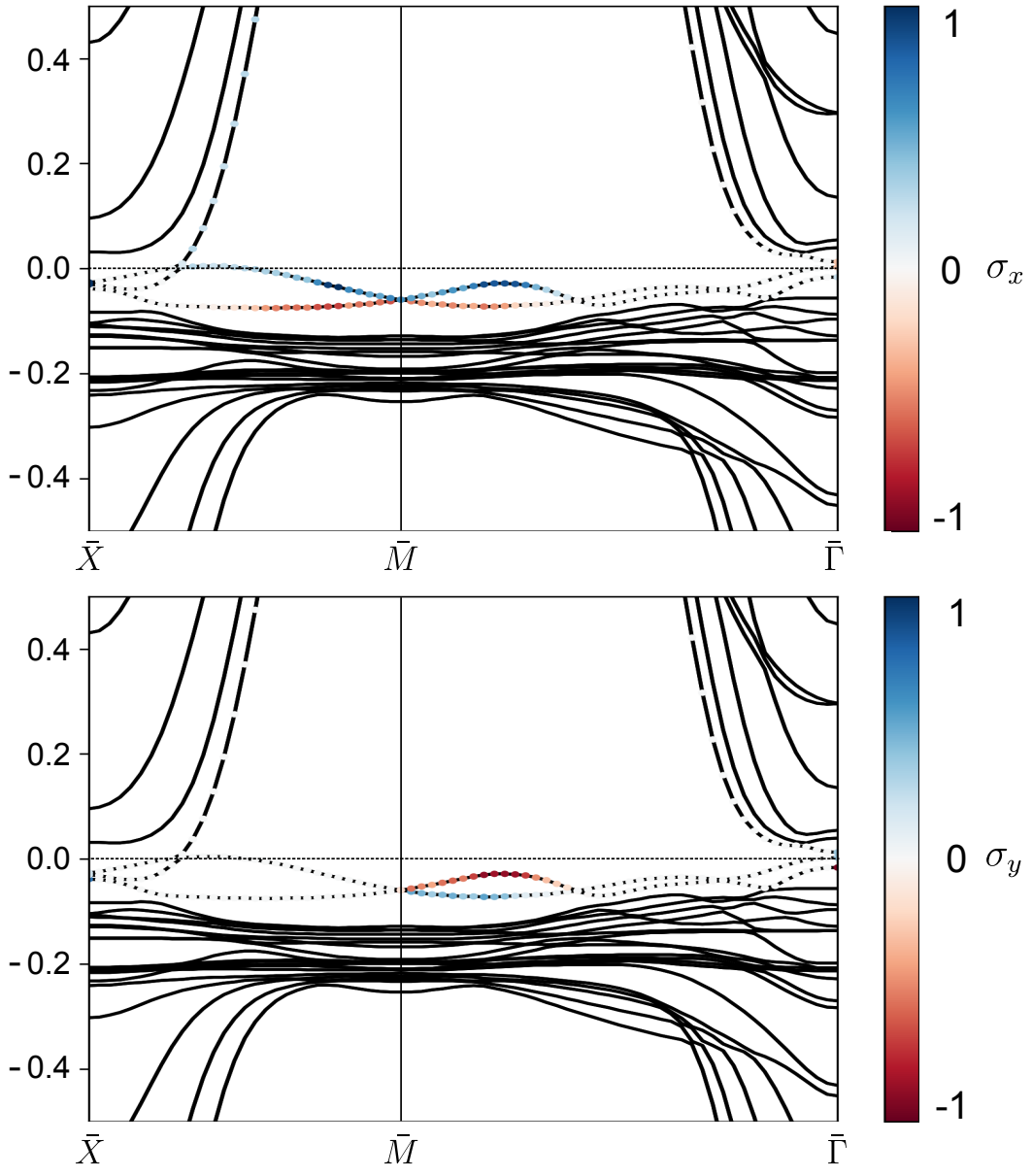

Figure 5.25: The 6 layer unrelaxed surface bands, with projections onto the anomalous $\bar{M}$ point bands and the band featuring the $\bar{X}$ point Dirac cone, in agreement with Kim et al (figure 5.23(g)). The spin projection is omitted for the other bands to remove visual clutter.

5.6 Surface reconstruction

The above concludes the main discussion of the comparison between the electrostatically perturbed DFT models and tight binding models, but the tight binding models are also useful to efficiently study some other effects that have been discussed in experiments. In particular, in response to the STM data, which measure very locally and so are sensitive to local changes in symmetry, it is also worthwhile discussing the possibility of surface reconstruction. Matt et al [65] postulate that the electrostatics of the Sm 1x1 termination leads to the buried Dirac cone by doping the surface with excess charge and that the 2x1 reconstruction commonly seen in STM over small regions experiences this less, accounting for the difference in measured Fermi velocity between STM and ARPES and the inferred STM spectral density. Consistent with this conclusion, I have shown in 5.4.1 that surface effects may change the position of the Dirac cone and can modify the Fermi velocity with the dominant contribution to this effect being from considering surface relaxation. However, I have already shown above that the buried Dirac cone is visible in tight binding, which has no knowledge of the electrostatic repulsion leading to band bending, which indicates that from the perspective of my model the surface band bending is *not* the cause of this phenomenon. It is plausible that other doping effects not captured by semi-local DFT are the cause of the observed features.

Some of these authors use DFT surface calculations to estimate the difference in surface energy and hence the relative stability of the 1x1 and 2x1 terminations. However, as the Sm 1x1 termination is nonstoichiometric, it is difficult to make conclusive statements about the ab initio thermodynamics without an estimate for the chemical potential of each species [145]. In SmB_6 this is a particularly onerous exercise, as the unit cell for Boron's most stable elemental form has 108 atoms per unit cell and a complex icosahedral structure. Instead, I shall take it as an experimental fact that a Sm 2x1 termination exists and is at least metastable. I shall

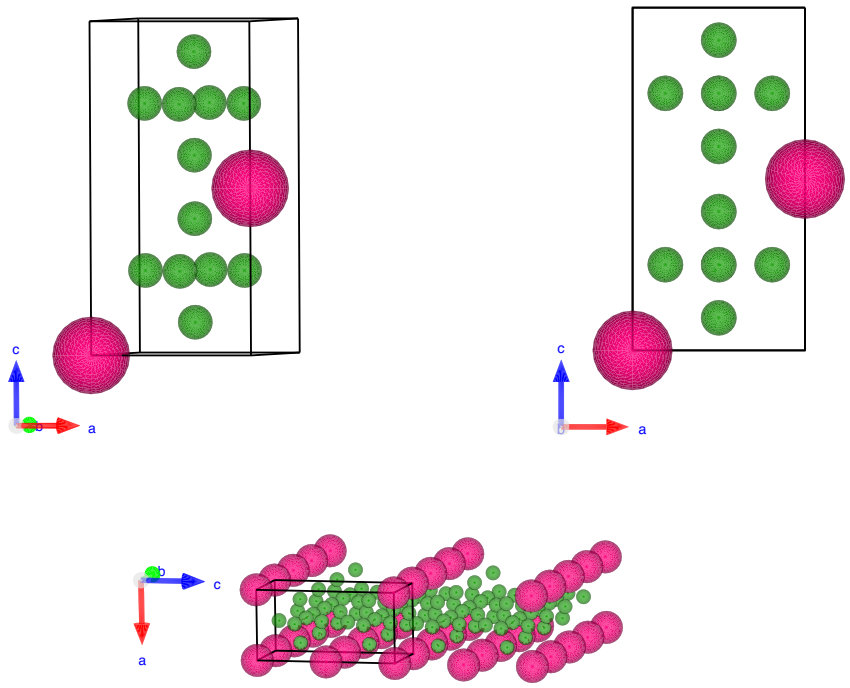

Figure 5.26: The modified primitive unit cell used to construct the Sm 2x1 surface reconstruction. The bulk structure is preserved, but the (stoichiometric) 2x1 surface termination is also produced.

demonstrate here that some general features of the Sm 2x1 reconstruction may be studied using minimal modifications to the tight binding slab approaches, in the hope that this might make clear which features can be explained without band bending.

In figure 5.26 I show a supercell structure that reproduces the correct bulk structure but can also reproduce the surface reconstruction when formed into a slab. By performing 40 layer tight binding slab calculations on this I obtain the folded band structure of the reconstructed surface; the 'doubled' Dirac cone at the surface is visible around $\bar{\Gamma}$, caused by the folding of one of the $\bar{X}$ point cones onto the supercell $\bar{\Gamma}$ point (figure 5.27).

Looking at a constant energy slice of this we gain some further insight into the interplay between electrostatic perturbation and the surface states. Hlawenka et al

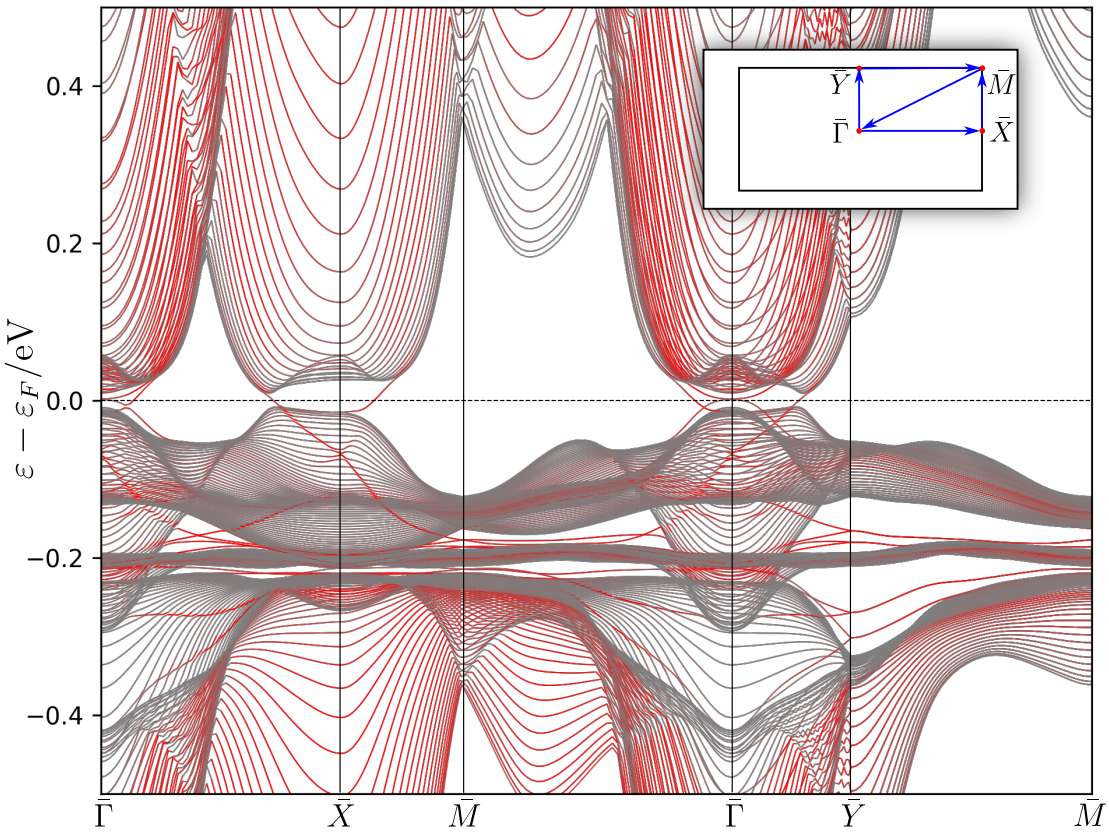

Figure 5.27: The band structure of a 40 unit cell thickness slab with 2x1 surface reconstruction, as described in the main text. The same qualitative features are visible, with the Dirac cone along the k_y direction folded onto $\bar{\Gamma}$. The $\bar{X}$ cone is positioned identically with respect to the Fermi level as in the 1x1 terminated model. Inset is the surface Brillouin zone showing the modified k-path for the new folded Brillouin zone.

[146] noted that the double cone structure of the umklapp of the $\bar{X}$ cone onto $\bar{\Gamma}$ under reconstruction looks very similar to the structure seen under Rashba splitting [142], not a topological surface state. This criticism is not totally ruled out by the data, given the generally mediocre energy resolution in SmB_6 ARPES studies. Hlawenka also attributes the $\bar{\Gamma}$ pocket as being parabolic; in my theoretical data this Dirac cone does indeed look fairly parabolic until extremely close to the Dirac point, as seen for example in figures 5.7 and 5.28. Hlawenka's conclusions are partially contradicted by the spin-ARPES data [123], and I would like to point out another related phenomenon in figure 5.29. The fact that the $\bar{\Gamma}$ point Dirac point lies so close

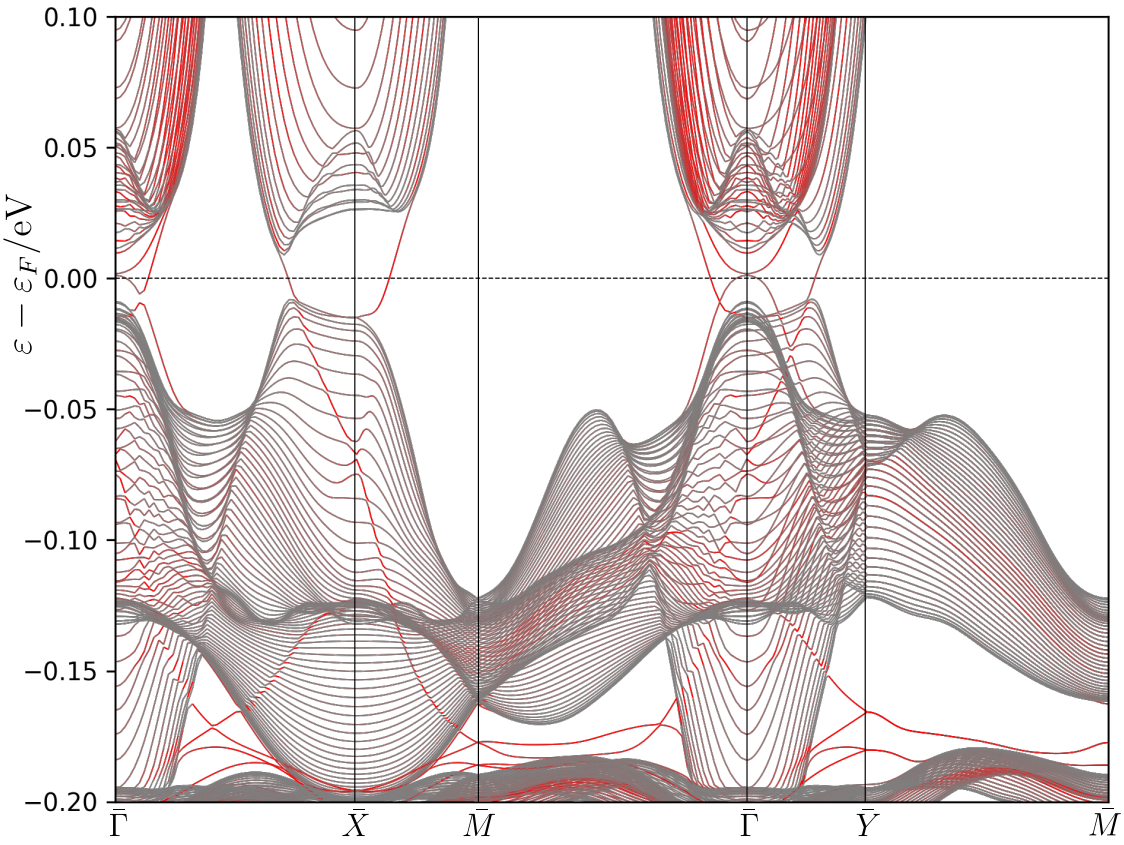

Figure 5.28: The band structure of a 40 unit cell thickness slab with 2x1 surface reconstruction, zoomed in to the region in energy around the Fermi level.

to the Fermi level means that the observed spin texture depends strongly on the local electrostatics. Doping the surface by just 5 meV, the Dirac cone at $\bar{\Gamma}$ changes spin texture, giving two counter-propagating helical states. Given that the STM data and my computational results imply a renormalisation at the surface of order 10s of meV and considering the role local impurity potentials may play, this demonstrates that it is difficult to make any sort of definitive judgement about the SmB_6 ground state even from an ARPES measurement with perfect access to the spin texture.

Because these calculations take place entirely within tight binding, they cannot include the surface electrostatic effects. It would be natural to perform similar DFT calculations on a 2x1 terminated slab. However, these calculations are extremely intensive so have not been performed at present.

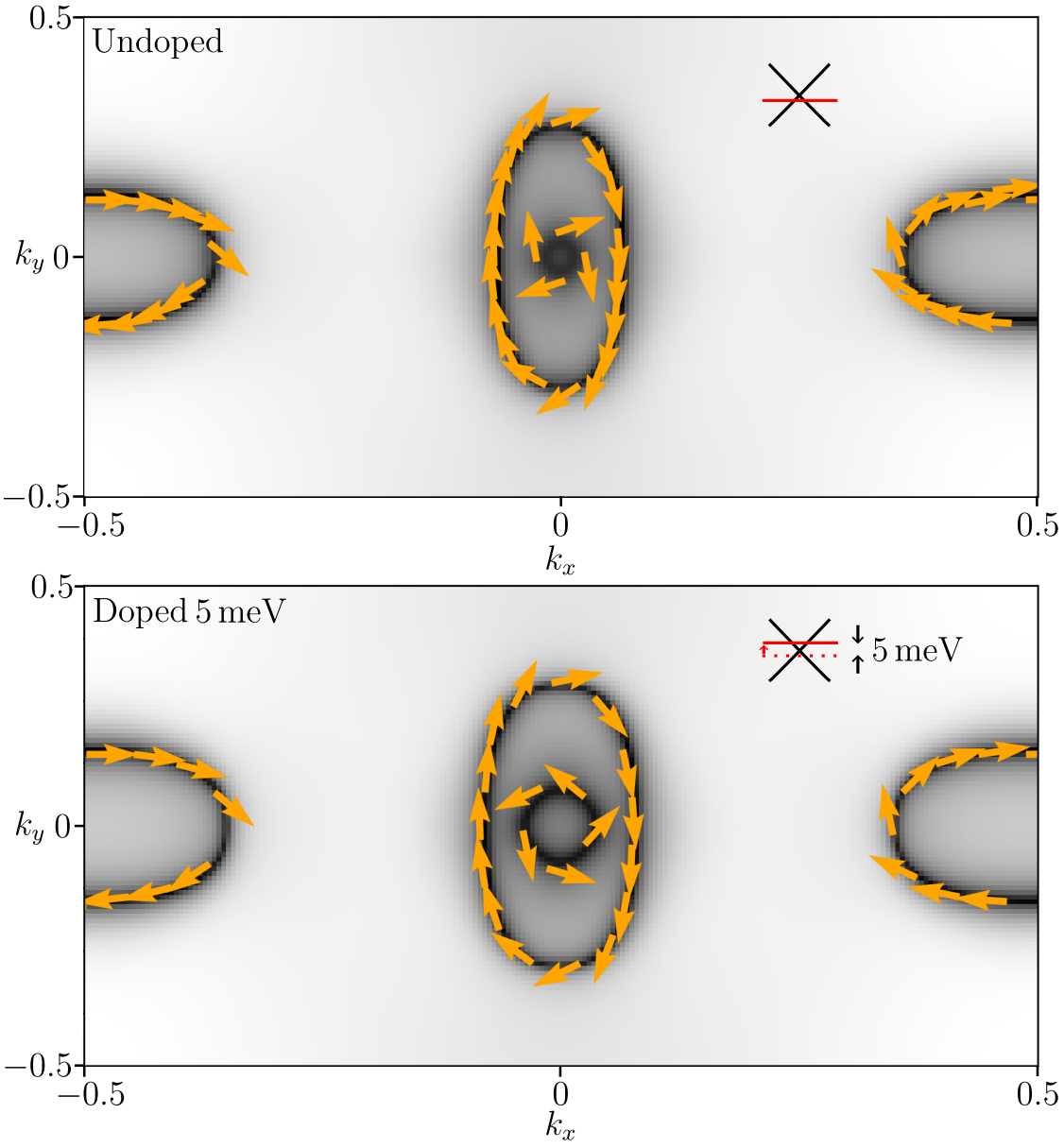

Figure 5.29: Topological insulating behaviour under reconstruction, resembling Rashba effect. After doping the surface by 5 meV, the $\bar{\Gamma}$ point Dirac cone switches spin texture, leading to two counter-propagating helices around the high symmetry point. Given the apparent role that the termination driven surface doping plays, it is important that care is taken when ascribing the causes of features in observed spectra

5.7 Future outlooks

The above study shows a preliminary set of DFT and TB analyses of the $SmB6_6$ electronic structure with an emphasis on understanding local electrostatics. There is a qualitative and partly quantitative agreement with experiment but there are nonetheless several further possible modifications related to the way in which electronic correlations are treated. Semi-local DFT relies on using given exchange-correlation functionals to model the interactions between electrons, so it is possible that the results of my calculations are not truly descriptive of the real interacting ground state, even if features of the experiments are reproduced. Furthermore, I have used a Hubbard U interaction to qualitatively handle the f electron's mutual interaction, but this is a phenomenological mean field that may carry systematic errors that more detailed treatments may not. These factors mean it is difficult to be sure of the degree to which serendipitous error cancellation is responsible for this agreement. I have already described how other authors have found [118] that a Gutzwiller projection [134] can improve upon the bulk DFT results at the expense of not capturing the quantitative features at the surface. Given this, it is important to ask what other methods could be applied in order to incorporate the electron-electron interactions? Are there post-DFT methods that can reproduce the surface Fermi velocity and carrier density with greater accuracy? I describe here three possibilities for future investigation.

The first approach is to mix a fraction of the exact exchange operator into the exchange-correlation functional, known as hybrid functionals [147]. It is observed that band gaps calculated using this approach are in significantly closer agreement to experiment. Given that the Fermi velocity and carrier density of the surface states depends very strongly on the exact positions of the d/f band edges, these methods could well bring the calculated velocity closer to the experimental value. It would be possible in principle to apply these methods to SmB_6. Individual

DFT codes typically place specific requirements on the types of pseudopotentials that may be used to perform hybrid functional calculations; `QuantumESPRESSO` requires norm-conserving pseudopotentials. The only readily available relativistic pseudopotentials for samarium are from `pslibrary`, which are PAW and currently incompatible with hybrid functionals in the `QuantumESPRESSO` implementation of DFT. By generating a pseudopotential for samarium that is compatible with hybrid functional calculations this could be investigated. Alternatively, this could be done in a different DFT suite such as VASP or Wien2k, which have different requirements.

The second possibility is to incorporate some features of the exact electron-electron interaction within the *GW* approximation [148]. Recently, this methodology has been applied to Bismuth based topological insulators and achieved much closer agreement to experiment as compared to DFT [102] [103]. It would be instructive to apply these methods to SmB_6 in order to have a measure of the effects of the interactions, particularly given the large strength of interactions typical to d/f electron systems. These methods should not be expected to exactly reproduce the highly correlated ground state of SmB_6; the driving physics is Kondo coupling which flows to strong coupling under RG and features logarithmic vertex corrections [149], whereas *GW* neglects vertex corrections by design. However, we have already seen how GGA+U calculations can replicate many of the pertinent features of this complex system so SmB_6 appears to behave extremely similarly to the conventional model of a weakly coupled topological insulator. Incorporating more interaction effects allows us to strictly delineate between features that can be explained by mean field and perturbative methods from those that are exclusively the result of strong correlations. Using *GW* also places requirements on the type of pseudopotential, and there are no implemented codes that can perform *GW* calculations with the pseudopotentials I have used. This again motivates developing norm-conserving pseudopotentials for samarium compatible with these many body techniques.

I could also follow the treatment of Kim et al [140] in using DMFT, which is

frequently used to solve correlated f electron problems. However, DMFT represents a significant computational task and the methodologies are far less established than GW or hybrid functionals. Indeed, as we have seen in section 5.5, the DMFT results do not agree with experiment, estimating the bandgap to be an order of magnitude too small.

A further motivation for adding more complex interactions into the bulk is to gain further clarity over the energetic landscape which governs it. As briefly mentioned in section 4.4.1, there are several exotic explanations for the quantum oscillation data [131] [132]. Having a greater degree of certainty over the bulk interactions could provide information on the sorts of instabilities the system may be susceptible to, guiding further theoretical searches.

5.8 Conclusion

Through this chapter I have presented a systematically motivated model for the samarium hexaboride [100] surface, with an emphasis on comparison to experiment and incorporating as many local electrostatic effects as possible. I have presented data on the bulk system, tight binding slabs, DFT unrelaxed slabs, DFT relaxed slabs and a reconstructed tight binding slab, attempting to clarify the roles of various system properties to reconcile the conclusions of other authors. I find that the Dirac physics is robust to all these perturbations as expected, with energetic renormalisations of order 10 meV. By doing so I reach results for the Fermi surface and electron velocities that match up favourably with the ARPES experimental data, although there are some band renormalisations that are not observed in experiment and some features inconsistent with other computational studies, which warrant further systematic investigation. The carrier density is predicted with the correct order of magnitude, but is too small by a factor order unity. These results are obtained entirely using GGA+U (and related tight binding models),

which is notable as the bulk coupling between the d and f electrons SmB_6 is strong (in the renormalisation group sense). These results may be of interest to others attempting to model the strong correlation effects in this material, particularly because some of the features reproduced in this DFT model have previously been ascribed to being hallmarks of strong coupling.

References

[58] Liang Fu and C. L. Kane. "Topological insulators with inversion symmetry". In: *Phys. Rev. B* 76 (4 July 2007), p. 045302. URL: https://link.aps.org/doi/10.1103/PhysRevB.76.045302.

[64] Moon-Sun Nam et al. "How to probe the spin contribution to momentum relaxation in topological insulators". In: *Nature Communications* 9.1 (2018), p. 56.

[65] Christian E. Matt et al. "Consistency between ARPES and STM measurements on SmB_6". In: *Phys. Rev. B* 101 (8 Feb. 2020), p. 085142. URL: https://link.aps.org/doi/10.1103/PhysRevB.101.085142.

[76] Liang Fu, C. L. Kane, and E. J. Mele. "Topological Insulators in Three Dimensions". In: *Phys. Rev. Lett.* 98 (10 Mar. 2007), p. 106803. URL: https://link.aps.org/doi/10.1103/PhysRevLett.98.106803.

[83] Robert G Parr. "Density functional theory of atoms and molecules". In: *Horizons of Quantum Chemistry: Proceedings of the Third International Congress of Quantum Chemistry Held at Kyoto, Japan, October 29-November 3, 1979*. Springer. 1980, pp. 5–15.

[95] John P. Perdew et al. "Restoring the Density-Gradient Expansion for Exchange in Solids and Surfaces". In: *Phys. Rev. Lett.* 100 (13 Apr. 2008), p. 136406. URL: https://link.aps.org/doi/10.1103/PhysRevLett.100.136406.

[102] Irene Aguilera, Christoph Friedrich, Gustav Bihlmayer, and Stefan Blügel. "GW study of topological insulators Bi_2Se3, Bi_2Te_3, and Sb_2Te_3: Beyond the perturbative one-shot approach". In: *Phys. Rev. B* 88.4 (2013), p. 045206.

[103] Irene Aguilera, Christoph Friedrich, and Stefan Blügel. "Many-body corrected tight-binding Hamiltonians for an accurate quasiparticle description of topological insulators of the Bi_2Se_3 family". In: *Phys. Rev. B* 100.15 (2019), p. 155147.

[104] Giovanni Pizzi et al. "Wannier90 as a community code: new features and applications". In: *Journal of Physics: Condensed Matter* 32.16 (2020), p. 165902.

[106] Dominik Gresch et al. "Automated construction of symmetrized Wannier-like tight-binding models from ab initio calculations". In: *Physical Review Materials* 2.10 (2018), p. 103805.

[108] QuanSheng Wu et al. "WannierTools : An open-source software package for novel topological materials". In: *Computer Physics Communications* 224 (2018), pp. 405–416. URL: http://www.sciencedirect.com/science/article/pii/S0010465517303442.

[111] Shiro Funahashi, Kiyoaki Tanaka, and Fumitoshi Iga. "X-ray atomic orbital analysis of 4f and 5d electron configuration of SmB_6 at 100, 165, 230 and 298 K". In: *Acta Crystallographica Section B: Structural Science* 66.3 (2010), pp. 292–306.

[114] Maxim Dzero, Kai Sun, Victor Galitski, and Piers Coleman. "Topological Kondo Insulators". In: *Phys. Rev. Lett.* 104 (10 Mar. 2010), p. 106408. URL: https://link.aps.org/doi/10.1103/PhysRevLett.104.106408.

[115] Tetsuya Takimoto. "SmB_6: A promising candidate for a topological insulator". In: *Journal of the Physical Society of Japan* 80.12 (2011), p. 123710.

[116] Chang-Jong Kang et al. "Band Symmetries of Mixed-Valence Topological Insulator: SmB_6". In: *Journal of the Physical Society of Japan* 84.2 (2015), p. 024722.

[118] Feng Lu et al. “Correlated Topological Insulators with Mixed Valence”. en. In: *Phys. Rev. Lett.* 110.9 (Feb. 2013), p. 096401. URL: https://link.aps.org/doi/10.1103/PhysRevLett.110.096401 (visited on 05/18/2020).

[121] Juan Jiang et al. “Observation of possible topological in-gap surface states in the Kondo insulator SmB_6 by photoemission”. In: *Nature Communications* 4.1 (2013), p. 3010.

[122] Madhab Neupane et al. “Surface electronic structure of the topological Kondo-insulator candidate correlated electron system SmB_6”. In: *Nature Communications* 4.1 (2013), p. 2991.

[123] Nan Xu et al. “Direct observation of the spin texture in SmB_6 as evidence of the topological Kondo insulator”. In: *Nature Communications* 5.1 (2014), p. 4566.

[126] Michael M Yee et al. “Imaging the Kondo insulating gap on SmB_6”. In: *arXiv preprint arXiv:1308.1085* (2013).

[128] Zhen Zhang and John T. Yates Jr. “Band Bending in Semiconductors: Chemical and Physical Consequences at Surfaces and Interfaces”. In: *Chemical Reviews* 112.10 (2012). PMID: 22783915, pp. 5520–5551. URL: https://doi.org/10.1021/cr3000626.

[131] Debanjan Chowdhury, Inti Sodemann, and T Senthil. “Mixed-valence insulators with neutral Fermi surfaces”. In: *Nature Communications* 9.1 (2018), p. 1766.

[132] Inti Sodemann, Debanjan Chowdhury, and T. Senthil. “Quantum oscillations in insulators with neutral Fermi surfaces”. In: *Phys. Rev. B* 97 (4 Jan. 2018), p. 045152. URL: https://link.aps.org/doi/10.1103/PhysRevB.97.045152.

[133] Wolfgang Schmickler. “The potential of zero charge of jellium”. In: *Chemical Physics Letters* 99.2 (1983), pp. 135–139. URL: https://www.sciencedirect.com/science/article/pii/0009261483805454.

[134] Martin C. Gutzwiller. "Effect of Correlation on the Ferromagnetism of Transition Metals". In: *Phys. Rev. Lett.* 10 (5 Mar. 1963), pp. 159–162. URL: https://link.aps.org/doi/10.1103/PhysRevLett.10.159.

[135] Victor Alexandrov, Maxim Dzero, and Piers Coleman. "Cubic Topological Kondo Insulators". In: *Phys. Rev. Lett.* 111 (22 Nov. 2013), p. 226403. URL: https://link.aps.org/doi/10.1103/PhysRevLett.111.226403.

[136] Victor Alexandrov, Piers Coleman, and Onur Erten. "Kondo Breakdown in Topological Kondo Insulators". In: *Phys. Rev. Lett.* 114 (17 Apr. 2015), p. 177202. URL: https://link.aps.org/doi/10.1103/PhysRevLett.114.177202.

[137] J. M. Luttinger. "Fermi Surface and Some Simple Equilibrium Properties of a System of Interacting Fermions". In: *Phys. Rev.* 119 (4 Aug. 1960), pp. 1153–1163. URL: https://link.aps.org/doi/10.1103/PhysRev.119.1153.

[138] G. Binnig, H. Rohrer, Ch. Gerber, and E. Weibel. "7 × 7 Reconstruction on Si(111) Resolved in Real Space". In: *Phys. Rev. Lett.* 50 (2 Jan. 1983), pp. 120–123. URL: https://link.aps.org/doi/10.1103/PhysRevLett.50.120.

[139] Lennart Bengtsson. "Dipole correction for surface supercell calculations". In: *Phys. Rev. B* 59 (19 May 1999), pp. 12301–12304. URL: https://link.aps.org/doi/10.1103/PhysRevB.59.12301.

[140] Junwon Kim et al. "Termination-dependent surface in-gap states in a potential mixed-valent topological insulator: SmB_6". In: *Phys. Rev. B* 90 (7 Aug. 2014), p. 075131. URL: https://link.aps.org/doi/10.1103/PhysRevB.90.075131.

[141] Z.-H. Zhu et al. "Polarity-Driven Surface Metallicity in SmB_6". In: *Phys. Rev. Lett.* 111 (21 Nov. 2013), p. 216402. URL: https://link.aps.org/doi/10.1103/PhysRevLett.111.216402.

[142] Yua A Bychkov and É I Rashba. "Properties of a 2D electron gas with lifted spectral degeneracy". In: *JETP lett* 39.2 (1984), p. 78.

[143] Jin-Jian Zhou et al. “Engineering topological surface states and giant Rashba spin splitting in BiTeI/Bi_2Te_3 heterostructures”. In: *Scientific reports* 4.1 (2014), p. 3841.

[144] M. Aono et al. “LaB_6 and SmB_6 (001) surfaces studied by angle-resolved XPS, LEED and ISS”. In: *Surface Science* 86 (1979). Proceedings of the International Conference on Solid Films and Surfaces Tokyo, Japan, 5-8 July 1978, pp. 631–637. URL: https://www.sciencedirect.com/science/article/pii/0039602879904436.

[145] Karsten Reuter and Matthias Scheffler. “Composition, structure, and stability of RuO_2 (110) as a function of oxygen pressure”. In: *Phys. Rev. B* 65.3 (2001), p. 035406.

[146] Peter Hlawenka et al. “Samarium hexaboride is a trivial surface conductor”. In: *Nature Communications* 9.1 (2018), p. 517.

[147] Axel D. Becke. “A new mixing of Hartree–Fock and local density-functional theories”. In: *The Journal of Chemical Physics* 98.2 (Jan. 1993), pp. 1372–1377. eprint: https://pubs.aip.org/aip/jcp/article-pdf/98/2/1372/11046762/1372_1_online.pdf. URL: https://doi.org/10.1063/1.464304.

[148] Mark S. Hybertsen and Steven G. Louie. “Electron correlation in semiconductors and insulators: Band gaps and quasiparticle energies”. In: *Phys. Rev. B* 34 (8 Oct. 1986), pp. 5390–5413. URL: https://link.aps.org/doi/10.1103/PhysRevB.34.5390.

[149] Piers Coleman. *Introduction to many-body physics*. Cambridge University Press, 2015.

Appendices

A

Molecular wires for local gating

In chapter 2 I demonstrated through electromagnetics simulations that the screening effect of the spherical nanobeads prevents the use of a back gate to modify the local electric potential of a device. This means that gating is not possible with the two terminal design. From the discussions in chapter 2.4 it is clear that any gate must have an extremely close approach to the molecule at the centre of the device. This constraint implies that a device with gate must be a true three terminal device featuring multiple functional components, using components such as molecular wires to perform the gating. What might the performance and behaviour of such a system be? In this appendix I will give a theoretical description of the use of such a molecular wire with Coulomb interactions to apply a capacitive gate.

A.1 The molecular gating system

Consider a modification of the original dimer structure (figure A.1) to have a third terminal, with an extra molecule extending towards the centre. I will consider the molecule to have a wire-like delocalised region A and an electron accepting region B at the end. The exact properties of the molecule are not terribly important as the methods and principles here should hold in reasonable generality. I allow for inter and intra-site Hubbard like electron-electron repulsion on the molecule. The Hamiltonian of this system is

$$\begin{aligned}\mathcal{H} = &\underbrace{\sum_{\sigma}\left[\varepsilon_A a_\sigma^\dagger a_\sigma + \varepsilon_B b_\sigma^\dagger b + \sigma + t(a_\sigma^\dagger b_\sigma + b_\sigma^\dagger a_\sigma)\right]}_{\text{Molecular energy levels}} + \\ &\underbrace{U_A n_{A\uparrow} n_{A\downarrow} + U_B n_{B\uparrow} n_{B\downarrow} + \sum_{\sigma\sigma'} V_{AB} n_{A\sigma} n_{B\sigma}}_{\text{Coulomb repulsion}} + \\ &\underbrace{\sum_{k\sigma} c_{k\sigma}^\dagger c_{k\sigma} + \sum_{\sigma}\gamma(c_{0\sigma}^\dagger a_\sigma + a_{0\sigma}^\dagger c_{0\sigma})}_{\text{Lead and lead coupling}}\end{aligned} \quad \text{(A.1)}$$

Where $a_\sigma^\dagger$, $b_\sigma^\dagger$ are creation operators for the molecular sites A and B, and the creation operators for states in the lead are well approximated by delocalised states $c_{k\sigma}^\dagger$. I model the lead as a 1D chain and take the coupling to be to the terminating atom of the chain $c_{0\sigma}^\dagger$. This is not physical but is not important, as I will later take a Wide Band Limit in order to ignore the microscopic details of the leads. The geometry is depicted in figure A.1, with the above Hamiltonian applying only to the Gate electrode and gating molecule. If applying a voltage at G shunts electrons onto the molecule then the molecule can function as a capacitively coupled gate. Compare:

$$\begin{aligned} Q &= CV \\ e\langle n\rangle &= \int \mathrm{d}E f(E+\mu+eV)\Im[G_B] \end{aligned} \quad \text{(A.2)}$$

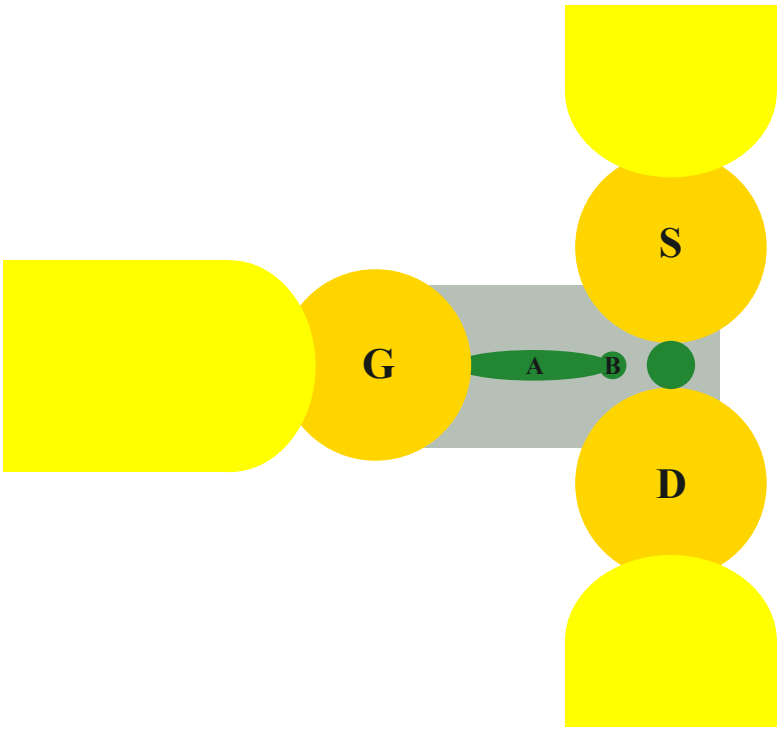

Figure A.1: A layout for using a molecular wire to locally modify the electrostatic potential on the molecule. The problems of 2.4 are solved by using a wire to achieve a much closer approach to the central molecular region. The two molecular sites A and B are labelled.

so that the spectral function $\Im[G]$[1] plays the role of a differential capacitance $\frac{\partial Q}{\partial V}$.

[1]Here, $\Im$ denotes the imaginary part.

A.2 Green function equation of motion techniques

I will analyse the above Hamiltonian using the Green function equation of motion technique. By combining the Heisenberg equation with the definition of the retarded Green function, a general method for solving interacting quantum problems is reached at the expense of introducing an uncontrolled approximation for the correlations. The Green function is defined in the time domain by

$$G^R(t) = -i\theta(t)\langle\{c(t), c^\dagger(0)\}\rangle \tag{A.3}$$

and in the Heisenberg picture the time dependence of any operator is given by

$$-i\frac{d}{dt}A = [\mathcal{H}, A]. \tag{A.4}$$

Consider now the Hamiltonian for a free particle $\mathcal{H} = \sum_k \epsilon_k c_k^\dagger c_k$. In the energy domain, the equation of motion for the Green function $G_k = -i\theta(t)\langle\{c_k(t), c_k^\dagger(0)\}\rangle$ is

$$\omega G_k = 1 - i\langle\{[\mathcal{H}, c_k], c_k^\dagger\}\rangle. \tag{A.5}$$

Applying fermionic commutation relations, the commutator yields $[\mathcal{H}, c_k] = \epsilon_k c_k$ and equation A.5 becomes

$$\omega G_k = 1 - i\varepsilon_k\langle\{c_k, c_k^\dagger\}\rangle = 1 + \varepsilon_k G_k \tag{A.6}$$

and therefore the free Green function is

$$G_k = \frac{1}{\omega - \epsilon_k} \tag{A.7}$$

as expected[2].

A.2.1 Higher order Green functions

The above method can be applied to more complex Hamiltonians. Consider the low energy effective Hamiltonian of a molecule (or equivalently a quantum dot) in second quantisation with a Hubbard interaction,

$$\mathcal{H} = \sum_{\sigma} \varepsilon_\sigma c_\sigma^\dagger c_\sigma + U n_\uparrow n_\downarrow \,. \tag{A.8}$$

The equation of motion technique applied to this Hamiltonian gives

$$\omega G_\sigma = 1 + \varepsilon_\sigma G_\sigma + U\langle\langle [n_\uparrow n_\downarrow, c_\sigma], c_\sigma^\dagger \rangle\rangle \tag{A.9}$$

$$= 1 + \varepsilon_\sigma G_\sigma + U\langle\langle n_{\bar\sigma} c_\sigma, c_\sigma^\dagger \rangle\rangle \tag{A.10}$$

where I have adopted the shorthand $\langle\langle \cdot, \cdot \rangle\rangle = -i\langle\{\cdot, \cdot\}\rangle$. Notice the appearance of a higher order Green function $\langle\langle n_{\bar\sigma} c_\sigma, c_\sigma^\dagger \rangle\rangle$ as a consequence of the interaction term. In more complex scenarios, finding the equation of motion of this Green function will in turn generate an even higher order Green function: the equation of motion of any n-point function will in general involve an $(n+1)$-point function. This is an example of the Kubo-Martin-Schwinger hierarchy [41], itself the quantum analog of the BBKGY hierarchy [150] in nonequilibrium statistical mechanics, where the equation of motion for the n particle distribution function is expressed in terms of the $n+1$ particle distribution function. On this occasion, by proceeding further a closure of the system of equations is reached. In the general case a choice of decoupling has to be made, whereby the high order Green functions are approximated in terms

[2] All frequencies in this appendix should be considered to have an infinitesimal positive imaginary component $\omega \to \omega + i\eta$ to guarantee the correct convergence and causality.

of lower order Green functions. The equation of motion for $\langle\langle n_{\bar{\sigma}} c_\sigma, c_\sigma^\dagger \rangle\rangle$ is

$$(\omega - \varepsilon - U)\langle\langle n_{\bar{\sigma}} c_\sigma, c_\sigma^\dagger \rangle\rangle = \langle n_{\bar{\sigma}} \rangle. \tag{A.11}$$

Substituting this into A.9 yields

$$G_\sigma = \frac{\omega - \varepsilon + U(\langle n_{\bar{\sigma}} \rangle - 1)}{(\omega - \varepsilon)(\omega - \varepsilon - U)} \tag{A.12}$$

which yields a density of states peaked at ε and $\varepsilon + U$, correct for a single level with Hubbard interaction [151].

A.3 Applying equation of motion techniques to capacitive gating

These techniques can be applied to study the behaviour of a molecular wire under bias. Using the Hamiltonian of the molecular wire described earlier, I have applied the equation of motion technique. The calculation is lengthy but follows the same basic procedure as the result, so I quote the result only. I have made decouplings of the type

$$\langle\langle c_{k\bar{\sigma}}^\dagger a_{\bar{\sigma}} c_{k'\sigma}, a_\sigma^\dagger \rangle\rangle \approx 0 \tag{A.13}$$

in order to close the system of equations. These are equivalent to ignoring superexchange between the leads and the molecule; this can be interpreted as ignoring Kondo resonances [152]. I have also taken the wide band limit, explained in B.2 to replace all details of the coupling to the leads with just a broadening Γ. The calculation is virtually identical to one performed in reference [153], which studied the current through a similar system connected to two leads. Setting the

coupling to the second lead in that work to zero and adopting the Wide Band Limit Approximation to ignore the band structure of the leads [41] the equations I have derived are recovered[3]. The Green functions of sites A and B are

$$\begin{aligned} G_A &= \left[g_A^{-1} - t^2 g_B^{-1}\right]^{-1} \\ G_B &= \left[g_B^{-1} - t^2 (g_A^{-1} + i\Gamma)\right]^{-1} \end{aligned} \tag{A.14}$$

where

$$g_B = g_B^{(0)} + \frac{V_{AB}}{\omega - \varepsilon_B}\left(g_B^{(1)} + g_B^{(2)} + \frac{U_B}{\omega - \varepsilon_B - U_B} g_B^{(3)}\right) \tag{A.15}$$

and

$$\begin{aligned} g_{B\sigma}^{(0)} =& \frac{1 - \langle n_{B\bar{\sigma}}\rangle}{\omega - \varepsilon_B} + \frac{\langle n_{B\bar{\sigma}}\rangle}{\omega - \varepsilon_B - U_B} \ , \\ g_{B\sigma}^{(1)} =& \frac{\left(1 - \langle n_{B\bar{\sigma}}\rangle\right)\langle n_{A\sigma}\rangle}{\omega - \varepsilon_B - V_{AB}\left(1 + \langle n_{A\bar{\sigma}}\rangle\right)} \\ &+ \frac{\langle n_{B\bar{\sigma}}\rangle\langle n_{A\sigma}\rangle}{\omega - \varepsilon_B - U_B - V_{AB}\left(1 + \langle n_{A\bar{\sigma}}\rangle\right)} \ , \\ g_{B\sigma}^{(2)} =& \frac{\left(1 - \langle n_{B\bar{\sigma}}\rangle\right)\langle n_{A\bar{\sigma}}\rangle}{\omega - \varepsilon_B - V_{AB}\left(1 + \langle n_{A\sigma}\rangle\right)} \\ &+ \frac{\langle n_{B\bar{\sigma}}\rangle\langle n_{A\bar{\sigma}}\rangle}{\omega - \varepsilon_B - U_B - V_{AB}\left(1 + \langle n_{A\sigma}\rangle\right)} \ , \\ g_{B\sigma}^{(3)} =& \frac{\langle n_{B\bar{\sigma}}\rangle\langle n_{A\sigma}\rangle}{\omega - \varepsilon_B - U_B - V_{AB}\left(1 + \langle n_{A\bar{\sigma}}\rangle\right)} \\ &+ \frac{\langle n_{B\bar{\sigma}}\rangle\langle n_{A\bar{\sigma}}\rangle}{\omega - \varepsilon_B - U_B - V_{AB}\left(1 + \langle n_{A\sigma}\rangle\right)} \ . \end{aligned} \tag{A.16}$$

Where Γ is the rate at which electrons tunnel onto the molecule and identical equations hold for g_A with $A \longleftrightarrow B$. These define self consistent equations for the occupation of the B site in response to an applied voltage. Consider the nonmagnetic case, where $\langle n_\uparrow\rangle = \langle n_\downarrow\rangle = \langle n\rangle/2$. Then, the occupation is given by

$$\langle n_B\rangle = \int \mathrm{d}E f(E + \mu + eV)\Im\left[G_B(\langle n_B\rangle)\right] \tag{A.17}$$

[3]The specifics of this approximation are explored more in appendix B

where f is the Fermi function and $\Im$ is as usual the imaginary part. The result of solving these self-consistent equations is shown in figure A.2 for a particular set of parameters. This method is fairly numerically unstable and sensitive to the starting guess for the occupations, due to the sharpness of the spectral functions involved. It is also strictly speaking only valid in equilibrium, so relies on the voltage being applied adiabatically slowly. A better methodology would be to use the more complex and robust nonequilbrium Green function method (which could also study the time dependence of such a system) [41] or quantum master equation techniques [154], although this is beyond the scope of this discussion. The system behaves as crudely expected; by applying a voltage the occupation of the molecule can be changed. Therefore, it is in principle possible via this method to place charge close to the molecule being studied. Supposing that a device such as this could be fabricated with a distance between the B site and central molecule of $O(1)$ nanometre, then the gating achievable could be expected to be roughly

$$V_{\text{gate}} = \frac{1}{4\pi\epsilon_0}\frac{e}{r} \approx 0.2V \tag{A.18}$$

which is in principle usable as a gate. This provides a strong motivation to develop DNA origami architectures capable of accommodating a second molecule to function as a local gate.

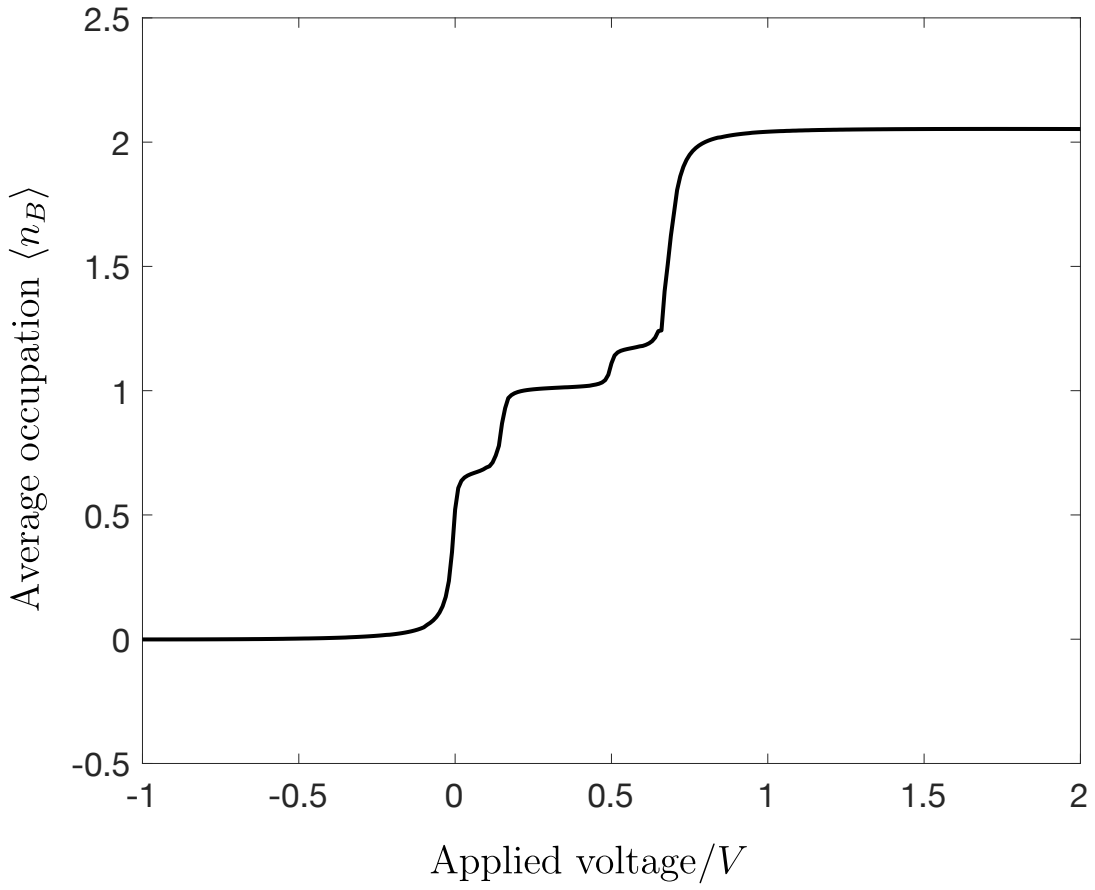

Figure A.2: The average occupation of the molecular wire system in the equation of motion method under an applied voltage for $\varepsilon_A = \varepsilon_B = 0$, $U_A = U_B = 0.5$, $V = 0.1$, $t = -0.2$, $\Gamma = -0.25$. The main plateau at $\langle n_B \rangle = 1$ is caused by the Hubbard U interactions with the subband structure caused by the Hubbard V. The couplings t, Γ broaden the transitions and weakly affect their position.

References

[41] Gianluca Stefanucci and Robert van Leeuwen. *Nonequilibrium Many-Body Theory of Quantum Systems: A Modern Introduction*. eng. New York: Cambridge University Press, 2013.

[150] C. Cercignani, V. I. Gerasimenko, and D. Ya. Petrina. "The BBGKY Hierarchy". In: *Many-Particle Dynamics and Kinetic Equations*. Dordrecht: Springer Netherlands, 1997, pp. 7–65. URL: https://doi.org/10.1007/978-94-011-5558-8_2.

[151] C Lacroix. “Density of states for the Anderson model”. In: *Journal of Physics F: Metal Physics* 11.11 (1981), p. 2389.

[152] Yigal Meir, Ned S. Wingreen, and Patrick A. Lee. “Transport through a strongly interacting electron system: Theory of periodic conductance oscillations”. In: *Phys. Rev. Lett.* 66 (23 1991), pp. 3048–3051. URL: https://link.aps.org/doi/10.1103/PhysRevLett.66.3048.

[153] JQ You and HZ Zheng. “Electron transport through a double-quantum-dot structure with intradot and interdot coulomb interactions”. In: *Phys. Rev. B* 60.19 (1999), p. 13314.

[154] B Novakovic and I Knezevic. “Quantum master equations in electronic transport”. In: *Nano-Electronic Devices: Semiclassical and Quantum Transport Modeling* (2011), pp. 249–287.

B

Models for tunnelling at the nanoscale

In chapter 2 I discussed briefly the models used in chapter 3 to characterise the transport through the nanoscale devices presented. Here I shall go through more detailed derivations of the models used.

B.1 Simmons' model

Under the assumption that the DNA forms a resistive barrier between the leads, the dominant transport mechanism should be quantum tunnelling of electrons from one lead to the other. This assumption is examined experimentally in chapter 3. In Simmons' model, this tunnelling is investigated in terms of the transport through a barrier of variable height $\phi(x)$, depicted in 2.11.

The transport is between a left and right electrode, along the x direction. The insulating nanogap can be modelled as an insulating region, of thickness s and with

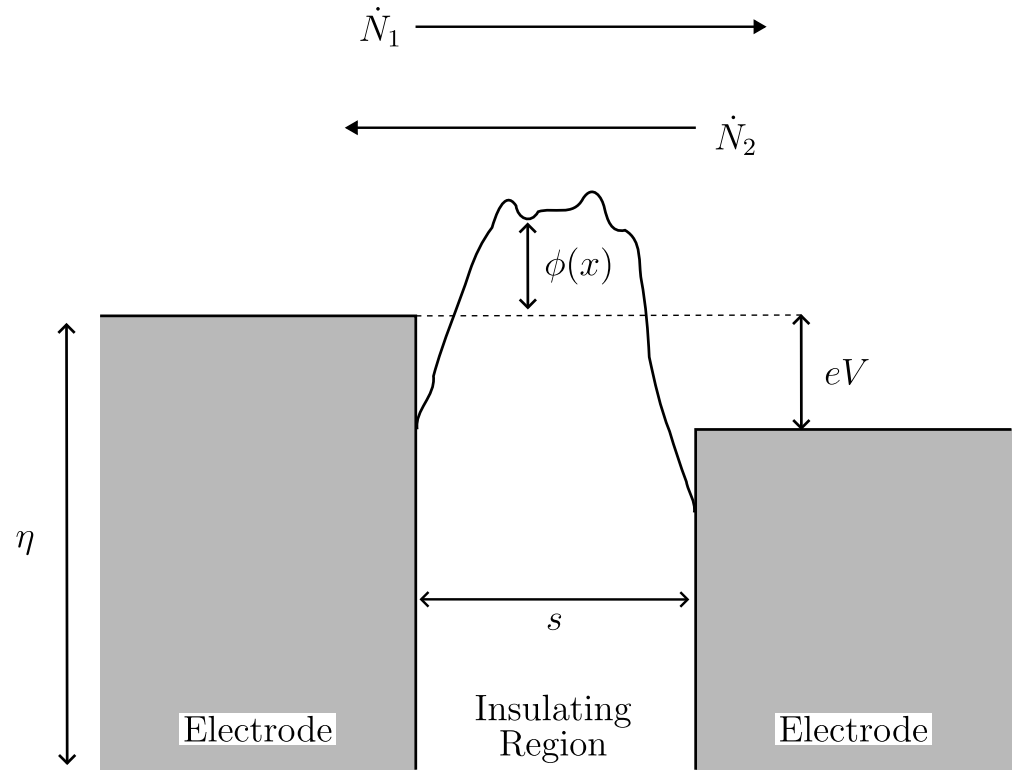

Figure B.1: The geometry for the tunnelling problem. Electrons tunnel between two electrodes, offset from each other by a voltage eV. The tunnelling is through a region of potential $\phi(x)$, thickness s.

potential $\phi(x)$. The probability for an electron incident on the barrier to tunnel through is therefore, in the WKB approximation,

$$D(E_x) = \exp\left[-\frac{2}{\hbar}\int_0^s (2m(\phi(x) - E_x))^{\frac{1}{2}}\,\mathrm{d}x\right], \tag{B.1}$$

where E_x is defined as $p_x^2/2m$, the kinetic energy along x, and the potential $V(x)$ is equal to the lead potentials outside the barrier region. The number of electrons per unit time that tunnel from the left region to the right is then given in terms

of the velocities $v_{x,y,z}$ by

$$\dot{N}_1 = \int_0^{v_m} \mathrm{d}v_x \, v_x n(v_x) D(v_x), \tag{B.2}$$

$$n(v_x) = \frac{2m^4}{(2\pi\hbar)^3} \int \mathrm{d}v_y \mathrm{d}v_z \, n_F(E). \tag{B.3}$$

I have followed Simmons in assuming an isotropic velocity distribution, and allowed the left electrode to contain states up to an energy E_m, which is given by the work function of the metal. He rewrites this in terms of the polar coordinate energy $E_r = (1/2m)(p_y^2 + p_z^2)$ to yield

$$\dot{N}_1 = \frac{m^2}{2\pi^2\hbar^3} \int_0^{E_m} \mathrm{d}E_x \, D(E_x) \left(\int_0^{\infty} \mathrm{d}E_r \, \mathcal{J} n_F(E) \right). \tag{B.4}$$

The $\mathcal{J}$ refers to the Jacobian and I have attempted to make clear in this equation the fact that the bracketed term, which is equal to $n(v_x)$, depends on E_x via integrating out the y and z dependence. There is of course also a backflowing current from lead 2 to lead 1: allowing the first electrode to lie at an energy eV with respect to the second one, it is given by

$$\dot{N}_2 = \frac{m^2}{2\pi^2\hbar^3} \int_0^{E_m} \mathrm{d}E_x \, D(E_x) \left(\int_0^{\infty} \mathrm{d}E_r \, n_F(E + eV) \right) \tag{B.5}$$

and therefore the total current density is

$$\begin{aligned} J &= e(\dot{N}_1 - \dot{N}_2) \\ &= \frac{m^2}{2\pi^2\hbar^3} \int_0^{E_m} \mathrm{d}E_x \, D(E_x) \left(\int_0^{\infty} \mathrm{d}E_r \, (n_F(E) - n_F(E + eV)) \right). \end{aligned} \tag{B.6}$$

Simmons' key insight here is that the integral in the WKB expression can be accurately modelled by replacing the tunnelling junction potential with its average value $\bar{\phi}$ and including a factor labelled $\beta(V)$ that asymptotically corrects

for the deviations from this,

$$D(E_x) \approx \exp\left[-\frac{2\beta(V)s(2m)^{\frac{1}{2}}}{\hbar}(\eta + \bar{\phi} - E_x)^{\frac{1}{2}}\right], \tag{B.7}$$

where $\beta \approx 1$ when $eV << \bar{\phi}$ and $\beta \approx 1 - O((eV)^2)$ for intermediate eV. The case of high voltage is not relevant to this thesis.

After some more algebraic manipulations and approximations to order $\hbar$ (consistent with the use of WKB), Simmons arrives at

$$J = \frac{e}{4\pi^2\hbar(\beta s)^2}\left[\bar{\phi}\exp\left(-\frac{2\beta s(2m)^{\frac{1}{2}}}{\hbar}\bar{\phi}^{\frac{1}{2}}\right) - (\bar{\phi} + eV)\exp\left(-\frac{2\beta s(2m)^{\frac{1}{2}}}{\hbar}(\bar{\phi} + eV)^{\frac{1}{2}}\right)\right] \tag{B.8}$$

for the current density at 0K. This has the appealing interpretation of two counterpropagating current densities from electrodes 1 and 2, directly traceable to the form of B.6. A typical voltage curve is shown in figure B.2.

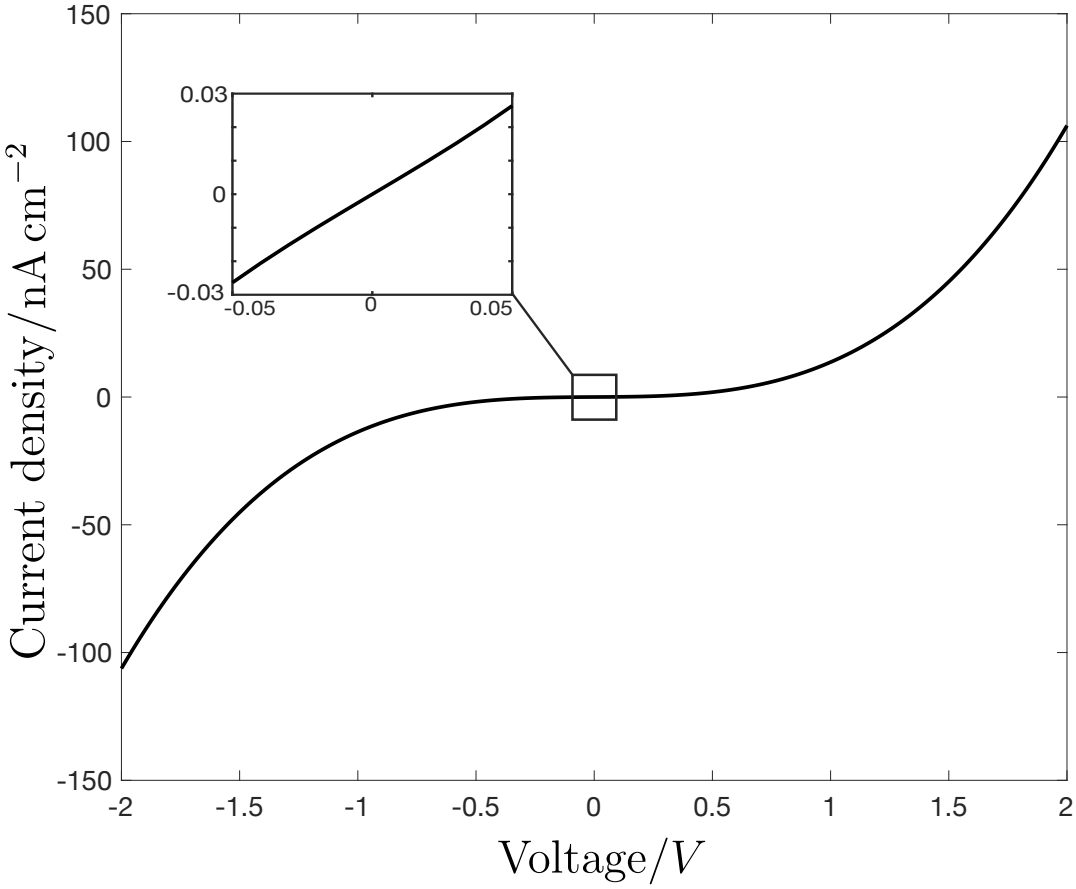

Figure B.2: A typical J-V profile from the model above, with $\bar{\phi} = 0.5$ eV, $s = 3$ nm. The inset shows the ohmic behaviour in the limit $V \to 0$. β is set to 1, as the error induced is <1% for almost the whole range. Deviations of around 6% at the extremes are seen if β is accounted for correctly.

B.2 Resonant tunnelling through a molecular level

What, then, is the current through a nanogap containing a molecule? The molecule can be thought of as having states occupied up to the 'highest occupied molecular orbital' (HOMO) coupled to leads filled up to the Fermi level. After interaction there may be some changing of the levels due to hybridisation and the final situation will look somewhat like figure B.3, where the Fermi level of the leads lies somewhere in the gap between the HOMO and the lowest unoccupied molecular orbital (LUMO). I will assume that the transport is dominated by transport through only a single

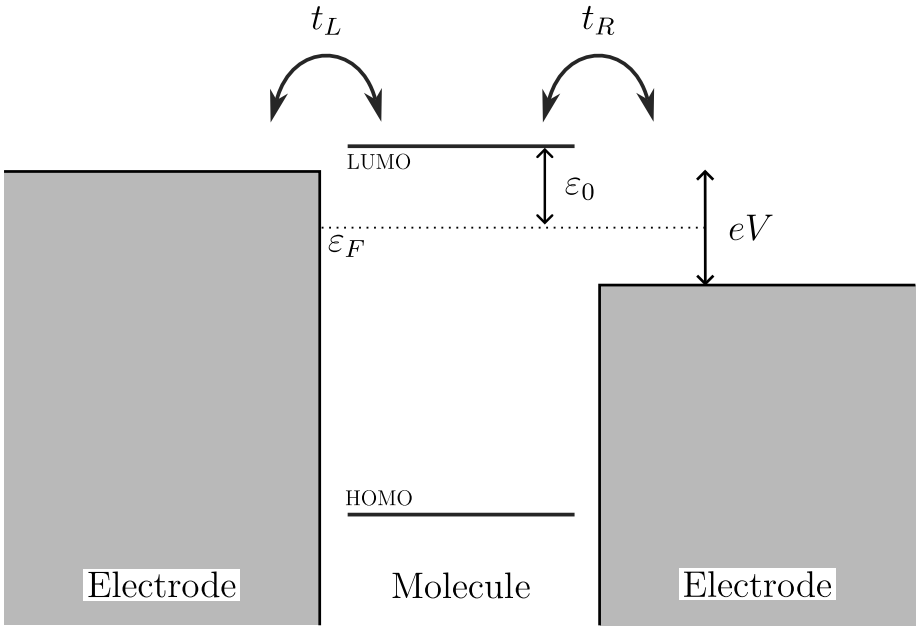

Figure B.3: The resonant tunnelling through a single molecular level at energy ε_0. The leads are offset from each other by eV, and the HOMO and LUMO are both shown. Only the LUMO will be considered when discussing the transport here.

level ε_0, such that the Hamiltonian is given by

$$\mathcal{H} = \mathcal{H}_L + \mathcal{H}_R + \sum_\sigma \varepsilon_0 a_\sigma^\dagger a_\sigma + \sum_{j=L/R} \left(t_j \sum_\sigma (a_\sigma^\dagger c_{j\sigma} + h.c.) \right) \tag{B.9}$$

where the lead Hamiltonians are given by $\mathcal{H}_{L/R}$. The $a_\sigma^\dagger$ operator creates an electron on the molecule with spin σ. The $c_{j\sigma}^\dagger$ operators create an electron on lead j with spin σ.

Scenarios such as the above are best considered within the Landauer-Büttiker approach [40], where the problem is treated in terms of scattering. This section will be phrased in terms of Green functions; introducing the theory fully is beyond the scope of this thesis but the reader is invited to read any of the excellent books and reviews on the topic [42] [41] [155] for an introduction; there is also a minimal

introduction to Green functions in appendix A. The central region is considered in terms of a transmission function $T(E)$ which is related to the Green functions as

$$T(E) = 4\,\mathrm{Tr}[\Gamma_L G^r_{00} \Gamma_R G^a_{00}] \tag{B.10}$$

with $\Gamma_{L/R}$ the imaginary part of the advanced self energy $\Gamma_{L/R} = \Im[\Sigma^a_{L/R}]$ and $G^{r/a}_{00}$ the retarded/advanced Green function of the molecular region including the interactions. Using this, Landauer finds the current under symmetrical bias to be

$$I(V) = \frac{G_0}{e} \int \mathrm{d}E\; T(E,V)\,[n_F(E - eV/2) - n_F(E + eV/2)] \tag{B.11}$$

where n_F again stands for the Fermi function. This problem therefore reduces to finding the Green function of the central region, which follows from the Dyson equation for the Green function, $\mathbf{G} = \mathbf{g} + \mathbf{gVG}$. Treating the hopping between the leads and molecule as a perturbation, the only nonzero elements of the Dyson equation are

$$G_{00} = g_{00} + g_{00} t_L G_{L0} + g_{00} t_R G_{R0} \tag{B.12}$$

$$G_{L0} = g_{LL} t_L G_{00} \tag{B.13}$$

$$G_{R0} = g_{LL} t_R G_{00}. \tag{B.14}$$

Solving this system of equations gives the Green function of the molecule including the self energy introduced by the coupling[1]:

$$G^{r/a}_{00} = \frac{1}{E - \varepsilon_0 - \Sigma^{r/a}_{00}(E)} \tag{B.15}$$

$$\Sigma^{r/a}_{00}(E) = t_L^2 g^{r/a}_{LL}(E) + t_R^2 g^{r/a}_R R(E). \tag{B.16}$$

[1]This type of self energy is known as an *embedding self energy* and is extremely common in these sorts of calculations.

This suffices to formally solve the problem given that the Green function of the leads is in principle knowable from ab initio simulation, but I will invoke a common approximation known as the Wide Band Limit Approximation (WBLA) to gain an analytical expression for the current[2]. The lead Green function is related to the metallic lead's density of states as $\Im[g^{r/a}(E)] \propto \rho(E)$ which in the WBLA is taken to be approximately constant around the Fermi level. The Green function obeys various analytical properties which then also fix the real part to be constant, which I absorb into ε_0, such that $\Sigma_{00}^{r/a} = \mp i(\Gamma_L + \Gamma_R)$ for some scattering rate constants defined as $\Gamma_{L/R} = \pm i g^{r/a}_{LL/RR} t^2_{L/R}$, where the Green functions $g^{r/a}$ are now pure imaginary such that the Γ are real. Substituting this into the equation for the transmission function B.10 gives a Breit-Wigner lineshape

$$T(E) = \frac{4\Gamma_L\Gamma_R}{(E-\varepsilon_0)^2 + (\Gamma_L+\Gamma_R)^2}. \tag{B.17}$$

From hereon, let $\Gamma = \Gamma_L + \Gamma_R$. At $T \to 0$, the Fermi functions become step functions and equation B.11 may be integrated exactly, yielding

$$\begin{aligned} I(V) &= \frac{4G_0\Gamma_L\Gamma_R}{e}\int_{-eV/2}^{eV/2} \mathrm{d}E\, \frac{1}{(E-\varepsilon_0)^2+\Gamma^2} \\ &= \frac{4G_0\Gamma_L\Gamma_R}{e\Gamma}\left[\arctan(\frac{eV}{2\Gamma}+\frac{\varepsilon_0}{\Gamma}) + \arctan(\frac{eV}{2\Gamma}-\frac{\varepsilon_0}{\Gamma})\right]. \end{aligned} \tag{B.18}$$

A typical trace is shown in figure B.4. Notice that the sharp increase in conductance occurs at twice the molecular level: this is due to the symmetric coupling to the leads. This is shown diagrammatically in figure B.5. Each lead moves away from the Fermi level by $eV/2$ and the resonance condition is only achieved when the left read reaches ε_0, which happens at $eV = 2\varepsilon_0$. If the couplings are different, it is a reasonable assumption that the energy level is renormalised by an amount

[2]There are further difficulties with using ab initio methods to accurately model experimental data in these types of models that are beyond the scope of this thesis.

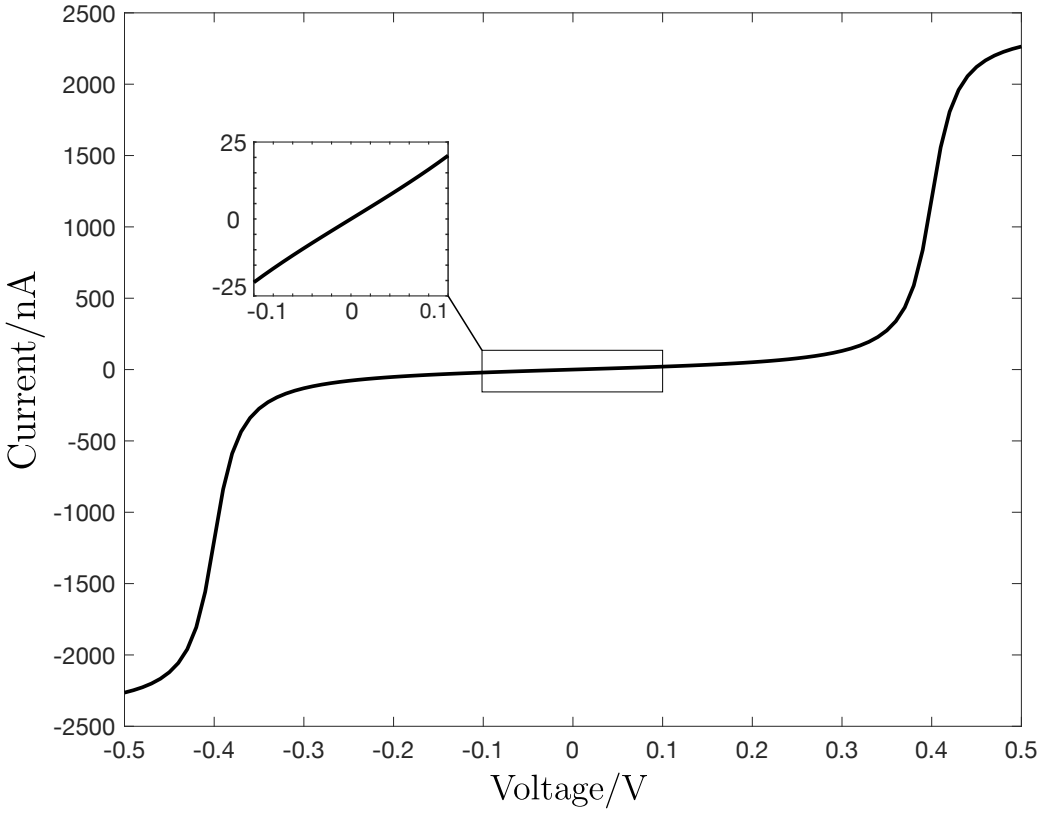

Figure B.4: A typical I-V curve for the resonant tunnelling model above, with $\epsilon_0 = 0.2$ eV and $\Gamma_L = \Gamma_R = 5$ meV. Note the conductance decreases towards zero when the level moves outside the voltage window.

proportional to the difference between the couplings:

$$\varepsilon = \varepsilon_0 + \frac{V}{2}\frac{\Gamma_L - \Gamma_R}{\Gamma_L + \Gamma_R}. \tag{B.19}$$

I have used this asymmetric form of the model in order to fit the data featured in chapter 3.

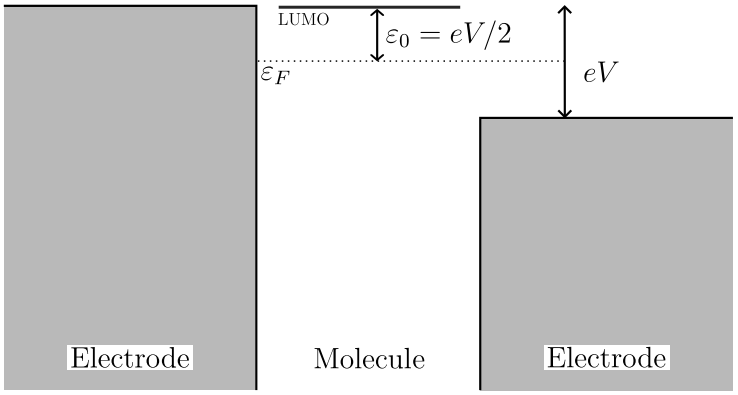

Figure B.5: A demonstration of the position of the peak in conductance under symmetric coupling. Each lead is displaced from the Fermi level by $eV/2$, such that resonance is achieved at $eV = 2\varepsilon_0$.

B.3 Temperature dependence from Variable Range Hopping

If instead the transport is more accurately thought of as resulting from a network of disordered sites undergoing hopping, a more appropriate model may be Mott Variable Range Hopping [44] [45]. This type of model could be relevant to, say, the DNA origami structure, for reasons explored in the main text. Consider such a network, and the states near the Fermi level. Temperature broadens the levels, and the hopping between dilute sites with wavefunctions $|i\rangle$, $|j\rangle$ should scale like

$$\langle i|j\rangle \sim \exp(-r_{ij}/a) \tag{B.20}$$

for some characteristic length scale a on order the average spacing. Given the states are disordered, they are not necessarily aligned in energy. This leads to an

extra Boltzmann like weight factor $\exp(\varepsilon_{ij}/kT)$. In a universal sense, the resistivity should therefore be expected to scale like

$$\rho = \rho_0 \exp\left[\frac{\langle r_{ij}\rangle}{a} + \frac{\langle \varepsilon_{ij}\rangle}{kT}\right] \tag{B.21}$$

as long as the temperature is small compared to the energy scales. Allow the disorder average over the energies to be equal to some characteristic energy near the Fermi level ε_0 and substitute the typical separation $\langle r_{ij}\rangle = N(\varepsilon_0)^{-1/d} = g(\varepsilon_F)\varepsilon_0$, d the number of dimensions. Then, the resistivity is

$$\rho = \rho_0 \exp\left[\frac{1}{N^{1/d}a} + \frac{\varepsilon_0}{kT}\right] \tag{B.22}$$

This resistivity comes from a set of disordered 'bands' around the Fermi level. Given the exponential sensitivity, it is reasonable to assume that the transport is dominated by those bands which minimise the resistivity as a function of ε_0. At large ε_0, the first term vanishes and decreasing ε_0 decreases ρ. However, in the region where both terms are comparable, decreasing ε_0 leads to an increase in resistivity. Therefore, a minimum must exist from the competing effects of the scarcity of overlaps within the window and thermal activation. At this minimum the Mott Variable Range Hopping law is produced, with temperature dependence

$$\rho = \rho_0 \exp[(T_0/T)^{1/(d+1)}] \tag{B.23}$$

for some temperature scale T_0, which may be straightforwardly tested.

References

[40] M. Büttiker, Y. Imry, R. Landauer, and S. Pinhas. "Generalized many-channel conductance formula with application to small rings". In: *Phys. Rev. B* 31 (10

1985), pp. 6207–6215. URL:
https://link.aps.org/doi/10.1103/PhysRevB.31.6207.

[41] Gianluca Stefanucci and Robert van Leeuwen. *Nonequilibrium Many-Body Theory of Quantum Systems: A Modern Introduction*. eng. New York: Cambridge University Press, 2013.

[42] Juan Carlos Cuevas and Elke Scheer. *Molecular electronics: an introduction to theory and experiment (World scientific series in nanoscience and nanotechnology, vol. 1)*. eng. Singapore: World Scientific Publishing Co. Pte. Ltd, 2010.

[44] N.F. Mott. "Conduction in glasses containing transition metal ions". In: *Journal of Non-Crystalline Solids* 1 (1 1968), pp. 1–17.

[45] Boris I. Shklovskii and Alex L. Efros. "Variable-Range Hopping Conduction". In: *Electronic Properties of Doped Semiconductors*. Berlin, Heidelberg: Springer Berlin Heidelberg, 1984, pp. 202–227. URL:
https://doi.org/10.1007/978-3-662-02403-4_9.

[155] D. A. Ryndyk, R. Gutié rrez, B. Song, and G. Cuniberti. "Green Function Techniques in the Treatment of Quantum Transport at the Molecular Scale". In: *Springer Series in Chemical Physics*. Springer Berlin Heidelberg, 2009, pp. 213–335. URL: https://doi.org/10.1007%2F978-3-642-02306-4_9.

C

An overview of topological band theory

In this section I give a somewhat more detailed overview of the topological band theory in order to expand upon the qualitative statements in sections 4.2.2 and 4.2.3 and should be considered a replacement for the more mathematically inclined reader. In doing so I make no attempt at mathematical rigour and will use suggestive arguments where possible, but do at least attempt to be precise as to the mathematical properties that are giving rise to the behaviour. There is a greater focus on exposition and derivation than in the rest of this thesis, as the technical details motivate specific choices made in the chapter on my DFT findings. In presenting this subject I lean heavily on the work in references [70, 71, 73, 74]. Where possible I phrase the statements in terms of differential forms (which form a very natural language in which to speak about manifolds): an accessible overview of the mathematics of manifolds can be found in, for example, reference [72]. The result, that a nonzero Chern number is possible in 2 dimensional quantum matter,

is used to motivate the $\mathbb{Z}_2$ invariant which I make use of in chapter 5.

C.1 Chern insulators

With the notion of bands accounted for, I now wish to phrase the problem in a more mathematical fashion. This will reveal a path towards seeing the wavefunction in a different way, sensitive not only to local properties of $\mathcal{H}(\mathbf{k})$ but to global, topological features arising from the structure of the wavefunction as a map between different manifolds. The motivating question is, given a set of occupied bands, does there exist some smooth unitary map onto any other set of bands with the same symmetries? This question will be answered in the negative, as a consequence of the topological structure of the Bloch functions.

Consider the Bloch functions of the filled bands in some insulating system. These define a complex Hilbert space $\mathfrak{H}_{\mathbf{k}} \cong \mathbb{C}^n$ at every $\mathbf{k}$, with n the particle number (neglecting spin). The collection of these vector spaces over $\mathbf{k}$ is known in geometric language as the bundle[1] and the properties of this bundle as a function of $\mathbf{k}$ will be the source of interesting behaviour. In order to study the bundle, it is necessary to have a choice of gauge and a notion of connection in order to traverse the bundle. That is, a way to speak about the relationship between the basis vectors at some point $\mathbf{k}$ and the basis vectors at some other point $\mathbf{k}' = \mathbf{k} + \mathrm{d}\mathbf{k}$. As the properties I am interested in are topological, the exact choice of connection is not important, but the most natural choice is the Berry connection. By taking two Bloch functions evaluated at two infinitesimally nearby points in the Brillouin zone, I write

$$\langle u(\mathbf{k})|u(\mathbf{k}')\rangle = \langle u|\left(1 + \mathrm{d}\mathbf{k}\cdot\nabla_k\right)|u\rangle = \exp(i\mathcal{A}\cdot\mathrm{d}\mathbf{k}) \tag{C.1}$$

[1] A bundle comprises a manifold, here the Brillouin torus, to which another manifold is attached at every point. This manifold is the Hilbert space $\mathfrak{H}$ here.

which defines the Berry connection [70]

$$\mathcal{A} = \frac{1}{i} \langle u | \nabla_k | u \rangle \tag{C.2}$$

or in a more geometric, coordinate free form

$$A = \frac{1}{i} \langle u | \mathrm{d}u \rangle \tag{C.3}$$

where d is the exterior derivative [72]. This A is the Berry connection 1-form.

I wish to use now a commonly used toy model to demonstrate the way that topological properties can arise from a band structure. The model was first studied by Dirac in reference [156], and rephrased in more modern mathematical terms in reference [157]. The motivating question is this: What are the consequences of the fact that the Brillouin zone and the wavefunction live in spaces with in general different overall geometries? Consider a two band model,

$$\mathcal{H}(k) = h_0(\mathbf{k})\mathbf{1} + \mathbf{h}(\mathbf{k}) \cdot \boldsymbol{\sigma} \tag{C.4}$$

where $\boldsymbol{\sigma}$ is a vector of Pauli matrices. Any 2x2 Hermitian matrix may plainly be written in this basis. Take, without loss of generality, $h_0 = 0$ and $\mathbf{h}(\mathbf{k}) \neq 0$ for all $\mathbf{k}$. Then, the band energies are

$$\varepsilon(\mathbf{k}) = \pm |\mathbf{h}(\mathbf{k})| \tag{C.5}$$

and the system is insulating in the whole Brillouin zone at half filling. In the following discussion, the number of dimensions will be taken to be $d = 2$, with generalisations to $d = 3$ covered in the main text. Allowing $\mathbf{h}$ to be written in terms

of spherical coordinates the eigenvector for the filled bands takes the form

$$u = \begin{pmatrix} -\sin(\theta/2) \\ e^{i\varphi}\cos\theta/2 \end{pmatrix}, \tag{C.6}$$

which is independent of the magnitude of $\mathbf{h}$. Therefore, the parameter space of the wavefunction takes values exclusively from the surface of a sphere, $\mathbb{S}^2$. The consequences of this will follow in the most general sense by considering maps from the Brillouin zone $\cong \mathbb{T}^2$ to the 2-sphere $\mathbb{S}^2$ [71].

The most important feature to notice is that, as written, the wavefunction becomes undefined in the limit $\theta \to \pi$, as the phase becomes indeterminate. To attempt to fix this problem, one might try multiplying by $e^{i\varphi}$, but this does not solve the issue. The singularity is merely moved to $\theta \to 0$. This is in fact a fundamental feature of the bundle from the sphere! There is always an obstruction to defining a smooth gauge over the space - this will be a hallmark feature of a topologically nontrivial phase. The best that can be done in this case is to define two separate gauges for the 'north' and 'south' halves of the sphere and patch them together over the equator, defining the maps U_N, $U_S : \mathbb{S}^2 \to \mathbb{C}^2$ such that

$$u_S = \begin{pmatrix} \sin(\theta/2)e^{-i\varphi} \\ \cos(\theta/2) \end{pmatrix} \in U_S \ , \qquad u_N = \begin{pmatrix} \sin(\theta/2) \\ \cos(\theta/2)e^{i\varphi} \end{pmatrix} \in U_N. \tag{C.7}$$

Together they form an open cover of the sphere and their overlap is topologically equivalent to a line around the equator [71] [73]. The gauge transformation that maps between these two coordinate charts is

$$t_{SN} = e^{i\varphi}. \tag{C.8}$$

There are several natural mathematical tools to quantify the consequences of this obstruction and way in which it is affected by the properties of $\mathbf{h}$, the most relevant

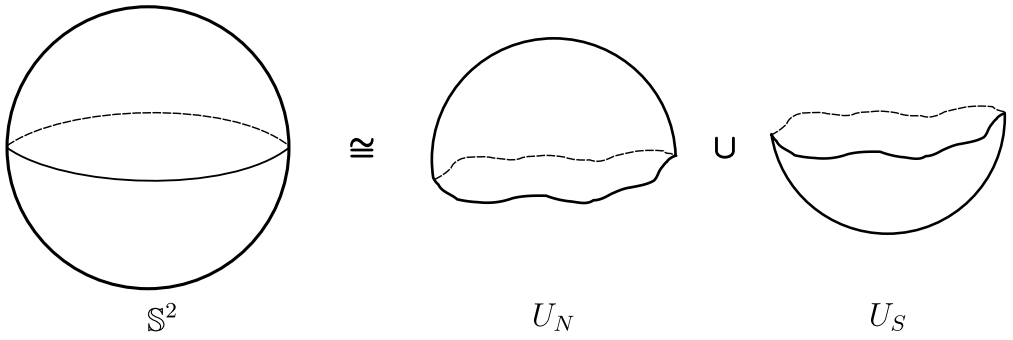

Figure C.1: The partitioning of $(S)^2$ into the two smooth gauges U_N, U_S. Together they form a smooth cover.

being the (first) Chern number. Defining first the Berry field strength 2-form

$$F = \mathrm{d}A \tag{C.9}$$

or, in a pseudovector coordinate representation [73]

$$\mathcal{F}_{\mu\nu} = \frac{1}{i}\left[\nabla_\mu \langle u| \nabla_\nu |u\rangle - \nabla_\nu \langle u| \nabla_\mu |u\rangle\right] = \nabla_\mu \times \mathcal{A}_\nu, \tag{C.10}$$

then the Chern number is defined in $d = 2$ as the integral of this over the whole Brillouin zone[2]

$$Ch = \frac{1}{2\pi}\int F = \frac{1}{2\pi}\int \mathrm{d}k_x \mathrm{d}k_y (\mathcal{F}\cdot \hat{k}_z) \tag{C.11}$$

with the unit vector $\hat{k}_z = \hat{k}_x \times \hat{k}_y$. It should be noted that this is sloppy notation and the treatment works perfectly well in a strict $d = 2$ where there is no notion at all of k_z.

How can it be seen that this quantity telegraphs the presence of some topological

[2]As written, F is a differential 2-form, so the integral $\int F$ is only defined over a 2 dimensional Brillouin zone; this is the reason for choosing $d = 2$. No measure is required in the first equality as F is a differential form.

obstruction? In the coordinate representation, the Berry field strength (sometimes called Berry curvature) is the curl of the Berry connection, so when integrating it over the Brillouin zone it is natural to wish to apply Stokes' theorem. The boundary of the torus is $\partial\mathbb{T}^2 \cong 0$, so if the Berry connection were everywhere defined the Chern number must be equal to zero. So, a nonzero Chern number signals the presence of an obstruction to the definition of a smooth Berry connection over the Brillouin zone.

Denote by $\mathbf{h}^{-1}(U_{N,S}) \subset \mathbb{T}^2$ the preimage of $U_{N,S}$ in the Brillouin zone, that is the region of the Brillouin zone that, via $\mathbf{h}(k)$, maps to $U_{N,S}$. Denote also by $\mathbf{h}^\star A$ the pullback of A by $\mathbf{h}$. This makes clear in a differential geometric context the obvious fact that $A(\mathbf{h}(\mathbf{k})) = A(\mathbf{k})$, while keeping track of the types of spaces involved. $\mathbf{h}^\star A$ should be read as A, but acting on the domain of $\mathbf{h}$ [72]. Then the calculation in terms of differential forms proceeds by applying Stokes' theorem on the smooth sections:

$$Ch = \frac{1}{2\pi}\left[\int_{\mathbf{h}^{-1}(U_N)} F + \int_{\mathbf{h}^{-1}(U_S)} F\right] \tag{C.12}$$

$$= \frac{1}{2\pi}\left[\int_{\partial\mathbf{h}^{-1}(U_N)} \mathbf{h}^\star A_N + \int_{\partial\mathbf{h}^{-1}(U_S)} \mathbf{h}^\star A_S\right] \tag{C.13}$$

Note that if Stokes' theorem applied universally over the sphere, in a situation where there were no singularities, the integral would vanish and the Chern number would be zero, again demonstrating that the Chern number signifies the degree to which Stokes' theorem fails.

This expression is rather intimidating, but we have all the tools needed to evaluate it. The first step is to write it as a single integral: Consider that the boundaries of the regions U_N, U_S are oppositely oriented: $\partial\mathbf{h}^{-1}(U_N) = -\partial\mathbf{h}^{-1}(U_S)$. This lets us write

$$Ch = \frac{1}{2\pi}\left[\int_{\partial\mathbf{h}^{-1}(U_N)} \mathbf{h}^\star A_N - \mathbf{h}^\star A_S\right] \tag{C.14}$$

The final step is to relate the Berry connections on the boundary region. Under

the gauge transformation t_{SN} the Berry connection is given [71]

$$A_N = \frac{1}{i}\langle u|\, e^{-i\varphi}\mathrm{d}e^{i\varphi}\,|u\rangle = A_S + \frac{1}{i}e^{-i\varphi}\mathrm{d}e^{i\varphi} = A_S + \mathrm{d}\varphi. \tag{C.15}$$

Substituting this into equation C.14:

$$Ch = \frac{1}{2\pi}\left[\int_{\partial \mathbf{h}^{-1}(U_N)} \mathbf{h}^\star A_N - \mathbf{h}^\star A_S\right] \tag{C.16}$$

$$= \frac{1}{2\pi}\int_{\partial \mathbf{h}^{-1}(U_N)} \mathrm{d}\varphi \in \mathbb{Z}. \tag{C.17}$$

This is nothing but the winding number of φ. So, the Chern number counts the number of windings of the transition functions between regions of smooth gauge. As with the above argument, it may be regarded in this way as a measure of the barrier to applying Stokes' theorem. This same calculation may be seen in detail in coordinate representation, without differential geometry, in [73].

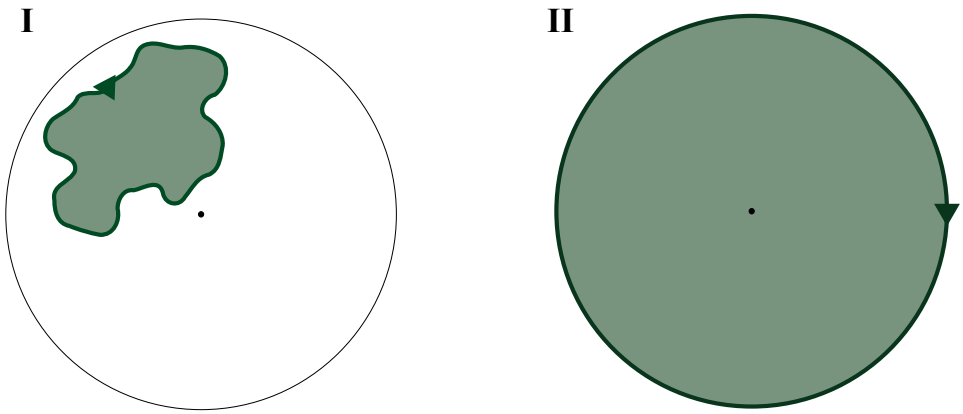

Figure C.2: Illustration of the degree of the map **h**. In example I, **h** does not cover the origin so the degree is zero. In example II, the map covers the space once, and this map has degree +1. Higher degree maps are possible if **h** covers the space multiple times and negative degrees are admissible taking into account the orientation of **h**.

The above calculations demonstrate that a Chern number is admissible when considering maps between a torus and a sphere. However in order to link it to some microscopic model, with the view to hunt for Hamiltonians that will have these properties, it is necessary to connect it to the toy model above. Inserting the equations for the eigenvectors, it is found after some algebra that

$$Ch = \frac{1}{4\pi}\int_{BZ} \frac{\mathbf{h}}{|\mathbf{h}|^3} \cdot \left(\frac{\partial \mathbf{h}}{\partial k_x} \times \frac{\partial \mathbf{h}}{\partial k_y}\right) \mathrm{d}k_z, \tag{C.18}$$

which is the *degree* of $\mathbf{h}$ [158]. Consider the shape that $\mathbf{h}$ maps out as it evolves through the Brillouin zone: this integral counts the number of times that the surface defined by the evolution engulfs the origin (see figure C.2). This will happen once for each time $\mathbf{h}$ 'covers' the sphere, in the spherical representation given above. The presence of absence of these vortices is given by the details of the Hamiltonian, and therefore the physical system.

C.2 Topological $\mathbb{Z}_2$ insulators

The above discussion makes clear the potential for topological effects to arise in quantum matter, but the $\mathbb{Z}$ invariant is not directly relevant to electronic insulators without magnetic fields. The sensitivity of topological behaviour to the details of the Hamiltonian motivates the study of the symmetries of these Hamiltonians, in search of structure that can lead to topologically nontrivial behaviour. This will come in the form of time reversal symmetry (TRS). In this section I will summarise the steps that lead to the presence of a $\mathbb{Z}_2$ valued topological invariant in TRS insulators in two dimensions. The considerations of 4.2.4 then motivate the three dimensional topological insulator.

Time reversal symmetry is an antiunitary symmetry Θ obeyed by non-magnetic

fermionic matter, satisfying

$$\Theta\mathcal{H}(\mathbf{k}) = -\mathcal{H}(-\mathbf{k})\Theta^{-1} \tag{C.19}$$

on the Hamiltonian, and

$$\Theta\left|u_n(\mathbf{k})\right\rangle = \left|u_{n'}(-\mathbf{k})\right\rangle \tag{C.20}$$

on the eigenstates. There are two vital consequences of this symmetry on the system. The first of these is Kramers' theorem: the time reversed partner of a state $|u(\mathbf{k})\rangle$ is also an eigenstate, with the same energy. This partitions the Hilbert space (and the Brillouin zone, via the pullback) into a $U(2)$ symmetric set of Kramers pairs. The second useful consequence is the vanishing of the total Chern number. To see this, partition the Hilbert space via the above procedure into $\{|u^I(\mathbf{k})\rangle, |u^{II}(\mathbf{k})\rangle\}$. Then, under time reversal the Berry connection evaluated on one 'half' of each Kramers doublet is

$$\Theta\mathcal{A}^I = \frac{1}{i}\sum_n \Theta\left[\langle u^I(\mathbf{k})|\,\partial_{\mathbf{k}}\,|u^I(\mathbf{k})\rangle\right] \tag{C.21}$$

$$= \frac{1}{i}\sum_n \langle u^{II}(k)|\,(-\partial_{\mathbf{k}})\,|u^{II}(\mathbf{k})\rangle \tag{C.22}$$

$$= -\mathcal{A}^{II} \tag{C.23}$$

So the overall Berry connection vanishes, leading to zero total Berry curvature and zero Chern number [74]. Nonetheless, this system does in fact admit a topological invariant. Imagine again that it were possible to isolate a single member of each Kramers doublet. Then, in $d = 2$ the $\mathbb{Z}_2$ invariant is given by

$$\nu = (-1)^{Ch^I} = (-1)^{Ch^{II}} \in \mathbb{Z}_2. \tag{C.24}$$

Even though the partitioning into half a Kramers pair is not well defined, the above invariant is independent of the choice so is a well defined topological invariant. This quantity is equivalent to evaluating the parity of the Chern number (odd/even) in an effective Brillouin zone defined by the following: Consider a cover of the Brillouin zone $\{(-\pi, \pi) \times (-\pi, \pi)\}$, and list the elements of this set. For each element $\mathbf{k}$, remove the element $\Theta\mathbf{k} = (-k_x, -k_y)$ iff $\mathbf{k} \neq \Theta\mathbf{k}$. The remaining entries are then 'half' of the Brillouin zone, including the 4 time reversal invariant momenta (TRIM) located at $\Gamma : (0, 0)$, $X : (\pi, 0)$, $Y : (0, \pi)$ and $M : (\pi, \pi)$.

Why then should the above constitute an interesting topological invariant? Consider once again the obstruction based definition of the Chern number in the prior sections. The Chern number in the effective Brillouin zone Ch^I counts the number of vortices leading to obstructions to defining a smooth gauge [75]. Each of these vortices has a Chern number counting the degree of the vortex. The diagram shows two scenarios with $\nu = 1$, with an even number of vortices in the effective Brillouin zone, chosen to be the right half plane $k_x \geq 0$. Via smooth gauge transformations denoted by the arrows, it is always possible to move around these vortices and annihilate vortices of opposite degree (shown in blue and red). However, the diagram C.4 shows a scenario with a nontrivial topological invariant $\nu = -1$[3]. There is only one vortex in the effective Brillouin zone and no smooth gauge transformation can remove the obstruction. The Bloch bundle is therefore nontrivial and this system is in the topological $\mathbb{Z}_2$ insulating phase, and will feature all of the same consequences of nontrivial topology mentioned previously, namely the metallic surface states.

This concludes the more detailed discussion of topological band theory, leading directly into section 4.2.4.

[3]Please note that due to constraints imposed by the precise mathematical details, moving the vortices through the TRIM is forbidden.

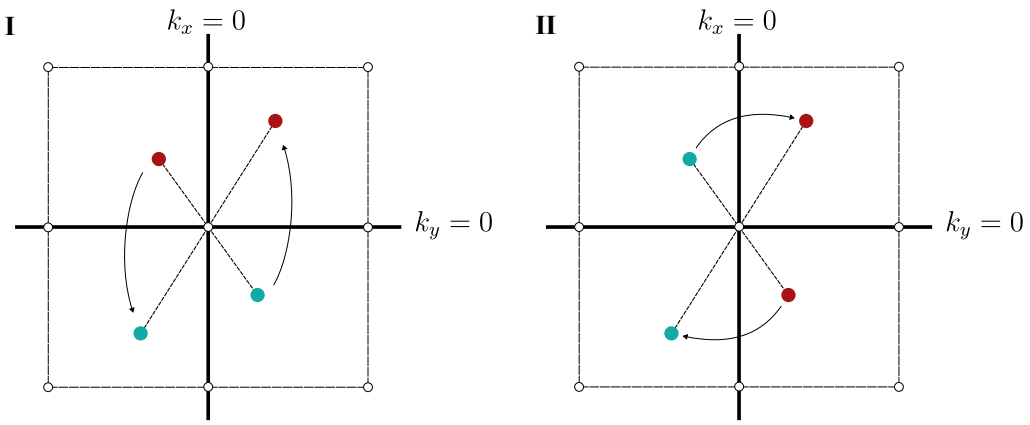

Figure C.3: Two trivial (non-topological) examples of even numbers of vortices in the EBZ. The vortices may be removed via smooth gauge transformations. Reproduced with permission from [71].

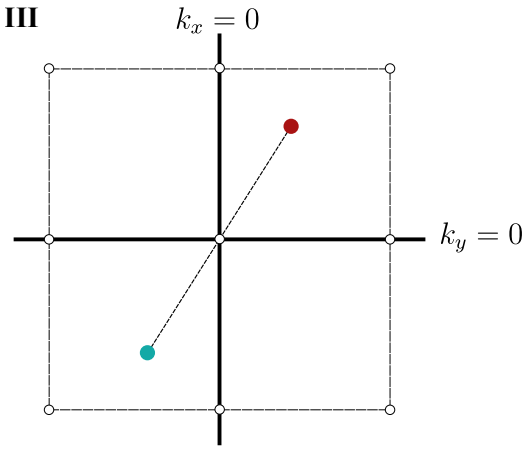

Figure C.4: A topologically nontrivial case, with only 1 singularity in the EBZ. This vortex cannot be removed smoothly. Reproduced with permission from [71].

References

[70] Mikio Nakahara. *Geometry, topology and physics*. CRC press, 2003.

[71] Michel Fruchart and David Carpentier. "An introduction to topological insulators". In: *Comptes Rendus Physique* 14.9-10 (2013), pp. 779–815. URL: https://doi.org/10.1016%2Fj.crhy.2013.09.013.

[72] David Bachman. *A geometric approach to differential forms*. Springer Science & Business Media, 2012.

[73] B.A. Bernevig and T.L. Hughes. *Topological Insulators and Topological Superconductors*. Princeton University Press, 2013. URL: https://books.google.co.uk/books?id=wOn7JHSSxrsC.

[74] Masatoshi Sato and Yoichi Ando. "Topological superconductors: a review". In: *Reports on Progress in Physics* 80.7 (July 2017). arXiv:1608.03395 [cond-mat], p. 076501. URL: http://arxiv.org/abs/1608.03395 (visited on 01/15/2023).

[75] C. L. Kane and E. J. Mele. "Z_2 Topological Order and the Quantum Spin Hall Effect". In: *Phys. Rev. Lett.* 95 (14 Sept. 2005), p. 146802. URL: https://link.aps.org/doi/10.1103/PhysRevLett.95.146802.

[156] Paul Adrien Maurice Dirac. "Quantised singularities in the electromagnetic field". In: *Proceedings of the Royal Society of London. Series A, Containing Papers of a Mathematical and Physical Character* 133.821 (1931), pp. 60–72.

[157] Masatsugu Minami. "Dirac's monopole and the Hopf map". In: *Progress of Theoretical Physics* 62.4 (1979), pp. 1128–1142.

[158] Edward Witten. "Three lectures on topological phases of matter". In: *La Rivista del Nuovo Cimento* 39 (2016), pp. 313–370.

D

Further details of DFT calculations

Here I shall provide further details on the steps taken to ensure convergence of the DFT results as well as explaining methodology. The parameters that should be well converged for the bulk model are the plane wave cutoff energy eCut and the k-point grid density. For slab models, the thickness of vacuum between the slabs is extremely important as well if the two surfaces are not to interact, so I demonstrate the convergence of this as well.

Converging the energy cut-off

Running the unit cell calculations at a large number of cut off energies with very large k-point density ($25 \times 25 \times 25$) allows the convergence to be inspected. The energy is assumed to be well converged at the end of the plot at eCut= 200 Ry and the converged cutoff energy taken to be the smallest cutoff such that the total energy per atom deviates not more than 7 meV (0.5 mRy). This figure

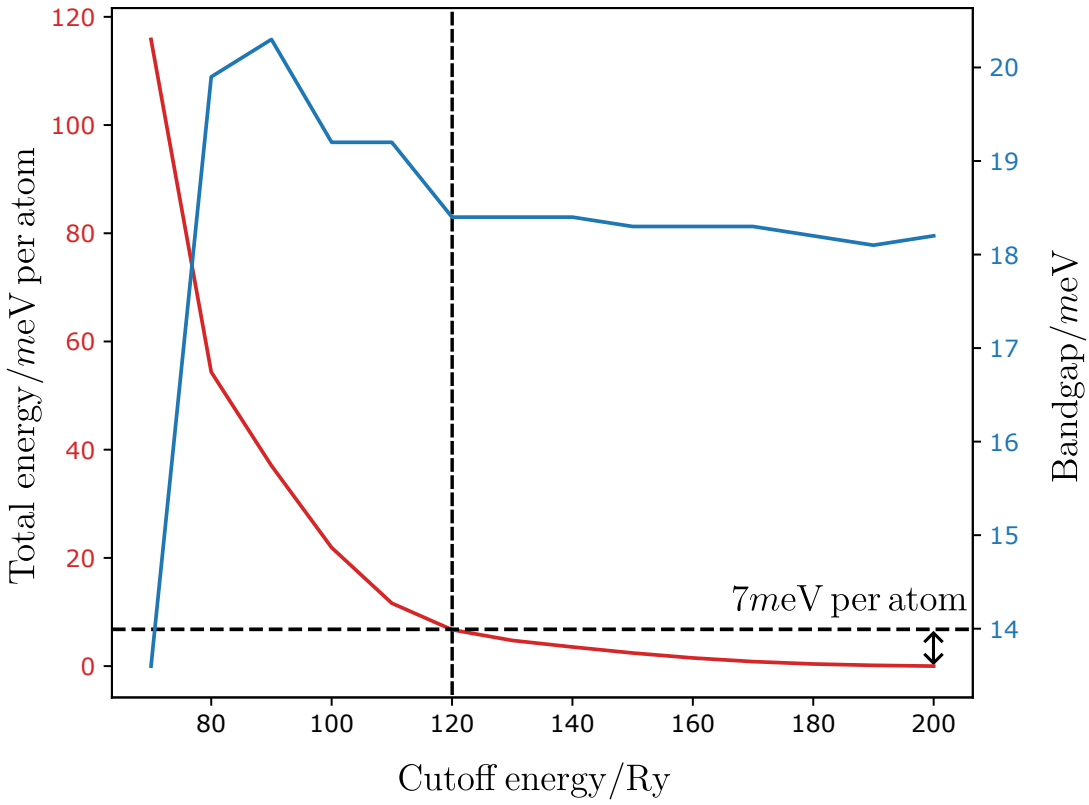

Figure D.1: The energy and bandgap convergence for the unit cell. The threshold for the energy cutoff is shown, implying that convergence is reached around eCut =120Ry.

is somewhat arbitrary but numbers of this order of magnitude are common. I find that eCut =120 meV is a suitable cutoff for convergence. The bandgap has converged within 0.2 meV at this energy.

Converging the number of k-points

Repeating the calculation with a converged cutoff energy (120 Ry) at varying k point densities, the same exercise may be repeated to check convergence. The results are in D.2, with the number of k points N_k referring to the number in the $N_k \times N_k \times N_k$ grid generated in the Brillouin zone.

The energy is seen to be insensitive to the k-point convergence, with deviations of far below 1 meV seen with increasing density. An at first alarming phenomenon happens with the bandgap - oscillations are seen as a function of increased k-point

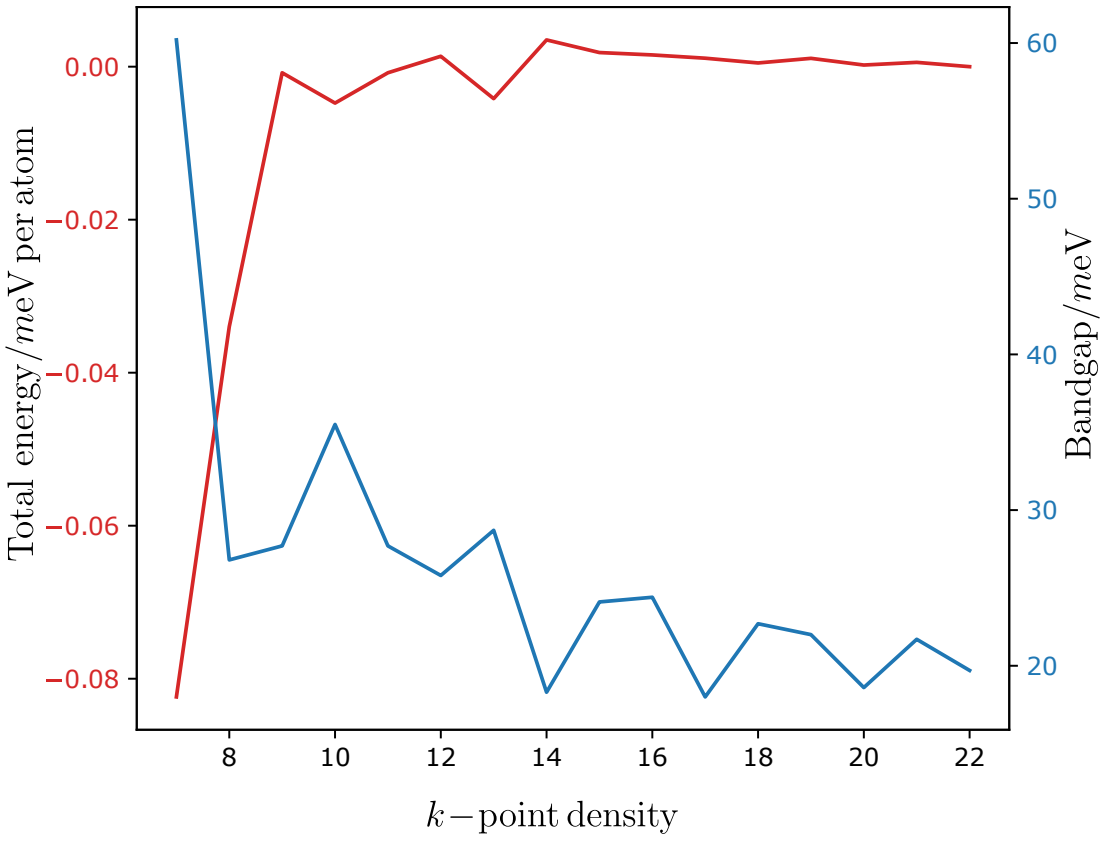

Figure D.2: The convergence of bandgap with k-points. The oscillatory behaviour in the bandgap is explored in the text

density. These however are well explained: the bandgap is very small, of order 10 meV, and so is very sensitive to how the space is discretised. Consider the example in figure D.3, which demonstrates how denser k point sampling does not always lead to a more accurate estimates of features like bandgaps. The aliasing argument encourages taking the lower bound of the calculated bandgaps as the true converged DFT bandgap, motivating taking $\varepsilon_{gap} \approx 18 \pm 1$ meV. Any inaccuracies fixed by denser sampling should be $O(1\,\text{meV})$, from inspecting the convergence graph. Given that this is the only instance where the position of bands to order meV is needed, I shall take the number of k-points $N_k = 14$ to alleviate computational load.

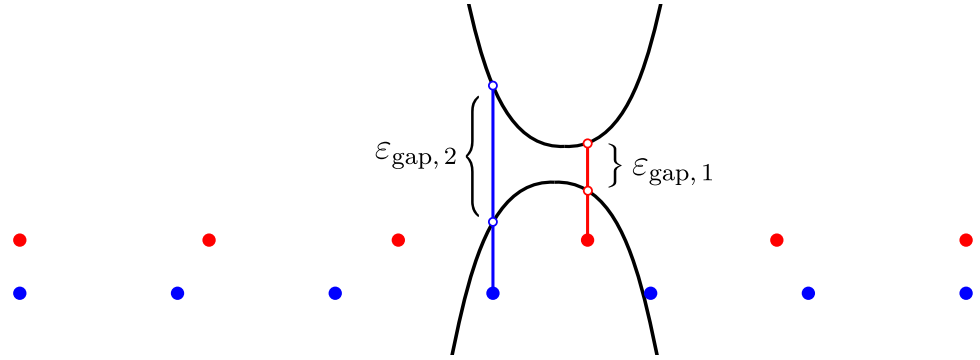

Figure D.3: A depiction of aliasing affecting estimates of the bandgap. The red dots symbolise discretising a line in the Brillouin zone with 6 points, and the blue symbolise this with 7 points. The bandgap calculated with the coarser sampling is actually a closer estimate to the true bandgap than with the finer sampling. This happens as the position of the band edges become well approximated by some m/N_k, then are less well approximated by $m'/(N_k + 1)$.

Converging the air gap

To study surfaces in periodic DFT a slab geometry must be constructed, comprising several layers of the material separated by a volume of vacuum. This vacuum region should be several unit cell thicknesses deep, so that the two surfaces do not interact. Here I show the total energy of a 4 unit cell deep slab with varying quantities of vacuum. The total energy changes by less than a meV once 4 layers is reached, so I have performed all slab calculations with 4 layers of vacuum between slabs, a thickness of 16.4 Å.

Investigating dependence on Hubbard parameter

In chapters 5, I made use of a Hubbard parameter to increase the splitting of the f multiplet, to guarantee the $j = 7/2$ states do not interfere with the physics at the Fermi level. Does varying this parameter significantly modify any of my conclusions about the surface states? In order to have some confidence that the ground state is not hugely affected, I prepared a wannierised DFT model with no Hubbard parameter and calculated the slab surface spectrum. This spectrum is shown in figure D.5 and exhibits the same qualitative features as the model

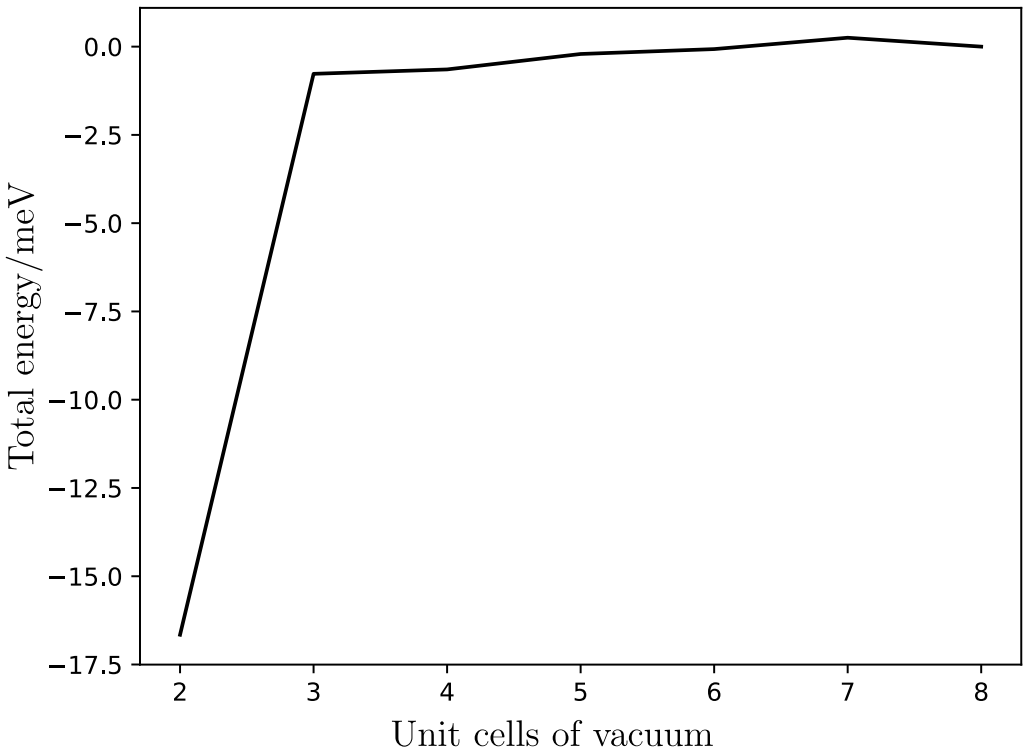

Figure D.4: The total energy of a 4 layer slab with varying thicknesses of vacuum in between slabs. The energy is zeroed with respect to the calculation with 8 layers of vacuum.

considered in the main text. The $\bar{X}$ point Dirac cone is recessed below the Fermi level to a comparable degree, and the Fermi velocity measures 300 meVÅ on the $\bar{X} \to \bar{M}$ path. There is a reduction in Fermi velocity on the $\bar{\Gamma} \to \bar{X}$ path due to a band hybridising with the Dirac cone near the Fermi level. As the features are qualitatively comparable, I have not investigated this further.

A second occasion where checking the role of the Hubbard potential is important is in section 5.5, where I show that the spurious $\bar{M}$ point bands disappear under a change in termination. Performing a Boron terminated slab calculation with $U = 0$ I obtain a band structure D.6. Again, the spurious bands have been removed. There is a fair amount of messiness caused by the thin slab and possible hybridisation with the low lying $j = 7/2$ states, but as ever the qualitative features remain.

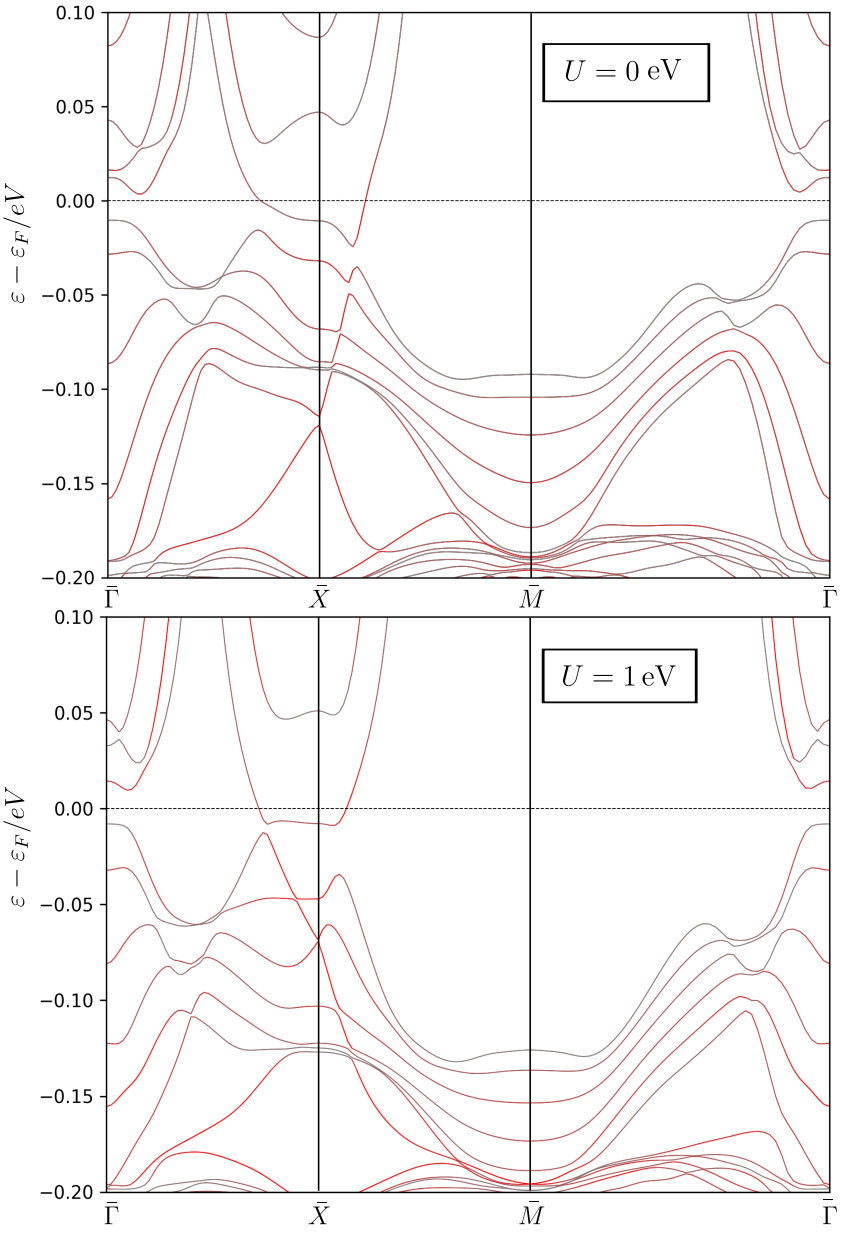

Figure D.5: The surface spectrum for a tight binding slab of thickness 6 with no Hubbard U, compared to the 6 layer slab with $U = 1$ eV from the main text. The same qualitative features remain, with approximately the same Fermi velocity seen in the recessed Dirac cone. If the energy axis is extended upwards, the $j = 7/2$ states intrude on the $U = 0$ band structure in an unphysical manner.

Finding the Fermi velocities

For the slab models, I have provided the band velocity of the $\bar{X}$ point topological surface state in order to compare with experiment. This velocity is found by

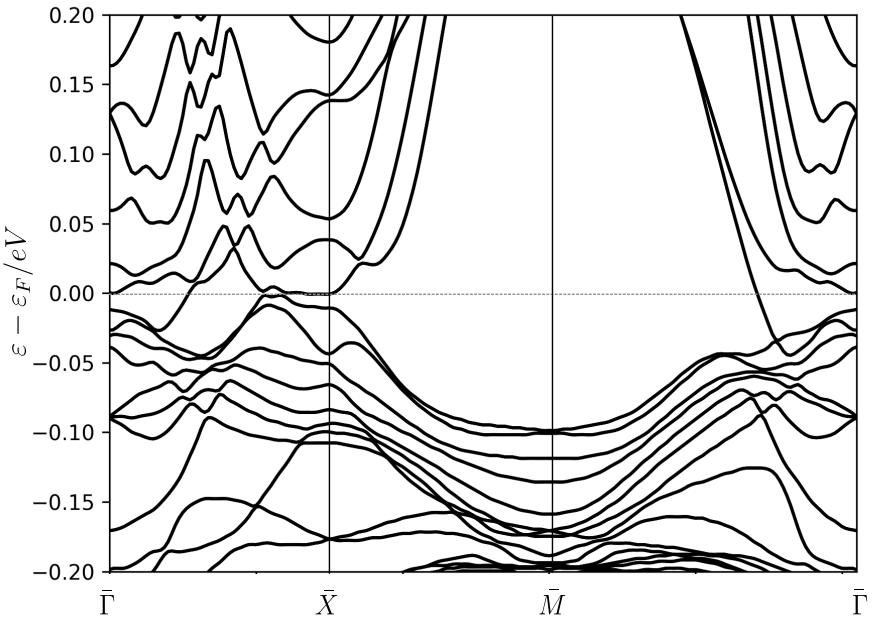

Figure D.6: The DFT slab band structure with 6 full layers featuring Boron termination. The $\bar{M}$ point bands do not contribute, in accordance with the main text.

isolating the band in the DFT calculation which crosses the Fermi level and numerically differentiating, as in the example depicted in figure D.7. The numerical differentiation is sensitive to the grid of k-points so I only give velocities to a precision 50 meVÅ. It is possible to exactly define velocities for Wannier tight binding models but this is not implemented in the software used to generate the slab models, so I used this method there also.

Because the electrostatic renormalisation is on order the size of the gap, the part of the band which crosses the Fermi level strongly depends on the local electrostatics, renormalising the band velocity significantly. The velocities are tabulated, from bands evaluated at 30 k-points:

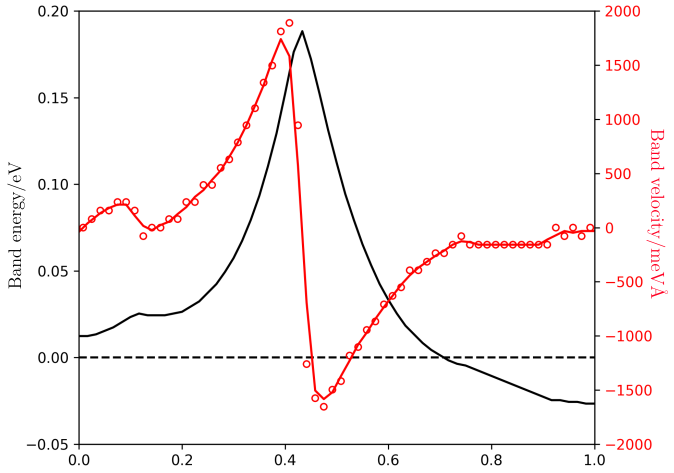

Figure D.7: Demonstration of the procedure used to estimate the Fermi velocities of the DFT models. The band crossing the Fermi energy is isolated and numerically differentiated at 60 k-points, plotted as red circles in between each pair of k-points. This can be obtained with smoothing with a Savitsky-Golay derivative, window length 4 and polynomial order 2, plotted as a red line.

DFT model	**Fermi velocity/meVÅ**
Unrelaxed, 6 layers	250
Unrelaxed, 8 layers	350
Relaxed, 6 layers	850
Relaxed, 8 layers	800

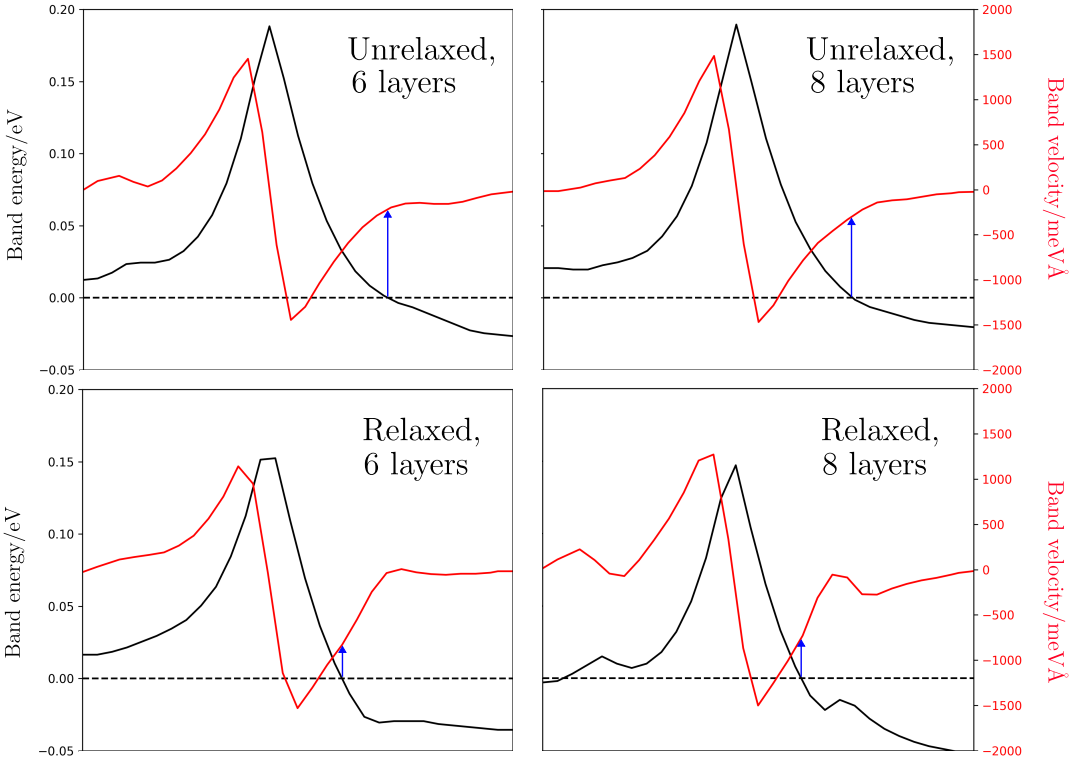

Figure D.8: Estimating the Fermi velocities of the $\bar{X}$ point Dirac cone. The shape and curvature of the band is affected by the renormalisation; because the renormalisation is on order the size of the gap, the Fermi velocity is strongly affected. On each figure the blue arrow shows the point the band crosses the Fermi level, demonstrating how even relatively minor renormalisations can have an outsize impact on Fermi velocity.

Bibliography

[1] Richard P. Feynman. "There's Plenty of Room at the Bottom". In: *Feynman and computation*. CRC Press, 2018.

[2] Arieh Aviram and Mark A. Ratner. "Molecular rectifiers". In: *Chemical Physics Letters* 29.2 (1974), pp. 277–283. URL: https://www.sciencedirect.com/science/article/pii/0009261474850311.

[3] Mickael L. Perrin, Enrique Burzurí, and Herre S. J. van der Zant. "Single-molecule transistors". en. In: *Chemical Society Reviews* 44.4 (2015), pp. 902–919. URL: http://xlink.rsc.org/?DOI=C4CS00231H (visited on 04/06/2020).

[4] Dong Xiang et al. "Molecular-Scale Electronics: From Concept to Function". In: *Chemical Reviews* 116.7 (Apr. 2016). Publisher: American Chemical Society, pp. 4318–4440. URL: https://doi.org/10.1021/acs.chemrev.5b00680 (visited on 03/06/2023).

[5] Michael N. Leuenberger and Daniel Loss. "Quantum computing in molecular magnets". en. In: *Nature* 410.6830 (Apr. 2001). Number: 6830 Publisher: Nature Publishing Group, pp. 789–793. URL: https://www.nature.com/articles/35071024 (visited on 03/29/2023).

[6] Eufemio Moreno-Pineda et al. "Molecular spin qudits for quantum algorithms". en. In: *Chemical Society Reviews* 47.2 (Jan. 2018). Publisher: The Royal Society of Chemistry, pp. 501–513. URL: https://pubs.rsc.org/en/content/articlelanding/2018/cs/c5cs00933b (visited on 03/29/2023).

[7] Andrea Morello et al. “Single-shot readout of an electron spin in silicon”. In: *Nature* 467.7316 (2010), pp. 687–691.

[8] Romain Vincent et al. “Electronic read-out of a single nuclear spin using a molecular spin transistor”. en. In: *Nature* 488.7411 (Aug. 2012). Number: 7411 Publisher: Nature Publishing Group, pp. 357–360. URL: https://www.nature.com/articles/nature11341 (visited on 03/29/2023).

[9] C. Godfrin et al. “Operating Quantum States in Single Magnetic Molecules: Implementation of Grover’s Quantum Algorithm”. In: *Phys. Rev. Lett.* 119.18 (Nov. 2017). Publisher: American Physical Society, p. 187702. URL: https://link.aps.org/doi/10.1103/PhysRevLett.119.187702 (visited on 03/29/2023).

[10] Yulin Chi et al. “A programmable qudit-based quantum processor”. en. In: *Nature Communications* 13.1 (Mar. 2022). Number: 1 Publisher: Nature Publishing Group, p. 1166. URL: https://www.nature.com/articles/s41467-022-28767-x (visited on 04/05/2023).

[11] Fanben Meng et al. “Orthogonally modulated molecular transport junctions for resettable electronic logic gates”. en. In: *Nature Communications* 5.1 (Jan. 2014). Number: 1 Publisher: Nature Publishing Group, p. 3023. URL: https://www.nature.com/articles/ncomms4023 (visited on 04/05/2023).

[12] Sergey Kubatkin et al. “Single-electron transistor of a single organic molecule with access to several redox states”. In: *Nature* 425.6959 (2003), pp. 698–701.

[13] Marco Carlotti et al. “Systematic experimental study of quantum interference effects in anthraquinoid molecular wires”. In: *Nanoscale Adv.* 1 (5 2019), pp. 2018–2028. URL: http://dx.doi.org/10.1039/C8NA00223A.

[14] Gavin David Scott and Douglas Natelson. “Kondo Resonances in Molecular Devices”. In: *ACS Nano* 4.7 (2010). PMID: 20568709, pp. 3560–3579. eprint:

https://doi.org/10.1021/nn100793s. URL: https://doi.org/10.1021/nn100793s.

[15] Hongkun Park et al. "Nanomechanical oscillations in a single-C60 transistor". In: *Nature* 407.6800 (2000), pp. 57–60.

[16] Ferry Prins et al. "Room-Temperature Gating of Molecular Junctions Using Few-Layer Graphene Nanogap Electrodes". In: *Nano Letters* 11.11 (2011). PMID: 22011188, pp. 4607–4611. eprint: https://doi.org/10.1021/nl202065x.

[17] Mark A Reed et al. "Conductance of a molecular junction". In: *Science* 278.5336 (1997), pp. 252–254.

[18] Latha Venkataraman et al. "Dependence of single-molecule junction conductance on molecular conformation". In: *Nature* 442.7105 (2006), pp. 904–907.

[19] Ke Bian et al. "Scanning probe microscopy". en. In: *Nature Reviews Methods Primers* 1.1 (May 2021). Number: 1 Publisher: Nature Publishing Group, pp. 1–29. URL: https://www.nature.com/articles/s43586-021-00033-2 (visited on 03/06/2023).

[20] G. Binnig, H. Rohrer, Ch. Gerber, and E. Weibel. "Surface Studies by Scanning Tunneling Microscopy". In: *Phys. Rev. Lett.* 49.1 (July 1982). Publisher: American Physical Society, pp. 57–61. URL: https://link.aps.org/doi/10.1103/PhysRevLett.49.57 (visited on 04/24/2023).

[21] J. Tersoff and D. R. Hamann. "Theory of the scanning tunneling microscope". In: *Phys. Rev. B* 31.2 (Jan. 1985). Publisher: American Physical Society, pp. 805–813. URL: https://link.aps.org/doi/10.1103/PhysRevB.31.805 (visited on 03/29/2023).

[22] L. A. Bumm et al. "Are Single Molecular Wires Conducting?" In: *Science* 271.5256 (1996), pp. 1705–1707. eprint: https://www.science.org/doi/pdf/10.1126/science.271.5256.1705. URL: https://www.science.org/doi/abs/10.1126/science.271.5256.1705.

[23] Suman Gunasekaran et al. “Near Length-Independent Conductance in Polymethine Molecular Wires”. In: *Nano Letters* 18.10 (2018). PMID: 30187756, pp. 6387–6391. eprint: https://doi.org/10.1021/acs.nanolett.8b02743. URL: https://doi.org/10.1021/acs.nanolett.8b02743.

[24] Nadrian C. Seeman. “DNA Nicks and Nodes and Nanotechnology”. In: *Nano Letters* 1.1 (2001), pp. 22–26. eprint: https://doi.org/10.1021/nl000182v. URL: https://doi.org/10.1021/nl000182v.

[25] Erez Braun, Yoav Eichen, Uri Sivan, and Gdalyahu Ben-Yoseph. “DNA-templated assembly and electrode attachment of a conducting silver wire”. In: *Nature* 391.6669 (1998), pp. 775–778.

[26] Paul W. K. Rothemund. “Folding DNA to create nanoscale shapes and patterns”. en. In: *Nature* 440.7082 (Mar. 2006). Number: 7082 Publisher: Nature Publishing Group, pp. 297–302. URL: https://www.nature.com/articles/nature04586/ (visited on 01/16/2023).

[27] Hartmuth C Kolb, MG Finn, and K Barry Sharpless. “Click chemistry: diverse chemical function from a few good reactions”. In: *Angewandte Chemie International Edition* 40.11 (2001), pp. 2004–2021.

[28] S Helmi and A Ardavan. Private communication. Jan. 2020.

[29] Veikko Linko and J. Jussi Toppari. “Self-Assembled DNA-Based Structures for Nanoelectronics”. en. In: *Journal of Self Assembly and Molecular Electronics* (2012), pp. 101–124. URL: https://www.journals.riverpublishers.com/index.php/JSAME/ (visited on 04/24/2023).

[30] Tali Dadosh et al. “Measurement of the conductance of single conjugated molecules”. In: *Nature* 436.7051 (2005), pp. 677–680.

[31] Sami Franssila. *Introduction to microfabrication*. John Wiley & Sons, 2010.

[32] James MacQueen et al. “Some methods for classification and analysis of multivariate observations”. In: *Proceedings of the fifth Berkeley symposium on mathematical statistics and probability*. Vol. 1. 14. Oakland, CA, USA. University of California Press, Berkeley, 1967, pp. 281–297.

[33] Nobuyuki Otsu. “A Threshold Selection Method from Gray-Level Histograms”. In: *IEEE Transactions on Systems, Man, and Cybernetics* 9.1 (1979), pp. 62–66.

[34] P. V. C. Hough. “Machine Analysis of Bubble Chamber Pictures”. In: *Conf. Proc. C* 590914 (1959). Ed. by L. Kowarski, pp. 554–558.

[35] Dana H Ballard. “Generalizing the Hough transform to detect arbitrary shapes”. In: *Pattern recognition* 13.2 (1981), pp. 111–122.

[36] Dong Xiang et al. “Three-terminal single-molecule junctions formed by mechanically controllable break junctions with side gating”. In: *Nano Letters* 13.6 (2013), pp. 2809–2813.

[37] Wai-Yip Lo et al. “Edge-on Gating Effect in Molecular Wires”. In: *Nano Letters* 15.2 (2015). PMID: 25603411, pp. 958–962. URL: https://doi.org/10.1021/nl503745b.

[38] Mickael L Perrin et al. “Large tunable image-charge effects in single-molecule junctions”. In: *Nature Nanotechnology* 8.4 (2013), pp. 282–287.

[39] John G. Simmons. “Generalized Formula for the Electric Tunnel Effect between Similar Electrodes Separated by a Thin Insulating Film”. In: *Journal of Applied Physics* 34.6 (June 1963). Publisher: American Institute of Physics, pp. 1793–1803. URL: https://aip.scitation.org/doi/10.1063/1.1702682 (visited on 04/05/2023).

[40] M. Büttiker, Y. Imry, R. Landauer, and S. Pinhas. “Generalized many-channel conductance formula with application to small rings”. In: *Phys. Rev. B* 31 (10 1985), pp. 6207–6215. URL: https://link.aps.org/doi/10.1103/PhysRevB.31.6207.

[41] Gianluca Stefanucci and Robert van Leeuwen. *Nonequilibrium Many-Body Theory of Quantum Systems: A Modern Introduction*. eng. New York: Cambridge University Press, 2013.

[42] Juan Carlos Cuevas and Elke Scheer. *Molecular electronics: an introduction to theory and experiment (World scientific series in nanoscience and nanotechnology, vol. 1)*. eng. Singapore: World Scientific Publishing Co. Pte. Ltd, 2010.

[43] A. Mangin et al. "Reduced work functions in gold electromigrated nanogaps". In: *Phys. Rev. B* 80 (23 Dec. 2009), p. 235432. URL: https://link.aps.org/doi/10.1103/PhysRevB.80.235432.

[44] N.F. Mott. "Conduction in glasses containing transition metal ions". In: *Journal of Non-Crystalline Solids* 1 (1 1968), pp. 1–17.

[45] Boris I. Shklovskii and Alex L. Efros. "Variable-Range Hopping Conduction". In: *Electronic Properties of Doped Semiconductors*. Berlin, Heidelberg: Springer Berlin Heidelberg, 1984, pp. 202–227. URL: https://doi.org/10.1007/978-3-662-02403-4_9.

[46] Danny Porath, Alexey Bezryadin, Simon De Vries, and Cees Dekker. "Direct measurement of electrical transport through DNA molecules". In: *Nature* 403.6770 (2000), pp. 635–638.

[47] P. J. de Pablo et al. "Absence of dc-Conductivity in λ-DNA". In: *Phys. Rev. Lett.* 85 (23 Dec. 2000), pp. 4992–4995. URL: https://link.aps.org/doi/10.1103/PhysRevLett.85.4992.

[48] K Andrews. Private communication. Feb. 2023.

[49] Linda A Zotti et al. "Revealing the role of anchoring groups in the electrical conduction through single-molecule junctions". In: *Small* 6.14 (2010), pp. 1529–1535.

[50] Patrick Zwick, Diana Dulić, Herre S. J. van der Zant, and Marcel Mayor. "Porphyrins as building blocks for single-molecule devices". In: *Nanoscale* 13 (37 2021), pp. 15500–15525. URL: http://dx.doi.org/10.1039/D1NR04523G.

[51] Edmund Leary et al. "Detecting mechanochemical atropisomerization within an STM break junction". In: *Journal of the American Chemical Society* 140.2 (2018), pp. 710–718.

[52] Francesca Tavazza et al. "Electron transport in gold nanowires: Stable 1-, 2-and 3-dimensional atomic structures and noninteger conduction states". In: *Phys. Rev. Lett.* 107.12 (2011), p. 126802.

[53] Jun Kondo. "Resistance minimum in dilute magnetic alloys". In: *Progress of Theoretical Physics* 32.1 (1964), pp. 37–49.

[54] P. W. Anderson. "Localized Magnetic States and Fermi-Surface Anomalies in Tunneling". In: *Phys. Rev. Lett.* 17 (2 July 1966), pp. 95–97. URL: https://link.aps.org/doi/10.1103/PhysRevLett.17.95.

[55] Michael Pustilnik and Leonid Glazman. "Kondo effect in quantum dots". In: *Journal of Physics: Condensed Matter* 16.16 (2004), R513.

[56] F. D. M. Haldane. "Scaling Theory of the Asymmetric Anderson Model". In: *Phys. Rev. Lett.* 40 (6 Feb. 1978), pp. 416–419. URL: https://link.aps.org/doi/10.1103/PhysRevLett.40.416.

[57] D. J. Thouless, M. Kohmoto, M. P. Nightingale, and M. den Nijs. "Quantized Hall Conductance in a Two-Dimensional Periodic Potential". In: *Phys. Rev. Lett.* 49 (6 Aug. 1982), pp. 405–408. URL: https://link.aps.org/doi/10.1103/PhysRevLett.49.405.

[58] Liang Fu and C. L. Kane. "Topological insulators with inversion symmetry". In: *Phys. Rev. B* 76 (4 July 2007), p. 045302. URL: https://link.aps.org/doi/10.1103/PhysRevB.76.045302.

[59] C.L. Kane. "Topological Band Theory and the Z2 Invariant". en. In: *Contemporary Concepts of Condensed Matter Science*. Vol. 6. Elsevier, 2013, pp. 3–34. URL: https://linkinghub.elsevier.com/retrieve/pii/B9780444633149000019 (visited on 01/16/2023).

[60] Qing Lin He et al. “Topological spintronics and magnetoelectronics”. In: *Nature materials* 21.1 (2022), pp. 15–23.

[61] Sankar Das Sarma, Michael Freedman, and Chetan Nayak. “Majorana zero modes and topological quantum computation”. In: *npj Quantum Information* 1.1 (2015), pp. 1–13.

[62] A Yu Kitaev. “Unpaired Majorana fermions in quantum wires”. In: *Physics-uspekhi* 44.10S (2001), p. 131.

[63] BS Tan et al. “Unconventional Fermi surface in an insulating state”. In: *Science* 349.6245 (2015), pp. 287–290.

[64] Moon-Sun Nam et al. “How to probe the spin contribution to momentum relaxation in topological insulators”. In: *Nature Communications* 9.1 (2018), p. 56.

[65] Christian E. Matt et al. “Consistency between ARPES and STM measurements on SmB_6”. In: *Phys. Rev. B* 101 (8 Feb. 2020), p. 085142. URL: https://link.aps.org/doi/10.1103/PhysRevB.101.085142.

[66] Felix Bloch. “Quantum mechanics of electrons in crystal lattices”. In: *Zeitschrift fur Phys* 52 (1928), pp. 555–600.

[67] Neil W Ashcroft and N David Mermin. *Solid state physics*. Cengage Learning, 1976.

[68] Mildred S Dresselhaus, Gene Dresselhaus, and Ado Jorio. *Group theory: application to the physics of condensed matter*. Springer Science & Business Media, 2007.

[69] Barry Bradlyn et al. “Topological quantum chemistry”. In: *Nature* 547.7663 (2017), pp. 298–305.

[70] Mikio Nakahara. *Geometry, topology and physics*. CRC press, 2003.

[71] Michel Fruchart and David Carpentier. “An introduction to topological insulators”. In: *Comptes Rendus Physique* 14.9-10 (2013), pp. 779–815. URL: https://doi.org/10.1016%2Fj.crhy.2013.09.013.

[72] David Bachman. *A geometric approach to differential forms*. Springer Science & Business Media, 2012.

[73] B.A. Bernevig and T.L. Hughes. *Topological Insulators and Topological Superconductors*. Princeton University Press, 2013. URL: https://books.google.co.uk/books?id=w0n7JHSSxrsC.

[74] Masatoshi Sato and Yoichi Ando. "Topological superconductors: a review". In: *Reports on Progress in Physics* 80.7 (July 2017). arXiv:1608.03395 [cond-mat], p. 076501. URL: http://arxiv.org/abs/1608.03395 (visited on 01/15/2023).

[75] C. L. Kane and E. J. Mele. "Z_2 Topological Order and the Quantum Spin Hall Effect". In: *Phys. Rev. Lett.* 95 (14 Sept. 2005), p. 146802. URL: https://link.aps.org/doi/10.1103/PhysRevLett.95.146802.

[76] Liang Fu, C. L. Kane, and E. J. Mele. "Topological Insulators in Three Dimensions". In: *Phys. Rev. Lett.* 98 (10 Mar. 2007), p. 106803. URL: https://link.aps.org/doi/10.1103/PhysRevLett.98.106803.

[77] B. Andrei Bernevig, Taylor L. Hughes, and Shou-Cheng Zhang. "Quantum Spin Hall Effect and Topological Phase Transition in HgTe Quantum Wells". In: *Science* 314.5806 (2006), pp. 1757–1761. eprint: https://www.science.org/doi/pdf/10.1126/science.1133734. URL: https://www.science.org/doi/abs/10.1126/science.1133734.

[78] Chao-Xing Liu et al. "Model Hamiltonian for topological insulators". In: *Phys. Rev. B* 82 (4 July 2010), p. 045122. URL: https://link.aps.org/doi/10.1103/PhysRevB.82.045122.

[79] Haijun Zhang et al. "Topological insulators in Bi_2Se_3, Bi_2Te_3 and Sb_2Te_3 with a single Dirac cone on the surface". In: *Nature physics* 5.6 (2009), pp. 438–442.

[80] Feliciano Giustino. *Materials modelling using density functional theory: properties and predictions*. Oxford University Press, 2014.

[81] P. Hohenberg and W. Kohn. "Inhomogeneous Electron Gas". In: *Phys. Rev.* 136 (3B 1964), B864–B871. URL: https://link.aps.org/doi/10.1103/PhysRev.136.B864.

[82] W. Kohn and L. J. Sham. "Self-Consistent Equations Including Exchange and Correlation Effects". In: *Phys. Rev.* 140 (4A 1965), A1133–A1138. URL: https://link.aps.org/doi/10.1103/PhysRev.140.A1133.

[83] Robert G Parr. "Density functional theory of atoms and molecules". In: *Horizons of Quantum Chemistry: Proceedings of the Third International Congress of Quantum Chemistry Held at Kyoto, Japan, October 29-November 3, 1979*. Springer. 1980, pp. 5–15.

[84] Paolo Giannozzi et al. "QUANTUM ESPRESSO: a modular and open-source software project for quantum simulations of materials". In: *Journal of Physics: Condensed matter* 21.39 (2009), p. 395502.

[85] Paolo Giannozzi et al. "Advanced capabilities for materials modelling with Quantum ESPRESSO". In: *Journal of Physics: Condensed matter* 29.46 (2017), p. 465901.

[86] James C. Phillips and Leonard Kleinman. "New Method for Calculating Wave Functions in Crystals and Molecules". In: *Phys. Rev.* 116 (2 1959), pp. 287–294. URL: https://link.aps.org/doi/10.1103/PhysRev.116.287.

[87] DR Hamann, M Schlüter, and C Chiang. "Norm-conserving pseudopotentials". In: *Phys. Rev. Lett.* 43.20 (1979), p. 1494.

[88] Richard M Martin. *Electronic structure: basic theory and practical methods*. Cambridge university press, 2020.

[89] N. Troullier and Jose Luis Martins. "Efficient pseudopotentials for plane-wave calculations". In: *Phys. Rev. B* 43 (3 Jan. 1991), pp. 1993–2006. URL: https://link.aps.org/doi/10.1103/PhysRevB.43.1993.

[90] E. Engel, A. Hock, and S. Varga. "Relativistic extension of the Troullier-Martins scheme: Accurate pseudopotentials for transition-metal elements". In: *Phys. Rev. B* 63 (12 Mar. 2001), p. 125121. URL: https://link.aps.org/doi/10.1103/PhysRevB.63.125121.

[91] Andrea Dal Corso. "Pseudopotentials periodic table: From H to Pu". In: *Computational Materials Science* 95 (2014), pp. 337–350.

[92] J. P. Perdew and Alex Zunger. "Self-interaction correction to density-functional approximations for many-electron systems". In: *Phys. Rev. B* 23 (10 1981), pp. 5048–5079. URL: https://link.aps.org/doi/10.1103/PhysRevB.23.5048.

[93] John P. Perdew and Yue Wang. "Accurate and simple analytic representation of the electron-gas correlation energy". In: *Phys. Rev. B* 45 (23 1992), pp. 13244–13249. URL: https://link.aps.org/doi/10.1103/PhysRevB.45.13244.

[94] John P. Perdew, Kieron Burke, and Matthias Ernzerhof. "Generalized Gradient Approximation Made Simple". In: *Phys. Rev. Lett.* 77 (18 1996), pp. 3865–3868. URL: https://link.aps.org/doi/10.1103/PhysRevLett.77.3865.

[95] John P. Perdew et al. "Restoring the Density-Gradient Expansion for Exchange in Solids and Surfaces". In: *Phys. Rev. Lett.* 100 (13 Apr. 2008), p. 136406. URL: https://link.aps.org/doi/10.1103/PhysRevLett.100.136406.

[96] P. E. Blöchl. "Projector augmented-wave method". In: *Phys. Rev. B* 50 (24 Dec. 1994), pp. 17953–17979. URL: https://link.aps.org/doi/10.1103/PhysRevB.50.17953.

[97] Vladimir I. Anisimov, Jan Zaanen, and Ole K. Andersen. "Band theory and Mott insulators: Hubbard U instead of Stoner I". In: *Phys. Rev. B* 44 (3 July 1991), pp. 943–954. URL: https://link.aps.org/doi/10.1103/PhysRevB.44.943.

[98] Matteo Cococcioni and Stefano De Gironcoli. "Linear response approach to the calculation of the effective interaction parameters in the LDA+ U method". In: *Phys. Rev. B* 71.3 (2005), p. 035105.

[99] Gregory H. Wannier. "The Structure of Electronic Excitation Levels in Insulating Crystals". In: *Phys. Rev.* 52 (3 1937), pp. 191–197. URL: https://link.aps.org/doi/10.1103/PhysRev.52.191.

[100] Christian Brouder et al. "Exponential Localization of Wannier Functions in Insulators". In: *Phys. Rev. Lett.* 98.4 (Jan. 2007). Publisher: American Physical Society, p. 046402. URL: https://link.aps.org/doi/10.1103/PhysRevLett.98.046402 (visited on 01/16/2023).

[101] Horia D. Cornean, Domenico Monaco, and Stefan Teufel. "Wannier functions and Z_2 invariants in time-reversal symmetric topological insulators". en. In: *Reviews in Mathematical Physics* 29.02 (Mar. 2017). arXiv:1603.06752 [cond-mat, physics:math-ph], p. 1730001. URL: http://arxiv.org/abs/1603.06752 (visited on 01/16/2023).

[102] Irene Aguilera, Christoph Friedrich, Gustav Bihlmayer, and Stefan Blügel. "GW study of topological insulators Bi_2Se3, Bi_2Te_3, and Sb_2Te_3: Beyond the perturbative one-shot approach". In: *Phys. Rev. B* 88.4 (2013), p. 045206.

[103] Irene Aguilera, Christoph Friedrich, and Stefan Blügel. "Many-body corrected tight-binding Hamiltonians for an accurate quasiparticle description of topological insulators of the Bi_2Se_3 family". In: *Phys. Rev. B* 100.15 (2019), p. 155147.

[104] Giovanni Pizzi et al. "Wannier90 as a community code: new features and applications". In: *Journal of Physics: Condensed Matter* 32.16 (2020), p. 165902.

[105] Nicola Marzari et al. "Maximally localized Wannier functions: Theory and applications". In: *Rev. Mod. Phys.* 84 (4 Oct. 2012), pp. 1419–1475. URL: https://link.aps.org/doi/10.1103/RevModPhys.84.1419.

[106] Dominik Gresch et al. "Automated construction of symmetrized Wannier-like tight-binding models from ab initio calculations". In: *Physical Review Materials* 2.10 (2018), p. 103805.

[107] M P Lopez Sancho, J M Lopez Sancho, J M L Sancho, and J Rubio. "Highly convergent schemes for the calculation of bulk and surface Green functions". In: *Journal of Physics F: Metal Physics* 15.4 (Apr. 1985), p. 851. URL: https://dx.doi.org/10.1088/0305-4608/15/4/009.

[108] QuanSheng Wu et al. "WannierTools : An open-source software package for novel topological materials". In: *Computer Physics Communications* 224 (2018), pp. 405–416. URL: http://www.sciencedirect.com/science/article/pii/S0010465517303442.

[109] Alekseevich Abrikosov, Lev Petrovich Gorkov, and Igor Ekhielevich Dzyaloshinski. *Methods of quantum field theory in statistical physics*. Courier Corporation, 2012, pp. 51–54.

[110] M. Nauenberg. "Renormalization group solution of the one-dimensional Ising model". In: *Journal of Mathematical Physics* 16.3 (Sept. 1975), pp. 703–705. eprint: https://pubs.aip.org/aip/jmp/article-pdf/16/3/703/7453907/703_1_online.pdf. URL: https://doi.org/10.1063/1.522584.

[111] Shiro Funahashi, Kiyoaki Tanaka, and Fumitoshi Iga. "X-ray atomic orbital analysis of 4f and 5d electron configuration of SmB_6 at 100, 165, 230 and 298 K". In: *Acta Crystallographica Section B: Structural Science* 66.3 (2010), pp. 292–306.

[112] A. Menth, E. Buehler, and T. H. Geballe. "Magnetic and Semiconducting Properties of SmB_6". In: *Phys. Rev. Lett.* 22 (7 Feb. 1969), pp. 295–297. URL: https://link.aps.org/doi/10.1103/PhysRevLett.22.295.

[113] Z Fisk et al. "Kondo insulators". In: *Physica B: Condensed Matter* 223 (1996), pp. 409–412.

[114] Maxim Dzero, Kai Sun, Victor Galitski, and Piers Coleman. "Topological Kondo Insulators". In: *Phys. Rev. Lett.* 104 (10 Mar. 2010), p. 106408. URL: https://link.aps.org/doi/10.1103/PhysRevLett.104.106408.

[115] Tetsuya Takimoto. "SmB_6: A promising candidate for a topological insulator". In: *Journal of the Physical Society of Japan* 80.12 (2011), p. 123710.

[116] Chang-Jong Kang et al. "Band Symmetries of Mixed-Valence Topological Insulator: SmB_6". In: *Journal of the Physical Society of Japan* 84.2 (2015), p. 024722.

[117] Maxim Dzero, Jing Xia, Victor Galitski, and Piers Coleman. "Topological kondo insulators". In: *Annual Review of Condensed Matter Physics* 7 (2016), pp. 249–280.

[118] Feng Lu et al. "Correlated Topological Insulators with Mixed Valence". en. In: *Phys. Rev. Lett.* 110.9 (Feb. 2013), p. 096401. URL: https://link.aps.org/doi/10.1103/PhysRevLett.110.096401 (visited on 05/18/2020).

[119] Zhong Wang, Xiao-Liang Qi, and Shou-Cheng Zhang. "Topological invariants for interacting topological insulators with inversion symmetry". In: *Phys. Rev. B* 85 (16 Apr. 2012), p. 165126. URL: https://link.aps.org/doi/10.1103/PhysRevB.85.165126.

[120] Jinchao Zhao, Peizhi Mai, Barry Bradlyn, and Philip Phillips. *Failure of Topological Invariants in Strongly Correlated Matter*. 2023. arXiv: 2305.02341 [cond-mat.str-el].

[121] Juan Jiang et al. "Observation of possible topological in-gap surface states in the Kondo insulator SmB_6 by photoemission". In: *Nature Communications* 4.1 (2013), p. 3010.

[122] Madhab Neupane et al. "Surface electronic structure of the topological Kondo-insulator candidate correlated electron system SmB_6". In: *Nature Communications* 4.1 (2013), p. 2991.

[123] Nan Xu et al. "Direct observation of the spin texture in SmB_6 as evidence of the topological Kondo insulator". In: *Nature Communications* 5.1 (2014), p. 4566.

[124] Dong-Choon Ryu et al. "Topological surface states on the nonpolar (110) and (111) surfaces of SmB_6". In: *Phys. Rev. B* 103 (12 Mar. 2021), p. 125101. URL: https://link.aps.org/doi/10.1103/PhysRevB.103.125101.

[125] Harris Pirie et al. "Imaging emergent heavy Dirac fermions of a topological Kondo insulator". In: *Nature Physics* 16.1 (2020), pp. 52–56.

[126] Michael M Yee et al. "Imaging the Kondo insulating gap on SmB_6". In: *arXiv preprint arXiv:1308.1085* (2013).

[127] Lin Jiao et al. "Additional energy scale in SmB_6 at low-temperature". In: *Nature Communications* 7.1 (2016), p. 13762.

[128] Zhen Zhang and John T. Yates Jr. "Band Bending in Semiconductors: Chemical and Physical Consequences at Surfaces and Interfaces". In: *Chemical Reviews* 112.10 (2012). PMID: 22783915, pp. 5520–5551. URL: https://doi.org/10.1021/cr3000626.

[129] Gang Li et al. "Two-dimensional Fermi surfaces in Kondo insulator SmB_6". In: *Science* 346.6214 (2014), pp. 1208–1212.

[130] Máté Hartstein et al. "Intrinsic bulk quantum oscillations in a bulk unconventional insulator SmB_6". In: *IScience* 23.11 (2020), p. 101632.

[131] Debanjan Chowdhury, Inti Sodemann, and T Senthil. "Mixed-valence insulators with neutral Fermi surfaces". In: *Nature Communications* 9.1 (2018), p. 1766.

[132] Inti Sodemann, Debanjan Chowdhury, and T. Senthil. "Quantum oscillations in insulators with neutral Fermi surfaces". In: *Phys. Rev. B* 97 (4 Jan. 2018), p. 045152. URL: https://link.aps.org/doi/10.1103/PhysRevB.97.045152.

[133] Wolfgang Schmickler. "The potential of zero charge of jellium". In: *Chemical Physics Letters* 99.2 (1983), pp. 135–139. URL: https://www.sciencedirect.com/science/article/pii/0009261483805454.

[134] Martin C. Gutzwiller. "Effect of Correlation on the Ferromagnetism of Transition Metals". In: *Phys. Rev. Lett.* 10 (5 Mar. 1963), pp. 159–162. URL: https://link.aps.org/doi/10.1103/PhysRevLett.10.159.

[135] Victor Alexandrov, Maxim Dzero, and Piers Coleman. "Cubic Topological Kondo Insulators". In: *Phys. Rev. Lett.* 111 (22 Nov. 2013), p. 226403. URL: https://link.aps.org/doi/10.1103/PhysRevLett.111.226403.

[136] Victor Alexandrov, Piers Coleman, and Onur Erten. "Kondo Breakdown in Topological Kondo Insulators". In: *Phys. Rev. Lett.* 114 (17 Apr. 2015), p. 177202. URL: https://link.aps.org/doi/10.1103/PhysRevLett.114.177202.

[137] J. M. Luttinger. "Fermi Surface and Some Simple Equilibrium Properties of a System of Interacting Fermions". In: *Phys. Rev.* 119 (4 Aug. 1960), pp. 1153–1163. URL: https://link.aps.org/doi/10.1103/PhysRev.119.1153.

[138] G. Binnig, H. Rohrer, Ch. Gerber, and E. Weibel. "7 × 7 Reconstruction on Si(111) Resolved in Real Space". In: *Phys. Rev. Lett.* 50 (2 Jan. 1983), pp. 120–123. URL: https://link.aps.org/doi/10.1103/PhysRevLett.50.120.

[139] Lennart Bengtsson. "Dipole correction for surface supercell calculations". In: *Phys. Rev. B* 59 (19 May 1999), pp. 12301–12304. URL: https://link.aps.org/doi/10.1103/PhysRevB.59.12301.

[140] Junwon Kim et al. "Termination-dependent surface in-gap states in a potential mixed-valent topological insulator: SmB_6". In: *Phys. Rev. B* 90 (7 Aug. 2014), p. 075131. URL: https://link.aps.org/doi/10.1103/PhysRevB.90.075131.

[141] Z.-H. Zhu et al. "Polarity-Driven Surface Metallicity in SmB_6". In: *Phys. Rev. Lett.* 111 (21 Nov. 2013), p. 216402. URL: https://link.aps.org/doi/10.1103/PhysRevLett.111.216402.

[142] Yua A Bychkov and É I Rashba. "Properties of a 2D electron gas with lifted spectral degeneracy". In: *JETP lett* 39.2 (1984), p. 78.

[143] Jin-Jian Zhou et al. "Engineering topological surface states and giant Rashba spin splitting in BiTeI/Bi_2Te_3 heterostructures". In: *Scientific reports* 4.1 (2014), p. 3841.

[144] M. Aono et al. "LaB_6 and SmB_6 (001) surfaces studied by angle-resolved XPS, LEED and ISS". In: *Surface Science* 86 (1979). Proceedings of the International Conference on Solid Films and Surfaces Tokyo, Japan, 5-8 July 1978, pp. 631–637. URL: https://www.sciencedirect.com/science/article/pii/0039602879904436.

[145] Karsten Reuter and Matthias Scheffler. "Composition, structure, and stability of RuO_2 (110) as a function of oxygen pressure". In: *Phys. Rev. B* 65.3 (2001), p. 035406.

[146] Peter Hlawenka et al. "Samarium hexaboride is a trivial surface conductor". In: *Nature Communications* 9.1 (2018), p. 517.

[147] Axel D. Becke. "A new mixing of Hartree–Fock and local density-functional theories". In: *The Journal of Chemical Physics* 98.2 (Jan. 1993), pp. 1372–1377. eprint: https://pubs.aip.org/aip/jcp/article-pdf/98/2/1372/11046762/1372_1_online.pdf. URL: https://doi.org/10.1063/1.464304.

[148] Mark S. Hybertsen and Steven G. Louie. "Electron correlation in semiconductors and insulators: Band gaps and quasiparticle energies". In: *Phys. Rev. B* 34 (8 Oct. 1986), pp. 5390–5413. URL: https://link.aps.org/doi/10.1103/PhysRevB.34.5390.

[149] Piers Coleman. *Introduction to many-body physics*. Cambridge University Press, 2015.

[150] C. Cercignani, V. I. Gerasimenko, and D. Ya. Petrina. "The BBGKY Hierarchy". In: *Many-Particle Dynamics and Kinetic Equations*. Dordrecht: Springer Netherlands, 1997, pp. 7–65. URL: https://doi.org/10.1007/978-94-011-5558-8_2.

[151] C Lacroix. "Density of states for the Anderson model". In: *Journal of Physics F: Metal Physics* 11.11 (1981), p. 2389.

[152] Yigal Meir, Ned S. Wingreen, and Patrick A. Lee. "Transport through a strongly interacting electron system: Theory of periodic conductance oscillations". In: *Phys. Rev. Lett.* 66 (23 1991), pp. 3048–3051. URL: https://link.aps.org/doi/10.1103/PhysRevLett.66.3048.

[153] JQ You and HZ Zheng. "Electron transport through a double-quantum-dot structure with intradot and interdot coulomb interactions". In: *Phys. Rev. B* 60.19 (1999), p. 13314.

[154] B Novakovic and I Knezevic. "Quantum master equations in electronic transport". In: *Nano-Electronic Devices: Semiclassical and Quantum Transport Modeling* (2011), pp. 249–287.

[155] D. A. Ryndyk, R. Gutié rrez, B. Song, and G. Cuniberti. "Green Function Techniques in the Treatment of Quantum Transport at the Molecular Scale". In: *Springer Series in Chemical Physics*. Springer Berlin Heidelberg, 2009, pp. 213–335. URL: https://doi.org/10.1007%2F978-3-642-02306-4_9.

[156] Paul Adrien Maurice Dirac. "Quantised singularities in the electromagnetic field". In: *Proceedings of the Royal Society of London. Series A, Containing Papers of a Mathematical and Physical Character* 133.821 (1931), pp. 60–72.

[157] Masatsugu Minami. "Dirac's monopole and the Hopf map". In: *Progress of Theoretical Physics* 62.4 (1979), pp. 1128–1142.

[158] Edward Witten. "Three lectures on topological phases of matter". In: *La Rivista del Nuovo Cimento* 39 (2016), pp. 313–370.